University of Stavanger

Faculty of Science and Technology

MASTER'S THESIS

Study program/ Specialization: Offshore Technology Marine and Subsea	Spring semester, 2016 Open / ~~Restricted access~~
Writer: Preben Bøgwald	..... (Writer's signature)
Faculty supervisor: Professor Arnfinn Nergaard External supervisor(s):	
Thesis title: Concept evaluation of tethered station keeping system for a mono-hull floating offshore vertical axis wind turbine	
Credits (ECTS): 30	
Key words: Tension Leg Platform Vertical Axis Wind Turbine Submerged docking station Hydrodynamic modelling Dynamic analysis Parameter analysis Renewable energy	Pages: 193 + enclosure: 15 + CD Stavanger, 14.06.2016 Date/year

Front page for master thesis
Faculty of Science and Technology
Decision made by the Dean October 30th 2009

(Page left intentionally blank)

Abstract

The objective of this thesis is to perform a concept evaluation of novel station keeping concept for offshore vertical axis wind turbines based on the well-known tension leg platform (TLP) principle. The main characteristic of this concept is the two-stage approach of installing the turbine offshore. In general terms the concept consists of four major components: the turbine, cylindrical floater, submerged docking station and an array of vertical top tensioned tethers. The idea behind this concept is that the docking station is towed out to the field and attached to the tethers prior to the float out operation of the turbine. The turbine is towed out on separate cylindrical floater, which is mated to the docking station, situated at a certain depth below sea level. The top-tensioning of the tendons is achieved in two stages, first by de-ballasting the docking station to maintain a level of pre-tension prior to the mating procedure with the turbine floater. The turbine floater, which also maintains a certain mass of temporary ballast to achieve operating draft, is later used to achieve the desired pre-tension for the operating condition after installation. This concept was applied for patenting in Norway by Prof. A. Nergaard on 31st June 2009 and granted 20th September 2010 (Patent no. 329254).

In this thesis the aim was to determine a set of promising floaters and docking stations by assessing relevant parameters based on spreadsheet calculations. The key considerations here were sufficient pre-tension capacity and stability in float out for a vertical axis wind turbine with a rated power of 2.3 MW. Adjustments were made to the principal dimensions such as the diameters, drafts, pontoon radii and ratios of permanent ballast to temporary ballast to achieve stable floaters and docking stations that satisfied a set of design criteria. Due to limited available research on this particular concept, the design criteria were set based on existing information on horizontal axis wind turbine TLPs, along with several engineering assumptions.

In general terms the work presented in this thesis cover three principal stages: spreadsheet analysis of parameters, hydrodynamic modelling and dynamic simulation in one operational and extreme sea state. The parameter study resulted in the selection of three cases with combined displacements ranging between 6047 and 9811 m^3, with associated pre-tension capacities per tendon between 5.3 and 10 MN. Following the selection of cases, work was done to determine the frequency dependent added mass and potential damping properties of each case along with the specification of load and displacement RAOs. These properties were used to create a new set of vessels in OrcaFlex to assess the motion characteristics and tendon tension for the two aforementioned environmental conditions. The analysis conducted in this thesis was limited to linear effects only, i.e. second order effects were neglected.

The objective of the thesis was to evaluate this concept based on the results obtained from the dynamic simulation in terms of loads at the floater-docking station connection, the tension in the tendons under both environmental conditions and assess the motion characteristics of each case.

The results obtained for the selected cases resulted in slack tendons in the severe sea state corresponding to a 50-year storm, which indicated that the selected cases did not satisfy the requirement for this type of station keeping concept. Despite the fact that none of the cases were sufficient to survive the storm, some trends were uncovered for possible further work on this concept to reach a suitable combination of parameters. The main problems that were found for this concept was the bending moment at the connection between the floater and docking station, and the occurrence of slack. In the 50-year storm, maximum bending moments between 270 and 320 MNm were found, exceeding the capacity of standard collet connectors, which was the envisioned connection method in this thesis.

In regards to slack tendons, it was found here that an increased pontoon radius (>35 m) would yield significantly improved results in terms of avoiding slack, which coincided with the studied literature. A reduction in draft of the floater component, which in this thesis ranged between 50 and 60 m, would also result in improvements for both the connection load and the loss of tension in the downwind tendon. Higher pre-tension was also found to give lower variation in tendon load, coinciding with the studied literature

It should be noted that the work of Bachynski, E. E. on *Dynamic analysis of Horizontal Axis Wind Turbine TLPs* has been of great value, in relation to this thesis, to establish the necessary background theory on the TLP concept for wind turbines. In addition to this, the work has also provided valuable insight into the determination of preliminary design criteria for the proposed design.

Acknowledgements

This thesis marks the end of a five-year study program in Offshore Technology Marine and Subsea at the University of Stavanger.

First I would like to thank my thesis supervisor, Professor Arnfinn Nergaard, for proposing the topic as well as providing guidance throughout the course of this thesis. It has been an interesting and challenging experience to study this novel concept. In addition to this I would also like to thank Professor Muk Chen Ong for helping obtain the DNV HydroD software license, as well as looking over some of the results obtained from the preliminary trials in HydroD and OrcaFlex.

I would also like to thank my family and friends for their tremendous support throughout this semester and the course of my studies here at the University of Stavanger. The hard work and gruelling hours put into this thesis could not have been done without their support.

Last but not least, I would also like to acknowledge the work of Bachynski, E. E., which has been particularly helpful in providing valuable insight into the complex nature of the tension leg platform for offshore wind turbines. This work helped to establish the design criteria for pre-design work and also provided a useful means of comparison for results regarding TLP characteristics.

Preben Bøgwald

University of Stavanger, 2016

Norway

Table of Contents

Abbreviations

	Name
BDS	Buoyant Docking Station
BM	Buoyancy Module
CAD	Computer Aided Design
CC	Central Column
CFD	Computational Fluid Dynamics
COB	Centre of Buoyancy
COG	Centre of Gravity
DNV	Det Norske Veritas
DOF	Degree of Freedom
EC	Environmental Condition
FEM	Finite Element Method
FQUAD	Forced quadrilateral element
HAWT	Horizontal Axis Wind Turbine
ID	Identification
JONSWAP	Joint North Sea Wave Observation Project
LC	Load Case
LWT	Linear Wave Theory
Ms	Mesh setting
NORCOWE	Norwegian Centre of Offshore Wind Energy
OD	Outer Diameter
PBF	Permanent Ballast Fraction
PO	Pontoon
QTF	Quadratic Transfer Function
RAO	Response Amplitude Operator
SWL	Still Water Level
TLP	Tension Leg Platform
TLPWT	Tension Leg Platform Wind Turbine
VAWT	Vertical Axis Wind Turbine
VIV	Vortex induce vibrations
WADAM	Wave Analysis by Diffraction and Morison Theory
WS	Wet Surface
WT	Wall Thickness

Nomenclature

Note that most symbols are explained under their respective equation in the document. The table below serves as a summary of selected symbols with an accompanying explanation.

Symbol	Explanation/description
V_∞	Far field undisturbed wind velocity
λ_t	Tip speed ratio
ω	Angular frequency
M	Mass
I	Moment of inertia
I_{WP}	Water plane area moment of inertia
∇	Displaced volume
$\overline{\mathrm{KB}}$	Distance to centre of buoyancy from keel
$\overline{\mathrm{BM}}$	Distance to metacentre from centre of buoyancy
$\overline{\mathrm{KG}}$	Distance to centre of gravity from keel
$\overline{\mathrm{GM}}$	Metacentric height
$\overline{\mathrm{BG}}$	Distance to centre of gravity from centre of buoyancy
ρ	Density of medium
M_R	Righting moment
M_O	Overturning moment
U_{10}	1-hour reference wind velocity at 10 m reference height
F_W	Wind force
ϕ	Velocity potential function
ξ_0	Regular wave amplitude
k	Wave number
u	Horizontal wave particle velocity
λ	Wave length
T	Period
ϵ	Phase angle
$S(\omega)$	Wave spectra as a function of frequency
H_s	Significant wave height
T_p	Peak period
ω_p	Spectral peak frequency
γ	Spectral peak shape
σ_s	Spectral width parameter
A_{wp}	Water plane area
$F_{t,0}$	Pre-tension in tendon
l_0	Initial tendon length
E_t	Modulus of elasticity of the tendon material
a_t	Transverse added mass
H	Wave height
D	Diameter
$\mathbf{M}$	Mass matrix
$\mathbf{A}(\omega)$	Added mass matrix as a function of frequency
$\mathbf{B}(\omega)$	Potential damping matrix as a function of frequency
$\mathbf{B_V}$	Viscous damping matrix
$\mathbf{C}$	Hydrostatic stiffness matrix
$\mathbf{K}$	Mooring stiffness matrix
$\boldsymbol{\eta}$	Position vector (based on the degrees of freedom)
T_n	Natural period
$S_{\eta,i}(\omega)$	Response spectrum in a certain degree of freedom *i*

1 Introduction

1.1 Sources of energy and climate change

Climate change and pollution are some of the major challenges associated with today's production of energy and efforts are being made to make the transition from conventional fossil fuels to reduce emissions to such an extent that the average temperature does not reach/exceed the 2°C mark [1]. The main contributor to climate change is the emission of carbon dioxide and other associated exhaust particles that are being vented into the earth's atmosphere as a by-product from the burning of fossil fuels for energy. Fossil fuels, which is a common term used for oil, natural gas and coal, make up most of the so-called energy mix at present as shown in the chart (2013) below [2].

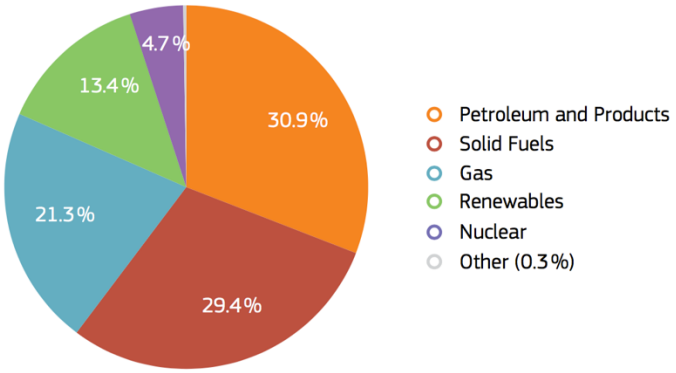

Figure 1-1: World energy production by fuel for 2013 (Source: IEA, August 2015 retrieved from [2])

The figure above presents the world energy production divided into categories depending on its source. As can be observed from this figure, as per 2013, the energy derived from renewable sources amounted to 13.4% which is expected to increase significantly in the coming years in order to reduce emissions. The renewables category presented in the chart above includes sources such as hydroelectric power, solar energy and wind.

1.2 Wind energy

Wind energy plays an important role in the energy mix in the European Union. According to the EWEA, in 2015 15.6% of supplied power came from wind amounting to a total of 141.6 GW. At present most of the electricity from wind is generated by horizontal axis wind turbines (HAWT) situated onshore, which equates to about 131 GW of the total supplied power from wind. The offshore wind capacity is currently at 11 GW [3].

Several HAWTs have been installed offshore in shallow waters where the average water depth for offshore wind farms in 2015 was 27.2 m according to EWEA [4] in the North Sea using bottom-fixed installations such as the monopile, tripod, jacket structures etc. An illustration of the various foundations for offshore wind turbines has been provided in Figure 1-2. As of 2015 the majority of the 3313 offshore wind turbines were installed on monopile foundations (80.2%) where floating alternatives only amounted to 0.1% according to statistical reports for 2015 by EWEA [4].

As of yet there have not been installed any floating offshore wind farms that supply electric power to shore except for a few conceptual turbines such as Statoil's 2.3 MW Hywind prototype situated 10 km off the coast of Karmøy in Norway [5]. The turbine was installed in 2009 in a water depth of approximately 200 m. The Hywind prototype is a HAWT supported by a floating ballast stabilized substructure referred to as a SPAR buoy (refer to the figure below) categorized with a deep draft and low centre of gravity. Other examples of floating offshore wind turbines such as the semi-submersible and the tension leg platform have been presented in the figure below with associated turbine sizes and allowable water depths.

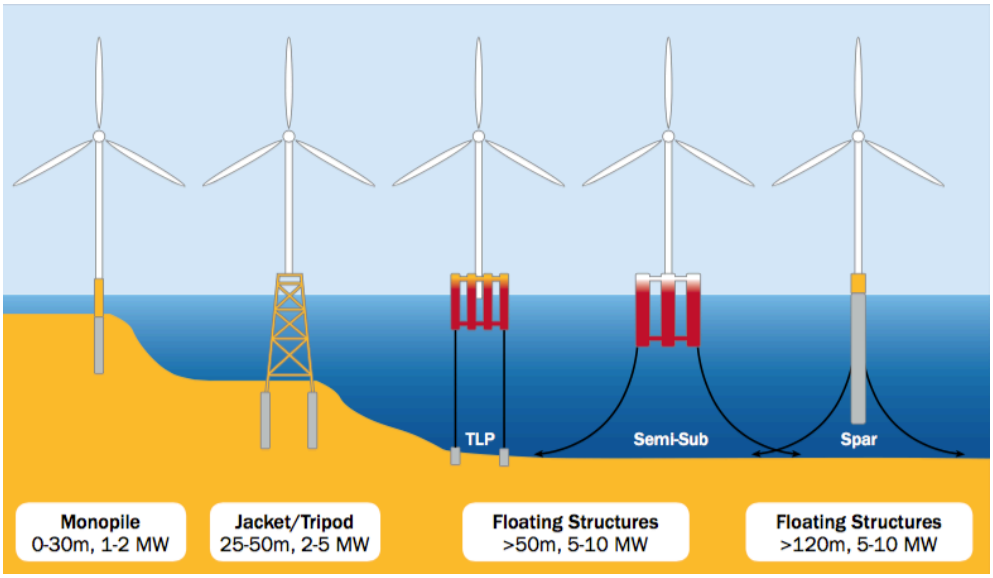

Figure 1-2: Illustration of different offshore wind turbine foundations [6]

2 Objective

2.1 Introduction to concept

The objective of this thesis is to conduct a concept evaluation study of a tension leg platform substructure (TLP) using a novel mating/installation concept. The turbine is kept in position using a permanently submerged tethered docking station. The concept, in principle, consists of four major structural components namely the mono-hull floater, the buoyant docking station (BDS), an array of tensioned tethers (e.g. hollow steel tubes under tension) and an anchoring system at the seabed.

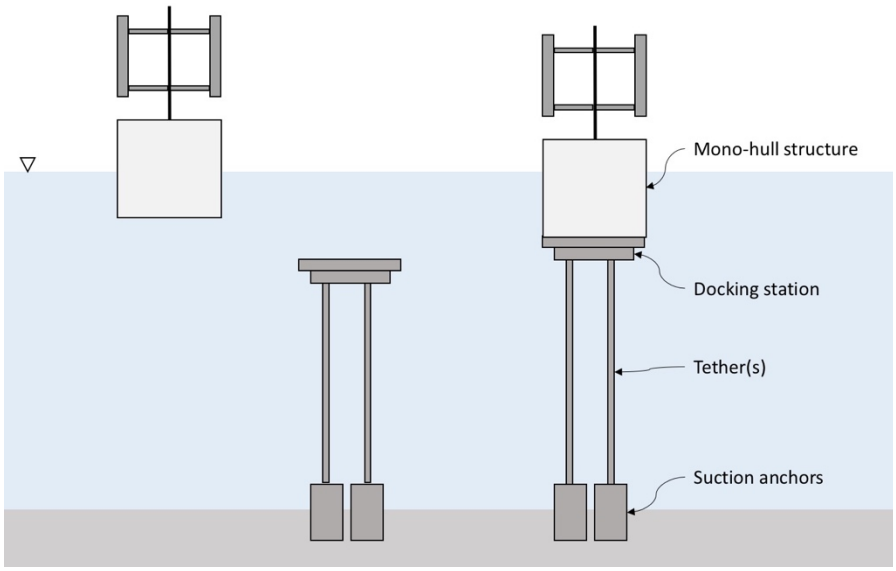

Figure 2-1: Illustration of the mating concept adapted from sketch by Nergaard, A. [7]

The superior motion characteristics of the TLP concept is one of the main drivers for this type of mooring system due to lower motion-induced loadings on the turbine tower (for HAWT) [8]. The concept will allow for installation of the anchoring system before the mono-hull floater arrives on site with the wind turbine installed prior to float-out and facilitating an efficient connection to the anchor system. The anchoring system is de-coupled from the main floater until physical connection is established between the floater and the buoyant docking station. Another possibility with this design is to facilitate the installation of offshore wind turbines in deeper waters where conventional catenary mooring chains would require significant increases in hull displacement in order to carry the added weight of the suspended chains [9].

This concept aims to achieve a simpler installation of offshore wind turbines with a potentially limitless depth rating [10] and reduced subsea footprint compared with a conventional catenary mooring system. Another important factor that has been considered in regards to this concept is the possibility of interchangeable floater systems, where defect turbines can be replaced by disconnecting it from the docking station, installing a backup turbine and towing the defect turbine with the associated floater back to shore for sheltered maintenance.

2.2 Thesis objective

The objective of this thesis is to evaluate the patented concept presented in the the previous section for a 2.3 MW vertical axis wind turbine. The evaluation process is to be conducted with focus on key performance parameters including: general motion characteristics, tension variation in the tendons and loads at the connection point. These performance characteristics are to be evaluated based on a set of dynamic simulations, in the linear domain, where both operational and survival conditions are to be analysed. In order to provide a basis for comparison, three cases are to be identified, where each case consists of a mono-hull floater and a docking station, with certain structural dimensions. In addition to this, tendon properties shall also be established for the dynamic simulation with focus on cross-sectional yielding and neutral buoyancy. The tendons are to be held constant in this thesis and will not be optimized.

The structural dimensions are to be determined based on a parametric study, where factors such as tow-out stability, pre-tension capacity, achievable submergence, ballast volumes etc. are to be evaluated. The parametric study will be carried out by spreadsheet calculations and shall provide a basis for establishing the three cases for further modelling and assessment under both an operational and a 50-year storm condition. The case selection process shall be carried out by reference to design criteria, which are to be based on existing literature (such as [11]) and/or engineering assumptions.

In regards to the turbine section, this is to be based on estimated properties with reference to the 2.3 MW turbine in NORCOWE reports [12] and [13]. The turbine modelling in this thesis is limited to establishing inertial properties and estimates for the static wind load acting on the structure. The dynamic analyses are limited to the substructures only, i.e. the components in contact with the water; hence a simplified wind model is to be implemented without modelling the turbine. Note that marine operations are not to be analysed in this thesis as this would exceed the scope of work.

In essence the thesis will answer the question whether or not this concept can be implemented technically through a quantitative approach, based on results obtained from a linearized model.

2.3 Scope of work

The scope of work for this thesis is somewhat broad in terms of the number of elements to be covered considering the fact that this is a novel station keeping concept in the field of offshore wind turbines. As presented in Section 2.1, the concept features a TLP docking station with a dis-connectable, separate structure, housing the generator as well as providing a floating platform for the vertical axis wind turbine (VAWT). This creates a requirement for float-out stability for both components in a separated state but also requires that the mated structure shall be able to resist the imposed environmental loads. This is a significant engineering challenge and in order to address this issue in the given time frame it was necessary to limit the scope of work to the determination of a set of three promising floaters and docking stations as well as conducting a limited number of linearized dynamic simulations.

The analysis is limited with focus on the substructures, i.e. the components in contact with water, where a simplified model for the wind turbine is used. The simplified wind turbine model does not take into account the dynamic aspects of the wind turbine, hence a static, yet representative, applied load is used to represent the total load contribution from wind. The structural load from power generation is represented by a statically applied torque representative of the rated power output for the 2.3 MW VAWT. The environmental conditions to be studied had to cover one operational condition (with torque) and one storm condition (parked condition, no torque).

Dynamic simulations require information about the structures' hydrodynamic properties, which means that a set of hydrodynamic analyses have to be carried out for each selected case. Subsequently there are a number of deliverables required to satisfy this scope of work, which are presented in the figure below.

Figure 2-2: Deliverables for scope of work

In order to determine the cases (preliminary design) to be analysed further it is necessary to first develop a set of design criteria for use in early design work. The design criteria are to be set with reference to existing work in the field of offshore TLP wind turbines. Since there are no existing structures that feature the same concept analysed here, it is necessary to base the design criteria on existing single-component TLPWT systems, making engineering assumptions where needed.

After having set the design criteria, the next step in the scope of work is to perform a parametric analysis by spreadsheet calculations, where a number of parameter combinations were to be analysed. The selection of promising floaters and docking stations are to be selected based on this parametric study (part of the preliminary design deliverable). Due to the extensive number of variables present it is necessary to limit the parametric study. These limitations are discussed in the concept description and parameter definition chapter.

The next steps in the scope of work are to conduct the hydrodynamic analyses and dynamic simulations for the promising cases. The results from these analyses provide the basis for the evaluation of the concept. In addition to this, recommendations for future work are also to be provided based on the conclusions drawn from the analyses.

3 Thesis structure

The thesis is structured such that all relevant background theories are presented and explained prior to establishing the models for the different concepts. The background theory section will cover wind turbines with reference to both HAWT and VAWT, elements of wind theory, wave theory, hydrodynamics and associated loadings, stability of vessels, station keeping and dynamics as well as providing some insight into the workings of the simulation software package.

After the presentation of the state of art and background theories, a chapter will cover the general properties and characteristics of TLPs with particular reference to earlier work in literature. Following this is a description of the concept in greater detail with focus on each of the four main system components: hull, BDS, tethering system and the anchoring system. The relevant parameters are also defined in this chapter.

Following the description of the concept, the estimated model for the VAWT (primarily limited to inertial properties) will be presented. The VAWT model is assumed constant across all the identified, plausible combinations of substructures and docking stations. The description of the concept is also followed by chapters covering each component in the system in greater detail referring to parameter ranges in the design space, which parameters are active throughout the analysis, and a presentation of the basic functional requirements for the docking station. Although the connection system is not to be analysed in great detail here, an idea for a possible connection method is presented, which may be analysed in the future.

The environmental conditions are presented following the concept description. These are largely based on [11] with one exception for the primary environmental condition (EC1), which was an arbitrary mild condition used for estimating the static pitch angle during the preliminary design phase.

A description of the analysis procedure with reference to selected aspects of the spreadsheet analysis, hydrodynamic modelling (HydroD) and general setup of the OrcaFlex model is provided following the definition of the environmental conditions. In the analysis procedure chapter, focus has been given to the process of creating the hydrodynamic model in HydroD as well as building a new vessel type in OrcaFlex, along with a description of the general tendon arrangement. This chapter also includes information regarding the importance of mesh densities with accompanying illustrations.

Due to the number of steps in the analysis procedure, the results from the spreadsheet stage are presented prior to the identification of cases. The design criteria used during the spreadsheet analysis are provided alongside the results for ease of reference. The spreadsheet stage is a critical step in defining the promising cases that are to be taken further for hydrodynamic analysis and dynamic simulation. An alpha-numeric numbering system is also presented, which will be used for consistent referencing to the selected cases and mesh models throughout this thesis. The numbering system is primarily used in the results and discussion phase.

The structural/inertial properties of the selected cases are presented under the identification of cases chapter for the individual structures (floaters and docking stations) and possible combinations of these (combined cases). Since the hydrodynamic modelling stage requires the mated system to be ballasted to its operational draft, in the absence of a mooring system, inertial properties are provided including temporary ballast. In the dynamic simulation stage, the inertial properties need to be specified excluding temporary ballast, hence an additional set of inertial properties are presented to reflect this state.

Following this chapter, the results for both the hydrodynamic analysis and dynamic simulation are provided on a case-by-case basis. This has been selected in order to maintain consistent flow in the analysis procedure. After the results for each case has been presented, the general discussion of trends and effects across the cases are provided. In this sections comparisons are made between the cases to identify effects associated with a change in a parameter or series of parameters where possible. In the discussion chapter, limitations and sources of errors are also discussed.

Based on the explanations and identified trends uncovered in the discussion a conclusion is provided with reference to any recommendations for future work. Other relevant information is included in the appendices, which are stored electronically (Appendix A) and attached in paper form at the end of the main document (Appendices B, C, D).

4 State of art

4.1 Hywind

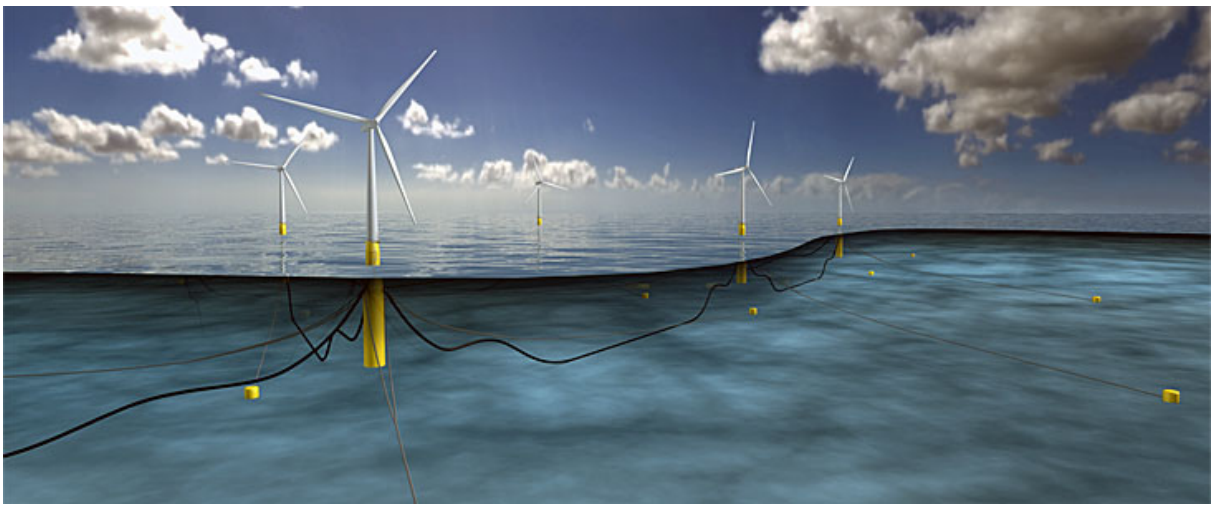

Figure 4-1: Hywind floater concept [14]

The Hywind concept is a horizontal axis offshore wind turbine situated off the coast of Karmøy in Norway, developed by Statoil. The concept has the following dimensions and properties as listed in the table below.

Table 4-1: Hywind pilot facts [5]

	Value	Unit
Turbine size	2.3	MW
Turbine weight	138	tons
Turbine height	65	m
Rotor diameter	82.4	m
Draft hull	100	m
Displacement	5300	m^3
Diameter at water line	6	m
Diameter of submerged body	8.3	m
Water depths	200	m
Mooring	3	lines

The floater concept is a mono-hull SPAR buoy with draft and diameter as presented in the table above. The system is kept on location by three catenary mooring lines. The structure was built as a proof of concept, which has been taken further to develop a 6 MW turbine, which will be implemented off the coast of Scotland in waters greater than 100 m [14]. The wind park to be installed near Buchan Deep will have a total power capacity of 30 MW (5 turbines).

4.2 Gwind

Figure 4-2: Gwind VAWT floater concept [15]

The Gwind floater concept is a VAWT currently at the prototype stage. The current prototype is called the Spinwind 1, and is a small scale VAWT which has been built as a proof of concept [15]. The company believes that this concept will be the best option for offshore wind turbines, as a competitor to the more traditional HAWT such as the Hywind floater concept from Statoil. Gwind states that the superior characteristics of this type of floater arise due to fact that the heavier components are positioned lower in the floater compared to the HAWT-type, meaning that the design may be optimized with smaller floaters due to the reduced need for low loads [15].

4.3 PelaStar TLP

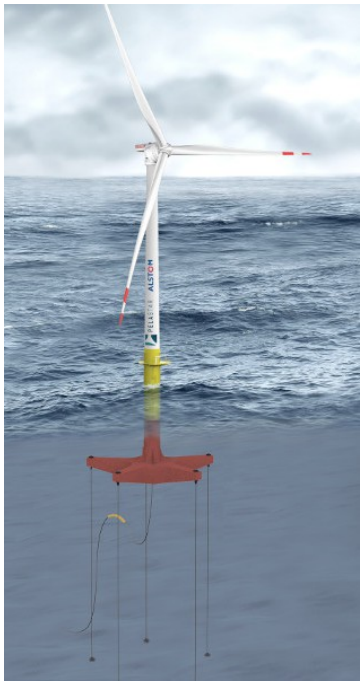

Figure 4-3: PelaStar TLP [16]

The PelaStar offshore TLP wind turbine system is presented in the figure above. This system consists of an upper column which is mated to the turbine tower, a lower hull with five arms with redundancy to avoid single point failure [16]. The tendons used for this prototype TLP are made of fibre rope attached to the ends of the arms as illustrated in the figure. The power cable is connected to the lower hull by a flexible pipe as can be observed from the figure [16].

The design features in-shore installation of the topside and substructure for simpler offshore installation. According to PelaStar LLC this design is "demonstrator ready" and it is estimated/planned that this type of design may be installed near Cornwall in 2016-2017 [16].

4.4 Tracy TLP

Figure 4-4: Tracy TLP [17]

In 2007 Tracy, C. conducted a parametric analysis of floating wind turbines, where several different floater shapes were analysed ranging from shallow draft, large diameter floaters, to large draft, small diameter floaters [17]. The analysis was conducted using several different programs: LINES, WAMIT and FAST, but these will not be covered in detail here. The water depths in Tracy's thesis was generally 200 m, with displacements ranging between 5250 to 14350 m^3 for two different sea states [17]. Note that the wind turbine model was NREL 5 MW.

4.5 Bachynski TLP

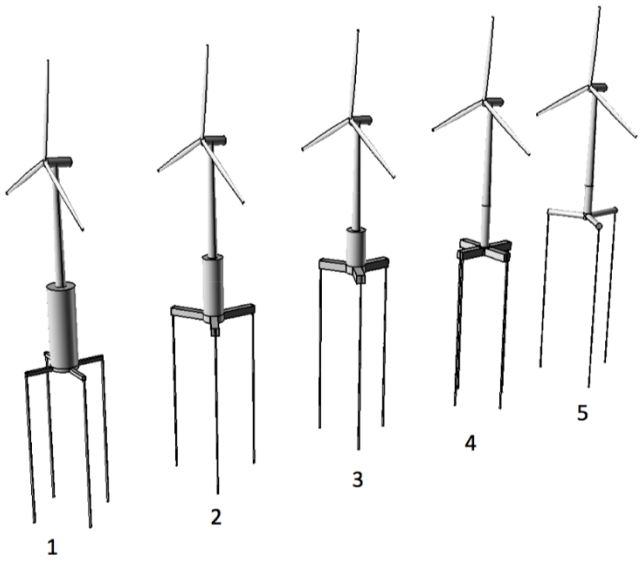

Figure 4-5: Bachynski TLPWTs [11]

Similarly, to Tracy, C., Bachynski, E. E. also conducted a parametric TLPWT analysis covering 5 baseline TLPWT designs. These have been shown in the figure below. These designs had displacements ranging between 5655-11866 m^3 with diameters in the waterline varying between 6.5 and 18.0 m. The drafts ranged between approximately 28 and 55 meters. The pre-tensions varied between 5 and 8.2 MN, with varying pontoon cross-sections and dimensions. The designs analysed by Bachynski, E. E. were TLP structures aimed at 5 MW offshore HAWT [11]. This set of TLPWTs are revisited in Section 6.

5 Background theory

In this section the necessary background theory for the analysis will be covered. Due to scope limitations and a primary focus on subsea systems the theoretical background for wind turbines and wind theory are limited to simple force and moment calculations based on the projected area of the affected structures and the distance from action vector to the centre of gravity of the structure. The station keeping concept is primarily intended for use with offshore vertical axis wind turbines, but the basic characteristics of both HAWTs and VAWTs are covered in the following section. In addition to this, motions of vessels, wave theory, wave loads on structures and basic dynamic principles are covered.

5.1 Wind turbines

Wind turbines are generally divided into two categories depending on their axis of rotation: horizontal- (HAWT) and vertical axis wind turbines (VAWT). The turbines can also be grouped into two sub-categories depending on the environment in which they are installed namely: onshore and offshore. The following sub-chapters will cover the basic traits of both the HAWT and the VAWT.

5.1.1 Horizontal axis wind turbines (HAWT)

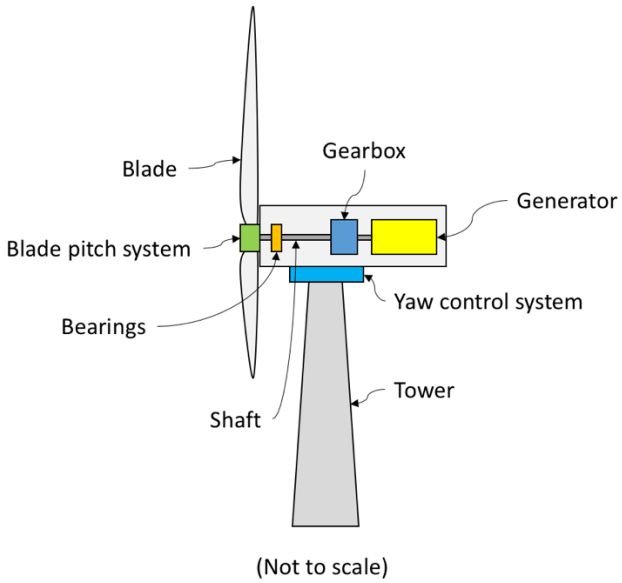

Figure 5-1: Simplified illustration of the components in a HAWT (adapted from [18])

The horizontal axis wind turbine consists of three basic systems: rotor, tower and foundation. In the figure above the tower and rotor system have been illustrated based on Figure 3.5 in Ch. 3 in [18]. The rotor consists of angled blades, usually three spaced at 0°, 120° and 270° (angles referring to rotor disc), rotating about a central point referred to as the rotor hub. The blades are pitch-able in order to adjust the blade angle to maximize efficiency for the given wind condition [18]. The blade pitch system is positioned in the rotor hub in order to establish a mechanical connection to the blades. In addition to adjusting the blade angle, the HAWT also requires adjustment capabilities for positioning the swept rotor area into the wind [18]. This requirement is met by implementing a yaw control system, which allows for rotation of the rotor system about the vertical axis.

For floating offshore applications one of the key issues with the HAWT is that the nacelle containing both the gearbox and the generator, both of which have substantial mass, is positioned at the top of the tower. This means that the centre of gravity (COG) of the HAWT is located relatively high above sea level, which is important to consider when dealing with vessel stability.

5.1.2 Vertical axis wind turbines (VAWT)

5.1.2.1 Description of components

In contrast to the propeller-like shape of the HAWT there are several different designs for the VAWT. Some of the more common VAWT designs include the Savonius-, Darrieus- and the H-rotor (depicted below). The Savonius-rotor differs from the latter two designs as it uses drag instead of lift to rotate around its central axis [18]. In this thesis the H-rotor-type design will be considered as this is similar to the design currently being tested (in small scale) by Gwind.

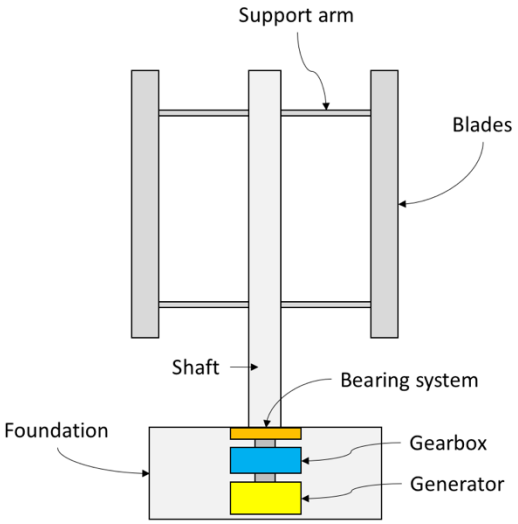

Figure 5-2: Simple illustration of a H-rotor VAWT

The figure above illustrates a simplified design of the H-rotor VAWT. As can be observed from this figure the bearing system, gearbox (may be omitted for direct drive applications) and generator are situated in the foundation of the structure. The turbine blades are mounted perpendicular to the shaft using support arms as illustrated. One principal difference between the HAWT and the VAWT is that the VAWT does not need a yaw control system [19].

One of the benefits with this type of design for offshore applications is that, compared with its counterpart (the HAWT), it boasts greater stability characteristics due to its low centre of gravity (generator and other equipment is positioned in the foundation rather than at the top of the tower) [15]. Another notable benefit is the improved access for maintenance personnel since most of the rotating components are situated near sea level [20].

5.1.2.2 Power rating and torque

The following equations are used to determine the torque generated by the turbine system. The first step is to calculate the angular velocity [12].

$$\omega = \lambda_t \cdot \frac{V_\infty}{r} \qquad (5.1)$$

Where λ_t is the tip speed ratio, V_∞ is the far-field wind velocity and r is the radius of the turbine rotor. The torque can then be calculated by the following expression.

$$T = \frac{P}{\omega} \qquad (5.2)$$

Where P is the power rating and ω is the angular velocity.

5.2 Motions of vessels

5.2.1 Substructures

There are several different types of floating substructures used for supporting topside equipment, some of these include the ship-shape mono-hull, SPAR, multi-column semi-submersible and shallow draft large diameter cylindrical structures (e.g. Eni's Goliat FPSO in the Barents Sea). In this thesis the primary focus will be mono-hull floaters with a cylindrical shape (similar to that of the SPAR) as illustrated in the figure below.

5.2.2 Degrees of freedom

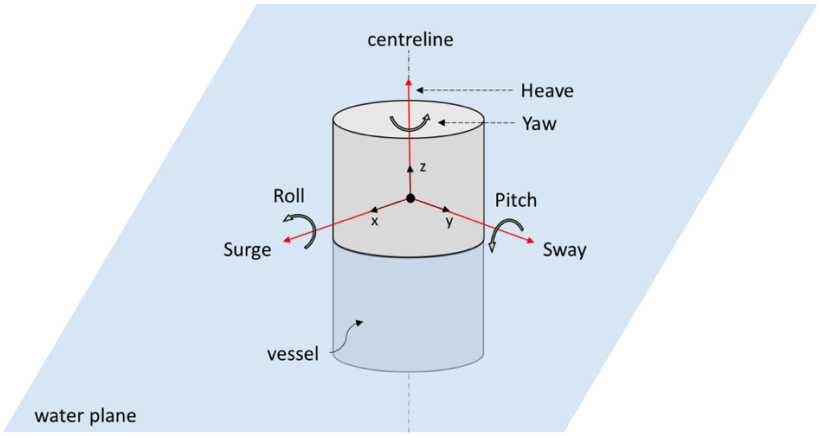

Figure 5-3: 3-dimensional representation of the degrees of freedom for a floating vessel (based on [9])

The figure above shows a 3-dimensional view of the six degrees of freedom (DOF) for a cylindrical floating vessel [9]. The red arrows indicate translational motions with respect to the given coordinate system and the green arrows represent rotational motions. For a cylindrical vessel the pitch and roll motions are equivalent due to the symmetrical shape of the floater. The numerical annotations used for these DOF's are presented in the table below. The motion in a certain DOF is expressed using η_i where i is the DOF (similar to the system used in [11]).

Table 5-1: Numerical form of the six degrees of freedom

Translational DOF	Numerical form	Rotational DOF	Numerical form
Surge	η_1	Roll	η_4
Sway	η_2	Pitch	η_5
Heave	η_3	Yaw	η_6

5.2.3 Typical vessel motion characteristics

The table below presents a comparative overview of typical vessel motion characteristics in each of the 6 DOF's for a selection of possible floaters for offshore wind turbines, based on DNV-OS-J103 Section 5.1.1 Table 1-5 [21]. C represents the "compliant" mode of motion and R represents the "restrained" mode of motion. As can be observed from the table below TLP's are restrained in heave, roll and pitch. DNV states that the compliant motion will generally be in the order of meters and the restrained motion in orders of cm [21]. Restrained motions occur for the TLP due to tension in tendons and the elastic properties of steel.

Table 5-2: Comparison of vessel specific motions in 6 DOF [21]

Vessel type	η_1	η_2	η_3	η_4	η_5	η_6
Semi-submersible	C	C	C	C	C	C
Deep draft floaters	C	C	C	C	C	C
Tension Leg Platform	C	C	R	R	R	C

5.2.4 The response amplitude operator (RAO)

The response amplitude operator is sometimes referred to as a transfer function which relates the motion amplitude of the vessel to the wave amplitude [22]. These are typically expressed as a ratio of vessel motion to wave motion amplitude in the given degree of freedom (refer to Figure 5-3). In addition to the aforementioned ratio, the RAOs are also defined by phase shifts of the motion relative to the wave elevation. The RAOs also exhibit frequency dependence, where the general relationship is that high frequency waves will tend to result in relatively small to negligible vessel motions, whereas low frequency waves generally tend to result in larger vessel motions [22].

In many applications of the RAO there is also a dependency on wave direction relative to the coordinate system of the vessel. This direction dependence is best explained for a ship shape structure where beam sea (90° relative to the longitudinal axis) will tend to excite the structure to roll more severely compared to head sea (0° relative to the longitudinal axis). For cylindrical column-stabilized structures, with lateral symmetry, the RAOs in for example surge and sway tend to have similar values but with different dependence on the wave directions. The direction dependence is linked to the definition of the degree of freedom [22]. If one considers the same right-handed coordinate system as presented in Figure 5-3, where surge represents a positive/negative horizontal translation along the x-axis and sway is defined as a translation parallel to the y-axis. If wave direction 0° (wave travels in positive x-direction) is assumed, then the response of the vessel is a pure translation in surge with no sway component. Shift the wave direction to 90° and one will observe a translation in pure sway with no surge component. Wave directions in between these two extremes ($\theta \leq 180°$) will tend to result in a coupled translation with same radial magnitude but with different surge and sway motions, based on basic vector mathematics.

A similar behaviour is observed for the roll and pitch degrees of freedom as explained for the surge and sway components. Some degrees of freedom however, express what is referred to as direction independence. A prime example of a direction independent RAO is that for heave [22]. Note that this assumes that the vessel is a symmetric column similar to that which has been illustrated in Figure 5-3. Deviations from this may occur depending on the vessel at hand, as stated in [22] where resonance peaks in heave may be different, for example, for 0° and 90° wave headings.

The response amplitude operator and its use is revisited, with reference to mathematical formulations (in heave), under the dynamic analysis sub-chapter following the definition of the equations of motion.

5.2.5 Stability of vessels

Vessel stability is an important concept to consider when dealing with floating structures. There are several different parameters to take into account such as vessel shape, payloads, location of payload as well as excitation from an externally applied load. In stability it is common to consider both static and dynamic stability. Journee and Massie (2001) state that the static stability of a floating vessel is a measure of the vessels up-righting capability when subjected to force or overturning moment [22].

The equation used to determine the initial stability of a vessel is shown below [9]. This is the general formula for calculating the metacentric height.

$$\overline{\mathrm{GM}} = \overline{\mathrm{KB}} + \overline{\mathrm{BM}} - \overline{\mathrm{KG}} \qquad (5.3)$$

Where $\overline{\mathrm{GM}}$ represents the distance between the COG (G) and the metacentre (M) of the vessel, $\overline{\mathrm{KB}}$ is the distance between the keel (K) and the COB (B), $\overline{\mathrm{BM}}$ is the distance between the COB and the metacentre and $\overline{\mathrm{KG}}$ is the distance between the keel and the COG. The locations of G, B, M and K need to be determined in order to calculate the stability of the vessel, which will be covered by the following subsections.

5.2.5.1 Centre of gravity (G) and moments of inertia

The equation for calculating the COG is presented below.

$$\mathrm{COG}_a = \frac{1}{M} \cdot \sum_{i}^{n} m_i a_i \qquad (5.4)$$

Where a is the axis of interest (x, y, z), M is the total mass of the structure, m_i is the mass of an individual component and a_i is the distance to the COG of component i from a common reference point (for vessel stability this point will always be the keel).

In addition to the centre of gravity it is also necessary to be able to estimate the moments of inertia for the vessel about the three axes defined under the degrees of freedom sub-chapter. Since the structures are generally composed of cylindrical structures (hollow and solid to represent hull and ballast contributions respectively) the following equations are required to determine the inertial properties [23].

$$I_{XX,\text{hollow}} = I_{YY,\text{hollow}} = \frac{m}{12}(3(r_O^2 + r_i^2) + h^2) \quad (5.5)$$

$$I_{ZZ,\text{hollow}} = \frac{m}{2}(r_O^2 + r_i^2) \quad (5.6)$$

$$I_{XX,\text{solid}} = I_{YY,\text{solid}} = \frac{m}{12}(3r_O^2 + h^2) \quad (5.7)$$

$$I_{ZZ,\text{solid}} = \frac{m}{2}r_O^2 \quad (5.8)$$

Where m is the mass of the component, r_O is the outer radius, r_i is the inner radius and h is the height/length of the component. When computing the total moment of inertia about the centre of gravity for the floater the individual contributions were added by Steiner's theorem (parallel axis theorem).

5.2.5.2 Centre of buoyancy (B)

The centre of buoyancy (COB) is in general, only dependent on the geometric structure of the hull and the total mass of floating object. The COB is possible to determine by Archimedes' principle where the total mass of the object must be equal to the amount of water displaced, which is calculated using the following expression.

$$m_w = \rho_w \nabla \quad (5.9)$$

Where ∇ represents the volume of water displaced, dependent on the cross-section of the vessel parallel to the water plane and its draft. The draft of the vessel can be calculated from this equation by setting the mass of water equal to the total mass of the vessel and dividing by the cross-sectional area and the density of water. The COB is then found at the centre of the submerged volume, which for a uniform cylinder is equal to half the draft, measured from the keel.

For irregular submerged volumes the COB must be calculated by sectioning the structure using the same basic principles as finding the COG for an irregular structure, refer to equation (5.4).

5.2.5.3 Metacentre (M)

According to Journée and Massie (2001) there are two metacentres to consider in vessel stability namely the initial metacentre and the metacentre [22]. The initial metacentre is a point along a line that intersects the vertical axis of an initially stable floating vessel through the COB and a line that intersects this line after the vessel has been heeled to a certain angle (small angle) which results in a new COB. The new COB is a result of the heeling action which immerses a separate part of the vessel at the same time as a corresponding volume emerges on the opposite side of the vessel [22]. This is illustrated by the following diagram for gravity stabilized floater based on Figure 2.9 Chapter 2.3 in [22].

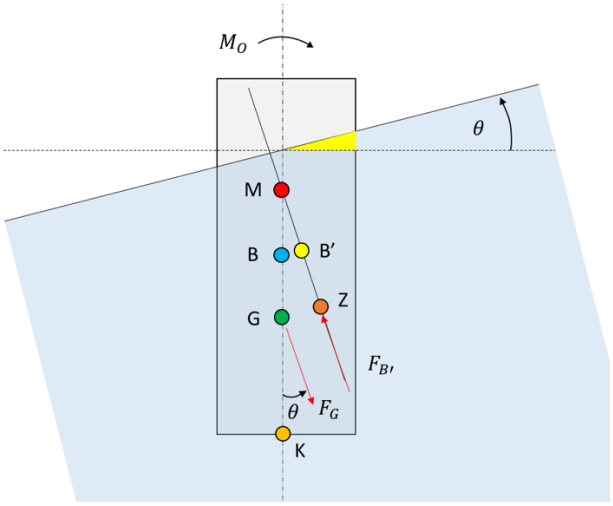

Figure 5-4: Illustration of metacentre at small angle of pitch (adapted from [22])

The figure (viewed with respect to the hull) above shows an exaggerated movement of the COB (labelled B in the diagram) to a new position B' (also note that the distance between B and M is also exaggerated in this figure, as will become apparent in the next sub-section). This movement is due to the shifting of submerged volume represented by yellow shade on the right hand side of the centreline. The metacentre (labelled M) shows the location where the perpendicular line (w.r.t. sea level) through the initial COB (B) and B' intersect. θ represents the heeling angle.

The metacentre shifts upwards for larger angles of heel because of the significant increase in the vertical shift of COB [22]. For the purposes in this thesis, where small angles of heel are assumed unless stated otherwise, the initial metacentre and metacentre will coincide. Journée and Massie suggest that this approximation of coinciding metacentres is valid up to angles of heel 10° [22].

5.2.5.4 Calculating the distance between COG and M

As presented earlier the measure of stability is found by calculating the distance between the COG and the metacentre. This involves calculating the distance between the keel and the COB, the distance between COB and the metacentre as well as the distance from keel to COG. In this section the individual equations will be presented for a vertical, surface-piercing, cylindrical hull.

For a flat-bottomed, uniform cylindrical structure the distance from keel to COB is given by the following equation [9].

$$\overline{\mathrm{KB}} = \frac{d}{2} \qquad \textbf{(5.10)}$$

Where d is the draft of the structure. The distance between the COB and metacentre is determined by calculating the area moment of inertia of the water plane (I_T) and dividing this by the total submerged volume (∇). The equation is presented below which is valid for small and larger angles of inclination (Scribanti Formula, [22]).

$$\overline{\mathrm{BM}_\theta} = \frac{I_{WP}}{\nabla} \cdot \left(1 + \frac{1}{2}\tan^2\theta\right) \xrightarrow{\theta < 10^\circ} \overline{\mathrm{BM}} = \frac{I_{WP}}{\nabla} \qquad \textbf{(5.11)}$$

The angle θ is determined based on Figure 5-4 and if this is sufficiently small (in radians), then the result is as presented on the right hand side of the equation above. Note that M_θ represents the metacentre and M represents the initial metacentre (for more information refer to Ch. 2.3.6 in [22]).

The area moment of inertia of the water plane I_{WP} is, for a cylindrical cross section, as follows [24].

$$I_{WP} = \frac{\pi}{64} D_O^4 \qquad \textbf{(5.12)}$$

Where D_O is the outer diameter of the column. After having found these values all that remains is to find the COG relative to the keel using the equation presented earlier. It is also worth mentioning that when the stability equation is used for single-column-stabilized units such as a SPAR floater, the area moment of inertia in the water plane (and the area in the water plane) tends to be small compared to for example a barge vessel. The implication of this is that $\overline{\mathrm{BM}}$ becomes negligible in comparison to $\overline{\mathrm{KB}}$ and $\overline{\mathrm{KG}}$. This means that the stability equation can be simplified to the following.

$$\overline{\mathrm{GM}} = \overline{\mathrm{KB}} - \overline{\mathrm{KG}} \tag{5.13}$$

5.2.5.5 Stability of a submerged body

The stability of a submerged body is calculated in a similar manner to that of a surface-piercing floater, but equation (5.3) must be adjusted. A submerged body has no water-plane area, hence the contribution from $\overline{\mathrm{BM}}$ is zero [22]. The expression for $\overline{\mathrm{GM}}$ for a submerged body is the same as the equation for the single-column-stabilized unit (5.13).

5.2.5.6 Angle of heel/pitch in static conditions

The angle of heel/pitch in static conditions is estimated based on equilibrium of overturning and righting moments using the following expressions presented in [22].

$$M_R = \rho g \nabla \cdot \overline{\mathrm{GZ}} \tag{5.14}$$

Where M_R is the righting moment, ρ is the density of the medium (1.025 kg/m^3), ∇ is the submerged volume and $\overline{GZ}$ is referred to as the stability lever arm and is calculated using the following expression.

$$\overline{\mathrm{GZ}} = \overline{\mathrm{GM}_\theta} \cdot \sin\theta \tag{5.15}$$

Where $\overline{\mathrm{GM}_\theta}$ is the metacentric height for larger angles of heel (> 10°), which is found by similar procedure as the metacentric height for smaller angles of heel, $\overline{\mathrm{GM}}$, except $\overline{\mathrm{BM}_\theta}$ is used rather than the small angle approximation $\overline{\mathrm{BM}}$. This means that the following expression can be used to determine $\overline{\mathrm{GM}_\theta}$ in terms of heeling angle (θ) and the small angle approximation of $\overline{\mathrm{GM}}$ (as presented in [22]).

$$\overline{\mathrm{GM}_\theta} = \overline{\mathrm{GM}} + \frac{1}{2}\overline{\mathrm{BM}} \cdot \tan^2\theta \tag{5.16}$$

From these expressions it is possible to determine an estimate for the static heel angle. Note that if the single-column-stabilized approximation to the stability equation is applied, then the righting moment equation is as follows.

$$M_R = \rho g \nabla \cdot \overline{\mathrm{GM}} \cdot \sin\theta \tag{5.17}$$

This means that it is possible to compute the pitch angle at static equilibrium between the overturning and righting moments by utilizing the following equation, obtained by algebraic manipulation.

$$\theta = \sin^{-1}\left(\frac{\rho g \nabla \cdot \overline{\mathrm{GM}}}{M_O}\right) \tag{5.18}$$

5.3 Wind theory

This chapter will cover the necessary wind theory required to establish a wind velocity profile, calculate the wind pressure and subsequently the wind load acting on a certain geometric shape.

5.3.1 Wind velocity profile

There are several different models that can be used to represent the change in wind velocity with height. These models typically use a logarithmic or power law profile as suggested in DNV-RP-C205 under wind conditions. The equation for the power law model is presented below [25].

$$U(z) = U_{10} \cdot \left(\frac{z}{10}\right)^{\alpha} \quad \textbf{(5.19)}$$

Where U_{10} is the reference 1-hour mean wind velocity, z is the height above sea level and α is a factor. For offshore conditions this factor will typically be 0.14 according to DNV-RP-C205. U_{10} depends on the location of the field of interest at a given reference height of 10 m above sea level [25].

It is worth noting that DNV GL specifies that the wind model shall not be extrapolated beyond 100 m, but in the spreadsheet calculations the wind profile has been extrapolated to cover the entire height of the wind rotor. Winds in the upper layers above 100 m may be affected by geostrophic winds, which are not captured by the wind model above [25].

5.3.2 Wind pressure

The wind pressure depends on two main parameters, namely the wind velocity with a certain reference period (1 hour) and height ($U_{T,z}$) but also the density of air (ρ_a) with a certain moisture content and temperature [25]. The equation for the wind pressure is, according to Section 5.2 in DNV-RP-C205, as follows:

$$q_w = \frac{1}{2}\rho_a U_{T,z}^2 \quad \textbf{(5.20)}$$

A common value for the density of air is 1.266 kg/m^3 (dry, 15°C) [25]. The wind pressure equation above is used for calculating the wind loadings, which are covered in the section below.

5.3.3 Wind loadings

The force acting on an exposed surface is dependent on the wind pressure and the surface area of the structure. The magnitude of the wind load depends on direction of the incoming wind and the shape coefficient which is expressed, according to Section 5.3 in DNV-RP-C205, as follows.

$$F_W = C \cdot q \cdot S \cdot \sin\alpha \quad \textbf{(5.21)}$$

Where C is the shape coefficient, q is the wind pressure, S is the projected area and α is the angle between the wind and the axis of the exposed surface [25]. As can be observed from this equation the maximum magnitude of the force exists when the wind velocity is perpendicular to the surface area if all else is equal.

5.3.4 Coefficients

In order to establish the wind force on a wind exposed surface it is necessary to determine the drag coefficient/shape coefficient for the specific geometry. Shape coefficients are possible to establish with reference to DNV-RP-C205. For circular cylinders it is necessary to determine the roughness factor and the Reynolds number for the specific flow regime.

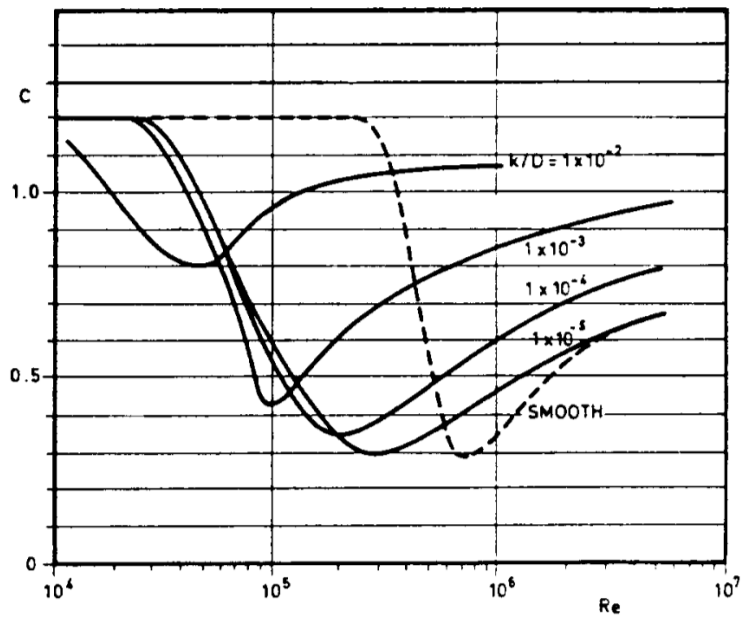

Figure 5-5: Drag coefficient for circular cylinder (steady flow) from DNV-RP-C205 [25]

5.4 Wave theory

5.4.1 Linear wave theory

Linear wave theory (LWT) is the simplest form of describing ocean waves where a wave is described by a uniform sinusoidal shape as illustrated in the figure below [9].

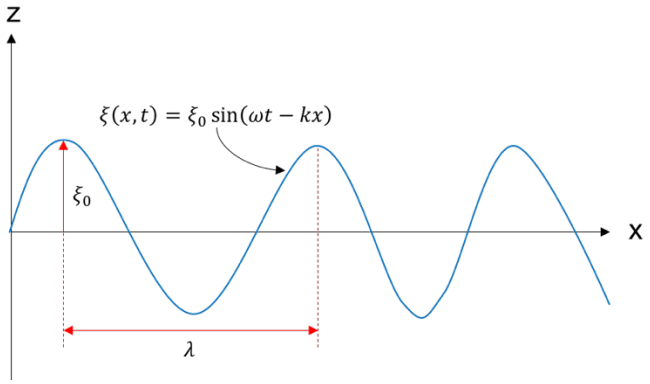

Figure 5-6: Instantaneous linear wave surface profile

The surface profile illustrated above is derived from what is referred to as the velocity potential function given by the equation below [9].

$$\phi(x,z,t) = \frac{\xi_0 g}{\omega} \frac{\cosh k(z+d_w)}{\cosh(kd_w)} \cos(\omega t - kx) \quad \textbf{(5.22)}$$

Where ξ_0 is the amplitude of the wave, ω is the wave frequency, k is the wave number, d_w is the water depth, z is the reference depth (vertical position), t is time and x is a position. The potential function can then be used to determine the horizontal and vertical particle velocities/accelerations with depth, which allows for calculating the hydrodynamic loadings at a later stage. The velocities and accelerations are found by derivation of the potential function as shown below, where u and $\dot{u}$ respectively represent the velocity and acceleration in the horizontal [9].

$$u = \frac{\partial \phi}{\partial x}, \qquad \dot{u} = \frac{\partial u}{\partial t}, \qquad w = \frac{\partial \phi}{\partial z}, \qquad \dot{w} = \frac{\partial w}{\partial t}$$

For deep water (d_w / λ > 0.5) the potential function can be simplified to the following expression [9].

$$\phi_{\text{deep}}(x,z,t) = \frac{\xi_0 g}{\omega} e^{kz} \cos(\omega t - kx) \quad \textbf{(5.23)}$$

The expression for the horizontal velocity in deep water is presented below.

$$u_{\text{deep}}(x,z,t) = \frac{\xi_0 g}{\omega} \cdot k \cdot e^{kz} \sin(\omega t - kx) \quad \textbf{(5.24)}$$

The expression for the horizontal acceleration in deep water is presented below.

$$a_{\text{deep}}(x,z,t) = \xi_0 g \cdot k \cdot e^{kz} \cos(\omega t - kx) \quad \textbf{(5.25)}$$

As can be observed from these two equations, the acceleration and velocity are 90° out of phase with one another. The wave number is an important parameter in wave kinematics and can be expressed, for deep water, by the following expression.

$$k = \frac{2\pi}{\lambda} \quad \textbf{(5.26)}$$

Where the wavelength λ can be expressed by the dispersion relation for deep water, in terms of the wave period, in the following manner [9].

$$\lambda = 1.56 \cdot T^2 \quad (5.27)$$

5.4.2 Irregular sea and the wave spectra

In contrast to the linear wave theory, a real sea state is an irregular, random process [25]. Irregular waves are possible to model by the superposition of several regular sinusoidal wave profiles (Fourier analysis). The wave elevation of an irregular sea can be expressed using the following expression [26].

$$\xi = \sum_{j=1}^{N} \xi_j \sin(\omega_j t - k_j x + \epsilon_j) \quad (5.28)$$

Where ω_j is the angular frequency, k_j is the wave number and ϵ_j is a random phase angle. The random phase angle is uniformly distributed in the interval [0, 2π]. The wave amplitude ξ_j can be determined from the wave spectrum using the following expression.

$$\frac{1}{2}\xi_j^2 = S(\omega_j) \cdot \Delta\omega \quad (5.29)$$

Where $S(\omega_j)$ is the wave spectrum at angular frequency ω_j and $\Delta\omega$ represents a frequency interval [26]. The wave spectrum is based on wave measurements obtained in a certain area and are usually expressed, for short-term sea states, as a function of constant H_s and T_p. By short-term sea states it is meant that the time-frame is limited in duration, e.g. less than 10 hours [26]. Constant H_s and T_p are assumed for short-term sea states because the wave climate is not likely to change within a short interval, unlike long-term sea states where the wave climate is likely to change, i.e. H_s and T_p are not constant. Long-term sea states are typically used for determining the percentage of time when a certain combination of H_s and T_p appears, which is often presented using a scatter diagram [26].

A wave energy spectrum is defined as a function which represents the energy in a sea state in terms of the wave frequency and is often used to characterise a certain sea state [9].

In absence of field specific data there are several different pre-defined wave spectra available, two of which are the JONSWAP and Pierson-Moskowitz spectrum. The wave spectra presented here can be characterized by three parameters namely the significant wave height, the peak period and the peak shape factor.

5.4.2.1 Pierson-Moskowitz spectrum

DNV-RP-C205 Section 3.5.5.1 presents the expression for the Pierson-Moskowitz spectrum in the following manner [25].

$$S_{PM}(\omega) = \frac{5}{16} \cdot H_S^2 \omega_p^4 \cdot \omega^{-5} \exp\left(-\frac{5}{4}\left(\frac{\omega}{\omega_p}\right)^{-4}\right) \quad (5.30)$$

Where H_S is the significant wave height, ω_p is the spectral peak frequency and ω is the angular frequency. This wave spectrum is suitable for fully developed sea [9]. Although this type of spectrum is not used here, it is used in the expression for the JONSWAP spectrum in the following section.

5.4.2.2 JONSWAP spectrum

DNV-RP-C205 Section 3.5.5.2 presents the expression for the JONSWAP spectrum in the following manner [25].

$$S_J(\omega) = A_\gamma S_{PM}(\omega) \gamma^{\exp\left(-0.5\left(\frac{\omega-\omega_p}{\sigma_s \cdot \omega_p}\right)^2\right)} \quad (5.31)$$

Where A_γ is a normalizing factor, $S_{PM}(\omega)$ is the expression for the Pierson-Moskowitz spectrum, γ is a parameter representing the peak shape of the spectrum (non-dimensional), σ_s is the spectral width parameter which varies between σ_a and σ_b depending on the frequency ω.

$$A_\gamma = 1 - 0.287 \ln \gamma \quad \textbf{(5.32)}$$

The JONSWAP spectrum is, in contrast to the Pierson-Moskowitz spectrum, able to describe a sea state characterised as developing as well as fully developed sea [9]. Note that the JONSWAP spectrum is equal to the Pierson-Moskowitz when the peak shape parameter γ is 1, i.e. the JONSWAP spectrum is similar to the PM-spectrum, but with a more pronounced peak at the peak frequency for shape factors greater than 1 [9] as can be observed in the figure below. An example of a PM-spectrum and a JONSWAP spectrum with an H_s of 4 and a T_p of 8 (and peak shape parameter γ of 2) was generated in Mathcad 15 as presented below.

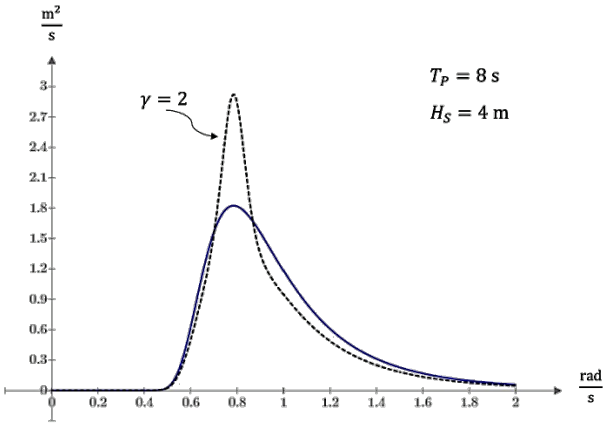

Figure 5-7: Example of a JONSWAP and a PM spectrum

5.4.2.3 Generating an irregular sea surface profile from a wave spectrum

The figure below shows an illustration of how the wave spectrum in the frequency domain can be used to generate an irregular sea surface profile in the time domain [26].

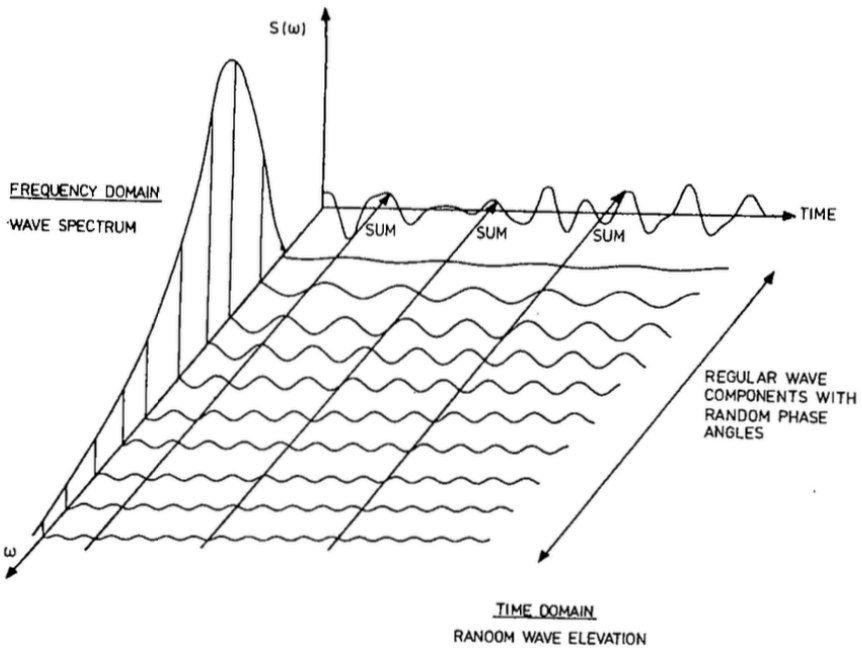

Figure 5-8: Generation of an irregular surface profile from a wave spectrum [26]

As can be observed from the figure above the frequency domain can be used to extract several regular wave components based on a given wave spectrum. Note that in order to produce a random surface profile, phase angles are selected at random as stated in the figure above.

This method is typically used in dynamic simulation software to generate a wave profile for establishing the motions and loads acting on a vessel. Note that the random phase angle generation may not always be random, which is the case for some dynamic simulation software such as Orcina's OrcaFlex. The random phase angles are generated by what is referred to as a pseudo-random process [27], where a specific seed is used to generate the "random" numbers. The significance of this is that for a given wave spectrum (in the frequency domain), the generated wave elevation (in the time domain) is identical across simulations for a specified simulation time [27]. This trait is beneficial when comparing the loads and motions for the selected vessels during the dynamic simulation phase as all cases experience the same set of waves, i.e. the same global maxima in the simulation period is always observed at the same point in each simulation.

5.5 Wave loads on structures

Prior to this section the general environmental loads have been presented namely the wind and wave loads respectively. For marine structures both wind and wave loads are considered to be the main incident load sources. In this section the wave loads on structures are presented, with reference to Faltinsen, who states in [26] that loads on marine structures, subjected to regular waves, can be divided into two categories: hydrodynamic (hydro-mechanical) loads and wave excitation loads. These loads can then be super-positioned to determine the total loading acting on the structure. The figure below (which is largely based on Fig. 3.1 in [26], but modified to represent the case at hand) presents the basic principle of calculating the total load.

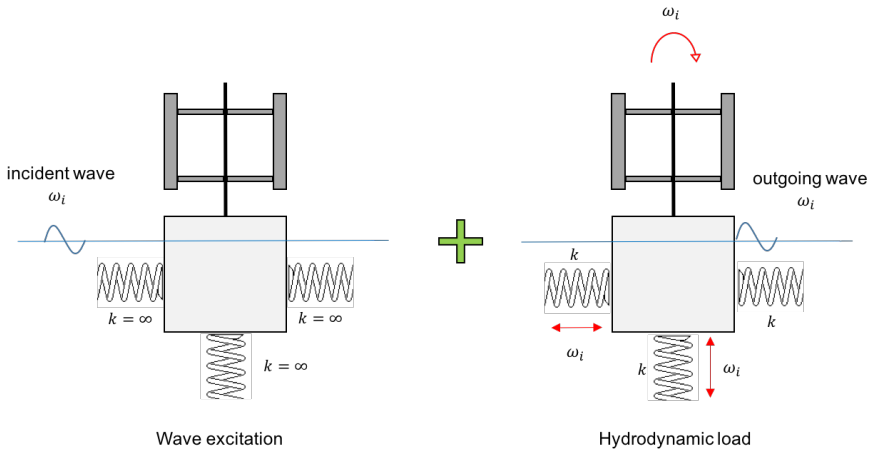

Figure 5-9: Wave induced loading based on [26]

The figure above shows the stiffness components but does not show the damping components due to lack of space in the diagram. In this section it is attempted to cover the basic concept of hydrodynamic loading and first order linear wave induced excitation loads. Note that both of these categories are hydrodynamic loads, but in this chapter the term hydrodynamic loadings (or hydro-mechanical loads [22]) are assigned to the restoring forces from forced oscillation (right hand side in the figure above) and wave excitation loads are given for the restrained condition (left hand side in the figure above).

5.5.1 Hydro-mechanical loadings

Hydromechanical loads are divided into three main categories: restoring terms (hydrostatic stiffness), added mass and damping. Faltinsen states that hydrodynamic loads are determined by the restoration forces acting on the body due to the forced oscillation of the structure (without incident waves) [26]. The frequency of oscillation is equal to the wave frequency in order to be compatible with super-positioning of the the two aforementioned terms.

From right side in the figure above, the "hydrodynamic load" contribution to the total force is presented. The added mass, damping and hydrostatic stiffness contributions are key here. The hydrodynamic loading section of the total load also introduces an element of radiation, which are the waves generated by the vessel motion, which in turn generate outgoing waves [25]. Note that mooring stiffness also contributes to the total stiffness of the system, which is included under the following sub-section.

5.5.1.1 Hydrostatic and mooring stiffness

Hydrostatic stiffness is used to specify how the weight and buoyancy forces vary when the vessel moves relative to a reference point [28]. The submerged geometry of the vessel and stability characteristics are the governing variables for the hydrostatic stiffness. The figure below presents the hydrostatic stiffness for the vessel in heave based on a similar figure found in [22].

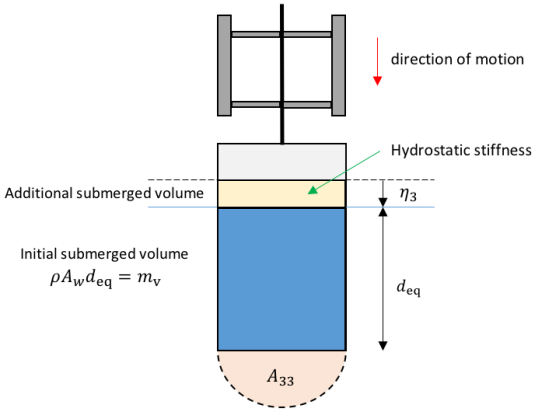

Figure 5-10: Hydrostatic stiffness in heave as a result of force motion

The hydrostatic stiffness must be calculated for each of the non-zero terms in the hydrostatic stiffness matrix. The hydrostatic stiffness matrix for a floating body, adapted from DNV-RP-C205 Section 7.2.1.4 is presented below [25].

$$\mathbf{C} = \begin{bmatrix} 0 & 0 & 0 & 0 & 0 & 0 \\ 0 & 0 & 0 & 0 & 0 & 0 \\ 0 & 0 & \rho g A_{\text{wp}} & \rho g I_{\text{wp},2} & -\rho g I_{\text{wp},1} & 0 \\ 0 & 0 & \rho g I_{\text{wp},2} & \rho g\left(I_{\text{wp},22} + \nabla z_B\right) - M g z_G & -\rho g I_{\text{wp},12} & -\rho g \nabla x_B + M g x_G \\ 0 & 0 & -\rho g I_{\text{wp},1} & -\rho g I_{\text{wp},12} & \rho g\left(I_{\text{wp},11} + \nabla z_B\right) - M g z_G & -\rho g \nabla y_B + M g y_G \\ 0 & 0 & 0 & -\rho g \nabla x_B + M g x_G & -\rho g \nabla y_B + M g y_G & 0 \end{bmatrix}$$

Where ρ is the density of water, g is the gravitational constant, A_{wp} is the water plane area (x_B, y_B, z_B) is the centre of buoyancy, (x_G, y_G, z_G) is the centre of gravity, ∇ is the submerged volume, $I_{\text{wp,i}}$ is the first moment of the water plane area and $I_{\text{wp},ij}$ is the second moment of the water plane area [25]. If the centre of gravity and buoyancy is located at the centre line of a symmetric body, then the hydrostatic stiffness reduces to the following expression (note that the first moments and product moments of the water plane area also disappear for a cylindrical symmetric body without eccentricity [11]).

$$\mathbf{C}^{\text{SYM}} = \begin{bmatrix} 0 & 0 & 0 & 0 & 0 & 0 \\ 0 & 0 & 0 & 0 & 0 & 0 \\ 0 & 0 & \rho g S & 0 & 0 & 0 \\ 0 & 0 & 0 & \rho g\left(I_{\text{wp},22} + \nabla z_B\right) - M g z_G & 0 & 0 \\ 0 & 0 & 0 & 0 & \rho g\left(I_{\text{wp},11} + \nabla z_B\right) - M g z_G & 0 \\ 0 & 0 & 0 & 0 & 0 & 0 \end{bmatrix}$$

An alternative formulation[1] to the pitch/roll hydrostatic stiffness is presented below, with an accompanying manipulation of the expression to show that the two expressions are equal.

$$C_{44} = \rho g \nabla \cdot \overline{\text{GM}} = \rho g \nabla \cdot (\overline{\text{BM}} + \overline{\text{KB}} - \overline{\text{KG}}) = \rho g\left(I_{wp,22} + \nabla z_B\right) - M g \cdot z_G \qquad \textbf{(5.33)}$$

The **mooring stiffness** contribution to the system stiffness is significantly greater than the hydrostatic stiffness. For TLP's the mooring stiffness matrix is largely governed by the number of tendons (n_t), the initial length of the tendons (l_0), pre-tension ($F_{t,0}$), the material of the tendon and the cross-sectional material area of the tendon (A_t)

[1] The alternative formulation was used in the spreadsheet calculations

[11]. It is worth noting that the stiffness in η_1 and η_2 are dependent on factors such as a translation in the horizontal plane, which will have an effect on the tension in the tendons.

The equations below are based on the assumption of small displacements as presented in Ch. 4.1.2.2 in [11].

$$k_{11} = \frac{F_{t,0}}{l_0} \quad (5.34) \qquad k_{33} = \frac{E_t A_t}{l_0} \quad (5.35)$$

Where $F_{t,0}$ is the pre-tension of the tendons, l_0 is the initial length of the tendon, E_t is the modulus of elasticity of the tendon material (for steel E_t is 210 GPa) and A_t is the cross-sectional material area of the tendon.

In order to establish the mooring stiffness matrix **K** it is necessary to take into account the contributions from all n_t tendons in each relevant degree of freedom. The stiffness values in surge, sway and heave are found by direct summation of the individual stiffness contributions from each tendon. For the pitch, roll and jaw motions the total stiffness can be calculated using the following equations [29].

$$K_{44} = K_{55} \approx \sum_{j=1}^{n_j} \left[k_{11} z_p^2 + k_{33} r_{tc}^2\right] \cos^2(\theta_j) \quad (5.36)$$

$$K_{66} \approx \sum_{j=1}^{n_j} k_{11} r_{tc}^2 \quad (5.37)$$

Where z_p is the vertical distance from mean sea level to the centre of the pontoons, r_{tc} is the radial distance from the centreline to the tendon connection point and θ_j is the angle between the positive *x*-axis to pontoon *j*. The coupled mooring stiffness contributions are equivalent due to the symmetrical properties of the structure. Estimations for these values are found by the following equation [29].

$$K_{51} = K_{15} \approx \sum_{j=1}^{n_j} k_{11} z_p \quad (5.38)$$

Where z_p is the depth of the pontoons relative to the sea surface.

5.5.1.2 Added mass

Added mass is a term used to refer to water particles that are influenced by the movement of a floating (or submerged) body where the effect reduces with distance away from the body [9]. Added mass is dependent on frequency of oscillation, vessel geometry and direction of movement [26], i.e. the added mass is different for a vessel oscillating in heave compared to the same vessel oscillating in surge. DNV-RP-C205 presents methods of calculating the added mass for different cross sections in Appendix D in [25]. The added mass with frequency dependence can be computed using software packages such as HydroD WADAM [30] (refer to section on hydrodynamic modelling).

In static conditions it is possible to estimate the added mass for a circular cross section by the following equations for a unit length [31].

$$a_t = \rho \cdot \pi \cdot \left(\frac{D}{2}\right)^2 \quad (5.39)$$

The transverse added mass (presented above) is valid for considering added mass in rotation and horizontal translations, whereas the added mass in heave, for a flat-bottomed structure, may be estimated by the following equations [9].

$$A_{33}[D] = \rho \cdot \pi \cdot \frac{D^3}{12} \quad (5.40) \qquad A_{33}[D, l] = a_t \cdot \int_0^l dl \quad (5.41)$$

The equation on the left shows the added mass in heave for a flat-bottomed cylinder which corresponds to half a sphere, where the only dependence is the diameter of the cylinder. The equation on the right however, is the added mass for the entire length l of the structure with a certain cross-section [9].

The added mass in pitch and roll for a vertical cylinder is given by the following formula as presented in [26].

$$A_{44} = A_{55} = a_t \cdot \left(\frac{h^3}{12} + h \cdot \overline{\mathrm{BG}}^2 \right) \quad \textbf{(5.42)}$$

Where a_t is the transverse added mass for a circular cross-section, h is the height of the cylinder and $\overline{\mathrm{BG}}$ is the distance between the centre of buoyancy and the centre of gravity of the system (for surface piercing columns this length is equivalen to $\overline{\mathrm{GM}}$ as $\overline{\mathrm{BM}} \approx 0$). Similar expressions for pitch added mass can also be found in [11] and [29]. The added mass in yaw for a cylindrical vessel is zero, but the presence of pontoons will affect the added mass in yaw, which can be approximated using the following equation[2] in terms of transverse added mass as expressed in [29].

$$A_{66} \approx \sum_{i=1}^{n_p} a_t \cdot \frac{1}{3} \left(l_p^3 - \frac{D^3}{2} \right) \quad \textbf{(5.43)}$$

Where l_p is the length of the pontoons and D is the diameter of the column to which the pontoons are attached. The in a 6 DOF system there are 6x6 added mass coefficients in the added mass matrix. If the vessel has zero speed and one vertical plane of symmetry half of these coefficients are zero, where non-zero added mass values are indicated in the matrix below [26].

$$\mathbf{A} = \begin{bmatrix} A_{11} & 0 & A_{13} & 0 & A_{15} & 0 \\ 0 & A_{22} & 0 & A_{24} & 0 & A_{26} \\ A_{31} & 0 & A_{33} & 0 & A_{35} & 0 \\ 0 & A_{42} & 0 & A_{44} & 0 & A_{46} \\ A_{51} & 0 & A_{53} & 0 & A_{55} & 0 \\ 0 & A_{62} & 0 & A_{64} & 0 & A_{66} \end{bmatrix}$$

The added mass matrix above can be simplified further, following the example of Bachynski, E. E. [11], to the following matrix with non-zero values presented.

$$\mathbf{A} = \begin{bmatrix} A_{11} & 0 & 0 & 0 & A_{15} & 0 \\ 0 & A_{22} & 0 & A_{24} & 0 & 0 \\ 0 & 0 & A_{33} & 0 & 0 & 0 \\ 0 & A_{42} & 0 & A_{44} & 0 & 0 \\ A_{51} & 0 & 0 & 0 & A_{55} & 0 \\ 0 & 0 & 0 & 0 & 0 & A_{66} \end{bmatrix}$$

These matrix values are consistent with the individual equations presented earlier. Deviations from this simplified mass matrix may occur for the coupled components such as, for example, A_{45}. This was observed from some added mass matrices found in HydroD in the hydrodynamic modelling stage in this thesis. If one considers the relative magnitudes of these off-diagonal values, they tend to yield small values compared to the diagonal values, with one exception being heave, which typically yields lower added mass values than the other non-zero added mass matrix values presented above. Also note that by symmetry $A_{24} = A_{42}$ and $A_{15} = A_{51}$. Following the example of [11] only the added mass matrices presented in the nearest added mass matrix are evaluated in this thesis.

It is worth noting that similarly to [11] the added masses are established by adding the contributions from each respective component, for example the effect of pontoons on total heave added mass are added without taking into account any interaction effects. However, the added mass is not evaluated for the buoyant docking station in the spreadsheet calculations, only the floater section is covered in the spreadsheet with regard to this. The simplicity of the floater geometry allows for the determination of added mass by use of the aforementioned equations.

[2] Inconsistency between expressions for added mass in yaw in [11] and expression presented in the appendix of [29]. The latter expression was selected.

5.5.1.3 Damping

Hydrodynamic damping effects are characterised as either potential damping (sometimes referred to as wave damping) or viscous damping. Potential damping, which will be evaluated here, occurs due to the transfer of energy from the oscillating motion of the system, due to the generation of waves. This type of damping is proportional to the velocity of the cylinder in a linear system [22]. Damping effects are typically concerned with the dissipation of energy from the system [22]. The viscous damping effect occurs due to friction, the generation of vortices and separation, however in contrast to potential damping this effect is non-linear. Similarly, to the previously discussed added mass contribution, the damping coefficients also exhibit frequency dependence [26], but with a more pronounced effect than that which is observed for added mass.

Journeé and Massie also state that the potential damping of deeply submerged objects is zero as these do not generate waves on the water surface [22]. This feature is particularly important for further discussion of the damping contribution of the pontoons. Dampening coefficients are determined for specific geometries using designated software such as HydroD, as is the case in this thesis, or by estimation from model testing [25].

The damping matrix can be simplified similarly to the added mass matrix presented earlier for a vessel with one plane of lateral symmetry and zero speed [26].

$$\mathbf{B} = \begin{bmatrix} B_{11} & 0 & B_{13} & 0 & B_{15} & 0 \\ 0 & B_{22} & 0 & B_{24} & 0 & B_{26} \\ B_{31} & 0 & B_{33} & 0 & B_{35} & 0 \\ 0 & B_{42} & 0 & B_{44} & 0 & B_{46} \\ B_{51} & 0 & B_{53} & 0 & B_{55} & 0 \\ 0 & B_{62} & 0 & B_{64} & 0 & B_{66} \end{bmatrix}$$

In regards to further simplification of this matrix, the same reasoning can be applied to the damping matrix as was presented for the previous added mass matrix [11].

$$\mathbf{B} = \begin{bmatrix} B_{11} & 0 & 0 & 0 & B_{15} & 0 \\ 0 & B_{22} & 0 & B_{24} & 0 & 0 \\ 0 & 0 & B_{33} & 0 & 0 & 0 \\ 0 & B_{42} & 0 & B_{44} & 0 & 0 \\ B_{51} & 0 & 0 & 0 & B_{55} & 0 \\ 0 & 0 & 0 & 0 & 0 & B_{66} \end{bmatrix}$$

Note that the potential damping values are evaluated by potential theory in HydroD and will not be discussed with reference to analytical methods to obtain these values by manual calculations. Again, note that the viscous damping effects are presented in a separate damping matrix $\mathbf{B_V}$ and is not evaluated in this thesis. Faltinsen states in Chapter 4 of [26] that potential damping values for TLPs are less significant where viscous effects become more important. However, viscous effects are non-linear and hence exceed the scope of work. The potential damping approach may therefore be a significant source of error in the dynamic simulation stage of this thesis, but this is to be discussed further under the limitations and sources of error chapters in this thesis. Note that in this thesis D is used to represent a potential damping value from this matrix with a corresponding 11 (i.e. D11 is equivalent to B_{11}).

5.5.2 1st order wave excitation load

Wave excitation loads are according to [26] composed of Froude-Kriloff and diffraction forces/moments. These forces and moments are determined based on incident waves acting on a structure, which is restrained from oscillating. This category of loading is presented on the left hand side of Figure 5-9.

5.5.2.1 General discussion of the wave excitation load components

The wave excitation load arises from an unsteady fluid pressure, which is as previously mentioned, divided into two components: the Froude-Kriloff and diffraction components. The Froude-Kriloff component corresponds to the force generated on the structure due to an undisturbed pressure field, whereas the diffraction component represents the force component acting on the structure due to the disturbance of the pressure field [26]. The disturbance from the cylinder leads to the generation of reflected waves and diffracted waves, which are collectively referred to as diffraction [32]. The diffraction force will vary in magnitude depending on the vessel's dimensions, where slender objects tend to have negligible effect on the pressure field, hence the diffraction force is significantly smaller than what may be observed for a larger vessel. An illustrative example can be to compare

the diffraction force of a top-tensioned riser (small dimension) vs. the hull of a SPAR production platform (large dimension). Since the dimensions of marine vessels vary greatly and the application for establishing the wave excitation loads depends on the case at hand, it is useful to refer to diagrams as presented below, which relate the diameter (or other characteristic dimension) of the vessel/structure to the wavelength of the incident regular wave to determine which effects dominate the wave excitation load. The figure below is retrieved from DNV-RP-C205 [25] and will be used for further discussion of the different wave load regimes.

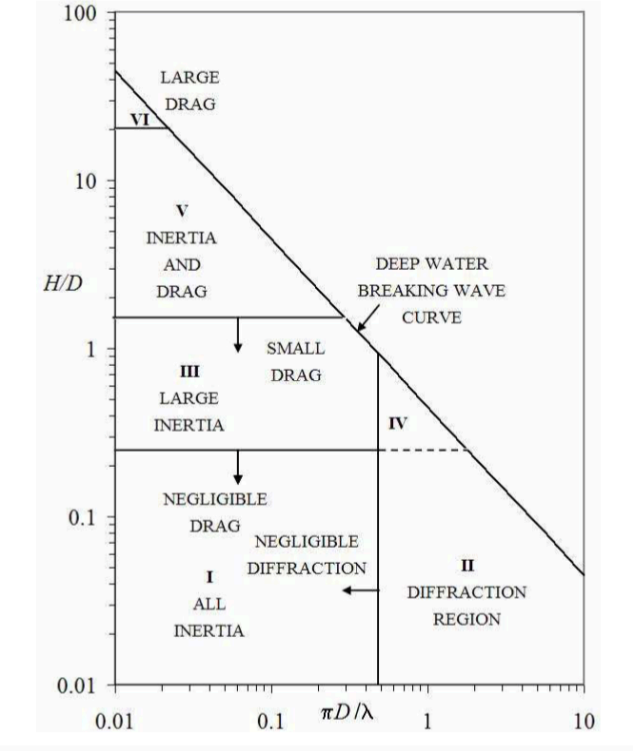

Figure 5-11: Wave load regimes [25]

As can be observed from the figure above there are in principle six different wave load regimes (labelled by roman numerals) for establishing the wave excitation load on a structure. In this figure D represents a characteristic dimension of the vessel (in this thesis this is the diameter of the vessel in the water line), H and λ represents the wave height and wavelength respectively. The diagonal line at the top of the figure represents the deep water wave breaking criterion, where the wave height/wave length ratio exceeds 0.14 [9].

If the diameter in the water line is large compared to the wavelength, the wave load regime falls into the diffraction region (II). In this section the diffraction effects are important, which typically applies for $\pi D/\lambda$ ratios larger than 0.5 (as observed from the figure above) [25]. For diameter-wavelength ratios below this one will typically observe negligible diffraction, which for small wave height-diameter ratios tends to be inertia dominated. The H/D ratio is an expression relating the wave height to the diameter of the vessel, which is by linear wave theory is an indirect expression of the relative velocity of the wave across the cylinder, ref. equation (5.24). The reason for this is the horizontal velocity's dependence on the amplitude of the wave. The H/D ratio is essentially an expression for the Keulegan-Carpenter number, which is a measure of the distance travelled by a fluid particle relative to the diameter of the structure during half a period [25]. An increase in the velocity contributes to a larger drag force, hence drag loads are generally more important for larger H/D ratios.

Potential theory is often used in software suites such as HydroD [33]. In this thesis the Morison formulation and first-order potential theory are discussed as these were used in spreadsheet calculations and during the hydrodynamic modelling stages respectively. For more information on second-order potential theory refer to [11] or [26].

5.5.2.2 Formulation 1: Morison's equation

Equation (5.44) is referred to as Morison's equation for a unit length of a submerged body with circular cross section [9]. This wave load formulation is limited to, what is typically referred to as small volume structures, which have negligible influence on the waves (i.e. negligible diffraction component) [25]. This equation consists of two

terms: the inertia term and the drag term. The inertia term depends on the horizontal[3] wave particle acceleration ($\dot{u}$), the added mass and the cross sectional area of the object. The drag term depends on the projected area, the drag coefficient and the square of the velocity (with direction maintained). Note that the velocity u is dependent on both the wave (u_w) and the current velocity (u_c), which can be added when analysing the force acting on the structure (structure must be fixed, i.e. there must not exist a large amplitude of translation). In this thesis current forces are neglected.

$$f(z,t) = f_M + f_D = \frac{\pi D^2}{4}\rho C_M \dot{u} + \frac{1}{2}\rho C_D \frac{\pi D^2}{4} u|u| \quad \textbf{(5.44)}$$

Morison's equation is however subject to a number of limitations as presented, for a cylinder, in the table below.

Table 5-3: Limitations to Morison's equation for a cylinder [9]

Criteria	Explanation
$\frac{D}{\lambda} < 0.2$	Acceleration should remain somewhat constant across the cylinder.
$\frac{a}{D} < 0.2$	The amplitude of translation, a, should be less than 0.2 times the diameter of the cylinder.
$\frac{H}{\lambda} < 0.14$	The wave height to wave length ratio must be below the breaking wave criterion.

The mass coefficient C_M as observed in Morison's equation is dependent on the ratio between the added mass and the total mass of the object (includes ballast). This can be expressed using the following equation [9] (note that the added mass, m_a, and the mass of the object, m_{obj}, are given per unit length in this expression).

$$C_M = 1 + \frac{m_A}{m_{\text{obj}}} \quad \textbf{(5.45)}$$

5.5.2.3 Formulation 2: Potential theory

A more complete formulation of the wave excitation load is found by potential theory. Potential theory is used to calculate first order radiation and diffraction effects for large volume structures [30]. This is used in the WADAM software, which in turn is based on WAMIT, where a 3D panel method is used to determine the velocity potentials and hydrodynamic coefficients for a certain structure [30]. Potential theory and how it is applied in WADAM is a complex and intricate problem and its full explanation exceeds the scope of work (and is best described in published work to the likes of [22], [26], [30]), hence this section only provides a general overview.

In potential theory loads are deduced from a velocity potential similar to that which was presented in equation (5.22) under linear wave theory. The potential theory operates based on the velocity potential of the irrotational motion of an incompressible and inviscid fluid. Typically, potential theory is solved numerically by the boundary element method, where there is a distribution of sources across the wetted body surface [25]. Sources are used to model the structure in the water, such as a cylinder, where stagnation points occur at the boundary of the structure to prevent the inbound flow from effectively entering the volume of the vessel. These sources are characterised by outwards radial flow from the source centre, the opposite of this is a sink, which has inwards radial flow towards the sink centre [22]. One of the key strengths of potential theory, is that it has the ability to generate complex flow patterns because of the ability to superposition several sources and sinks (which is due to the fact that it satisfies the linearity criterion inherent to the principle of superposition) [22].

As previously stated under the hydrodynamic loadings sub-chapter, there is an element of wave radiation that occurs due to the oscillating motion of the vessel. The oscillating structure is subjected to a form of motion damping, as energy is dissipated from the oscillation process due to wave radiation, skin friction, eddy making and viscous damping [25]. For this reason, it is necessary to utilize designated software (HydroD WADAM) to accurately obtain the damping coefficients and diffraction effects.

[3] In this section only the horizontal component is discussed.

5.5.3 Second order effects

Although second order effects are not a central part of this thesis it is deemed important to mention what the effects are and what is required in order to establish these. DNV-RP-C205 states that there are three motion time scales to which a floating/moored structure may respond to under wind, waves and current. These are categorised as wave frequency (WF), low frequency (LF) and high frequency (HF) motions [25]. Wave frequency motions are typically linear and have been discussed in the previous chapters.

Low frequency motions are usually caused by slowly varying wave, wind and current forces which can give rise to effects such as mean drift force [25]. These effects can be predicted by establishing difference frequency quadratic transfer functions (QTF), which are calculated by computer tools where second order effects are included [25]. An example of such software is DNV GL SESAM HydroD, which allows the user to generate a second order surface profile used to establish the difference frequency QTFs. The low frequency motions (drift) also requires viscous effects to be analysed as these are important here. Although the wave drift forces are generally important for TLP floater concepts, generation of such QTFs exceeds the scope of the present work and will not be discussed in further detail [25]. The difference frequency force, $q_{WA}^{(2-)}(t)$, in a random sea state is presented below.

$$q_{WA}^{(2-)}(t) = \mathrm{Re}\sum_{i,j}^{N} a_i a_j H^{(2-)}(\omega_i, \omega_j) e^{i(\omega_i - \omega_j)t} \quad \textbf{(5.46)}$$

The high frequency motions are considered to be higher order loads, i.e. non-linear phenomena, and can result in high frequency resonant vertical motions in TLPs [25]. DNV-RP-C205 states that TLPs have low Eigen periods (i.e. natural periods) in its vertical modes (heave, roll and pitch) due to the stiffness of the tendons. From a linear perspective, it is clear that there should not be significant resonant motion in this region as the energy of the waves at the higher frequencies (low periods) are typically low. However, due to the presence of non-linear wave and wave-body effects, the structure may also see significant excitation at periods at two and three times the natural period [25]. What this means is that if the natural period in heave (for TLP) is around 5 seconds, one may find excitation in wave periods 10 and 15 seconds, where there are significant concentrations of energy. This effect is sometimes referred to as higher order super harmonic responses [25]. Non-linear interaction with the TLP also induces phenomena referred to as ringing and springing, which are discussed to some extent under the TLP principle and considerations chapter later on. In contrast to the low frequency motions and the generation of difference-frequency QTFs, the high frequency effects require an establishment of sum frequency QTFs. The equation for the sum-frequency force is presented below [25].

$$q_{WA}^{(2+)}(t) = \mathrm{Re}\sum_{i,j}^{N} a_i a_j H^{(2+)}(\omega_i, \omega_j) e^{i(\omega_i + \omega_j)t} \quad \textbf{(5.47)}$$

As can be observed from the equation above, the two frequency components ω_i and ω_j are added together hence the name sum frequency force. This results in a higher frequency, which is in line with the application of this force. These equations (difference and sum frequency force contributions) are presented for reference only and are not used further due to scope limitations. Note that a_i and a_j are the individual wave amplitudes and $H^{(2+)}$ and $H^{(2-)}$ are the sum and difference frequency quadratic transfer functions respectively.

5.6 Dynamics

In this section the general form of the equation of motion is presented with reference to the definition of the mass matrix, and a general explanation of how the response in irregular waves is determine for a vessel.

5.6.1 The equation of motion

The equation of motion is presented below in matrix form. The dimensions of each of the matrices (and vectors) are given in parentheses below. Note that this equation presents stiffness contributions from both hydrostatics and the mooring system (i.e. for a free floating vessel **K** is zero).

$$[\mathbf{M} + \mathbf{A}(\omega)]\ddot{\boldsymbol{\eta}} + [\mathbf{B}(\omega) + \mathbf{B}_V]\dot{\boldsymbol{\eta}} + [\mathbf{C} + \mathbf{K}]\boldsymbol{\eta} = \mathbf{X}(\omega) \quad \textbf{(5.48)}$$

Where $\boldsymbol{\eta}$ is the motion vector for each degree of freedom (6x1), **M** is the mass matrix (6x6), **A** is the added mass matrix (6x6), **B** is the potential damping matrix (6x6), $\mathbf{B}_V$ is the viscous damping matrix, **C** is the hydrostatic stiffness matrix (6x6), **K** is the mooring stiffness matrix (6x6) and **X** is the external force vector (6x1) [11]. It is worth noting that the potential damping matrix values are referred to with prefix D in this document, i.e. D66 refers to potential damping in yaw.

For a 6-DOF system, DNV-RP-C205 Section 7.2.1.4 (pp. 101) states that the mass matrix for a floating body is as follows [25].

$$\mathbf{M} = \begin{bmatrix} M & 0 & 0 & 0 & M \cdot z_G & -M \cdot y_G \\ 0 & M & 0 & -M \cdot z_G & 0 & M \cdot x_G \\ 0 & 0 & M & M \cdot y_G & -M \cdot x_G & 0 \\ 0 & -M \cdot z_G & M \cdot y_G & I_{11} & I_{12} & I_{13} \\ M \cdot z_G & 0 & -M \cdot x_G & I_{21} & I_{22} & I_{23} \\ -M \cdot y_G & M \cdot x_G & 0 & I_{31} & I_{32} & I_{33} \end{bmatrix}$$

Where M is the total dry mass (including ballast), (x_G, y_G, z_g) are the x-, y- and z-coordinates of the COG and I_{ij} is the moment of inertia in a certain direction. For a symmetric floater the mass matrix can be expressed as follows, since the COG is non-zero in the z-coordinate only. According to Faltinsen [26] a laterally symmetric structure will also yield $I_{12} = I_{21} = I_{23} = I_{32} = I_{31} = I_{13} = 0$ which further simplifies the mass matrix as expressed below.

$$\mathbf{M}^{\text{SYM}} = \begin{bmatrix} M & 0 & 0 & 0 & M \cdot z_G & 0 \\ 0 & M & 0 & -M \cdot z_G & 0 & 0 \\ 0 & 0 & M & 0 & 0 & 0 \\ 0 & -M \cdot z_G & 0 & I_{11} & 0 & 0 \\ M \cdot z_G & 0 & 0 & 0 & I_{22} & 0 \\ 0 & 0 & 0 & 0 & 0 & I_{33} \end{bmatrix}$$

Note that the COG is measured from the keel of the vessel, i.e. z_G in the matrices above is equivalent to $\overline{\text{KG}}$ (refer to section on stability). The added mass, damping, hydrostatic and mooring stiffness matrices have been explained under the chapter on wave excitation loads and are not repeated here.

5.6.2 Natural period and resonance

The natural period is an important concept in dynamics because of problems associated with resonance. Resonance is characterized by large responses of a structure where the natural period and the period of the loading are locked into each other [9]. There is an associated natural period with each degree of freedom in a system which is calculated according to the following equation [25].

$$T_n = 2\pi \sqrt{\frac{M_{jk} + A_{jk}}{K_{jk} + C_{jk}}} \quad \textbf{(5.49)}$$

Where K and C are the associated mooring and hydrostatic stiffness in a certain degree of freedom respectively and M is the mass of the object. Note that A is the added mass matrix component for the respective degree of freedom. Note that for floating vessels it is important to consider the influenced mass of water (added mass) when calculating the natural period of the vessel as this has a direct contribution to the natural period as observed in the equation above. For rotational motions, the mass is presented as the moment of inertia in the degree of freedom.

5.6.3 Response in irregular waves

As previously stated, sea states are typically expressed in terms of wave spectra such as the JONSWAP spectra, which is used in this case. From the wave spectra (frequency domain) one is able to generate an irregular sea surface by the superposition of regular wave components with associated random phase angles [22]. The irregular wave (time domain), representing the forcing function on the right hand side of the equation of motion (5.48), can then be used to generate the irregular response of the vessel/structure. The responses are necessary to establish the translations, velocities and accelerations of the structure due to the incident waves. In order to generate the response, it is necessary to obtain information regarding the amplitude and phase characteristics, in other words one must obtain the response amplitude operator (RAO) [22]. Journeé & Massie has illustrated the relationship between the frequency domain and time domain for the irregular waves and the subsequent responses, which is presented in Figure 5-12.

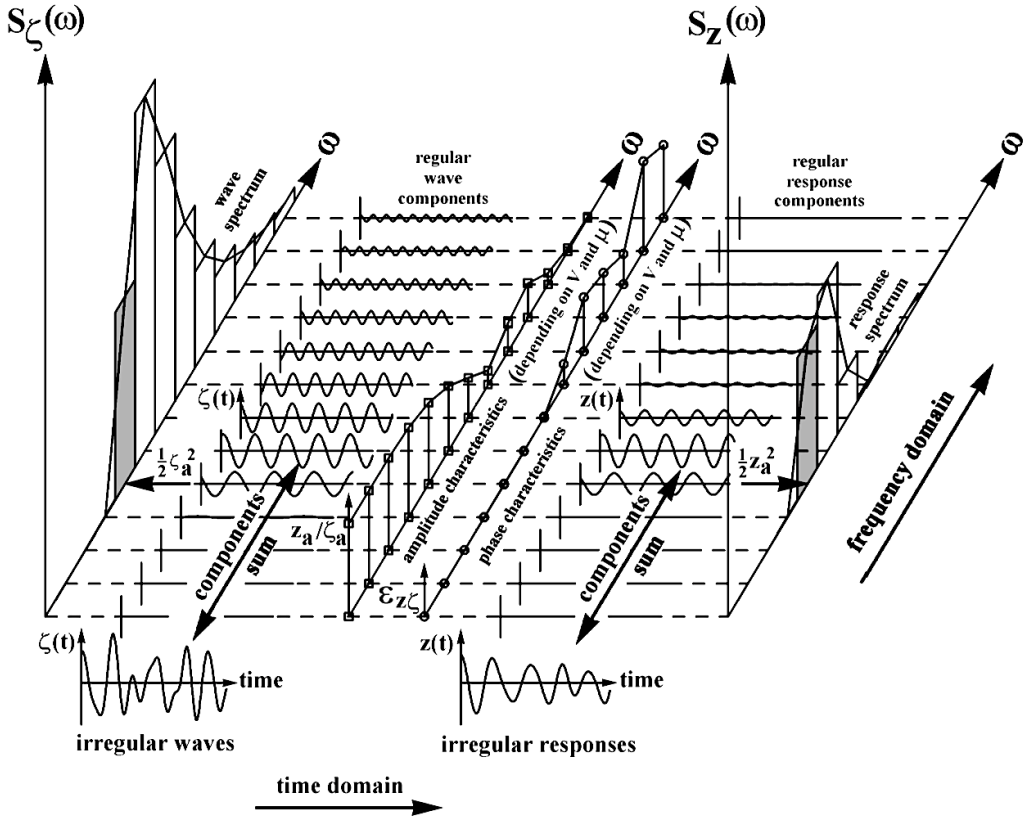

Figure 5-12: Principle of transfer of waves into responses [22]

In the figure above the process of establishing the response spectrum (right hand side) from the wave spectrum (left hand side) is illustrated. The figure is a clear illustration of how the frequency domain and time domain are linked together. Note that the centre of the figure shows the amplitude characteristics and phase characteristics, i.e. the response amplitude operator. In time domain simulations the response is typically given as a time history as presented at the bottom of the figure above.

5.6.3.1 Response amplitude operator and the response spectrum

As previously mentioned under the vessel motions chapter, the response amplitude operator is used to represent the ratio of vessel motion/load and incident wave amplitude. Usually one will have a separate displacement RAO and load RAO for establishing the vessel motion amplitude/wave amplitude and vessel load/wave amplitude ratios respectively. The mathematical expressions for the two RAOs are presented below for certain degree of freedom *i* [22].

$$\frac{F_{a,i}}{\xi_a}(\omega) \quad \textbf{(5.50)}$$

$$\frac{\eta_{a,i}}{\xi_a}(\omega) \quad \textbf{(5.51)}$$

Where ω is the angular frequency, ξ_a is the wave amplitude, $\eta_{a,i}$ is the motion amplitude in a certain degree of freedom and $F_{a,i}$ is the force amplitude in a certain degree of freedom. Equation (5.50) is the load RAO and equation (5.51) is the displacement RAO. As can be observed from these two equations, there is an element of frequency dependence as previously discussed and is presented above in terms of angular frequency ω. The RAOs are not easily determined by hand in irregular waves, hence it is necessary to look at regular waves to be able to explain how the RAOs are obtained. RAOs can be presented in the frequency domain (as a function of frequency), which is particularly useful for obtaining the response spectrum in irregular waves. The full derivation is not covered in this text, but can be found in, for example, Chapter 6.3 of [22]. A summary is provided here for illustrative purposes only. The basic procedure (for heave) is to insert the cyclic expressions for the heave response into the equation of motion (5.48). An example of such a cyclic expression for position (in heave) is presented below [22], where the velocity and acceleration can be determined by derivation of this expression.

$$\eta_3 = \eta_{a,3}\sin\left(\omega t + \epsilon_{3\xi}\right) \quad \textbf{(5.52)}$$

Where $\eta_{a,3}$ is the amplitude of the heave response, ω is the frequency, $\epsilon_{3\xi}$ is the phase characteristic. By inserting this equation and the derivatives (velocity and acceleration) into the equation of motion one can determine the the following expression which represents the amplitude characteristics of the RAO [22]. A pre-requisite here is that one must have defined the wave force.

$$\frac{\eta_{a,3}}{\xi_a}(\omega) = e^{-kd}\sqrt{\frac{\{C_{33} - A_{33}\omega^2\}^2 + \{B_{33}\omega\}^2}{\{C_{33} - (M_{33} + A_{33})\omega^2\}^2 + \{B_{33}\omega^2\}}} \quad \textbf{(5.53)}$$

Where C_{33} is hydrostatic stiffness in heave, A_{33} is the added mass in heave, B_{33} is damping in heave, M_{33} is the mass of the structure, k is the wave number and d is the draft. As previously mentioned, RAOs also exhibit a set of phase characteristics, which is not dependent upon the wave amplitude [22]. The phase shift in heave (motion) can be expressed by the following equation for regular waves [22].

$$\epsilon_{3\xi}(\omega) = \tan^{-1}\left\{-\frac{M_{33}B_{33}\omega^3}{(C_{33} - A_{33}\omega^2)\{C_{33} - (M_{33} + A_{33})\omega^2\} + \{B_{33}\omega\}^2}\right\} \text{ with : } 0 \leq \epsilon_{3\xi} \leq 2\pi \quad \textbf{(5.54)}$$

As can be observed from the equation above, the phase shift also exhibits frequency dependence. An example of a typical RAO for a vertically oriented cylinder is presented in Figure 5-13 from [22].

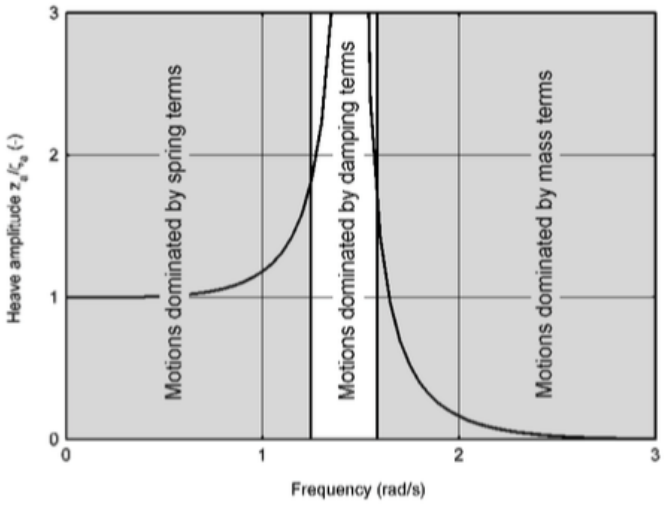

Figure 5-13: Typical RAO in heave [22]

As can be observed from the figure above, the low frequency range typically yields a heave amplitude of 1, which means that the vertical oscillation amplitude tends to follow the wave amplitude, i.e. the ratio is 1:1. For the higher frequencies, the motion in heave tends to zero because the wavelengths are much smaller than the diameter of the cylinder [22]. The middle section in the figure above, shows a region in which the motions are dominated by the damping terms. This is referred to as a region where the natural frequency of the vessel is close to the wave frequency, resulting in large motions. This phenomena is often referred to as resonance [22].

The response spectrum of a vessel in a certain degree of freedom characterises the vessel response for irregular waves defined by a certain input wave spectrum, such as for example a JONSWAP spectra defined by Hs, Tp and the peak factor. The RAO (or transfer function) can then be used in the following manner to link the two spectra [22].

$$S_{\eta 3}(\omega) = \left|\frac{\eta_{3,a}}{\xi_a}(\omega)\right|^2 \cdot S(\omega) \qquad (5.55)$$

This principle is illustrated in Figure 5-12 where the wave spectrum is on the left hand side of the figure and the corresponding vessel response spectrum is on the right hand side.

5.6.3.2 Frequency domain approach

The frequency domain approach is a method that is used to study systems in irregular sea states that exhibit linear characteristics, i.e. one neglects all transient effects, and analyse the linear superposed loads due to regular wave components derived from a wave spectra [25]. The frequency domain approach is dependent on linearity of the system as the fundamental principle behind the frequency domain approach is the principle of superposition (as illustrated in Figure 5-12). By this it is meant that one evaluates the response for several regular waves with certain frequencies and amplitudes from the wave spectra, then superposes these regular individual responses for each regular wave, in order to generate the irregular response of a vessel in an irregular sea state [22].

The frequency domain approach is useful in analysing linear systems due to the reduced computation time [34]. This type of approach is suitable for systems where the analysis is limited to first order wave loads and motions, added mass and damping effects without taking into account second-order effects.

This approach is used when generating the hydrodynamic coefficients for the structures in this thesis by use of the DNV GL software HydroD from the SESAM programme suite. A typical output from a frequency domain analysis are spectra for responses or loadings as functions of frequency, which provides information about how a system in this case responds to a certain sea state [22].

5.6.3.3 Time domain approach

Non-linear systems typically require that the time domain approach be used as the linear foundation of the frequency domain approach is violated [22]. In the time domain approach the equations of motion must be solved directly as a function of time, hence the name time domain approach. The key characteristic of the time domain

approach is the need to record the response/load for a number of time steps, for which the solution is calculated in the respective software. This type of approach requires information about the previous step in the time history, i.e. the response at the next time step builds on previous time step (memory). This memory characteristic is given by the fact that the motion in an interval is influenced by the motion of the system in the previous interval [22]. In order to illustrate the differences between the time domain approach and the frequency domain approach, the Cummins equation is presented below [22].

$$(M + A) \cdot \frac{\mathrm{d}^2}{\mathrm{dt}^2} x(t) + \int_0^\infty B(\tau) \cdot \frac{\mathrm{d}}{\mathrm{dt}} x(t - \tau) \cdot d\tau + C \cdot x(t) = X(t) \quad \textbf{(5.56)}$$

Where M is the mass of the system, A is the added mass, $x(t)$ is the translational or rotational displacement at time t, C is the spring coefficient, B is the retardation function, t and τ is time, and lastly $X(t)$ is the external load at a given time t. The significance here is that the responses and incident loadings are expressed as a function of time, unlike the frequency domain where these are functions of frequency. It is also noted that the external wave load as a function of time is determined from the wave spectra, hence this is generated by Fourier series based on the equation below [22].

$$X_{\mathrm{wave}}(t) = \sum_{n=1}^{N} \left(\frac{X_{\mathrm{wave},a_n}}{\xi_{a_n}} \right) \cdot \xi_{a,n} \sin\left(\omega_n t + \epsilon_n + \epsilon_{X_{\mathrm{wave}}\xi_{\mathrm{n}}}\right) \quad \textbf{(5.57)}$$

Where $X_{\mathrm{wave}}(t)$ is the time dependent wave load, N is the number of frequencies, ω_n is the wave frequency, ϵ_n is the phase shift of the wave, $\epsilon_{X_{\mathrm{wave}}\xi_{\mathrm{n}}}$ is the phase shift of the wave load, $\xi_{a,n}$ is the wave amplitude, and the ratio in the parentheses is the transfer function of wave load. As is clear from the equation above, the time domain approach is dependent on elements from the frequency domain, with particular reference to the wave excitation.

Since the system to be analysed in this thesis is limited to the linear effects the nonlinear aspects to the time domain analysis method will not be covered in detail here. One of the main benefits of the time domain approach is the ability to capture higher order load effects, but this requires extensive information about the vessel response, i.e. sum and difference frequency QTFs in addition to the conventional RAOs, added mass and potential damping as well as other damping sources (viscous effects) [22]. As discussed earlier, the non-linear sum and difference frequency forces are functions of time, which means that one is forced to analyse these effects in the time domain.

The time domain approach is used for dynamic simulations of the systems in OrcaFlex, but only linear effects are analysed. OrcaFlex has the ability to generate a frequency spectrum based on the time domain simulation, which is achieved by Fourier transformation [34].

6 Tension leg platform principles and design considerations

In this chapter the general station keeping principles and key characteristics of the TLP system are drafted with reference to the different components that make up the system. In addition to the general overview, some case specific design considerations are presented based on [8], [11], [29]. This section will establish the pre-requisites for the definition of the parameters under the concept description and presentation of parameters chapter following this.

6.1 Basic TLP station keeping principles

6.1.1 Overview of system structure

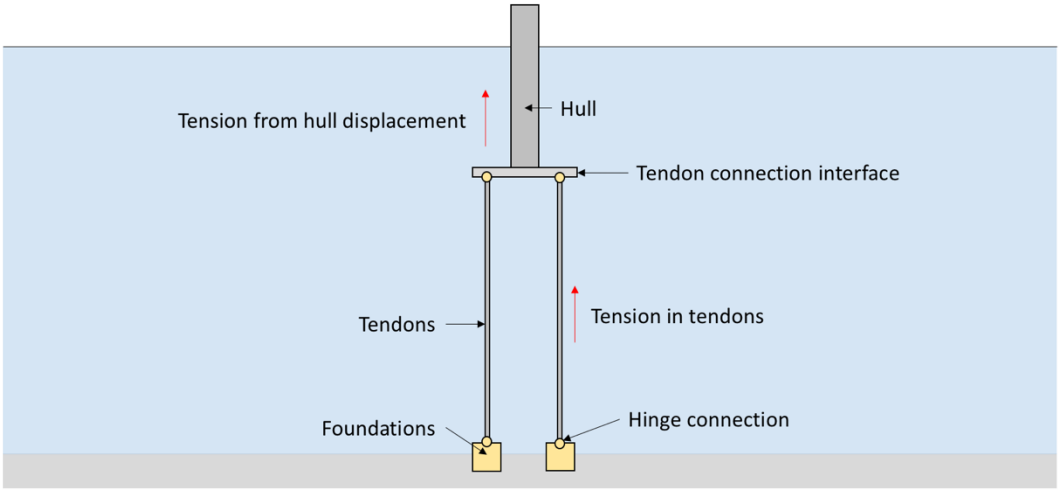

Figure 6-1: Illustration of a mono-hull TLP system

A TLP system is sometimes referred to as a tendon-stabilized system [21], in which the system obtains its stability characteristics from the tendons rather than the position of the metacentre relative to the centre of gravity as is the case for conventional floaters. The reason for this is that the gravity force not in equilibrium with the buoyancy force, i.e. the vessel displaces a greater mass of water than the structural mass. The additional restoring force for maintaining equilibrium arises due to the tendon stiffness [21]. Due to the systems dependence on the supplied restoring force for stability it is critical that the tendons remain intact throughout the operational life of the system, where loss of tendons will tend to have severe adverse effects on the system as a whole [21]. One of the main criteria for TLP systems are that the tendons should not experience a loss of tension, i.e. slack, as snap loads can occur, leading to tendon failure [21]. DNV-OS-J103 states that in some cases there may be some allowable element of slack present for a TLP structure but this requires a high level of redundancy [21].

In general terms the tension leg station keeping system consists of three main sections: foundation, tendons, and the hull structure. The main characteristic for a TLP platform is the suppression if vertical motions i.e. high resistance toward motions in heave [35]. The TLP does not efficiently suppress the motions in the surge and sway, i.e. there is a low resistance against motions in the horizontal plane [35]. Pitch and roll are, similarly to heave, also resisted by the mooring system [21].

The natural periods of TLPs differ widely in the 6 degrees of freedom, where surge, sway and yaw typically have long natural periods, and pitch, roll and heave typically have low natural periods [21]. According to DNV-OS-J103 the resonance periods for TLP systems are generally given by the length and pre-tension of the tendons, but also depend on the flexibility of the turbine system. In light of the natural periods DNV also states that the degrees of freedom; heave, roll and pitch will experience very small wave-frequency oscillations [21]. However these degrees of freedom are susceptible to higher order effects (such as sum-frequency wave forces), which can lead to what DNV refer to as high-frequency resonant oscillations, i.e. ringing and springing [21].

Ringing is a phenomenon that occurs for offshore structures with natural periods between 1 and 5 seconds, and is characterized by momentary deflections that occur at significantly higher frequencies than the incident wave frequencies and usually occurs as a result of a large, steep wave [36]. Bachynski & Moan stated in [36] that the modelling of ringing loads requires second order quadratic transfer functions and third order wave forces to capture

the ringing phenomena during simulation[4]. Springing is also dependent on sum-frequency effects and is sometimes referred to as super-harmonic resonance in the tendons [22]. It is worth noting that analysis of these effects exceed the present scope of work.

Another typical property of the TLP system is the phenomena referred to as set-down effects. Set-down effects refer to a change in draft of the structure due to large motions in the horizontal plane. DNV-OS-J103 refers to set-down as a kinematic coupling of horizontal motions and vertical motions [21]. The set down effect has been illustrated in the figure below.

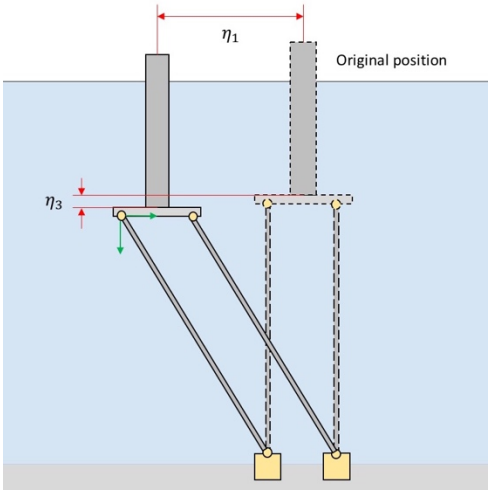

Figure 6-2: Illustration of the set-down effect

The figure used to illustrate the set-down effect above also shows the horizontal force component arising at the connection due to this offset. When the system experiences a load in the horizontal plane, there is a horizontal restoring force arising from the tendons to counteract this motion. The horizontal restoring force for small displacements is given by the following equation [35]. The equation assumes that the tendons are neutrally buoyant and that the tendons are allowed to rotate about the connection point to remain straight for a certain displacement in the horizontal plane.

$$F_R(\eta_1) = \frac{n_t T_t}{L_t} \cdot \eta_1 \qquad \textbf{(6.1)}$$

Where n_t is the number of tendons, T_t is the tension in each tendon, η_1 represents a displacement in surge (consistent with coordinate system under motions of vessels chapter) and L_t is the length of the tendons. The significance of this equation is that it shows that the length of the tendons has a negative impact on the horizontal restoring force, as one would expect as the axial stiffness reduces with length [37]. Another useful equation regarding the restoring effects from the tensioning system is the total restoring moment in yaw. Since the VAWT exerts torque on the system, about the vertical centreline, during operation [12] it is useful, in the spreadsheet stage, to estimate the restoring moment of the system in yaw. The restoring moment supplied by the tension leg system is given by the following equation also assuming neutrally buoyant tendons [35].

$$D_y(\eta_6) = R_y^2 \left(\frac{n_t T_t}{L_t}\right) \eta_6 \qquad \textbf{(6.2)}$$

Where R_y is the distance to each tendon from the axis of rotation and η_6 is a small angle in yaw.

[4] These higher-order effects (ringing and springing) exceed the scope of work in this thesis and focus will not be on capturing these loads at present due to the simplified wind model that is to be applied for the dynamic simulation.

6.1.2 Natural period of selected degrees of freedom for TLP

Since the TLP platform obtains its stiffness against heave from the tendons it is important derive the stiffness coefficient for these when calculating the natural heave period of the system as a whole. The two equations below are used to express the stiffness of the the tendons and the natural period in heave [35].

$$k_h = \frac{n_t A_t E}{l_t} \quad \textbf{(6.3)}$$

Where k_h is the stiffness of the tendons (in heave), n_t is the number of tendons, A_t is the cross sectional area of the tendon (cross section of the material), E is the Young's modulus for steel and L_t is the length of the tendons. The natural period in heave (T_h) is given by the following expression.

$$T_h = 2\pi \sqrt{\frac{M_h l_t}{n_t A_t E}} \quad \textbf{(6.4)}$$

Where M_h is the total mass including the added mass in heave. A typical period in heave for a TLP is between 2 and 4 seconds [35].

The natural period of the TLP in surge is given by the following equation as proposed in [35] assuming neutrally buoyant tendons.

$$T_s = 2\pi \sqrt{\frac{M_s l_t}{n_t T_t}} \quad \textbf{(6.5)}$$

Where M_s is the total mass in surge (includes added mass in surge). An example for a typical period in surge for a TLP is in the vicinity of 120 seconds [35]. Note that this value is not necessarily representative of smaller TLP's for use with offshore wind turbines.

The natural period in yaw is given by the expression below for pure rotation about the central vertical axis [35].

$$T_y = \frac{2\pi}{R_y} \sqrt{\frac{I_y l_t}{n_t T_t}} \quad \textbf{(6.6)}$$

Where I_y is the total mass moment of inertia in yaw where added mass has been accounted for.

6.2 Design considerations for TLPWT

This section will cover some of the conclusions made by other authors that have conducted previous studies of TLP wind turbines (TLPWT) with particular attention to modelled geometry, typical dimensions, environmental conditions, and dynamic loadings and responses. Particular references are made to [8], [11], [29]. It should be noted that the aforementioned references are closely linked.

6.2.1 TLP dimensions based on 5 MW HAWT TLP system

In order to provide a basis for the general requirements for TLP dimensions in the concept description phase it was deemed important to obtain typical values from source material on existing/tested TLPWT systems. Due to the extensive work conducted by Bachynski, E. E. and Moan, T. in this field, it was found to be a reasonable step in the parametric definition process to build on this prior work, to some extent. Due to the differences in turbine properties and overall scope of work between this thesis and the work conducted by Bachynski, E. E and Moan, T. the results and TLPWT properties are not directly comparable. However, the key considerations provided based on these authors' work are deemed relevant for use as a starting point for the work presented in this thesis.

The aforementioned authors submitted an article on *Design considerations for tension leg platform wind turbines* in 2012 [29] where the aim was to assess the structural response of a TLPWT system for several design parameters. The article presents a parametric study of five primary variations of single-column TLP designs, with an additional 40 iterations of the primary cases. The five initial designs served as the baselines for sensitivity analyses of additional parameters such as column diameter, pontoon radius, ballast fraction and water depth (has a direct effect on the tendon length) [29]. The baseline designs also featured different number of pontoons, where two designs had four and the remaining designs had three pontoons. In the table below the physical properties of TLPWTs 1-5 have been presented.

Table 6-1: Bachynski TLPWT properties [29]

	TLPWT 1	TLPWT 2	TLPWT 3	TLPWT 4	TLPWT 5
Diameter D_1 / D_2 (m)	18.0 / 18.0	14.0 / 14.0	14.0 / 14.0	6.5 / 10.10	6.5 / 6.5
Draft d (m)	45	35	22	29	17
Pontoon radius r_p (m)	27	32	28	25	32.5
Number of pontoons	4	2	3	4	5
Displacement (m^3)	11 866	7 263	5 655	4 114	2320
Tendon pretension (kN)	6 868	4 963	8 262	5 556	3384
Natural period η_1 (s)	56.27	52.26	41.86	34.22	40.13
Natural period η_3 (s)	0.55	0.75	0.60	0.52	0.60
Natural period η_5 (s)	2.77	2.81	2.75	2.74	2.69
Natural period η_6 (s)	13.99	17.97	18.63	19.83	19.59

The column diameters in the baseline cases varied between 6.5 and 18.0 m with substructure heights in the range of 23 to 52 m. The corresponding displacements ranged between 2 320 to 11 866 m^3. The authors limited the range of variables by assuming a fixed freeboard of 10 m for all designs, which has also been adopted here in this thesis. As can be observed from the table above, the drafts range between 17-45 m. It was stated that the initial stability of these vessel had not been verified [29].

6.2.2 Design criteria and parameters affecting performance

The design criteria established by Bachynski and Moan are presented in Table 6-2. These criteria were implemented to filter out poor parameter combinations for the baseline TLPWT designs prior to the simulation stage of the analysis. These criteria are to some extent adopted here for pre-design work but deviations from these criteria may occur due to the differences in power ratings and turbine type. It is initially hypothesised that the design criteria presented below will suffice to avoid slack in the tendons and excessive motions during the dynamic simulation phase presented in this thesis.

The tendons in the analysis by Bachynksi and Moan were hollow pipes made of steel with a thickness such that the pipes were neutrally buoyant in water [29]. The pre-tension of these tendons was an important part of this article where hull displacement and avoidance of slack were two key areas that were analysed. The buoyancy force, regulated by ballast (for TLP), which is dependent on the hull displacement, is the only parameter that affects the available pre-tension of the tendons.

Table 6-2: Design criteria for TLPWT according to Bachynski & Moan (2012) [29]

Description	Criteria	Comment
Natural period in surge and sway	> 25 s	Avoid first order wave excitation
Natural period in heave, roll and pitch	< 3.5 s	Avoid first order wave excitation
Mean offset limitation (in terms of water depth)	≤ 5 %	Limit angle at connection point for tendons.
Material cross sectional area	$\geq 2\, T_t \cdot \frac{SF}{\sigma_Y}$	Sufficient to prevent yielding of the material if tether is exposed to a loading equivalent to 2x initial tension value, with an applied safety factor (SF) of 2.
Hull displacement	≥ 2 000 m^3	For survival of extreme environmental conditions

As mentioned earlier the authors conducted a sensitivity analysis of some of the main parameters to determine the effects on platform motions[5], tendon tension and bending moment at the tower base. The results for changes in D_1 and D_2, d, r_p and ballast fraction were presented with reference to their effect on the overall variation in performance with reference to the factors above. The performance factors were given (for increases in the respective parameter only) in the form of qualitative assessments (based on quantitative analyses) of changes in performance with outcomes regarded either positive, negative, none or unclear. The most consistent improvement in performance was observed for changes in pontoon radius [29], where larger pontoon radii seemed to consistently lead to improved performance.

The authors concluded that designs with larger displacements led to improved motion characteristics (minimal motions) and that pre-tension was found to fall into the category of larger-the-better. Another conclusion made in this article was that the platform responses were sensitive to the natural periods and stiffness of the system [29]. It was also stated that the natural periods in surge and sway may be required to exceed the criteria presented above, where an interval between 45 and 70 seconds gave improved results in a storm scenario [29]. It is worth noting that, although the authors did state that increasing the pontoon radius was the most consistent way of improving the overall performance of the system, they had not conducted an analysis of the structural integrity of the hull. In addition to this Bachynski, E. E. and Moan, T. recommended a displacement ranging between 3500 and 6500 m^3 with a pontoon radius between 28 and 35 m (for turbines with power ratings of 5 MW) [29]. It is worth mentioning that the article focused on substructures for 5 MW HAWTs.

6.3 Environmental conditions for simulation

In 2013 Bachynski, E. E. and Moan, T. submitted an article on hydrodynamic models for TLPWT [8] as a continuation of the research conducted in [29]. The authors studied three hydrodynamic models for four TLPWT's with the same range of diameters and drafts as presented in the previous section. These hydrodynamic models were: first order potential flow with viscous drag, a combination of first and second order potential flow with viscous drag, and Morison's equation [8]. The authors conducted the analysis using four different environmental conditions, one of which was a storm condition (EC4), with increasing values for H_S, T_p, U_0, and I. The environmental conditions used in the referenced article is presented in Table 6-3.

Table 6-3: Environmental conditions – hydrodynamic modelling of TLPWT by Bachynski & Moan [8]

Condition	Hs (m)	Tp (s)	U (m/s)	I
1	2.5	9.8	8	0.20
2	3.1	10.1	11.4	0.17
3	4.4	10.6	18	0.15
4	12.7	14.1	50	0.11

Bachynski & Moan made references to sum-frequency and difference-frequency components for the second hydrodynamic model listed above, but stated that the difference-frequency component was not considered in its entirety (diagonal components are considered through Newman approximation) [8]. DNV GL states that the

[5] The platform motions analysed by Bachynski & Moan in [29] were surge, pitch, roll and jaw.

Newman approximation is valid when the natural frequency of the floater is very low (i.e. long natural period) [38].

It was concluded, from this article, that the Morison model was sufficiently accurate compared with the potential flow model for the smaller hull diameter, but generally over-predicted the forces (and motions) compared with the other two models [8]. However, there was evidence suggesting that there were significant variations (with the Morison model) in the prediction of loads, especially in pitch, when comparing normal operating conditions and larger waves [8]. It was also found that if the pontoons were larger, the structure was more sensitive to sum-frequency loadings in pitch [8]. The authors also found that tendon tension was sensitive to second order loads, and that larger TLPWTs were generally more sensitive to second order loads.

6.4 Tendon pre-tension and non-linear effects

Bachynski and Moan analysed 4 TLPWT designs in [8] for a 5 MW HAWT, with pretensions ranging between ~5 to 8 MN. The criteria here was to avoid slack, which is important to consider when assessing the TLP system as snap loads are likely to be imposed on the system if slack tendons were to occur [9]. Slack tendons may result in loss of tendon, i.e. tendon is disconnected from the vessel, which in turn may result in loss of the vessel [8]. Non-linear effects (sum-frequency loads) were found to have noticeable effect (2-9% increase) on the standard deviation in tendon tension [8]. Non-linear effects, based on the sum-frequency QTF were also found, by the aforementioned authors, to have a greater effect for TLPWTs with larger pontoons, deeper drafts and lower pre-tension. However, the sum-frequency effects and other non-linearity's are not considered in this thesis.

6.5 General concluding remarks

As presented in the prior sub-sections above, there are multiple aspects to consider regarding the determination of promising parameter combinations prior to the simulation phase identified in the scope of work earlier in this thesis. As stated under the thesis objective, the concept to be evaluated in this thesis features two separate structures which are floated out to the location of installation in separate operations. This means that inherent stability of the vessel(s) is a critical aspect to consider. Since the work by Bachynski, E. E. did not take into account the aspect of float-out stability, there are several limitations to the adoption of similar structural dimensions, for use in this thesis, based on the data contained in Table 6-1. In light of inherent stability, it is necessary to focus on structural parameters that will yield sufficient stability for the two vessels. For this reason, only the ranges of waterline diameters, pontoon radii and total displacements are adopted for reference purposes in this thesis. It is worth noting that the values presented in Table 6-1, are used to define the approximate upper and lower values of these respective parameters (these ranges are presented under the concept description and definition of parameters chapter).

In addition to the diameters, pontoon radii and total displacements, the pre-tension values presented in Table 6-1 are also considered in order to set the design criteria for use in this thesis. The range, represented by the upper and lower values found in [29], was around 5 to 8.2 MN (TLPWT 1-4 only).

The scope of work in this thesis is subject to significant limitations regarding non-linear effects, which were studied by Bachynski & Moan, as well as being subject to rigidity assumptions regarding the turbine shaft and structure as a whole. In regards to non-linear effects it was stated in [8] that systems with relatively large pontoons resulted in greater sensitivity to sum-frequency pitch loads. Since sum-frequency effects are not to be included here it was deemed suitable to limit the diameters of the pontoons to relatively small values.

7 Concept description and definition of parameters

This chapter seeks to define the overall function of the concept taking into account the various components, installation procedures and structural setup of the station keeping solution. The explanation of the concept will be accompanied by simple illustrations in order to explain the workings of the proposed design. The chapter is divided into subchapters where each section represents a key component of the concept but also includes a description of the installation procedure.

Note that the concept description presented here exceeds some areas of the scope, with particular reference to examples of tow-out setups, connection mechanism and power transmission. The scope of work is limited to finding three promising cases based on typical design criteria developed for HAWT TLP as stated under the TLP design considerations chapter.

7.1 Overview

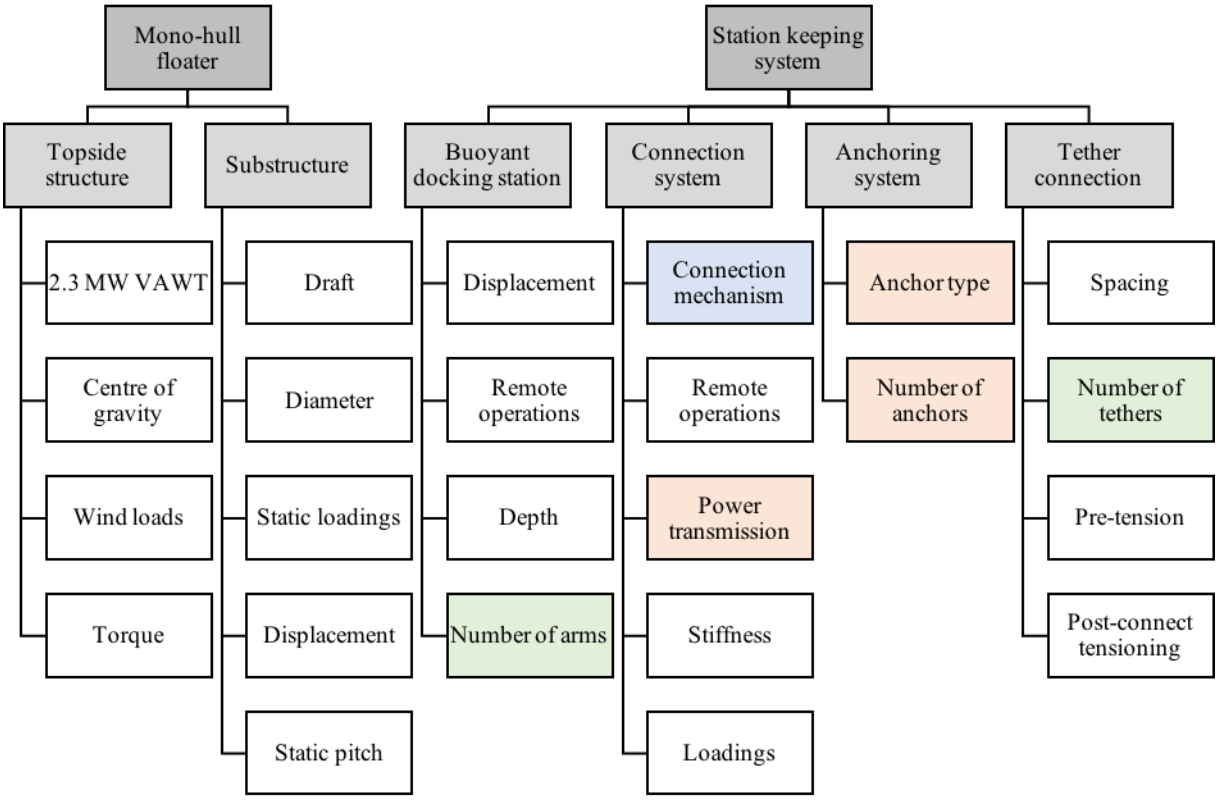

Figure 7-1: Concept considerations chart for mono-hull floater and station keeping system

The chart above presents some of the critical considerations concerning two of the major components for this concept. The installation procedure has been omitted from this chart as the basic principle will remain constant throughout the concept development phase. The concept is divided into two separate systems; the mono-hull floater and the station keeping system.

Note that the number of arms (labelled in green in the figure above) will be set to three in this analysis since this will lead to a simpler balance of forces, i.e. easier installation procedure [10].

7.2 Installation (mating) procedure

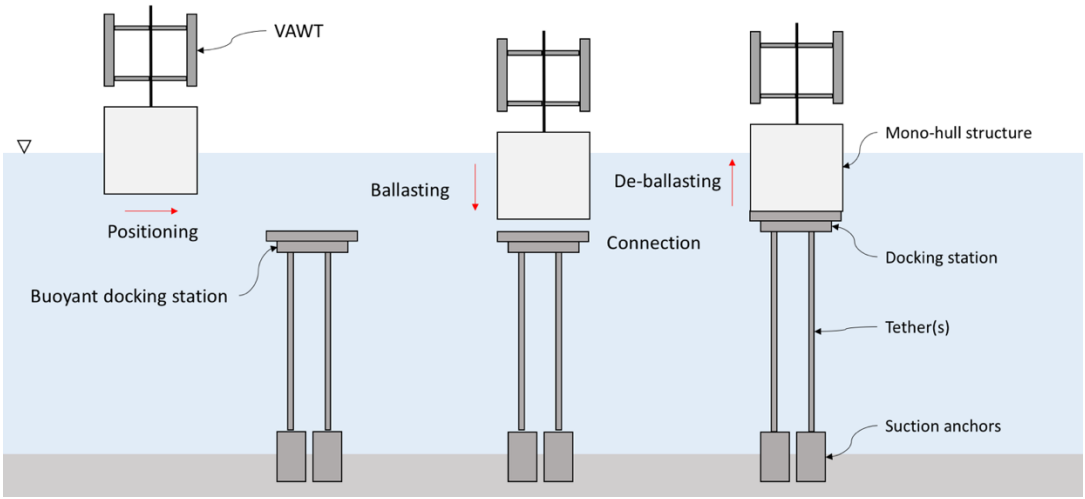

Figure 7-2: Mating procedure for a mono-hull floating VAWT (re-illustrated based on [7])

The figure above presents the basic principle behind the mating procedure between the floating offshore VAWT and the submerged buoyant docking station along with the associated components and systems [7]. The figure has basis in a conceptual sketch by Prof. A. Nergaard from 2009.

The mating procedure consists of four main stages: positioning (1), ballasting (2), connection (3) and de-ballasting (4) [7]. The positioning of the floater is a critical part of the installation procedure and will likely take place using tug-boats with acoustic positioning receivers and transducers mounted on the mono-hull and BDS to accurately measure the relative position between the two. Acoustic positioning systems are widely used in the offshore industry using either long baseline or short baseline signals depending on the accuracy required [39] however, this will not be covered here.

The ballasting phase of the operation will take place by flooding the ballast tanks with water to lower the floater further down into the water. When the ballasting operation is complete the connection phase will begin where it is critical that the connection interface is lined up accurately before the connection is made. When the connection has been made and verified the de-ballasting phase will begin. In this phase the ballast water will be ejected back into the ocean in order to increase the tension in the tethers by reduced vessel weight.

7.2.1 Tow-out operation

The following section will cover some of the critical considerations to a typical tow-out operation with respect to towing setup and draft requirements. Note that this section only provides some basic insight and will not be subjected to further analysis.

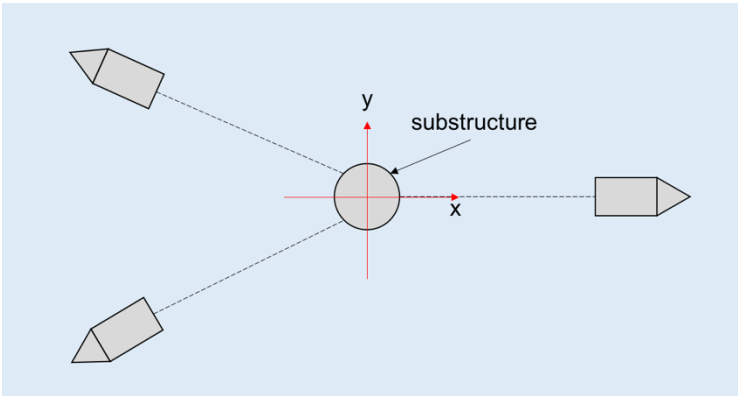

Figure 7-3: Typical 3 tug tow-out setup (based on [40])

The tow-out procedure is a critical for the installation sequence illustrated in Figure 7-2 as the substructure must have sufficient keel-seabed clearance en-route to the installation location [41] as well as sufficient stability in an un-moored state. The 3-tug tow setup above is adapted from Technip's tow-out operation setup as was conducted for the Hywind SPAR structure [40]. Deep drafts may impose several limitations on the selection of routes as illustrated in the figure below, where the initial draft is greater than the water depth at a certain location along the route.

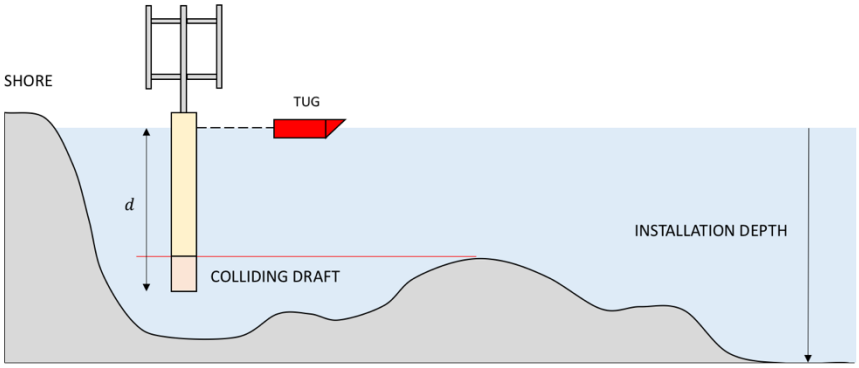

Figure 7-4: Variable water depth and impact on tow-out (based on [41])

The tow-out operation for the buoyant docking station can either take place in a fully submerged state or floating with pontoons out of the water. An illustration of the floating setup is presented in the figure below.

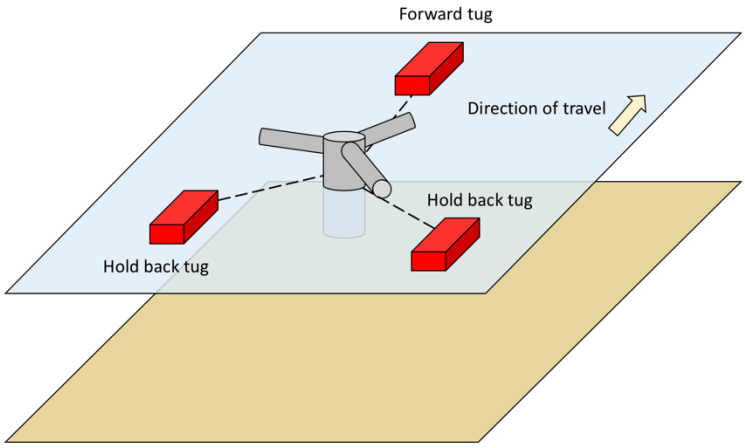

Figure 7-5: 3D view of the towing operation for the BDS in floating mode (based on [40])

A possible solution to the submerged tow-out setup is presented in the figure below. The solution presented here is based on Figure 7-11 in DNV-RP-H103 (submerged object attached to towed buoy) [42].

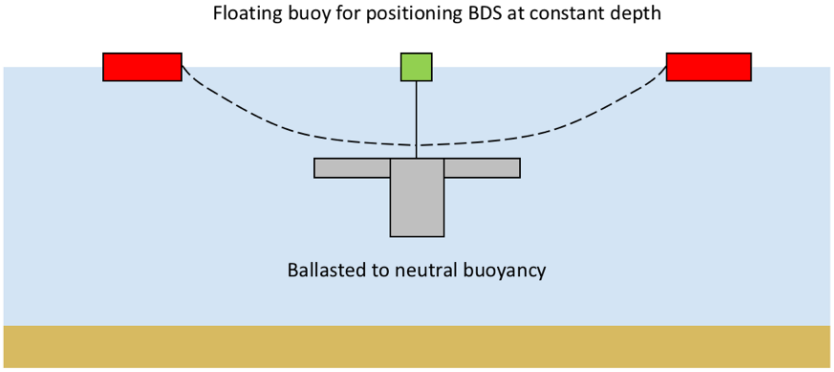

Figure 7-6: Tow-out for neutrally buoyant (submerged) BDS with float

The general criteria for the tow-out operation for both components is that the vessel shall remain stable in benign conditions. The tow-out phase is not to be analysed in this thesis, but initial stability in floating and submerged condition is presented.

7.3 Mono-hull floater

In this section the wind turbine and structural parameter ranges of the mono-hull floater are presented.

7.3.1 Wind turbine (topside)

The topside structure consists of one three-bladed 2.3 MW H-rotor VAWT with the dimensions as presented in the table below [13] and [12]. As previously mentioned, the topside structure will remain constant across all analyses in this thesis in order to limit the number of variables, and for purposes of comparison. A 3-D model of the wind turbine system is presented in the figure below.

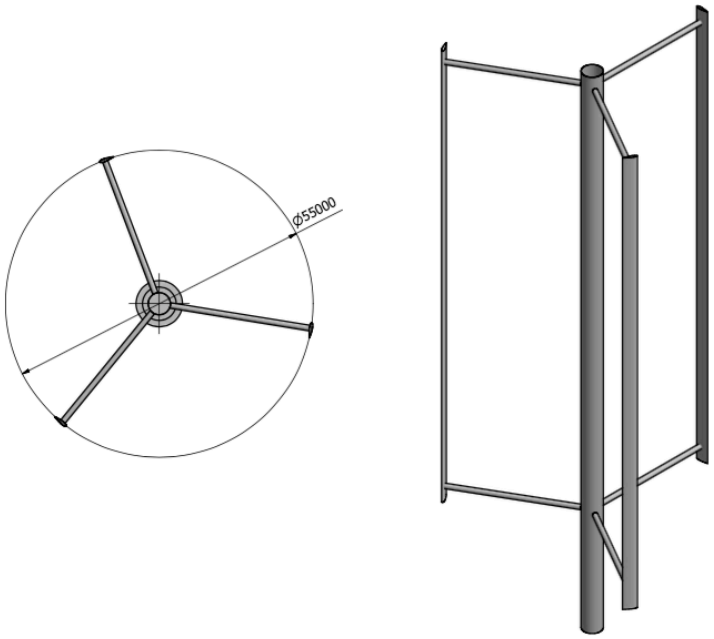

Figure 7-7: Estimated 3-D model for the 2.3 MW VAWT [43]

Table 7-1: Topside dimensions and related data (based on [12] and [13])

Description	Value	Comment
Number of blades	3	
Power production	2.3 MW	At wind speed of 12 m/s
Power coefficient	0.45	
Swept area	4895 m^2	
Mean diameter	55 m	
Length of blades	99 m	
Airfoil type	NACA 0021	
Chord length	2.75 m	
Blade thickness	0.58 m	Based on NORCOWE
Solidity ratio	0.3	
Tip speed ratio	3	
Bottom of rotor blade clearance to MSWL	23 m	for freeboard of 10 m
Mass of gear and generator	82 tonnes	COG at MSWL
Cut-out wind speed	25 m/s	

7.3.1.1 Inertial properties

The masses, with corresponding local COGs, are taken from [13] whereas blade dimensions are taken from [12]. There are uncertainties regarding the mass and COG for the 2.3 MW VAWT turbine analysed in [13] as these are not directly specified in the report. In order to provide a suitable estimation for the turbine a 3-D model was generated in Autodesk Inventor with Nilsen, S.[6] [43] using dimensions as presented in the table above to calculate the associated masses and moments of inertia of the turbine system. The model assumes a steel density of 7850 kg/m^3 for the stiffeners and the shaft, whereas the density of the air-foils are 1850 kg\m^3 (GRE Composite material [44]). The mass and local COG of the gear and generator was added after generating the 3-D model in order to find the total payload inertial properties. The table below shows the physical properties of the turbine system exported from the CAD model.

Table 7-2: Physical properties of turbine system [43]

Property	Value	Comment
Mass of turbine section [kg]	398587	Excludes gear and generator
Centre of gravity [m]	(0, 0, 58.9)	Measured from top of freeboard
Moment of inertia XX [kg·m^2]	5.30E+08	Local principal axis
Moment of inertia YY [kg·m^2]	5.30E+08	Local principal axis
Moment of inertia ZZ [kg·m^2]	1.00E+08	Local principal axis

The inertial properties of the generator have been estimated by a 1 diameter solid cylinder with a 1 m height (point mass). The density of this cylinder was estimated from the total mass of the generator (82 tons). The inertial properties calculated in Inventor have been presented in the table below.

Table 7-3: Physical properties of generator

Property	Value	Comment
Mass of generator [kg]	82000	
Centre of gravity [m]	(0, 0, 0.5)	Measured from SWL
Moment of inertia XX [kg·m^2]	1.19E+04	Local principal axis
Moment of inertia YY [kg·m^2]	1.19E+04	Local principal axis
Moment of inertia ZZ [kg·m^2]	1.02E+08	Local principal axis

These values are used to calculate the total inertia with respect to the centre of gravity for the substructures. Note that the values presented above are fixed for all cases with constant freeboard of 10 m.

7.3.1.2 Torque

The following calculations are based on the equations presented under the section on VAWT. In order to capture the loadings associated with this turbine it is necessary to determine approximate design values with particular emphasis on the generated torque and wind heeling moment from the turbine. In this section the generated torque will be estimated based on turbine characteristics and operational conditions as stated in [12]. The free stream velocity is given as 12 m/s, which is the operational wind speed in this case. A tip speed ratio of 3, power coefficient of 0.45 and a rotor radius of 27.5 m has been assumed based on [12].

The results are presented in the table below.

Table 7-4: Torque and rotational speed

	Value	Unit
Rotational speed	12.5	rpm
Torque	~1800	kNm

Further reference to the input torque, refers to the value presented in the table above.

[6] MSc student and colleague at the University of Stavanger analysing a catenary mooring system for the same 2.3 MW VAWT using a SPAR floater (Supervisor: Nergaard, A.).

7.3.2 Substructure

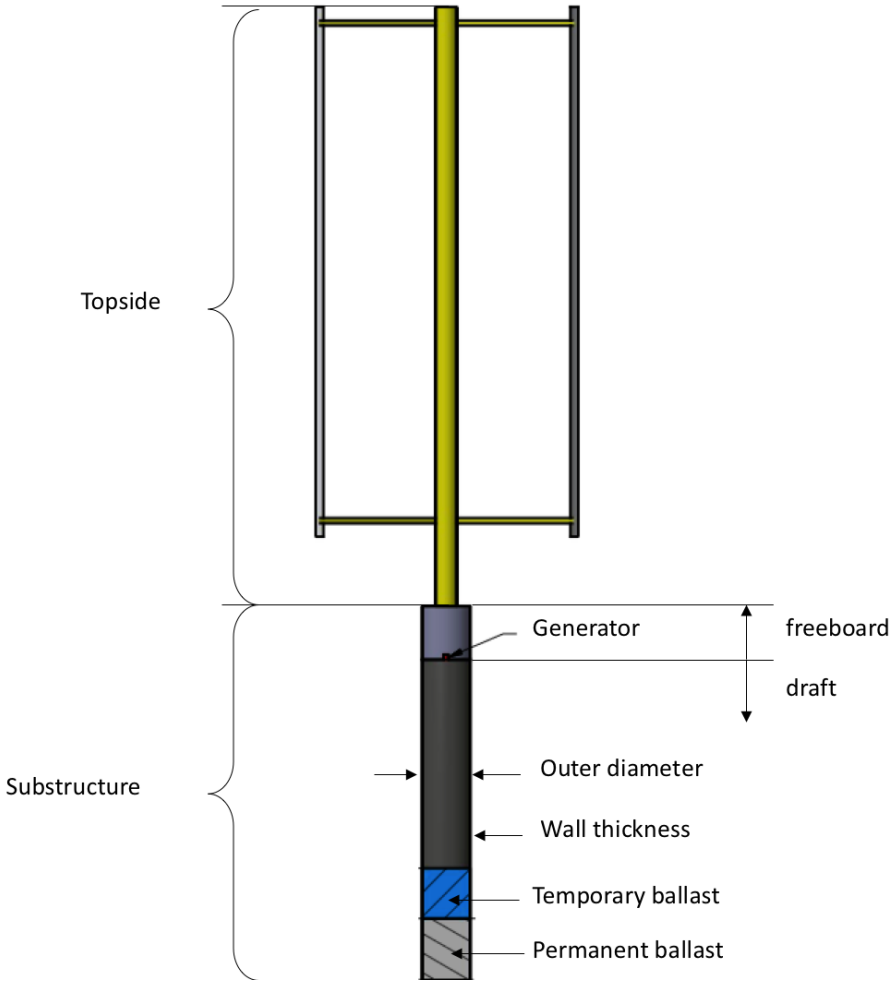

Figure 7-8: General representation of the substructure (with turbine)

The substructure is defined by four main input parameters namely the outer diameter, the operating draft, the average wall thickness and the permanent ballast fraction. From these parameters it is possible to estimate that total mass of the structure, the displacement, the location of centre of gravity, the moments of inertia about the COG and initial static stability. The table below show the typical parameter ranges for the input parameters.

Table 7-5: Input parameters – Substructure

Parameter		Low	High	Units	Comment
Outer diameter	$D_{\text{sub,ext}}$	8	12	m	
Draft	d	30	70	m	
Freeboard	f_b	10		m	Constant
Wall thickness	t_{sub}	25	80	mm	Structural integrity not verified.
Permanent ballast fraction	PBF	0	1	–	Adjusted for stability characteristics

The lowest draft in the table above was set to 30 m based on TLPWT 4 in [11] in order to cover a large range of drafts during the spreadsheet calculation phase. The design space for the outer diameter was set based on the dimensions of some of the structures analysed by Bachynski, E. E. in [11]. Some of the required output values for the substructure are presented in the table below.

Table 7-6: Outputs – Substructure

Description [unit]	Comment
Displacement [m^3]	
Dry mass [kg]	Topside, steel mass and permanent ballast included
Temporary ballast mass [kg]	Used for calculating the available pre-tension per tendon.
Centre of gravity w.r.t. Keel [m]	
Moments of inertia about COG [m]	
Metacentric height [m]	Calculated based on small angle assumption.
Added mass estimates	A11, A33, A55, A66 (used for natural periods)
Natural periods [s]	T33, T55
Available pre-tension per tendon [MN]	

7.4 Station keeping system

In this section the four major components of the station keeping system are presented. The sub-sections present the basic principle workings of each system with a list of associated parameters and ranges.

7.4.1 Buoyant docking station

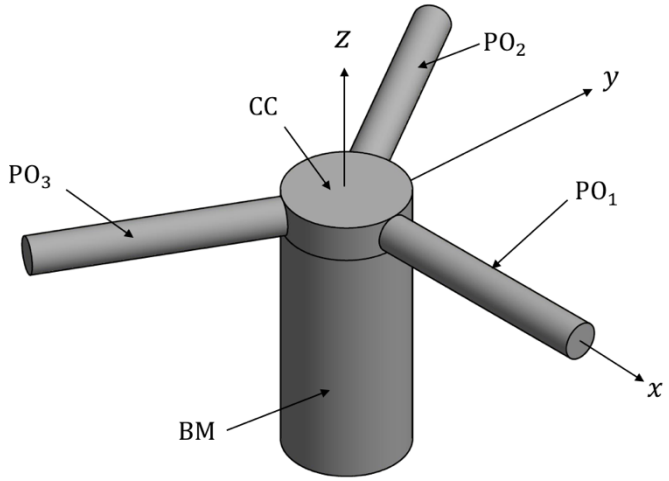

Figure 7-9: Buoyant docking station (3-D view)

The figure above shows the 3-dimensional model of the buoyant docking station (BDS) with the five major components labelled. The abbreviations used in this illustration are central column (CC), buoyancy module (BM) and pontoon (PO) with numbers 1-3. The coordinate system presented above is maintained throughout the analysis phase. The pontoon arrangement is similar to that which was observed in [29].

The two figures below show the basic parametric setup of the buoyant docking station. The pontoons are numbered counter-clockwise starting from the positive x-axis. The pontoon angle is measured relative to the positive x-direction in a counter-clockwise direction.

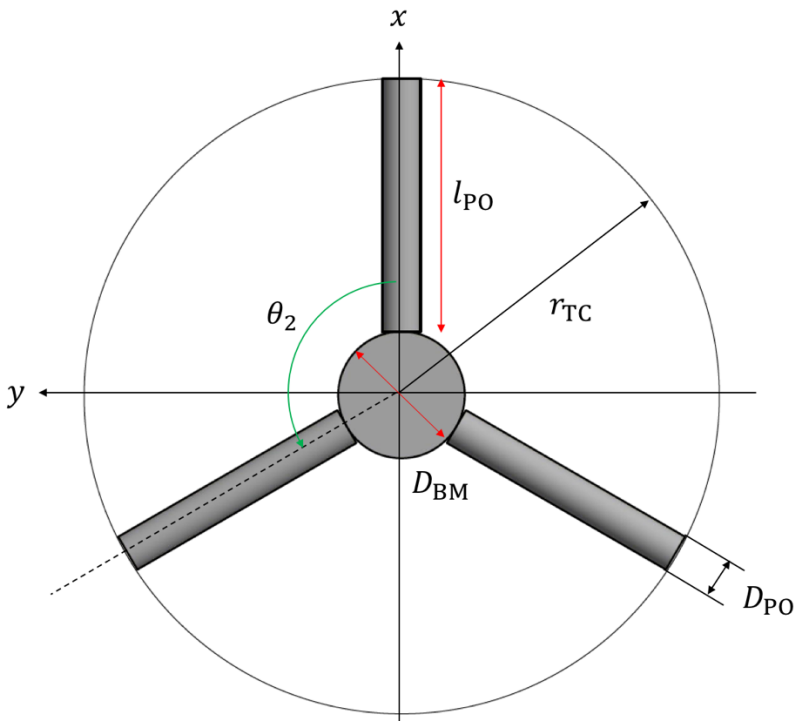

Figure 7-10: Buoyant docking station (top view)

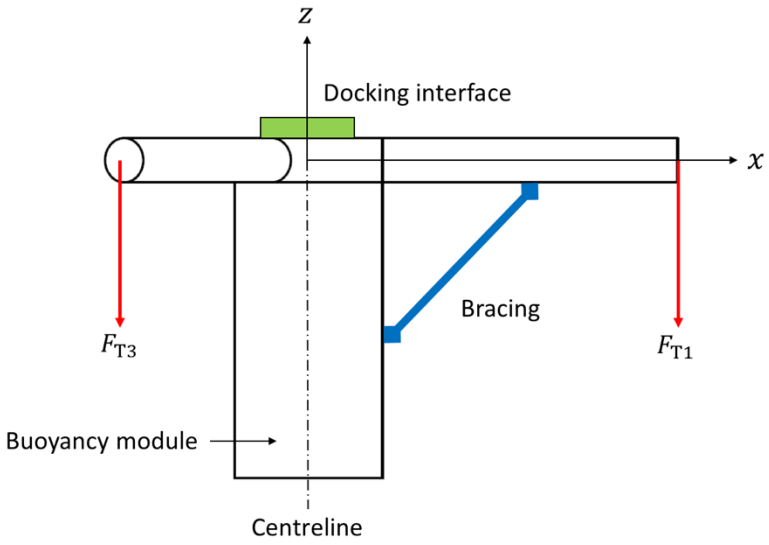

Figure 7-11: Buoyant docking station (side view)

The buoyant docking station (BDS) is a fully submerged body consisting of a docking interface, three pontoons, tether connection system, buoyancy module and an electric power cable connector. The governing structural design parameter of the BDS is the minimum required displacement for remaining neutrally buoyant at operating depth. Note that the displacement of the BDS is also required to be sufficiently large for suitable pre-tensioning of the tethers. The amount of permanent and temporary ballast is critical for stability and achievable pre-tension. The buoyancy module is fixed at the bottom of the structure as this is where ballast is stored during tow-out in order to maintain a low centre of gravity. In Figure 7-11 a bracing system is also presented for the pontoon coinciding with the positive x-axis. The brace will most likely be required in order to reduce the bending stresses at the connection between the pontoons and the central column, however this is not analysed here in this thesis. The brace will not be included in further work but is provided here for reference only.

The overview of BDS parameters is presented in the table below with reference to a low and a high value in the parametric range. It is worth noting that the parameters are decided based on requirements for displacement and motion characteristics.

Table 7-7: Overview of independent variables – Buoyant Docking Station

Parameter		Low	High	Units	Comment
Central column diameter	D_{CC}	8	12	m	
Central column height	h_{CC}	–	–	m	The height of the central column (excluding buoyancy module)
Tether radius	r_{TC}	–	–	m	Equal to the total radius in the cases analysed.
Pontoon length	l_{PO}	10	30	m	Critical stiffness parameter [29]
Pontoon angle	θ_j	–	–	°	The counter-clockwise angle from x-axis to pontoon *j*
Pontoon diameter	D_{PO}	3	6	m	Diameter of circular pontoon
Buoyancy module diameter	D_{BM}	8	12	m	
Buoyancy module height	h_{BM}	10	30	m	
Permanent ballast fraction	PBF	0	1	–	May be referred to in terms of percentages
Wall thickness	t_{i}	40	60	mm	Wall thickness for component *i*

The central column diameter and buoyancy module diameter have the same range as the diameters for the substructure. The central column height is fixed to the same dimension as the pontoon diameter in order to limit the number of variables. The pontoon lengths were selected based on presented pontoon radii in Table 6-1 presented earlier. The permanent ballast fraction (PBF) has a range of 0 to 100%, but should be as low as possible for increased pre-tensioning capability. The PBF is an indicator of how much of the total ballast is permanent, i.e. cannot be used for pre-tensioning the tendons.

Table 7-8: Overview of outputs – Buoyant Docking Station

Output		Comment
Dry mass [kg]	$m_{\mathrm{BDS,dry}}$	The mass of the structure without ballast
Required ballast [kg]	$m_{\mathrm{BDS,b}}$	The required mass of ballast for neutral buoyancy (includes both permanent and temporary ballast)
Displacement [m^3]	∇_{BDS}	The total external volume of the structure
Centre of gravity [m]	(x_G, y_G, z_G)	With respect to keel of structure.
Centre of buoyancy [m]	(x_B, y_B, z_B)	With respect to keel of structure.
Metacentric height r.t. COG [m]	$\overline{\mathrm{GM}}$	Submerged and floating stability
Temporary ballast [kg]	$m_{\mathrm{BDS,b,t}}$	Used to calculate the total deliverable force to the tendons
Force per tendon [N]	$\mathrm{T}_{\mathrm{t,i,1}}$	Deliverable force to tendon *i* from BDS.
Available ballasting height [m]		Verification cell to check that the total required ballast will fit in the buoyancy module.

Some of the initially identified functional requirements of this system are presented in the table below. The purpose of presenting this table is to provide an overview of what is expected from the design of a fit-for-purpose BDS.

Table 7-9: Functional requirements – Buoyant Docking Station

No.	Functional requirement	Comment
1	Provide sufficient buoyancy to prevent slack in tendons	
2	Regulate buoyancy (ballast) during installation	
3	Provide a platform for the docking system	System must be designed such that the body can be lowered
4	System for remote operations	Communications module for regulating ballast
5	Resist bending loads on pontoons due to tendon tension	Bracing as illustrated
6	Provide transmission of electricity from mono-hull to BDS	
7	Signal communication between hull and BDS	Simultaneous operation of individual ballast systems
8	Gauge tension in tethers	
9	Location tracking system (transducer)	Calibrated relative position to mono-hull floater during the connection phase.

7.4.2 Connection system

The connection system is a critical component in the design of the docking station as it must be capable of handling large stresses from tension, bending and should have sufficient fatigue resistance. One of the key functional requirements of the connection system is that it shall be possible to operate remotely. Another requirement is that the connection system shall be able to transfer generated power from the wind turbine to the distribution system attached to the docking station. An illustration of a proposed collet connection interface has been provided below.

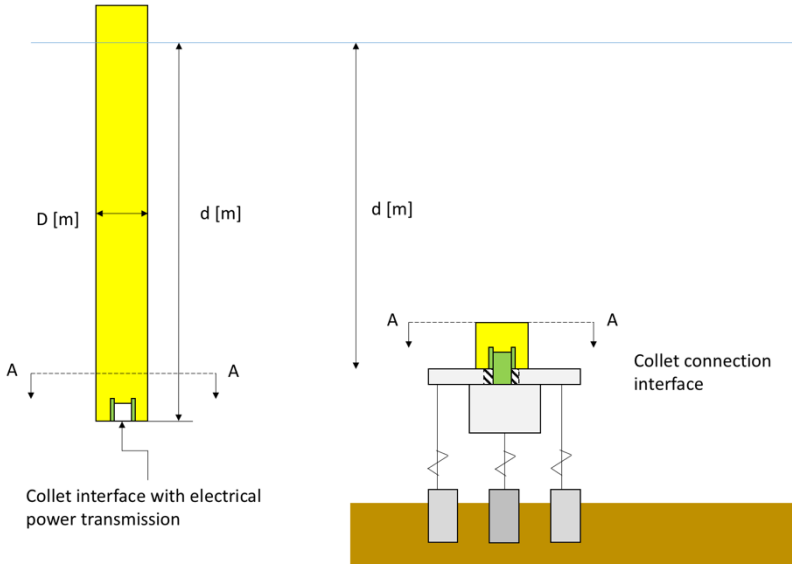

Figure 7-12: Collet connection interface

The connection interface will not be analysed in this thesis due to scope limitations. Qualitatively it may be beneficial to adopt the aforementioned collet connection interface due to its wide-spread use in the offshore oil and gas industry. Cameron state that their collet connectors, with ODs ranging between 1498 and 1911 mm, are able to handle bending moments between 4.0 – 14.9 MNm with preloads ranging between 1.09 – 53.6 MN [45]. The bending moments acting on the connection system is expected to be much greater than the capacity of the aforementioned collet connectors, which means that the connection system will require a significant increase in load bearing capacity if it is to be applied in this setting. The tension preload capacities however, are within range of what is expected to be sufficient for this purpose. The mating process for a collet connector is presented below, with an illustration of the envisioned method of power transfer within the bore-hole of this collet.

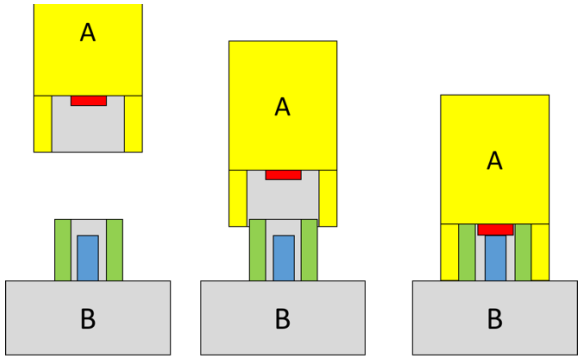

Figure 7-13: The three steps in the collet connection process (based on information in [45])

The red component represents the electrical connection at the floater end (section A) and the blue component represents the electrical connection at the docking station (section B). Further discussion of the connection concept is not covered in this thesis as this exceeds the scope of work, only the basic principle of a potential method is drafted.

In this thesis some coverage of the connection point is presented in the form of vertical loads and bending moments. The values obtained from the dynamic simulation are to be discussed briefly with regards to overall magnitude and load variation.

7.4.3 Tethering system

The tethering system consists of the n_t number of tendons where the tendons (also referred to as tethers) are assumed to be hollow steel cross-sections with a diameter D_t, wall thickness t_t and an initial length l_t. In order to optimize the deliverable pre-tension from the hull and BDS structures it is proposed that the tendons are neutrally buoyant. Neutral buoyancy is achieved for regular steel of density 7850 kg/m^3 if the wall thickness (measured in meters) is 0.034009 times the outer diameter (measured in meters)[7]. The input parameters for tethering system are presented in the table below.

Table 7-10: Input parameters – Tethering system

Description [unit]		Comment
Outer diameter [m]	D_t	
Wall thickness [mm]	t_t	Governed by the neutral buoyancy criterion.
Length [m]	l_t	Function of total water depth and depth of BDS.
Total number of tendons	n_t	
Material type	–	Yield strength and axial stiffness

In this thesis the material type is fixed to S355, with yield strength of 355 MPa [46], in order to limit the number of variables. The considered outputs for the tendons are spring stiffness and the tensile strength of the cross-section.

Note that to analyse the widespread effect of different tendon cross-sectional properties exceed the scope in the present work. In order to be able to compare the results obtained from the dynamic simulation stage it was proposed to maintain one type of tendon, which satisfied, the pre-determined design criteria as presented in Section 6.2.2.

7.4.4 Anchoring system

The anchoring system is not analysed in this thesis, but is assumed to be able to withstand the loads imposed on the system. The main considerations for the anchoring system are listed below [21].

- Installation method
- Type of seabed at particular location
- Type of anchor: suction, pile or gravity
- Soil strength at particular location
- Erosion of proximal soil

[7] Found by material-specific iteration comparing mass of steel to mass of water displaced based on similar relation as presented in [29].

8 Environmental conditions

8.1.1 Selected conditions

In order to capture a sufficient range of loadings on the structure in different environmental conditions, a few different combinations of sea states and wind speeds are presented for use in the dynamic simulation and spreadsheet calculations. The cases will cover stalled condition and operational condition for the wind turbine. Since the thesis is concerned with concept evaluation and not proposing an optimum design for a given location it is assumed to be sufficient to cover a relatively small number of environmental cases, considering the given time frame.

As wind and sea states are considered to be random processes it is in general relevant to set the environmental conditions to reflect a certain probability of exceedance e.g. 100-year storm conditions (probability of exceedance 0.01 in any given year) [47]. In this thesis an approximate 50-year environmental condition is used for EC3 based on [11].

The environmental condition cases are presented in the table below. The waves are to be modelled using JONSWAP spectra with peak shape factor 3.3, which is valid for the North Sea and North Atlantic [9]. The environmental conditions EC 2-3 presented below are identical to the environmental conditions 2 and 4 (respectively) selected by Bachynski & Moan in [8]. The first environmental condition presented in the table is an estimated mild condition state with low wind speed and small waves with shorter periods. It is worth noting that EC1 is not based on any probabilistic analysis of a certain sea states, it is only applied for accepting or rejecting certain substructures during the spreadsheet calculation stage presented at a later stage and was arbitrarily selected for pre-design work based on Figure 2.7 in [48]. The wave height and period were selected based on the scatter diagram in Table 3.2 in [48], as this was believed to be a relatively mild sea state. The purpose of establishing EC1 was to provide a means of estimating the static pitch angle of the vessel due to wave and wind loads, and is not used for design purposes.

Table 8-1: Environmental conditions

EC	U(Hub) [m/s]	H_S [m]	T_P [s]	T_Z [s]	Comment
1	7	1	6	–	Tow-out, linear wave
2	11.4*	3.1	10.1	7.85	JONSWAP
3	50*	12.7	14.1	10.96	JONSWAP

* The values presented in the table are provided for representation purposes only, based on the environmental conditions studied by Bachynski, E. E. in [11]. These velocities are not used for calculating the wind force acting on the structure. The wind forces are, for these conditions, based on the operational and stalled condition wind forces calculated by Hansen, T. in [12] as discussed under the spreadsheet results section at a later stage. The spectral densities for EC2 and EC3 are presented in Figure 8-1 and Figure 8-2 respectively (exported from OrcaFlex).

8.1.2 Current and tide conditions

No current and tide conditions were analysed in this thesis.

8.1.3 Setting the simulation time

Note that the the wind velocity at a 10-meter reference height is given as the 1-hour mean wind velocity, hence the simulation times must be set to 1 hour with reference to DNV-OS-J101. It is assumed that the environmental conditions analysed by Bachnyski & Moan in [8] are presented in terms of 1-hour periods. DNV-OS-J101 states that conversion factors should be implemented when simulating a sea state that differs from, for example a 3-hour period, for which the sea state has been calculated [49]. In conclusion the environmental conditions are analysed in OrcaFlex for a duration of 3600 seconds, corresponding to one hour.

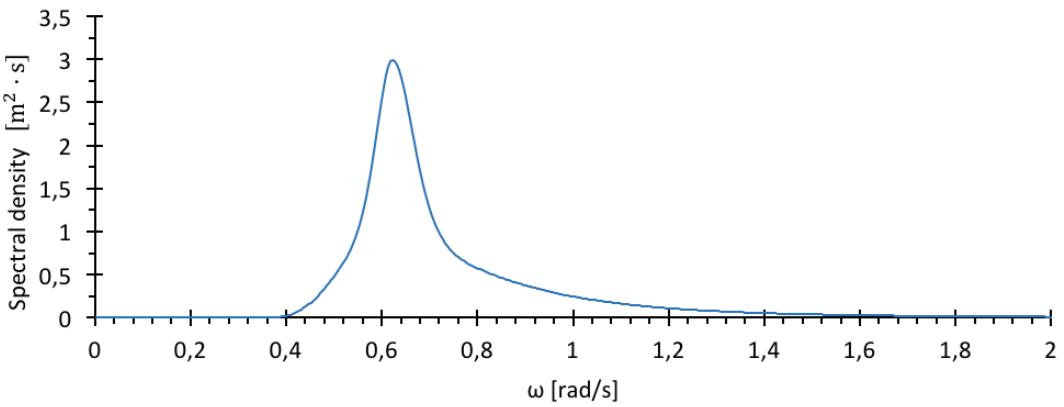

Figure 8-1: JONSWAP spectrum for EC2

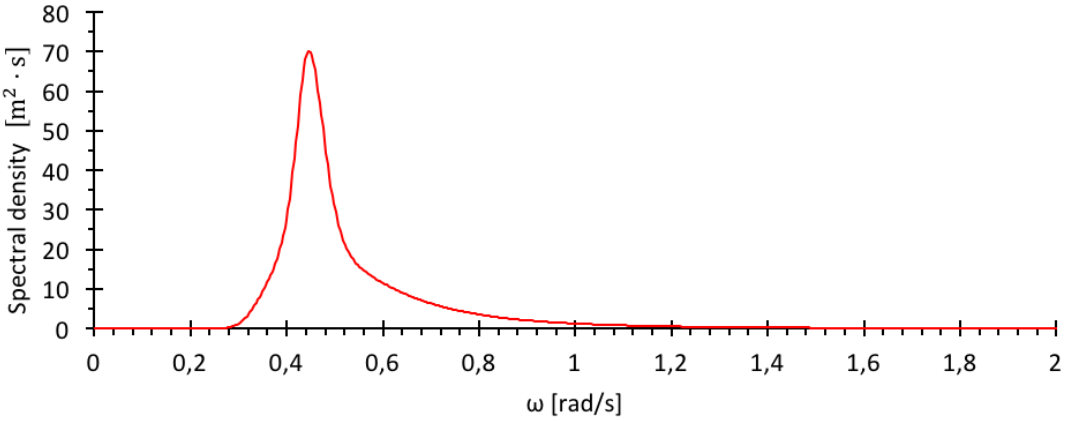

Figure 8-2: JONSWAP spectrum for EC3

9 Analysis procedure

The following chapter will cover the four steps in the analysis procedure including the spreadsheet calculation process, the case identification stage, as well as covering the basic processes for hydrodynamic modelling and dynamic simulation. The results from the spreadsheet calculations along with the identification of cases is presented following this chapter.

9.1 Overview

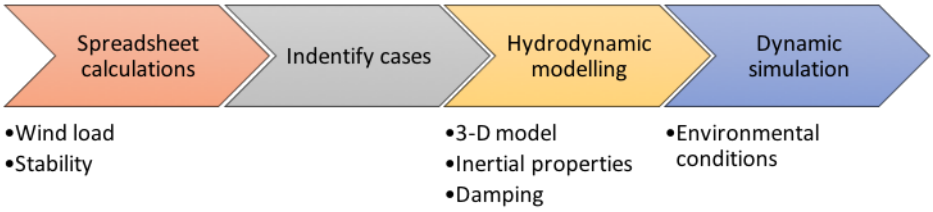

Figure 9-1: 4-stage method of analysis

A simplified overview of the method used in the analysis stage is presented in the figure above. The analysis consists of four principal stages, where the following stage builds upon the previous stage. The following sections present the method for each of the four stages. Note that the cases stage is a presentation of the cases to be analysed based on the spreadsheet calculations, which is presented under the spreadsheet results chapter.

9.2 Spreadsheet calculations

In the spreadsheet calculations there are six stages considered: topside, wind profile, substructure, wave profile, buoyant docking station and the connected system. The spreadsheets have some degree of communication as illustrated in the figure below.

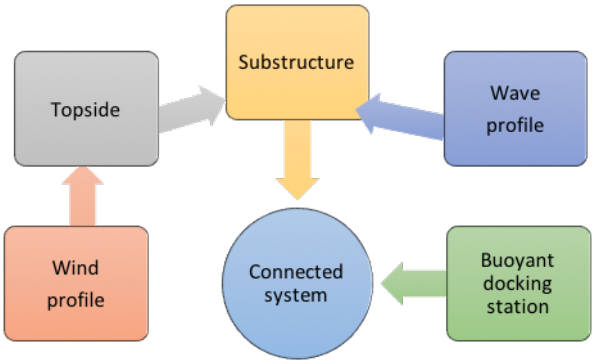

Figure 9-2: Communication paths for the spreadsheets

The topside and substructure spreadsheets are in direct communication, where the topside payload and wind load on the turbine are linked to the substructure for static pitch calculations. The wave profile is also in communication with the substructure for static pitch calculations. The substructure sheet is in communication with the combined case spreadsheet, which in turn is in communication with the buoyant docking station spreadsheet.

9.2.1 Wind load

The wind load spreadsheet is used to generate a wind velocity profile, which is used to calculate the loading on the topside structure defined in the topside spreadsheet. The wind profile is based on the power law profile under the background theory section presented earlier. The wind profile was generated by discretizing the space above SWL to the maximum height of the turbine at 10 m freeboard, into 122 1-meter-long segments. After having generated the wind profile it was necessary to compute the wind pressure and subsequently the wind load acting on each surface exposed to the wind. This requires the calculation of projected areas normal to the wind as well as estimates for the shape coefficients, which is provided in the topside calculation sheet.

9.2.2 Topside

The topside system is composed of two principal components, the turbine and the generator. The turbine and generator properties are specified in Section 7.3.1 on page 44, based on the generated CAD model. The topside spreadsheet calculations are therefore limited to establishing the centre of gravity of the two components specified with respect to SWL and an estimate of the total wind load on the structure. The SWL is used as a reference point as the freeboard remains constant in this analysis.

The wind load on the turbine is calculated for the parked state under a benign environmental condition. The environmental condition used for calculating this wind load is referred to as EC1, where the reference 1-hour wind velocity at 10 m is specified to be 6 m/s, corresponding to approximately 7 m/s at the centre of the blade. This value was selected arbitrarily for pre-design work.

The total wind load was calculated by importing the wind profile from the wind load spreadsheet. Due to the complexity of the air-foil system it was assumed valid to view the air foils as thin rectangles with dimensions equal to the chord length (2.75 m) and maximum thickness of the air foil (0.5775 m). The shape coefficients for these rectangles were found based on DNV-RP-C205 Section 5.4.2 [25] assuming a corner radius of 0 m yielding a r/b ratio smaller than 0.10 resulting in K_R factor of 1.0. The angle of attack of the wind flow relative to the projected area was 90°, i.e. perpendicular flow for maximum load. The shape coefficient for the projected area of the air foils was calculated based on DNV-RP-C205.

After having established the replacement model for the air foil in the spreadsheet it was necessary to compute the projected area and accompanying shape coefficient for the shaft. In order to compute the shape coefficient for the shaft the Reynolds number was calculated for given wind speed. The resulting shape coefficient was found, by reference to Figure 5-5, to be 0.7.

For the wind load calculations, the turbine was arranged in the following manner.

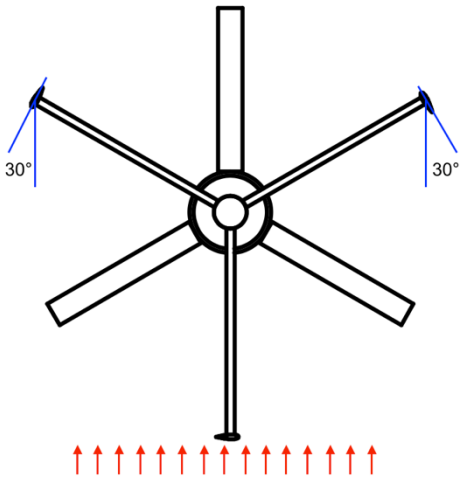

Figure 9-3: Arrangement of blades

The projected areas of the angled plates were reduced to 1.375 m^2 per meter length (from 2.75 m^2), due to the 30° angle relative to the flow of the wind. The red arrows indicate the direction of the incoming wind. Note that the shaft is shielded in this arrangement, but no shielding effects are included in the wind load estimation. The projected areas perpendicular to the flow along with the associated shape coefficients used are presented in the table below. Note that the projected area perpendicular to flow are given for unit lengths (discretisation lengths).

Table 9-1: Shape coefficients used in wind calculations

Element	Projected area ⊥ to flow	Shape coefficient	Comment
Shaft	4	0.7	
Blade 1	2.75	2	
Blades 2 and 3	1.375	2	Projected area per blade.
Units	m^2	–	

The calculated force distribution and total force are presented under spreadsheet results. Note that the wind load is later used in combination with the wave load on the substructure to calculate the overturning moment acting on the structure in EC1 to observe the static pitch of the given floater.

9.2.3 Wave profile

The wave profile was created by utilizing linear wave theory to generate a depth-dependent velocity profile and an acceleration profile based on a predetermined wave height and period. These input parameters are defined for EC1 under the environmental conditions chapter, where the wave height and wave period are defined for the linear wave.

9.2.4 Substructure

9.2.4.1 Inputs

The spreadsheet was built with seven main input variables: diameter, draft, temporary ballast density, permanent ballast density, freeboard, wall thickness and the permanent ballast fraction. In order to limit the number of variables when generating results, it was deemed sufficient to maintain constant values for the wall thickness, ballast densities, and freeboard, effectively reducing the number of variables to three. The focus of the spreadsheet analysis for this structure was to determine the location of COG, COB, $\overline{GM}$, mass of temporary ballast, the moment of inertia of the structure, the tow-out pitch, natural periods, added mass and the hydrostatic stiffness.

The substructure spreadsheet communicates with the topside spreadsheet to incorporate the mass of the payload but also the associated wind load.

9.2.4.2 Mass, COG, displacement, COB and ballast heights

The structural mass was calculated by summation of the topside mass and the mass of steel. The mass of steel was calculated based on the structural dimensions of the vessel to generate a total volume of steel and a material density of 7850 kg/m^3. The total mass of the system was calculated by taking into account the dry mass of the structure and the ballast mass. In order to obtain information regarding the total ballast mass, Archimedes' principle was used to determine the total mass of the structure required to obtain the input draft. After having obtained the total mass of ballast, the permanent ballast mass was calculated by specifying the permanent ballast density.

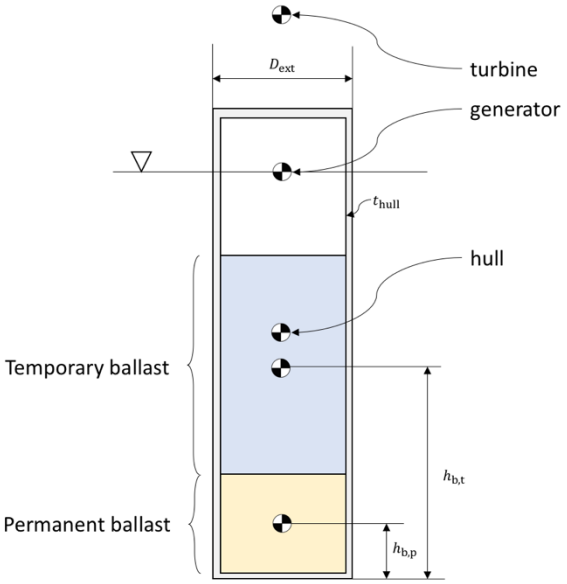

Figure 9-4: Determination of COG for Substructure

The figure above presents the five sections taken into account when calculating the COG for the substructure. The centres of gravity and centre of buoyancy are calculated with respect to the keel of the vessel structure using the equations presented in Section 5.2.5. The COG takes into account the contributions from end plates positioned at

the top and bottom of the structure, which have the same wall thickness as the rest of the hull. Permanent ballast (density 3300 kg/m^3) is positioned at the bottom of the structure and temporary ballast (1025 kg/m^3) is positioned above the permanent ballast as illustrated in the figure above. The required ballast is calculated based on the difference between the mass of the structure and the displaced water at the input draft.

9.2.4.3 Moments of inertia

The moments of inertia are calculated using the equations for hollow and solid cylindrical structures presented in Section 5.2.5.1. Parallel axis theorem has been applied about the global centre of gravity for the system where each local moment of inertia is determined based on the equations presented above. The moment of inertia of the ballast columns are determined by solid cylinders whereas the hull structure moment of inertia is determined by the hollow cylinder equations. The moments of inertia are later used to calculate the natural period in roll/pitch.

9.2.4.4 Stability

The stability of the vessel is determined based on the equation presented in Section 5.2.5. In the spreadsheet the COB and COG were calculated relative to the keel of the structure in the ballasted state. The stability in tow/stability in static condition is of importance in light of the installation and mating phase of the substructure and the vessel should not experience a large angle of static pitch under mild wind and wave conditions.

9.2.4.5 Static pitch

The static angle of the vessel is estimated using Morison's equation and the wind overturning moment acting on the structure for EC1. The spreadsheet was built with direct communication with the topside spreadsheet as mentioned earlier to take into account the wind load acting on the turbine. The moment generated by the wind force on each discretized element was calculated relative to the selected reference point. In the spreadsheet the static angle is calculated for the towing draft, which has been set to the operational draft of the structure in its moored state. The figure below presents the discretization of the hull, the overturning and righting moment contributions.

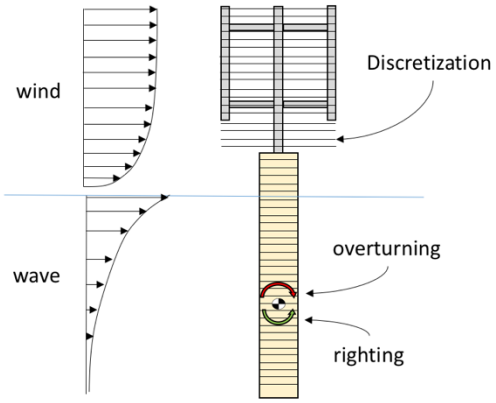

Figure 9-5: Discretization of hull

The wind load is calculated in the topside section earlier, with minor contribution from the exposed hull. The wave load induced rotational moment was estimated about the COG with cancellation effects arising from the wave load acting on the hull below the COG as observed in the figure above. The COG was used as the reference point for the overturning moment although the actual rotation point for a vessel is the metacentre [22]. This was done in order to give a conservative estimate for the pitch angle[8]. As stated, Morison's equation has been used for estimating the wave load on the structure where both drag and inertia effects are calculated.

The amplitude of motion criterion was assumed to be satisfied for the instantaneous wave load on the structure for the static pitch angle. This assumption is based on the expected towing method as observed earlier in Figure 7-3, where hold back tugs positioned off angle relative to the heading of the main tug. In an installation sequence the tugs will operate such that the vessel is prevented from travelling with the waves (refer to Figure 7-3), which consequently should reduce the amplitude of oscillation such that the Morison criteria in Table 5-3 is satisfied for

[8] Note that this conservative approach is valid for relatively small values for GM.

this estimation. It is worth noting that tow-out line contributions are not handled by the spreadsheet. The calculations are conducted in a static state, with the vessel at rest.

The corresponding pitch angle is determined based on the equations presented in Section 5.2.5.6. The method used in the spreadsheet calculation was based on a set of pre-defined righting moments at different angles of pitch. The angle of pitch was then determined by logical programming, where the righting moment was in equilibrium with the overturning moment.

9.2.4.6 Added mass and hydrostatic stiffness

In addition to this the added mass in surge, sway, heave, pitch, roll and yaw are also determined for each of the structures. The added mass calculations are conducted using the equations presented under the section on added mass. The output for added mass in the spreadsheet calculations is the total added mass for the entire length of the structure.

The hydrostatic stiffness in heave and roll/pitch was determined using the expressions noted in Section 5.5.1.1. This was later used in addition to the added mass calculations to determine the natural periods in heave, and pitch/roll.

9.2.4.7 Natural period

The natural periods in surge and sway are not of significance for an unmoored structure as there is no hydrostatic stiffness in this degree of freedom, hence the natural period is undefined based on the equation for the natural period.

$$T_{11} = 2\pi \sqrt{\frac{M + A_{11}}{0}}$$

The natural periods for heave and roll/pitch were calculated based on the previously determined information regarding added mass, hydrostatic stiffness and the structural mass/inertial properties of the system.

9.2.4.8 Pre-tension capacity

In addition, it was necessary to calculate the pre-tension capacity of each structure. This was calculated by taking into account the mass of temporary ballast by a simple conversion from mass to weight, then dividing this by the total number of tethers (in this thesis the number of tendons are fixed to a set of three).

9.2.4.9 Summary of results

The spreadsheet was built such that the results for each combination could be stored in a separate table. The separate table was organized such that the first columns provide information about the inputs used, followed by several output columns. Data obtained from the spreadsheet analysis could then be exported into a Pivot table, for plotting the results and assessing the effects of changing a certain parameter or a range of parameters. Some of the generated results are presented in Appendix A.

9.2.5 Buoyant docking station

The following section covers the basic steps in the spreadsheet for calculating stability, centres of buoyancy and gravity, displacement etc. based on an array of input variables. The equation for the volumetric ratio is also presented in this section, which is used for plotting the results.

9.2.5.1 Inputs variables

The inputs to the BDS spreadsheet were: pontoon length, pontoon diameter, central column diameter, central column height, wall thickness of each component, permanent ballast fraction, permanent ballast density, buoyancy module diameter and height.

The BDS is a rather complex structure when performing a parametric study due to the extensive number of variables present. The total number of variables handled by the spreadsheet is 11 (including the activation of temporary ballast and wall thickness for each component). In order to reduce the number of variables to a workable array it was decided to keep the following variables constant: the wall thicknesses and pontoon diameter. The central column diameter and height are dependent variables; hence the number of independent variables is reduced

to four. The independent variables are pontoon length, BM diameter, BM height and PBF. The ranges are defined in Section 7.4.1 (concept description chapter).

9.2.5.2 Volumetric ratio

In order to compare different combinations of the variable listed above it was proposed that a volumetric ratio was to be established during the spreadsheet calculations. The volumetric ratio was utilized to express the relative size of the non-ballast-able section of the BDS. The equation used for this purpose is presented below.

$$R_{\mathrm{V}} = \left(V_{CC} + \sum_{i=1}^{3} V_{\mathrm{PO},i} \right) \cdot V_{\mathrm{BDS}}^{-1} \qquad (9.1)$$

Where V_{CC} is the volume of the central column, $V_{\mathrm{PO},i}$ is the volume of pontoon i and V_{BDS} is the volume of the entire buoyant docking station. The use of this ratio requires some variables to remain constant. This is presented in the spreadsheet results chapter (Section 10.3.3).

9.2.5.3 Determination of COG and COB

The following illustration is used as a reference point for determining the COG and COB of the BDS in order to be able to compare the different dimensions to be analysed.

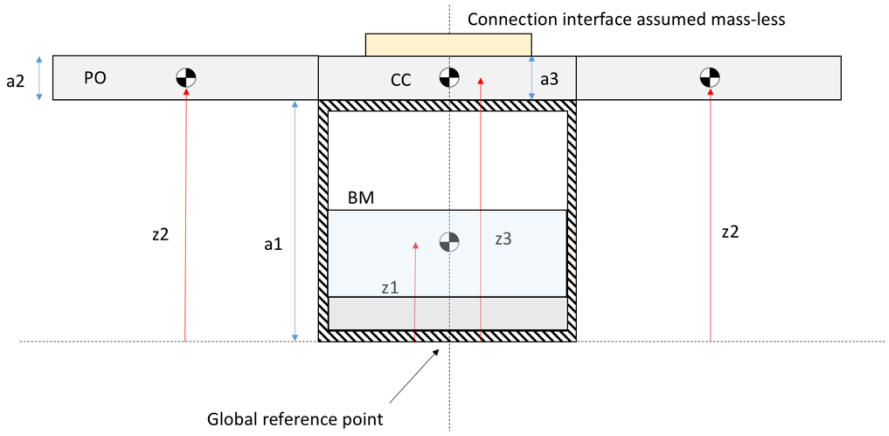

Figure 9-6: Coordinate system for determining the z-component of COG

The bracings mentioned in an earlier figure are not included in this diagram or in the determination of COG. The bracings are not to be considered in this analysis but should be implemented to alleviate some of the bending stresses at the connection between the pontoon and the central column. The determination of COB is completed in a similar manner in the calculation sheet. Both COB and COG are determined with reference to the keel of the structure.

9.2.5.4 Submergence

One of the primary characteristics of the submerged buoyant docking station is that it shall maintain a sufficient internal volume to house the required volume of ballast to achieve submergence. The spreadsheet inputs required for this calculation is the total external volume, the total internal volume available within the buoyancy module and the two ballast densities. In addition to this, the specification of the permanent ballast fraction is required to determine the ratio of permanent to temporary ballast to be contained within the buoyancy module.

The outputs from this section of the spreadsheet are temporary ballast height, permanent ballast height and total internal column height. These are then used to calculate the available internal column height at the required ballast mass. Logical programming gives a “go”/”no-go” message in the spreadsheet should the total required ballast column exceed the available space.

9.2.5.5 Stability

The stability calculations for buoyant docking station are conducted for two conditions: floating stability and submerged stability. For floating stability, the pontoons were to be held out of the wave area by removing the

temporary ballast in the structure. This is completed by the binary activation cell built into the spreadsheet, which toggles the temporary ballast on and off.

In addition to the floating stability, the spreadsheet also calculates submerged stability. This case requires the temporary ballast to be activated, as this results in complete submergence based on the mass of displaced water by Archimedes' principle. The submerged stability calculation builds on the calculated centres of buoyancy and the determined distances to centres of gravity of the structure and the ballast columns.

The equations used to establish the stability of the vessel are presented in the background theory chapter and are not repeated here.

9.2.6 Connected system

The connected system is limited to mooring stiffness calculations and stability for the entire system including temporary ballast for the spreadsheet calculations. Initial stability is calculated for the connected system, to verify the metacentric height prior to hydrodynamic modelling of the entire structure. Moments of inertia are only calculated for the mated system using 3-D modelling software under hydrodynamic modelling and are not calculated in the spreadsheet.

9.2.6.1 Total mass and displacements

The total masses for the un-ballasted condition (i.e. no temporary ballast) and the ballasted condition, along with displacements for operating draft. These calculations are prerequisite to the stability calculations.

9.2.6.2 Stability

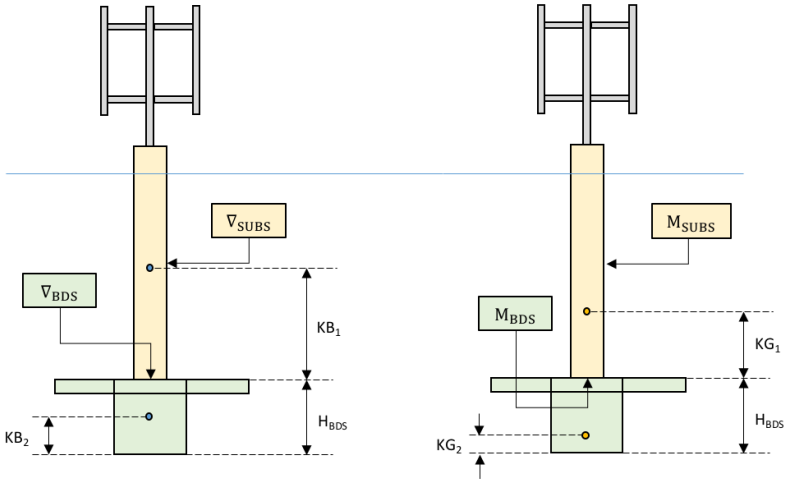

Figure 9-7: Stability calculations for free connected system

Stability of the connected system is determined by assuming that the structure is disconnected from the tethers where the BDS is ballasted to neutral buoyancy and the substructure is ballasted to the operational draft. The total submerged volume depends on the substructure displacement and the BDS displacement and can vary greatly depending on which combinations are selected. Stability for this system is critical for the hydrodynamic analysis of the mated vessel in HydroD to obtain the added mass, potential damping and RAOs.

9.2.6.3 Total pre-tension capacity

For the connected system the calculation of total pre-tension capacity per tendon is conducted. The pre-tension capacities of the substructure and the BDS vary significantly, which means that the total capacity must be evaluated for each combination. The spreadsheet for the connected system also included some basic calculations of stiffness in 11, 33 and 66. The natural periods were not established in the spreadsheet for this case.

9.2.6.4 Case selection

The case selections for the connected system were primarily based on total pre-tension capacity and obtaining a range of displacements, following to some extent the design criteria set by Bachynski and Moan in [8] and [29]. The results from this stage is presented under the spreadsheet results chapter.

9.3 Hydrodynamic modelling procedure

The hydrodynamic modelling process for the system consists of three stages as presented in the figure below. Several software packages are used in the modelling process such as Autodesk Inventor, GeniE and HydroD. An example is provided here for clarity representing the mated case A1-B1[9].

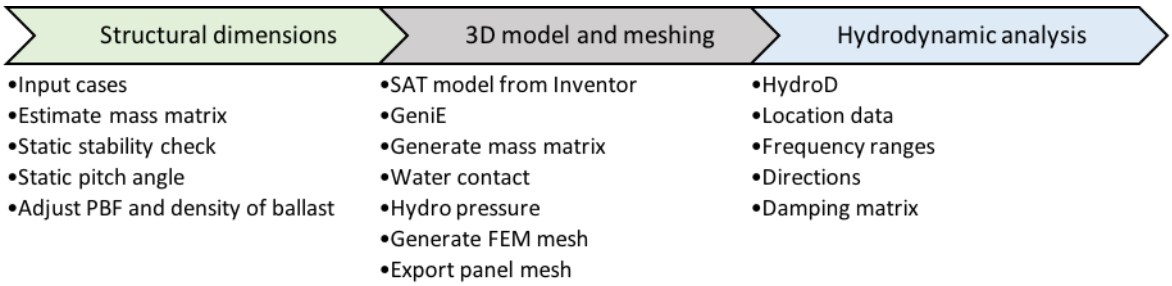

Figure 9-8: Stage diagram of hydrodynamic modelling process

The modelling process begins with the selected case dimensions from spreadsheet calculations as presented in Section 9.2 and will not be covered in detail here. Figures have been provided from the hydrodynamic modelling process for illustrative purposes. The figures used in this section are provided based on case A1-B1, which is defined under the case selection section presented at a later stage.

9.3.1 Creating the SAT model

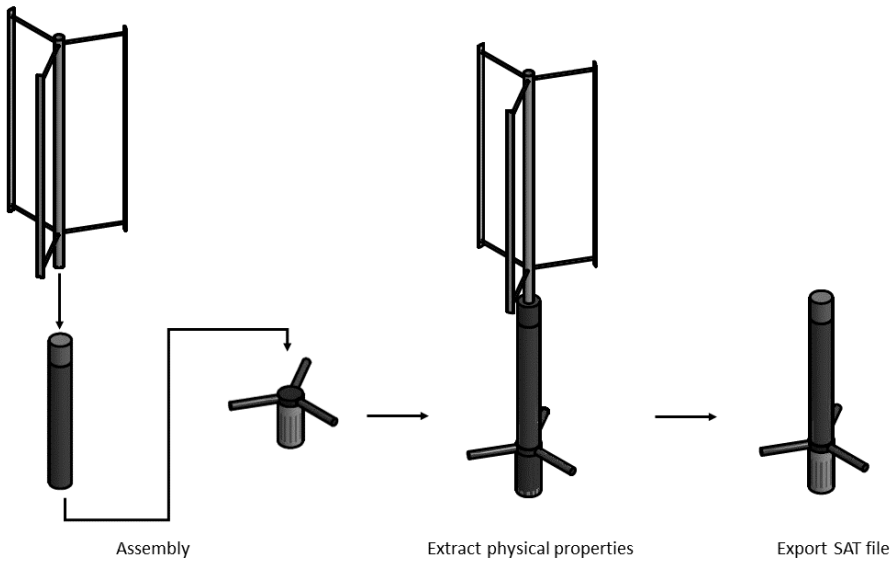

Figure 9-9: The SAT modelling sequence

The figure above shows the process of generating the SAT model in Autodesk Inventor. The stages are illustrated above, where the prerequisites include the construction of each individual component (turbine, substructure and BDS), followed by the assembly process. After the assembly is constructed physical properties such as the principal moments of inertia, centre of gravity and the total mass are extracted with and without including the temporary ballast. This is done to obtain an accurate mass model, required at a later stage in HydroD and OrcaFlex. After the extraction of physical properties, the turbine, generator, and all ballast components are removed from the model. This is illustrated in the right hand section of the figure above. These are removed from the model because they are not critical to the meshing phase in GeniE.

[9] A1-B1 refers to a combination of a selected substructure and a buoyant docking station presented under the identification of cases section in this thesis. This case was used in the illustrations presented in this chapter.

9.3.2 3-D structural model and panel mesh

The generated SAT file from the previous section was imported for further processing in Sesam GeniE v6.7-12. GeniE is a 3-D modelling tool capable of modelling complex geometries consisting of plates and beams with built-in hydrodynamic and structural load analysis [50]. The main goal was to achieve a representative panel mesh model for importing into HydroD. The figure below shows the modelling process in GeniE based on [50].

Figure 9-10: Generating .FEM file from .SAT file

9.3.2.1 Import SAT model

After importing the SAT model into GeniE it is necessary to remove the internals in the model to reduce the number of elements and nodes that are to be generated during the meshing process. GeniE models cylinders by defining a cylindrical shell with a certain thickness [50], and the SAT model essentially contains two shells with zero thickness, which are spaced such that the thickness property is defined between the two shells. The internal structural elements are not necessary to generate the external panel model as it is not the aim of this stage in the analysis phase to assess structural loads. After deleting the internal shells and plates, the user is left with an external shell model representing the structure illustrated on the right-hand-side in Figure 9-9.

9.3.2.2 Thickness properties

In general GeniE requires material properties to generate the mass model along with a specified hull thickness. Since this software is solely used to create a mesh model it is not required to specify the material properties. However, the software does require input data for the hull thickness in order to generate mesh. The structure is assumed to have a uniform wall thickness of 25 mm (this is more-or-less arbitrary, unless structural analysis is to be conducted). Note that the wall thickness does not necessarily need to represent the hull thicknesses selected in the modelling stage in Inventor as these factors are taken into account when generating the mass model in HydroD using the exported physical properties from the Inventor model (including temporary ballast).

9.3.2.3 Wet surface

The wet surface setting is used to define the proportion of the vessel that may come into contact with water. This stage is an important prerequisite for setting the dummy hydro pressure loading condition at a later stage in the analysis [50]. The wet surface must be defined for the entire structure in this case since the draft will vary from its static condition when running the hydrodynamic analysis in HydroD. The figure below presents the wet surface applied to the structure from Figure 9-9.

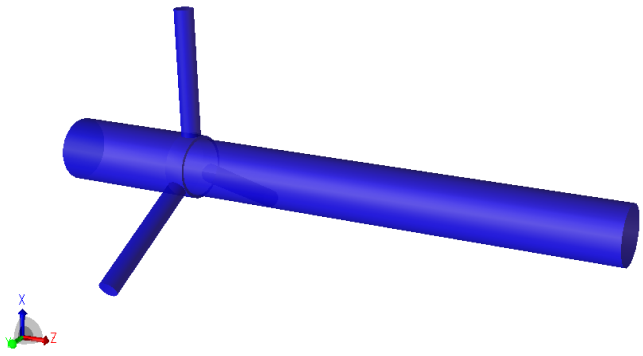

Figure 9-11: Wet surface

9.3.2.4 Mesh properties

In GeniE there are two categories of mesh properties that must be specified prior to running the analysis. These two categories are referred to as mesh option and mesh density [50]. The mesh option is used to specify the element preferences, i.e. whether the software should try to force quad elements, create regular mesh when possible etc. In this case mesh option is set such that the software shall force quad elements, prefer regular mesh, remove internal

vertices and remove internal edges. Quad elements refer to elements with four nodes and when forced in the mesh option the appearance of triangular elements are limited [50]. A screenshot of the FQUAD mesh property setup has been provided in the figure below.

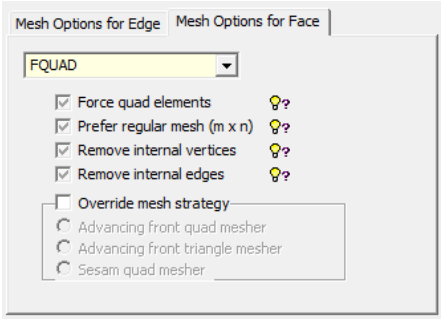

Figure 9-12: Screenshot of FQUAD mesh property

The mesh density property is used to assign the element length in meters for a specific surface. Different mesh densities can be specified for the individual components in the structure. One example is the pontoons on the BDS, which will require a finer mesh compared to the substructure hull as these have smaller diameters, which will affect the relative coarseness of the mesh. The mesh refinement has a direct effect on the number of nodes and elements in the meshed structure. In this thesis a uniform meshing case system has been implemented for reference purposes. The reason for establishing this system was that it is easier to compare the different mesh models, where the mesh densities are colour coded on the mesh model.

Table 9-2: Mesh identity with corresponding element length

Mesh identity	Element length [m]	C	Mesh identity	Element length [m]	C
m1	1		m4	0.5	
m2	2		m5	4	
m3	0.8		m6	0.7	

When generating the mesh models in GeniE, a screenshot is provided with a colour coding (C) overlay associated with the mesh identities presented in the table above.

The table below shows the effect of changing the element length for the entire structure. Note that these values are not to be used further but are provided as a reference to give an indication of the number of nodes an elements involved when increasing the mesh density.

Table 9-3: Element length vs. number of nodes and elements for uniform mesh density

Mesh identity	Element length [m]	No. nodes	No. elements
m5	4	324	336
m2	2	1051	1064
m1	1	3795	3811
m4	0.5	14565	14588

As can be observed from the table above the number of nodes increases exponentially with halving of the element length for a uniform element length across the structure. It is worth noting that for hydrodynamic panel models there is a restriction of the number of elements available, 15000 panels for basic part and 3000 for the surface panels as stated in Section 4.3 in [30]. Surface panels are generated in a separate .FEM file used for generating 2nd order results [33], which are not used here. The figure below shows a case when applying a coarse mesh on the entire structure, i.e. uniform mesh with element length of 4 m.

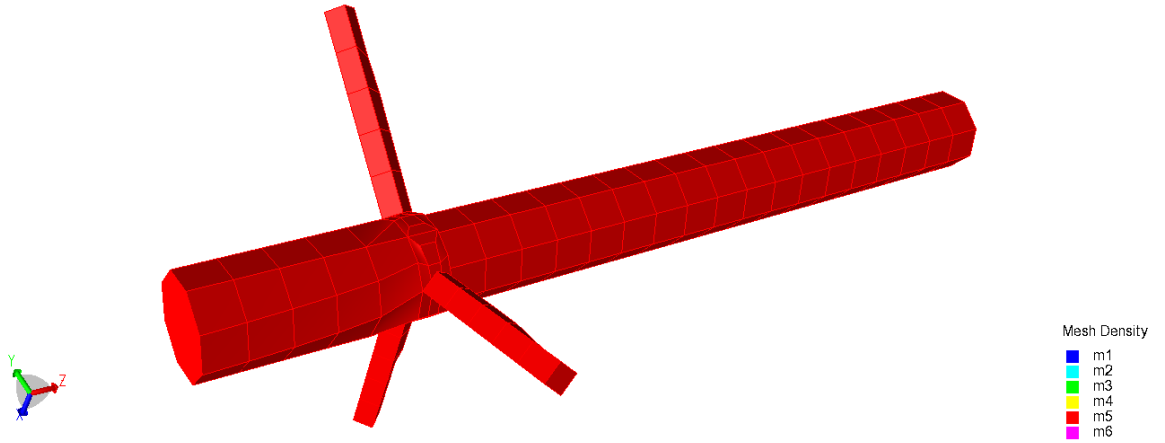

Figure 9-13: Coarse mesh with element length 4 m

The total number of nodes/elements for the meshed structure above are 324/336.

As can be observed from the figure above, an element length of 4 m with quad element forcing will create a mesh that does not sufficiently represent the intended shape of the structure. The main hull diameter is approximated by an octagon and the pontoon diameter by a square. The elements are significantly warped near connections as can be observed near the pontoons. By observation it can be concluded that element lengths of 4 m are too coarse for this model. The figure below shows a finer mesh where element length 1 m (m1) is applied to the large diameter structure and element length 0.5 m (m4) has been selected for the pontoons.

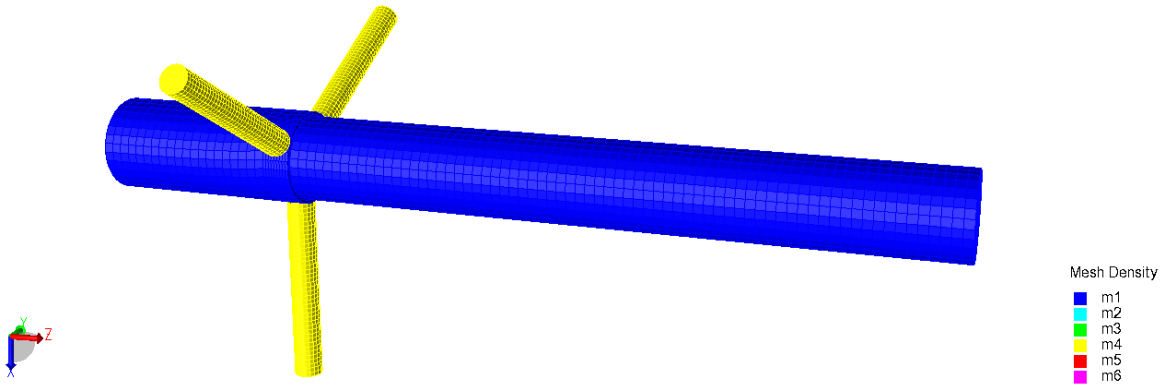

Figure 9-14: Combination of two finer mesh densities for the structure

The total number of nodes/elements for the meshed structure above are 5932/5955.

Too fine-a-mesh will generally lead to increased computing time, which means that there is a trade-off between mesh density and the time taken to perform the analysis [51]. The benefit gained from increasing the meshing density may not necessarily result in a significant increase in accuracy of the output result, which essentially means that time is wasted in simulation of structures with extremely fine mesh. Convergence studies with gradually finer mesh is one way of determining if the given mesh is sufficient for determining for example the pressure load on the structure. Finer mesh leads to an exponential increase in the number of elements and nodes as can be observed in Table 9-3.

9.3.2.5 Apply load case LC1

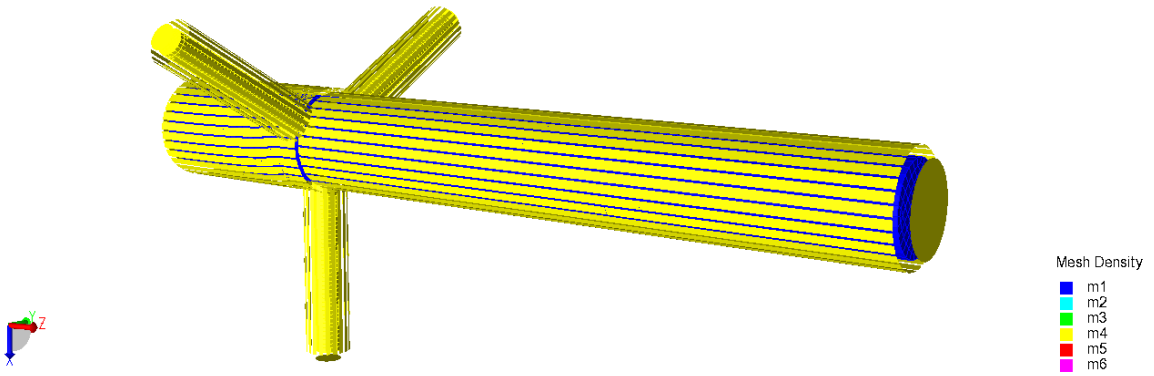

Figure 9-15: Load case LC1 – model

In the figure above the LC1 dummy load pressure has been applied to the entire wet surface (WS1). The dummy hydro pressure is required in order to use WADAM in HydroD [50]. The dummy load pressure is set for all surfaces that may come into contact with the water hence there is a unit load at the top section of the structure in case of full submergence.

9.3.2.6 Run analysis

The results from the FEM mesh generation have been presented in Figure 9-14 and Figure 9-15, with and without LC1 (dummy hydro pressure) respectively.

9.3.2.7 Export .FEM

The output from the analysis, i.e. the meshed panel with dummy hydro pressure load is exported to a .FEM file which will be imported into HydroD for hydrodynamic analysis. It is worth noting that a warning message concerned with missing input data is present for each of the mesh settings above, however this is believed to be linked to structural analysis which is not part of the scope in this context. It is concluded that this warning message can be overlooked as the key output from GeniE is the meshed panel model, which did not result in a warning message.

9.3.2.8 Convergence study

In order to determine if the damping and added masses are valid it is necessary to prepare multiple FEM files with refined mesh properties. Convergence studies are necessary to verify if the output values are representative for the "real" values, which is achieved by observing whether the output values change with increase in mesh refinement. If there is a relatively small change in values for a relatively large increase in the number of nodes/elements then the solution can be considered as sufficiently converged [51].

9.3.3 Hydrodynamic modelling

The hydrodynamic modelling in HydroD is conducted using the WADAM tool built into the program. HydroD can be used to calculate wave loads and conduct stability analyses for various floating structures [33]. In this project the aim is to extract added mass, potential damping, load RAOs and displacement RAOs. The software package is extensive in nature and as such only a segment of the software will be covered here. Tracing the steps of the model construction for the substructure is the main objective and all relevant inputs are presented here for clarity. The two figures below illustrate the hydrodynamic modelling sequence from the "WADAM wizard" in HydroD.

Figure 9-16: Stages 1-6 in hydrodynamic modelling sequence (based on WADAM wizard in HydroD)

Figure 9-17: Stage 7-11 in hydrodynamic modelling sequence (based on WADAM wizard in HydroD)

Prior to starting the hydrodynamic modelling sequence, it is necessary to determine which type of model is to be analysed in HydroD. Depending on the structure imported to HydroD, there are several different options to choose from in the WADAM wizard. The options include panel model, Morison model etc. depending on the construction of the model. In this case the panel model is selected as the basis for the HydroD model is a .FEM mesh file from GeniE.

The WADAM wizard states that the prerequisites for a panel model analysis is that there must exist a T*.FEM[10] file with designated hydro pressure load in load-case number 1. This was set in the GeniE software package mentioned earlier by applying LC1 to the wet surface. Compartments are ignored as these have not been modelled in GeniE. Compartments are used for adjusting ballast, which are not taken into account in this analysis as the total mass of the vessel including ballast is specified in the mass model. This is regarded as sufficient as only the operating/ mean towing draft (these two are equivalent in this study) is to be analysed. The WADAM wizard input settings used in the analysis are presented in the table below.

Table 9-4: Wadam wizard panel model input settings

Setting	Input
Domain	Frequency
Model	Element
Output matrix	Damping

9.3.3.1 Direction set

The first step is to create a direction set. The direction set is specified to cover a range between 0° and 180° with an interval value of 30°, since the vessel is symmetric in the XZ-plane. The interval value was defined based on previous vessel types in OrcaFlex. The directions need to be specified in order to generate the load and displacement RAOs as these exhibit direction dependence as discussed under the chapter on the response amplitude operator. Note that the direction 0° represents a wave propagation along the positive x-direction [33].

The direction convention is illustrated in Figure 9-18. Note that this is also valid for the conventions used in OrcaFlex. A 180° wave heading corresponds to head sea, whereas 0° is often referred to as following sea. The presentation of RAOs in the results section follow the convention presented below. Clockwise vs. counter clockwise conventions for the specification of intervals are not critical as the vessel is symmetric in this regard.

[10] This FEM file represents a mesh model exported from GeniE, and requires that a numbering system is used, i.e. T1.FEM, T2.FEM etc. for models consisting of more than one panel model [33].

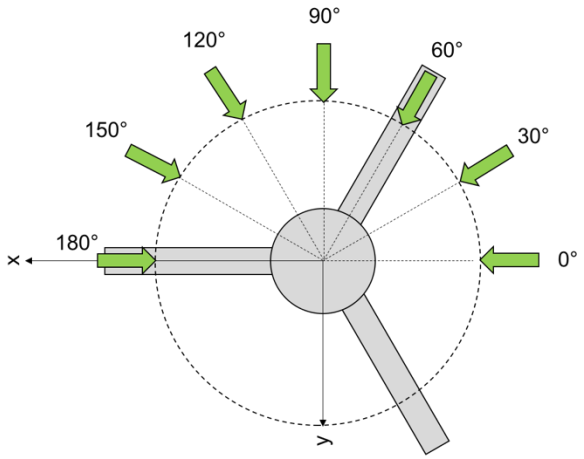

Figure 9-18: Wave direction conventions

9.3.3.2 Frequency set

In this thesis two different frequency sets are used. The first frequency set was specified in terms of angular frequencies between 0.05 and 5 with a step value of 0.1 rad/s, used for the convergence study. The convergence study was conducted with this frequency set to determine whether the mesh model is sufficiently dense to generate accurate results. The second frequency set was used to when generating the RAOs for the vessel, as OrcaFlex required extra data points in the upper tier of the frequency range[11]. The second frequency set was specified in terms of periods, ranging between 0.5 and 24 seconds with a step value of 0.5 seconds. The frequency set in both cases covered a relatively large spectrum of frequencies which were set so that the damping matrix is calculated for several different frequencies, since this is highly frequency dependent (refer to the section on added mass and damping for more information).

Table 9-5: Frequency sets

Identifier	Lower		Upper		Interval		Data points
	ω (rad/s)	Period (s)	ω (rad/s)	Period (s)	ω (rad/s)	Period (s)	
Frequency set 1	0.05	125.7	5	1.257	0.1	–	51
Frequency set 2	12.57	0.5	0.262	24	–	0.5	48

9.3.3.3 Location data

The location data in the hydrodynamic model include information about water density, kinematic viscosity and water depth. The water density was set to 1.025 kg/m^3, the kinematic viscosity was set to 1.19e-06 m^2/s and the water depth was specified as 200 m. Air density and kinematic viscosity were unchanged but do not apply to this case. Note that the water density and kinematic viscosity were unchanged from the standard value in HydroD.

9.3.3.4 Frequency domain condition

The frequency domain condition was set to contain the direction and frequency sets mentioned earlier. No wave amplitude is specified as this is valid only for WASIM simulations [33]. The WADAM user manual states that if no value is implemented here then the software automatically sets the wave amplitude to 1 m.

9.3.3.5 Hydro model

Next the hydro model is specified where the floating point in the x-direction is set to 0 m to centre the vessel in the origin. In order to be consistent with the coordinate system, care must be taken to model the vessel with pontoon 1 parallel to the x-coordinate system pointing outwards from the vessel in the positive x-direction.

[11] This was determined based on preliminary trial runs with the first frequency set in OrcaFlex. Running a simulation with frequency set 1, results in an error message regarding the higher frequency RAOs.

9.3.3.6 Panel model

After the hydro model is set, the panel model is imported into HydroD. The model is translated into the water to -*d* m in the z-direction to obtain the desired draft (*d*). No symmetry was activated for the panel model, because the entire model is represented in the .FEM file. If symmetry planes are activated the software misinterprets this information, which tends to give erroneous values for the water plane area[12].

9.3.3.7 Loading condition

Step 7 in the Wadam wizard is to create the loading condition. The z-water line is specified to 0 m. This category also requires input form the mass model to recalculate the location of the water plane based on mass and displacement. This is due to errors regarding the water-plane tolerance specified at 5% of the characteristic length of 10 m (which is a typical value for the models generated as part of this thesis) if a coarser mesh model is used.

Note that coarser mesh properties were assigned for the first run in series, which tends to result in reduced freeboard (sometimes referred to as ΔZ-waterline, where a negative value results in increased freeboard, and a positive value results in reduced freeboard). The reduced freeboard is caused by the meshing of the model in order to approximate a circular structure, meaning that there is a loss in volume of the structure as illustrated below based on [26].

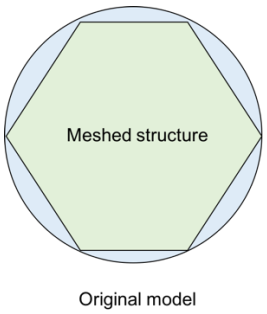

Figure 9-19: Meshed cross section vs. original model based on [26]

The blue shaded area between the meshed structure and the original model represent the loss in displaced volume due to meshed approximation of the original model. For short lengths the effect is not usually significant but considering the drafts of the models created in this thesis, the effect is more pronounced. Note that the loading condition is revisited after defining the mass model in the following section in order to compute the z-water line position from the mass model.

9.3.3.8 Mass model

Step 8 is to create the mass model. The mass model requires information about how the total mass, the centre of gravity and the radii of gyration which were specified earlier under the section covering the CAD model. The mass can also be calculated in HydroD by Archimedes' principle from the displaced volume of water. The specification of COG is relative to z = 0 m (the water plane). Note that this is relative to the initial origin, and is not adjusted to reflect the change in sea-level location as mentioned in the previous subsection.

9.3.3.9 Damping matrix

The damping matrix is generated by HydroD, but in this section it is possible to add any additional damping matrices. These are left as a 6x6 zero matrix with designation DampingMatrix1 as no additional frequency independent damping is included [33].

9.3.3.10 Create analysis

In this section the analysis is compiled, i.e. selection of loading conditions and which hydro models to take into account. It is also possible to specify incident wave spectrum in this case but these were left blank as the only required output from the model is the damping matrix, added mass, and load/displacement RAOs. Typically, one would add a wave spectrum to determine the response spectrum for a certain sea state (in-line with what was presented in Figure 5-12 on page 31 earlier) [22]. In this section the characteristic length is also specified. The characteristic length is used for converting the damping and added mass matrices to non-dimensional coefficients. It is often specified as the distance between the two outer points in the horizontal plane for the average surface.

[12] This was discovered during preliminary trial runs in this software.

For the given design space these characteristics lengths ranged between 9 and 12 m, corresponding to the outer diameter of the mono-hull floater.

9.3.3.11 Export data

A list of the exported data is presented in the table below with reference to the corresponding mesh setting.

Table 9-6: Overview of Exported data

Data set	Mesh setting	DOF	Direction	Frequency set
Added mass*	All	11, 33, 55, 66, 51, 24	NA	1, 2
Potential damping*	All	11, 33, 55, 66, 51, 24	NA	1, 2
Displacement RAOs	Selected mesh	ALL	0-180°	2
Load RAOs	Selected mesh	ALL	0-180°	2
Hydrostatic stiffness	Selected mesh	ALL	NA	2

Added mass and potential damping (per matrix position) are exported into Excel for frequency set 1. These are separately collected during each mesh study in order to determine if the solution has converged. When the solution has converged the displacement RAOs, load RAOs, and hydrostatic stiffness are exported in addition to the added mass and potential damping matrices (per frequency) for frequency set 2. The exportation of data is limited during the convergence study to save time, as RAOs for a non-converged solution are not necessary to store for use in the dynamic simulation.

All the values generated by HydroD are exported with reference to the centreline of the vessel at sea level [30], which must be maintained during the importation phase into OrcaFlex. In addition to the results reference point, OrcaFlex also requires information regarding the whether the phase angles associated with the displacement and load RAOs are leads or lags and how these are specified. From the WADAM user manual it was found that the phase angles are leads [30] expressed in degrees.

9.4 Dynamic simulation

The dynamic simulations of the TLP system is conducted in OrcaFlex. The following section will cover the modelling procedure with reference to relevant user input and the selected integration method. This chapter will cover the following sections:

1. Modelling procedure for the vessel
2. Modelling procedure for the tendons
3. Setup of the dynamic simulation
4. Output results

9.4.1 Modelling procedure – Vessel type method

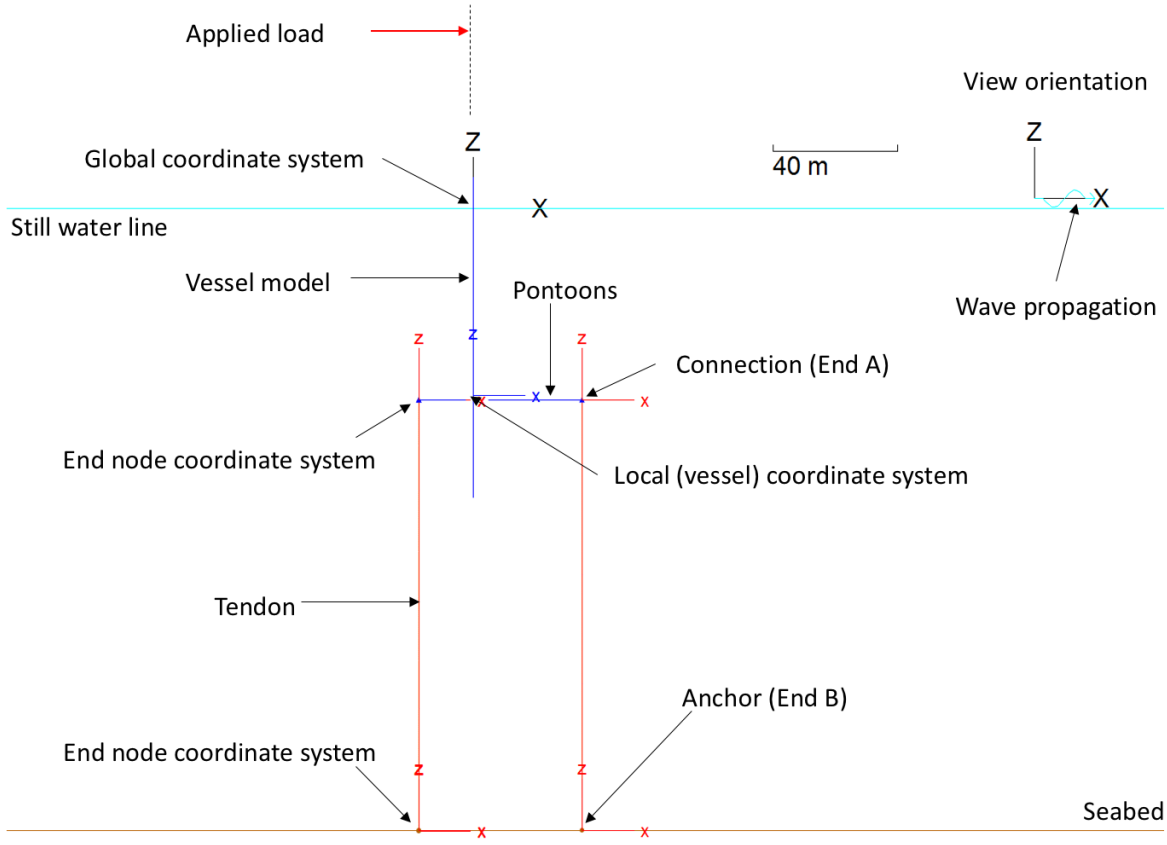

Figure 9-20: Vessel type model OrcaFlex (A1-B1)

The modelling procedure for the vessel consists of several steps: create a new vessel type, import the hydrodynamic properties and specify the inertial properties of the vessel. Since the model is limited to linear analysis only, several vessel properties are omitted (concerned with higher order effects and dynamic wind load). A screenshot of the model in its entirety has been provided in the figure above. Note that the vessel origin has been specified to the connection point between the floater and the docking station in order to obtain the forces acting in/about this region. The forces and moments are of particular interest regarding the imposed loads on the connection system. The statically applied wind load has been presented for clarity.

The vessel type is defined by an array of properties as listed in the table below, with reference to whether the property is to be included. Note that Table 9-7 is based on the vessel type property menu in OrcaFlex.

Table 9-7: Vessel type properties

Property	Included?	Property	Included?	Property	Included?
Structure	Yes	Sum frequency QTFs	No	Wind load	No
Conventions	Yes	Sea State RAOs	No	Drawing	Yes
Displacement RAOs	Yes	Stiffness, added mass and damping	Yes	Shaded drawing	No
Load RAOs	Yes	Other damping	No		
Wave drift QTFs	No	Current load	No		

The following sub-sections will cover each of the vessel properties listed above accompanied by an explanation of the required inputs, and reasons for inclusion/exclusion in the modelling procedure.

9.4.1.1 Structure

The structure is defined by mass, moment of inertia tensor and the centre of gravity for a given draft [52]. The values inserted represents the un-ballasted condition (i.e. no temporary ballast), with moments of inertia specified relative to the specified centre of gravity. The COG is defined relative to the vessel origin. Information about the vessel type length is also specified, which is taken as the diameter of the structure in the water plane.

9.4.1.2 Conventions

In order for OrcaFlex to understand how the RAOs are defined it is necessary to specify whether the amplitudes of the RAOs are given in terms of periods or frequencies, how the phase angles are defined (radians or degrees), and also whether the phases are lags or leads. The RAO phase conventions are specified in OrcaFlex as leads as stated in the WADAM user manual [30]. Specification of the DOFs are also required, where surge is specified as "forward", sway is defined as "port", heave is "up", roll is starboard "down), pitch is bow "down", and yaw is bow to "port". The displacement RAO rotational amplitudes are specified in terms of radians. Note that all conventions defined for the vessel in this category are valid for all drafts [52].

9.4.1.3 Displacement RAOs/load RAOs

Displacement RAOs are specified relative to the RAO origin and the phase origin. The RAO origin is (X, Y, Z) corresponding to SWL, and the phase origins are calculated by OrcaFlex (i.e. no user input for this specification needed). Note that the location of the RAO origin is always at the sea level in this case, as this is the reference point used in HydroD. For this reason, it is necessary to specify the RAO origin from the vessel origin for each specific case. An array of RAOs for several different periods are specified with certain interval (in this case 0.5 s) but also for an array of different directions (in this case 0-180° with 30° intervals). The periods used to define the RAOs corresponds to frequency set 2 as presented in Section 9.3.3.2.

As an example, for case A1-B1 the number of periods were 48, for 7 different directions resulting in a total number of displacement RAOs of 672 data points per degree of freedom, where both amplitudes and phase shifts are included.

The specification of load RAOs is completed in a similar manner. Again note that the values inserted here are only valid for the given draft, as the RAOs are draft dependent [52].

9.4.1.4 Wave drift and Sum-frequency QTFs

In order to obtain values for the QTFs it is necessary to conduct a second-order analysis in HydroD. This has not been assessed since the analysis is only conducted to uncover first order effects; a second-order analysis would exceed the scope of the present work. For more information on sum-frequency QTFs, refer to the second order effects chapter of this thesis or [11], [22], [26].

9.4.1.5 Sea state RAOs

In OrcaFlex the default value is "none" for the sea state RAOs, which means that the vessel is exposed to an undisturbed sea [53]. This category is usually applied for situations where multiple vessels are present in the analysis, where shielding effects must be taken into account as the sea-state is disturbed by the vessel [53]. This effect is not considered in this analysis as there is only one vessel present in the model.

9.4.1.6 Stiffness, added mass and damping data

The hydrostatic stiffness, added mass and damping data are imported based on the output from the hydrodynamic analysis discussed under Hydrodynamic Modelling. For the vessel type modelling procedure, the hydrostatic stiffness exhibits frequency independence, but is dependent on the draft (which is constant in this work). The hydrostatic stiffness matrix is defined for heave, pitch and roll with zero contributions in the other degrees of freedom [54].

Frequency dependence is present for both added mass and damping, which are specified for each period analysed in HydroD. Note that it is also possible to set added mass and damping as frequency independent under this menu, but this will in general lead to greater inaccuracies compared to using the frequency dependent values [54]. Since the frequency dependent values have been found by hydrodynamic analysis prior to the dynamic modelling phase, frequency dependent values are used.

In addition to the specification of added mass, damping and stiffness, the displaced volume and centre of buoyancy are specified manually here. The reference origin and origin datum position are also specified here, which are set to (0, 0, -*d*) since the model is built about a point coinciding with the connection area between section A and B (floater and docking station respectively).

9.4.1.7 Other damping

Other damping effects are zero in this model.

9.4.1.8 Current load

The current load is specified by a number of load coefficients and current areas and area moments. These are vessel properties are not evaluated since currents are not included in this analysis, in order to limit the scope of work to the given time frame.

9.4.1.9 Wind load

Since the model cannot accurately determine wind loads on the VAWT section of the system the wind load acting on the structure, calculated by OrcaFlex, is ignored. Applied loads and moments are used based on the NORCOWE reports for the 2.3 MW VAWT, as specified in Section 10.1.2.

9.4.1.10 Drawing

In order to present the vessel structure in both the two- and three-dimensional views in OrcaFlex it is necessary to prepare a simplified drawing of the vessel using an array of nodes and vertices. The drawing does not have an effect on the loads which means that it is not necessary to model the vessel with a high degree of accuracy, i.e. it only serves as a visual representation for the user. Figure 9-20 shows the visual representation in 2-D view. The drawings for each vessel are generated such that the origin is placed at the connection base between the floater and BDS. When constructing the two-dimensional drawing it is possible to specify the diameter of the line, which was set to the corresponding case. This is only used for the shaded 3-D view in OrcaFlex, and is not used to calculate the displaced volume, which is manually specified as the mass input represents the un-ballasted case (which would yield a smaller displaced volume based on equilibrium).

9.4.2 Modelling the tendons

In OrcaFlex, lines are used to represent pipelines, risers, catenary mooring chains, and may also be used to model TLP tendons. The lines are defined by an array of nodes and segments, which can be further divided into sections as presented in the figure below.

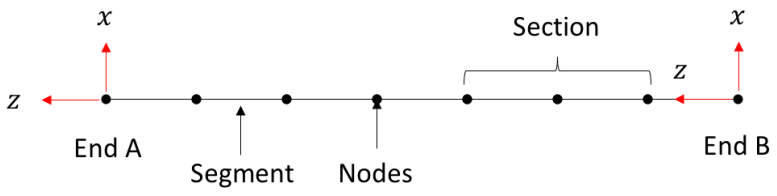

Figure 9-21: Line model based on [55]

As can be observed from this figure, the endpoints of the line model are designated by the letters A and B where A is usually connected to the vessel (this convention has been upheld in this analysis), and end B is connected to the seabed. Line ends may be designated as either free, fixed or anchored [55]. In theory it is possible to model the entire line with two nodes and one segment with the required length however, this will result in significant errors in the calculation of bending moments and the overall shape of the line. Proper discretization is critical for capturing accurate results for out-of-plane displacements and effective tension. In the user manual it was found that mass, drag and buoyancy are lumped at the nodes, hence a greater number of nodes will tend to give more accurate representation of the distribution of drag forces and mass distribution [55]. A fine discretization of the entire line into many segments will tend to yield more accurate results at the cost of increased computation time as is usually the case for FEM analysis.

9.4.2.1 Tendon arrangement

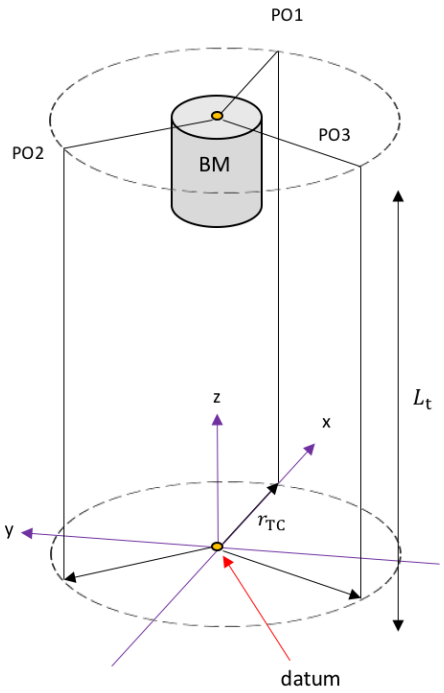

Figure 9-22: TLP datum (based on [10])

The arrangement of the tethers and pontoons are specified according to the global datum of the TLP system. The figure above shows the location of the datum based on an illustration provided in [10]. The tendon connection points are determined in the Cartesian coordinate system as illustrated in the figure above. OrcaFlex also recognizes the use of polar coordinates for attaching lines to the structure. Note that in the modelling process the TLP datum was placed with respect to the global coordinate system as follows (0, 0, -d_w). Where d_w is the water depth (which in this case is set to 200 m).

9.4.2.2 Line type properties

It is also necessary to specify the cross-sectional properties of the line segments i.e. outer diameter, wall thickness and material properties. The line type is also necessary to specify such as chain, wire, homogenous pipe or rope [55]. In this project the line type "homogenous pipe" was used to model the tendons as the tendons are hollow steel pipes.

Table 9-8: Line type properties

Line type	Material	Density	OD	WT	$\frac{m_a}{L}$	$\frac{m_w}{L}$	K_b	K_a
Tendon_1m	Steel	7850	1	34	810	5	2.55E9	21.87E9
Tendon_2m	Steel	7850	2	67	3193	-26	4.03E10	8.63E10
Units	–	kg/m^3	m	mm	kg/m	kg/m	N·m^2	N

Where OD is the outer diameter of the line type, WT is the wall thickness in mm, K_b is the bending stiffness and K_a is the axial stiffness. The line types were generated by OrcaFlex's line type wizard. The tendon properties and arrangement are presented below with reference to the given line type. The density of the content in these tendons

is 0 kg/m^3 (standard value). Note that line type "Tendon_1m" will be used across all dynamic simulations in this thesis. For optimized design it may be beneficial to adjust these properties with focus on stress and strain, but this is not considered in this analysis. Tendon_2m is presented for reference purposes only.

If a steel type S355 is assumed for the tendons, the tensile yield force in Tendon_1m equates to 36.63 MN. Assuming a material factor of 1.05, this tensile yield strength amounts to 34.88 MN. For Tendon_2m the tensile yield load is 137.56 MN with material factor 1.05. Tendon_1m was to be used for the analysis as it fulfils the requirement of pre-tension $\leq 0.33 \cdot T_y$ based on similar criteria in [29].

9.4.3 Setup of the dynamic simulation

9.4.3.1 Time steps and integration method

The time steps in seconds used for all analyses in this thesis are set to 0.05 seconds, with a maximum number of iterations at 100, and a tolerance level of 25E-6 (standard values). There are two integration methods available in OrcaFlex referred to as "implicit" and "explicit" integration methods. The explicit integration method is more robust and flexible than the implicit integration method, but requires a significantly longer simulation time due to significantly shorter time steps than what is required for the implicit method [56]. One of the main drawbacks of using the implicit method is that there are a number of limitations to its use compared to the explicit method. The implicit method cannot be used if the models are subject to superimposed motion, or a tension-controlled detailed winch with non-zero inertia is used, or if the simulation features time domain VIV models. The implicit method does not include seabed damping, solid damping or line clash damping [56].

Since the models in this thesis do not require time domain VIV models, or take into account any superimposed motions on the vessel, it is concluded that the implicit integration method is suitable for the dynamic simulations. However, the time steps must be verified for the accuracy of results in line with the recommendations from Orcina in [56]. The time steps used in the dynamic simulation were adjusted from the default values of 0.1 seconds to 0.05 seconds as stated above. The time steps were adjusted to this value in order to increase the accuracy of the results, as the user manual states that the implicit integration method is sensitive to time step variation. In order to check if the time step 0.05 seconds is sufficient, the simulations were also run with 0.1 second time steps, where the simulation statistics where cross-checked for a set of indicators (see Table 9-9) to observe the effect.

Note that one of the principal reasons for selecting the implicit integration method was that it was possible to increase the number of segments in the tendons significantly without increasing the computation time severely.

The duration of each simulation was set to 3.6E+08 seconds, which corresponds to 1-hour. This was set in line with the 1-hour averaging time for the wind velocity, as stated under Section 8.1.3. The OrcaFlex manual states that a ramping time for the wave train must be set prior to running the simulation. The importance of ramping time is that it smoothly builds up the wave and vessel motion prior to simulation start, to avoid un-realistic transient effects associated with the transition from the static state [34]. According to the user manual this ramping time must be greater than one wave period. The ramping time is set to 200 s, which means that the specified ramping time satisfies the aforementioned criterion (equivalent to at least 14 peak periods).

9.4.3.2 Verification of time step

As stated in the sub-section above, an initial sensitivity analysis of the time step is also conducted based on two relatively fine time steps of 0.1 and 0.05 seconds. The verification process consists of extracting the required outputs at a time step of 0.1 (default value), check the mean and standard deviation obtained from the time history. If there is a relatively small change between the values for 0.1 and 0.05 second time steps, then the time step should be sufficient for this purpose. Note that the number of elements in the tendons are held constant when verifying the time step in order to isolate the fluctuation of the results to a change in time step only and not tendon resolution. Note that these comparisons are valid because the wave record for each simulation for a specific environmental condition in this thesis is identical. This is due to the pseudo-random wave generation process specified in OrcaFlex, which establishes the random phase angles based on a given input seed. The randomness of process is solely dependent on the randomness of the input seed [27]. This seed method is constant for each case in a certain environmental condition, which validates this verification process. The time step sensitivity check was performed using the following set of indicators, evaluate for differences in mean and standard deviation.

Table 9-9: Time step sensitivity indicators

Variable	$\Delta\mu$	$\Delta\sigma$
Surge (η_1)	X	X
Heave (η_3)	X	X
Pitch (η_5)	X	X
Effective tension – Tendon 1	X	X
Effective tension – Tendon 2	X	X
Effective tension – Tendon 3	X	X

9.4.3.3 Applied wind load and torque

The applied wind load from positive X and associated moment about Y is calculated at the shaft base, i.e. the connection interface between the substructure and the turbine shaft as presented in the figure below.

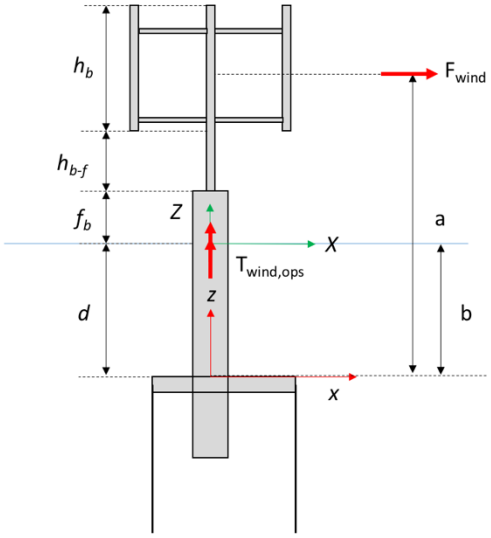

Figure 9-23: Applied wind load and moment action area

The values for the applied wind load and torque are presented in Table 9-10. The values are based on the NORCOWE CFD results presented in Section 10.1.2. The local coordinates of the vessel are presented with lower case letters z and x in the figure above, and the global coordinate system is presented using upper case letters Z and X. Where d is the distance from the SWL to the connection point between the substructure and the BDS, f_b is the freeboard (10 m), $h_{b\text{-}f}$ is the distance between the bottom of the rotor blades and the top of the substructure (13 m), and h_b is the height of the blades (99 m). The distance a represents the point of application for the horizontal wind load which is calculated by the following expression.

$$a(d) = \frac{h_b}{2} + h_{b-f} + f_b + d \rightarrow a(d) = 72.5 + d$$

The only variable in this case is d. The point of application for the operational torque is at the SWL, represented in this case by b which is equivalent to the distance between the SWL and the substructure-BDS connection interface at d meters below SWL.

Table 9-10: Applied loads

Environmental condition	Applied wind load	Point of application	Applied torque	Point of application
2	0.365	a	1.8	b
3	1.200	a	0	b
Units	MN		MNm	

It is worth noting that the applied wind load is specified with respect to the global coordinate system, in order to maintain a constant wind direction[13]. The applied wind load is set at a distance from the water line to the centre of the rotor (i.e. 72.5 m above sea level). The moment generated about the local axis of the vessel is calculated by OrcaFlex. Note that the applied torque is applied with reference to the local axis of the vessel, due to the vessel offset from the global coordinate when wind and wave loads are applied.

9.4.3.4 Wave direction

Due to the setup of the pontoons on the structure it was decided to assess the case where Tendon 1 is positioned downwind, such that all loads act at vessel direction 180° relative to the positive X-axis of the structure corresponding to a wave direction 0° in Figure 9-18. This wind/wave direction is identical to what was analysed in [8]. The setup is illustrated in the figure below.

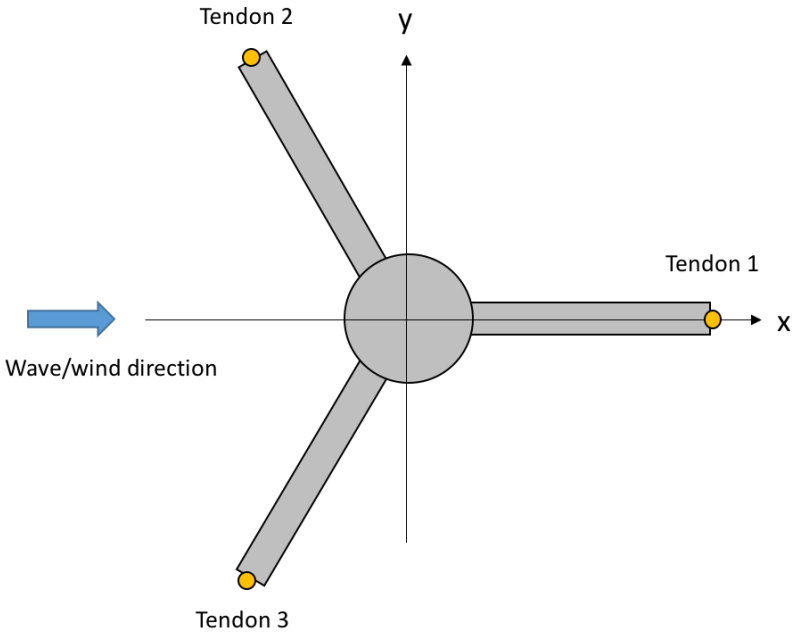

Figure 9-24: Wave direction relative to structure

This direction is considered to be the worst case scenario as all the compressive loads are absorbed in one tendon as observed from the illustration above. Typically, tendon 2 and 3 will experience an increase in tension (in this setup) as the positive pitch moment (in the same direction as the incident wave/wind) increases the restoring force in these tendons. Tendon 1 will experience a loss in tension because of the overturning moment generated by the wind and wave loads, will result in a compressive load.

[13] As the vessel rotates, the wind direction changes if this load is specified in the local coordinate system of the vessel. This can induce a sway motion, which should not arise for coinciding wind and wave in head sea.

9.4.4 Output results

The required output results from the dynamic simulation software are listed in the table below. The static state results are presented excluding the applied wind load. Where (#) indicates that statistics are exported for EC#.

Table 9-11: Overview of required output results

State	Output	Wind load	Time history	Statistics	EC
Static	Z-position of vessel	No	–	–	2, 3
	Pre-tension values in all tendons	No	–	–	2, 3
	Natural period of the system	No	–	–	2, 3
Dynamic	Effective tension all tendons	Yes	X	X	2, 3
	Declination angle for all tendons	Yes	–	X	2, 3
	Z-position of vessel	Yes	X	X	2, 3
	X-position of vessel	Yes	X	X	2, 3
	Rotation pitch	Yes	X	X	2, 3
	Rotation yaw	Yes	X	X	2, (3)
	Sea surface clearance (blades)	Yes	X	X	(2), 3
	Total dynamic Lx-Force	Yes	–	X	2, 3
	Total dynamic Ly-Moment	Yes	–	X	2, 3
	Total dynamic Lz-Force	Yes	–	X	2, 3
	Total static Lx-Force	Yes	–	X	2, 3
	Total static Ly-Moment	Yes	–	X	2, 3
	Total static Lz-Force	Yes	–	X	2, 3

10 Results from spreadsheet analyses

10.1 Topside

10.1.1 Centre of gravity of the topside

The topside outputs are presented in the table below based on the content in Section 7.3.1.

Table 10-1: Topside outputs

Description	Value	Comment
Total topside mass [kg]	480 587	Includes the estimated shaft properties.
Centre of gravity (x, y, z) [m]	(0, 0, 51.12)	With respect to the still water line at 10 m freeboard.
Mean diameter of rotor [m]	55	
Total height of topside [m]	112	Measured from 10 m freeboard.

As can be observed from the table above the total height of the topside is 122 m measured from mean sea level. As mentioned earlier, the wind velocity profile is assumed to be valid to this point in order to establish the wind pressure acting on the top of the turbine section.

10.1.2 Estimated wind load and comparison with NORCOWE CFD

The wind overturning moment is also calculated about the COG for the substructure in question, according to the conservative static pitch angle approach presented earlier. In addition to the wind force and moment there also exists an input torque to the system from the turbine in operational conditions. This torque is evaluated for establishing preliminary estimates for the induced yaw angle for the docking station only.

The torque generated from the operation of the wind turbine is set to 1800 kNm based on a mean wind speed of 12 m/s and a constant rotation of 12.5 rpm. The 12 m/s wind speed refers to the minimum wind speed across the blade (z = 23 m) which is approximately achieved by a 1-hour mean wind speed of 11 m/s at a reference height of 10 m according to the chosen wind velocity profile in Section 5.3.1.

Table 10-2: Comparison of wind force estimation vs. NORCOWE CFD [12]

Wind speed at hub	Estimated force on blades (E)	NORCOWE force calculations (N)	(E)/(N)	Mode
12 m/s	–	~365 kN	–	Operational
25 m/s	680 kN	~409 kN	1.66	Stand-still
60 m/s	2718 kN	~1200 kN	2.26	Stand-still

The wind speeds used by Hansen, T. in NORCOWE [12] were stated to be 12, 25 and 60 m/s without specific reference to height above sea level (in stand-still mode). The wind speeds to the left were selected such that the wind speed across the blades was similar to the two wind speeds analysed in the report. The estimated force on blades (E) does not include the force on the exposed shaft or substructure. As can be observed from the factor (E)/(N) on the right, there is considerable difference between the estimated force on the blades vs. the NORCOWE CFD simulations. This is as predicted due to the assumptions made when establishing the simplified geometry used for calculating the drag on the air-foil. Another reason for the larger values is that the wind profile used (for the 60 m/s case) does lead to a wind speed of 65 m/s at the top of the blade, which will add a considerable force contribution as the pressure increases by 22%.

Due to the fact that the wind forces are significantly larger based on the spreadsheet calculated estimation it was chosen to use the NORCOWE calculated results when analysing the structure in the dynamic simulation stage. As can be observed from the data in the table above, it is evident that the difference between the estimated values and the NORCOWE simulations increases with increasing wind velocity. The estimated overturning force from wind for the tow-out condition (EC1) is used based on the calculations made with the simplified air-foil geometry as the NORCOWE reports do not specify the wind force in this region. For the operational condition the NORCOWE force calculation in the direction of the wind resulted in a mean force of 365 kN (for 12 m/s). This value will be used for the operational mode as the wind velocity is approximately the same as the wind speed reported for EC2 (based on Bachynski & Moan [8]).

Another important factor is the possibility of decreased draft resulting in larger freeboard for the specific structure. This has an effect on the wind load estimation since the structure is lifted further into the air which means that more of the hull is exposed to wind and the turbine section will experience higher velocity winds as it is lifted due to increase the freeboard. This is not analysed in this thesis as operating draft is assumed for all cases.

The inaccuracies in the wind force calculation are due to the underlying assumptions associated with the shape coefficients, projected areas and omitting shielding effects. Ideally the wind turbine should be modelled in the dynamic simulation software (similar to [11]), but doing so would exceed the scope of the present work.

10.2 Substructure

10.2.1 Design criteria

The design criteria adopted for the substructure are presented in the table below.

Table 10-3: Design criteria – Substructure

Variable	Criteria	Comment
Initial stability ($\overline{GM}$) [m]	> 0	
Static pitch angle limit [degrees]	≤ 5°	Engineering assumption
Minimum pre-tension capacity per tendon	~2 MN	
Ballast height	–	Must be less than or equal to the available space in the structure.
Permanent ballast fraction	60-80%	Maintain permanent ballast in structure to aid in increasing natural period [29]

The case selection process is governed by the design criteria presented above.

10.2.2 Stability, displacement and the effect of PBF

The initial stability of the substructure is dependent on the diameter and the draft if all other input parameters remain constant (topside payload, ballast density and permanent ballast fraction). The substructure spreadsheet was used to determine the initial stability for all diameters and drafts in the design space presented in Table 7-5. The initial interval chosen for the diameters was 1 m, and 10 m for the drafts. A contour plot showing calculated values for $\overline{GM}$ is presented below. Note that all of the floaters presented in the figures below remain buoyant but the floater does not necessarily remain upright unless $\overline{GM}$ is positive. This is a characteristic of the method used to determine the amount of ballast.

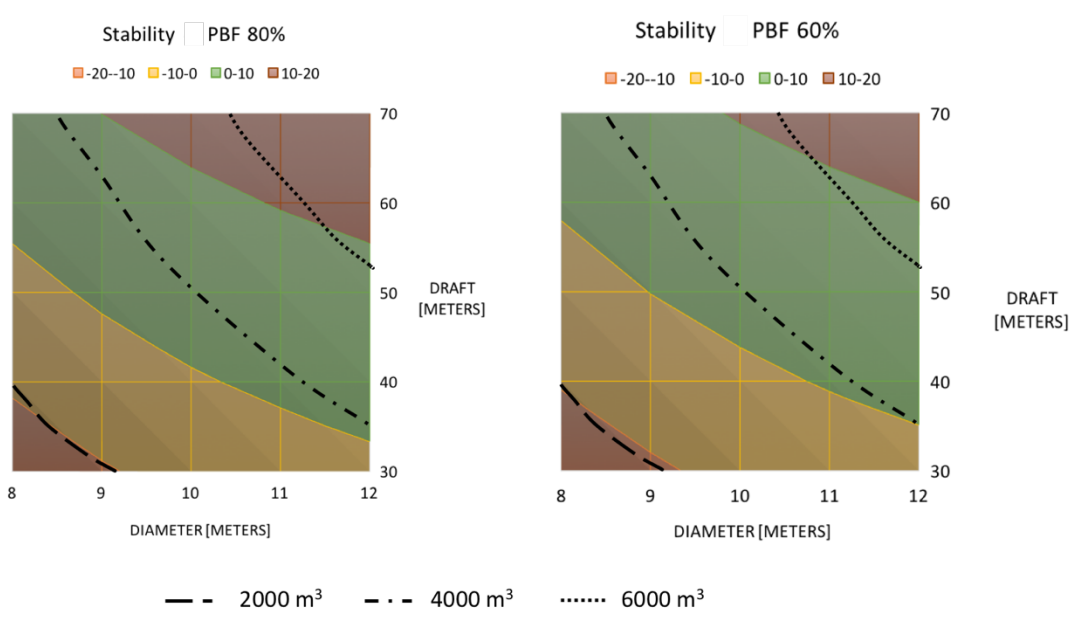

Figure 10-1: Stability and displacement for diameter-draft combinations at PBF 80% and 60%

The figure above shows the initial stability for the given draft-diameter combinations at permanent ballast fractions of 80% and 60%. The figure above also presents the displacement curves with values 2000, 4000 and 6000 m^3. As can be observed from the figure above, there is common trend for increasing $\overline{GM}$ with increase in draft and diameter. This is as expected because the centre of buoyancy increases with larger drafts, and the centre of gravity decreases with increase in diameter due to the increased internal surface area available for ballasting. As can be observed the general trend associated with lowering the PBF, is that there is a transition of bands towards the upper right hand corner of the figures. This is an indication of a reduction in $\overline{GM}$ as is expected due to the fact that a larger percentage of the total ballast has a lower density, leading to a larger volume of ballast required to achieve

the desired mass of ballast. Maintaining the same internal surface area, a larger volume of ballast will tend to increase the height of the ballast column, leading to an increase in $\overline{KG}$, which negatively affects the $\overline{GM}$. The reduction effects on stability are more pronounced in the upper tier of the displacements near the 6000 m^3 band, as can be observed from the intersection between the green and red bands.

10.2.3 Static heel angle

The static heel angle acceptance criterion was set to 5° heel angle for EC1. This criterion was set based on the assumption that the connection cannot be established at an angle greater than this.

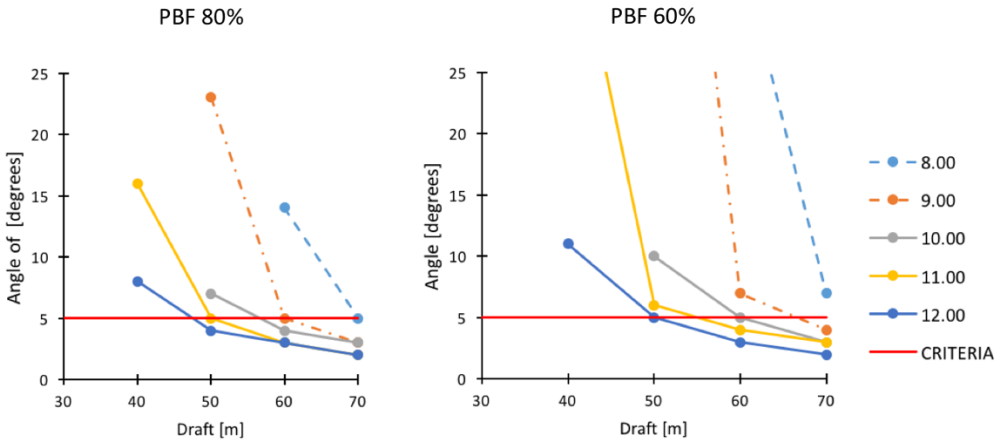

Figure 10-2: Pitch angles in EC1 for diameter-draft combinations

As can be observed in the figure above an increase in the external diameter will generally lead to a smaller pitch angle for similar drafts. It is worth noting that figure excludes unstable combinations, i.e. $\overline{GM} < 0$. The static pitch angle calculations seem to indicate that the minimum draft required for a pitch angle ≤ 5° is between 50 and 60 m for diameters between 9 and 12 m.

The effect of altering the permanent ballast fraction is significant for the static pitch angle as can be observed by comparing the two sub figures with PBF 80% and 60% respectively. The effect seems to be more pronounced for lower drafts with smaller diameters, as observed by the values that extend off the axes. These values have not been shown as the lower section of the plot becomes indistinguishable. The values are not as affected for the static angles that fall below the 5° criteria in PBF 80%. In other words, the static pitch angles that were relatively large for PBF80% tended to increase significantly with a reduction in PBF to 60%, but the change was not as significant for the lower pitch angles. This is most likely due to the significant reduction in $\overline{GM}$ for lower PBFs as discussed earlier.

It is worth noting that the static pitch angle is conservative as the overturning moment is to some extent overestimated. This is due to the over-prediction of wind force, as evident from the comparison of the spreadsheet calculations and the NORCOWE values obtained by CFD. In addition to this the moment arm was also increased from the pitch centre (metacentre) to the centre of gravity, which results in a greater overturning moment in line with the conservative approach.

10.2.4 Natural period

The natural period was calculated for heave and roll/pitch in the spreadsheet for the substructure, where the results are presented in the figures below. Note that unstable combinations are excluded from the figures, but these figures include the mono-hull floaters that exceed the pitch angle criteria.

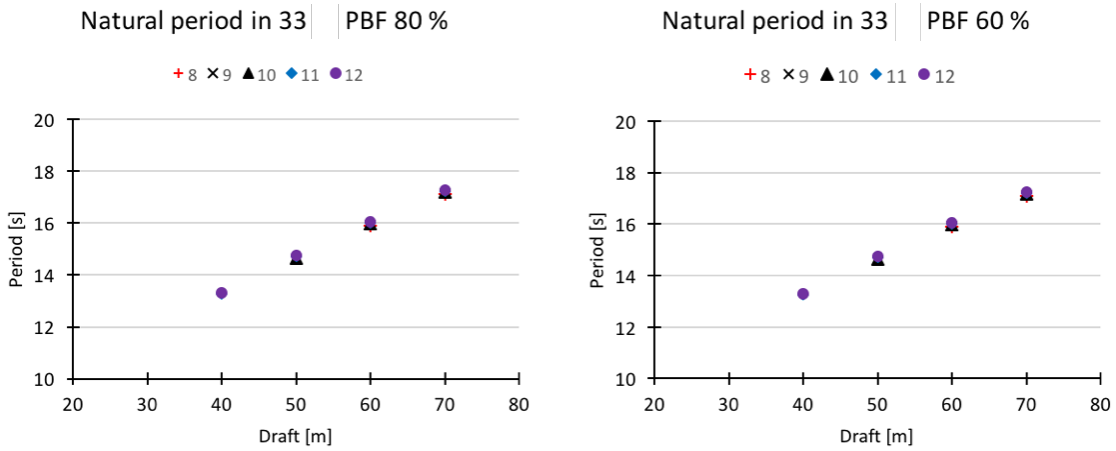

Figure 10-3: Natural period 33 for PBF 80 and 60 %

As can be observed from the figure above, the natural period in heave seems to linearly increase with draft but is not significantly affected by a change in diameter. This is likely due to the fact that the natural period is highly dependent on the mass of the system as the hydrostatic stiffness in heave is small for a column-stabilized unit (as can be observed from the equation presented under hydrostatic stiffness). There is no effect on the natural period in heave by altering the PBF, as is expected as the total mass remains the same and the natural period in this degree of freedom is unaffected by the initial stability of the system.

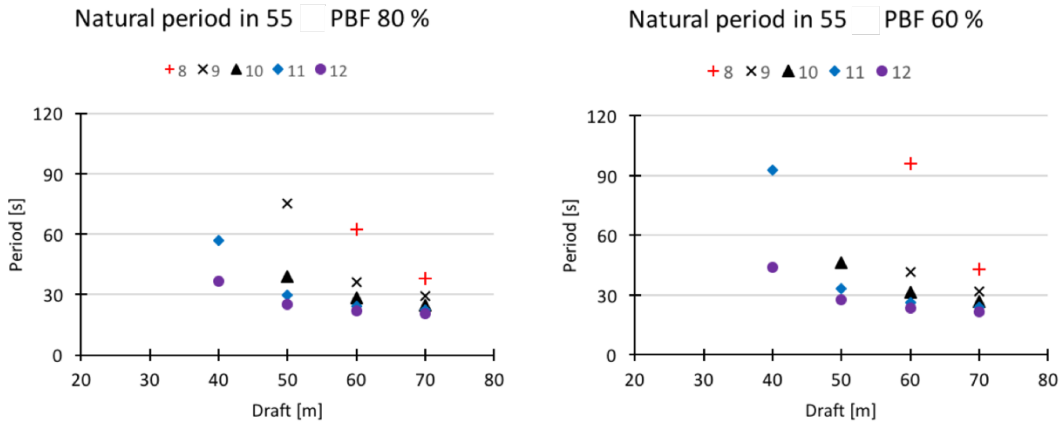

Figure 10-4: Natural period 55 for PBF 80 and 60%

The figure above shows the natural period in roll/pitch as a function of draft for several diameters in the design space where unstable combinations have been filtered out. The general tendency observed from this figure is that an increase in draft tends to lead to a reduction in the natural period. Subsequently a reduction in diameter leads to increased natural periods in pitch. The effect of changing the draft on the natural period in pitch is non-linear and the effect seems to decrease with an increase in draft in the upper tier, as can be observed for the OD12 m series. The effect of adjusting the permanent ballast fraction is more pronounced for the smaller drafts, as can be observed by comparing the two sub-figures above. The general tendency observed from this data was that the reduction in $\overline{GM}$ observed in the PBF 60% series for combinations, that also yielded low $\overline{GM}$ for PBF80%, experienced a more drastic effect on the natural periods in roll/pitch. Another observation was that the larger diameter combinations were generally unaffected by the change in PBF as these tended to have a relatively large $\overline{GM}$ for both PBF cases.

10.2.5 Available tension capacity per tendon

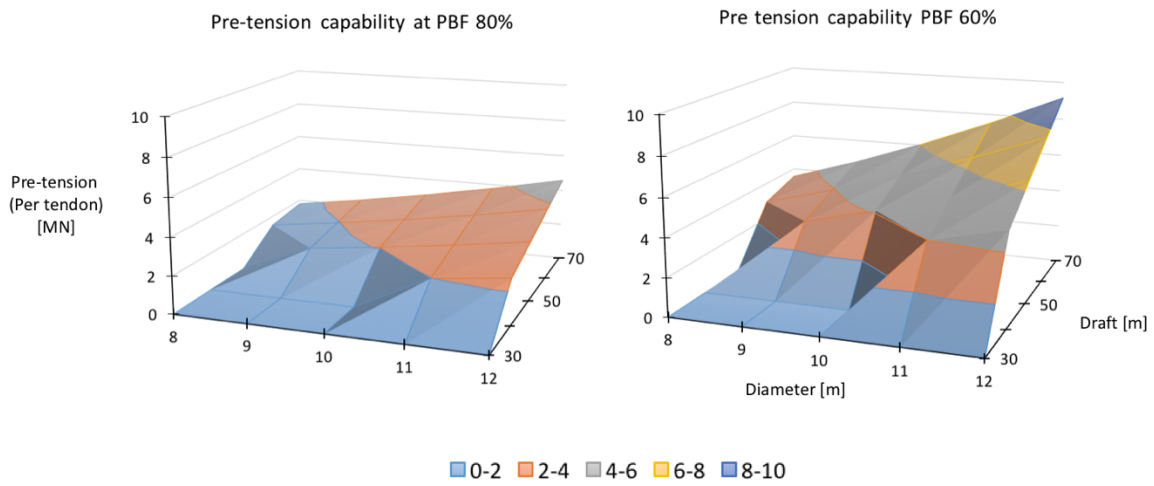

Figure 10-5: Available tension capacity per tendon in the design space for PBF 80% and 60%

The figure above shows typical tension capacities per tendon for the substructure at permanent ballast fractions of 80% and 60%. Available tension capacity is directly linked to the amount of temporary ballast in the structure at the given draft. The selected combinations are derived from Table 7-5. For unstable combinations where the calculated $\overline{GM}$ is less than or equal to zero the available tension capacity per tendon is set to zero. The available tension capacity is important to consider in the concept evaluation process, but depends on the BDS structure to which the substructure is mated. The requirement used in this context is that there shall be a surplus of buoyancy after mating to prevent the substructure from settling on the docking station. It is clear from this figure that there is a pronounced effect of decreasing the PBF from 80 to 60% where the combination OD12 d70 results in an increase in pre-tension capability from 4.58 MN to 9.15 MN.

10.2.6 Case selection

During the selection process there are a number of different aspects to consider. The main issues include float-out stability, static heel angle and pre-tension capacity. The float-out stability characteristics are important for tow-out operations and also depend on the natural periods in roll and heave, where issues associated with swell waves, for example, causing resonant motion in heave [9] should be adressed. The marine operation aspect here is not considered in detail, but data is presented on the natural periods for reference purposes. To take into account marine operations would exceed the scope of work. The substructure results can be found in Appendix A (electronically).

The following cases were selected for further analysis based on the aforementioned criteria. Total displacement, centre of gravity, centre of buoyancy, metacentric height, static pitch angle and pre-tension capacity per tendon (T) has been presented for the ballasted state (including temporary ballast). The mass properties of the three selected floaters are also presented below with reference to structural mass and the two categories of ballast mass.

Table 10-4: Selected cases for the substructure (ballasted state)

Case ID	OD	WT	H	PBF	ρ	∇	KG	KB	GM	Pitch	T
A1	9	25	70	80 %	3300	3817	24.22	30	5.87	5	1.97
A2	10	25	70	80 %	3300	4712	21.67	30	8.44	4	2.54
A3	12	25	60	80 %	3300	5655	17.35	25	7.83	4	3.16
Units	m	mm	m	–	kg/m^3	m^3	m	m	m	deg	MN

Table 10-5: Mass properties for selected cases

Case ID	Structural mass	Permanent ballast mass	Temporary ballast mass	Height of permanent ballast	Height of temporary ballast
A1	8.90E+05	2.41E+06	6.04E+05	11.63	9.37
A2	9.39E+05	3.11E+06	7.77E+05	12.12	9.75
A3	9.64E+05	3.86E+05	9.66E+05	10.44	8.40
Units	kg	kg	kg	m	m

10.3 Buoyant docking station

10.3.1 Design criteria

The design criteria for the buoyant docking station are presented in the table below. Note that these are acceptance criteria used to select cases for hydrodynamic analysis and dynamic simulation.

Table 10-6: Design criteria - BDS

		Comment
Metacentric height in float	> 0 m	
Metacentric height in submerged condition	> 0 m	
Minimum tension capacity per tendon*	3 MN	Minimum total pre-tension of combined system is 5 MN
Internal clearance above total ballast column	≥ 0 m	
Maximum allowable static yaw angle	3°	Based on generated torque in operational condition

*The minimum tension capacity per tendon was selected based on the pre-tension values from the TLPWTs analysed in [29]. Refer to the TLP design consideration chapter presented earlier in this thesis.

10.3.2 Matrix experiment setup

Table 10-7: Matrix experiment setup

Parameter	Low	Medium	High
BM Diameter	8	10	12
BM Height	10	20	30
PO Length	10	20	30
Colour coding			

Due to the relative complexity of the buoyant docking station compared to the mono-hull floater, it was necessary to establish a matrix experiment setup based on the design space presented in Section . The matrix experiment setup is based on a similar approach to what was observed in [57]. The basic procedure is to establish low, medium and high values in a pre-defined design space. From this, several combinations of parameters are established in order to evaluate a wide range of BDS geometries.

10.3.3 Volumetric ratios

The volumetric ratio was used throughout the interpretation of the results from the spreadsheet analysis stage for the buoyant docking station. The aim was to provide a single variable to represent the size of the pontoons relative to the structure as a ratio of total displacement. The volumetric ratio was used in order to be able to plot variables such as metacentric height, surplus displacement in float-out and variation in pre-tension. Note that the method of expressing these parameters in terms of volumetric ratio breaks down without maintaining some of the variables constant. The constants used in conjunction with the volumetric ratio are presented in the table below.

Table 10-8: Constants used in conjunction with volumetric ratio

OD PO	WT PO	WT CC	WT BM
3	60	40	40
m	mm	mm	mm

In order to utilize the volumetric ratio, the variables are limited to changes in pontoon length, buoyancy module diameter and height. Since the volumetric ratio is based on external properties only, there is no limitation in adjusting the permanent ballast fraction. Based on the design space presented under the concept description and definition of parameters chapter (Table 7-7 on page 49), the ratio is found to have a limited volumetric range. The volumetric range was established by checking the associated volumetric ratio for different combinations in the design space as presented in the table below.

Table 10-9: Volumetric ratios for selected combinations

Length PO	Diameter BM	Height BM	Volumetric Ratio
10	8	10	0.42
10	10	30	0.16
30	8	10	0.61
30	12	10	0.46
10	12	30	0.14
m	m	m	–

As can be observed from the table above, the volumetric range in the selected design space is (0.14, 0.61). Note that the table is built by selecting a low, medium, high value in the design space for pontoon length, BM diameter and height.

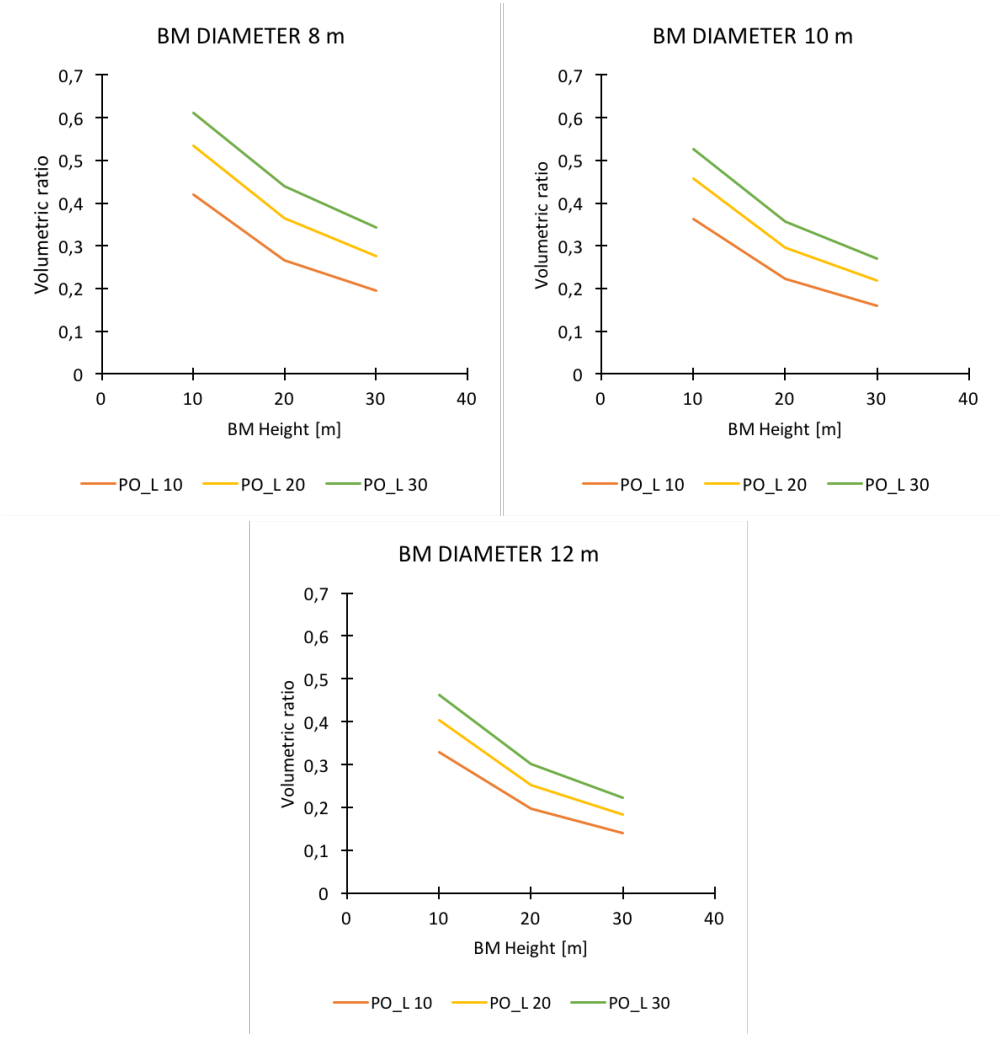

Figure 10-6: BM diameter, BM height and PO length effects on volumetric ratio

The figures above show the effect of changing the the BM diameter (separated into three figures), the BM height and the pontoon length (PO_L series) on the volumetric ratio. As can be observed from this figure the general effect of increasing the diameter is the reduction in volumetric ratio. This is due to the fact that the total volume of the pontoons becomes less significant when the BM is larger. The effect of increasing the pontoon length results in an increase in the volumetric ratio as expected based on the presented expression in (9.1) on page 59.

10.3.4 Stability with pontoons out of water

As previously stated under the concept description chapter there are two principal stages of stability to analyse: stability with pontoons out of the water and submerged stability. In this section the results from the first stability

stage is presented. The sub-chapter is setup such that an assessment of ballast fraction adjustment is conducted, followed by an isolated assessment of structural changes at constant PBF.

10.3.4.1 Adjustment of permanent ballast fraction

By utilizing the volumetric ratio, it is possible to determine the freeboard to the pontoons (analogous to surplus displacement) for the buoyancy module where several combinations of pontoon lengths, BM diameters and heights are evaluated. In order to determine the stability with the pontoons out of the water, it is necessary to first verify that the freeboard to the pontoons is adequate excluding temporary ballast. The freeboard was determined by subtraction of the BM draft from the total BM height. Note that the focus in this scetion is not the individual adjustments of structural parameters such as the pontoon length, BM diameter or BM height. The assessment is made to observe the effect of increasing the permanent ballast fraction. Structural assessments are handled at a later stage.

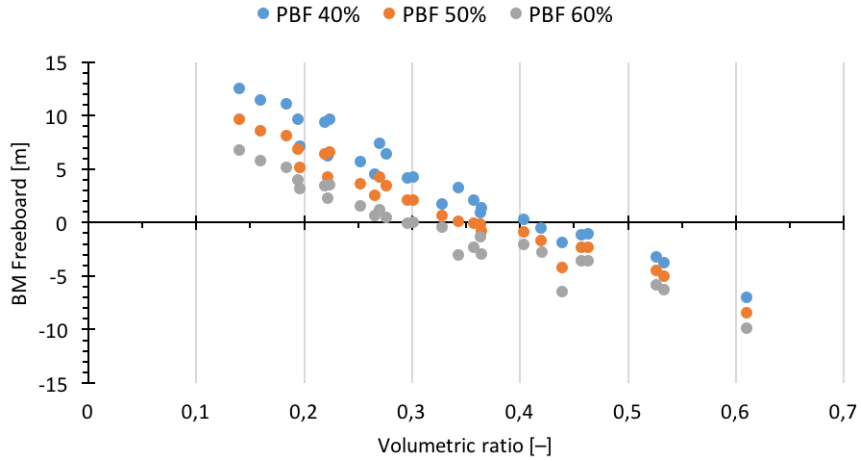

Figure 10-7: Volumetric ratio vs. buoyancy module freeboard at variable PBF

The figure above shows the volumetric ratio vs. freeboard for the buoyancy module without temporary ballast for three PBFs: 40%, 50% and 60%. Positive freeboard indicates that there is enough buoyancy in the buoyancy module to support the entire structure with the pontoons out of the water. In terms of volumetric ratio, the data above suggests that an increase in volumetric ratio will lead to a reduction in freeboard, as is expected since the vessel increases in mass due to the added structural weight at the top of the structure. An increase in PBF results in a decreased freeboard as a significant increase in the fraction of permanent ballast leads to increased initial weight of the floater. In general, a volumetric ratio between 0.30 and 0.42 will result in negative freeboard, which means that the pontoons will enter the water in these cases. This violates the floating stability criteria, as float out stability is only evaluated given that the pontoons remain out of the water line.

Note that values for negative freeboard are omitted from the figure below as the stability calculations are erroneous when the pontoons enter the water.

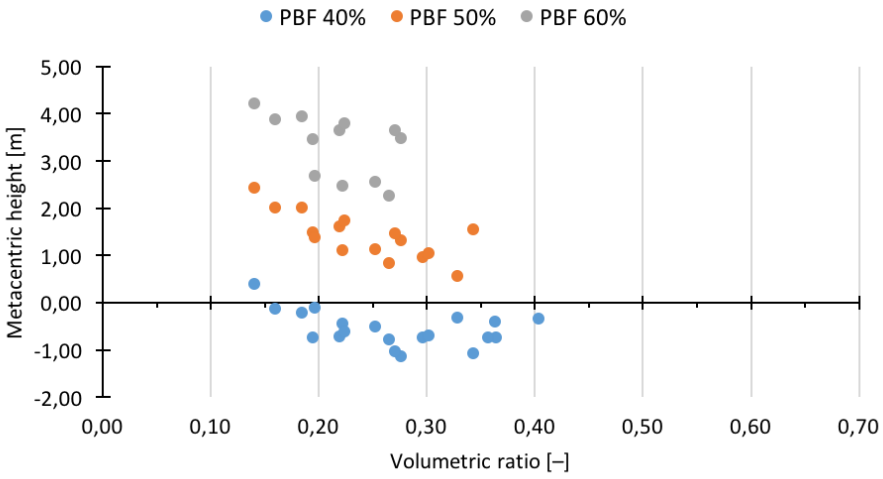

Figure 10-8: Metacentric height in float vs. volumetric ratio at variable PBF

As can be observed from Figure 10-8, the vessel is stable when floating solely by the buoyancy module for volumetric ratios ranging between 0.14 and 0.33 for a PBF of 50%, whereas stability is only achieved for a volumetric ratio of 0.14 at 40% PBF. For PBF 60%, there is a restriction on the available data for establishing floating stability in the specified design space. This is because of the loss of freeboard at lower volumetric ratios. It seems that there is a general trend of a reduction of two meters of metacentric height when changing the permanent ballast fraction from 50% to 40%. For the structural changes assessment in the next chapter, a PBF of 50% has been assumed based on the results presented above. However, a PBF of 40% may have other benefits, as will become clear at a later stage. The reason being that the loss of pre-tension capacity, at the expense of float out stability (with pontoons out of the water) may not justify opting for increased PBFs.

10.3.4.2 Isolated assessment of structural alterations

Due to the complexity of the underlying relations between the floating stability and the input parameters (BM diameter, BM height and PO length), the following figures have been provided to give an indication of the effects each of the aforementioned parameters have on the metacentric height and freeboard by assessment of structural alterations only. In order to clarify what the effects are, the matrix experiment (Section 10.3.2) was used. The matrix experiment consisted of 27 experiments (3x3x3) where the outputs include $\overline{GM}$ in float-out, surplus displacement (analogous to the freeboard assessment presented in the previous section), and available pre-tension (see Section 10.3.6) to assess the associated effects from a change in input parameter. The colour coding as presented in Table 10-7 is withheld across all the following plots for clarity. The corresponding volumetric ratio is constant across all plots; hence it is possible to identify the associated parameters for a data point by this colour coding. Additional results are presented in Appendix A.

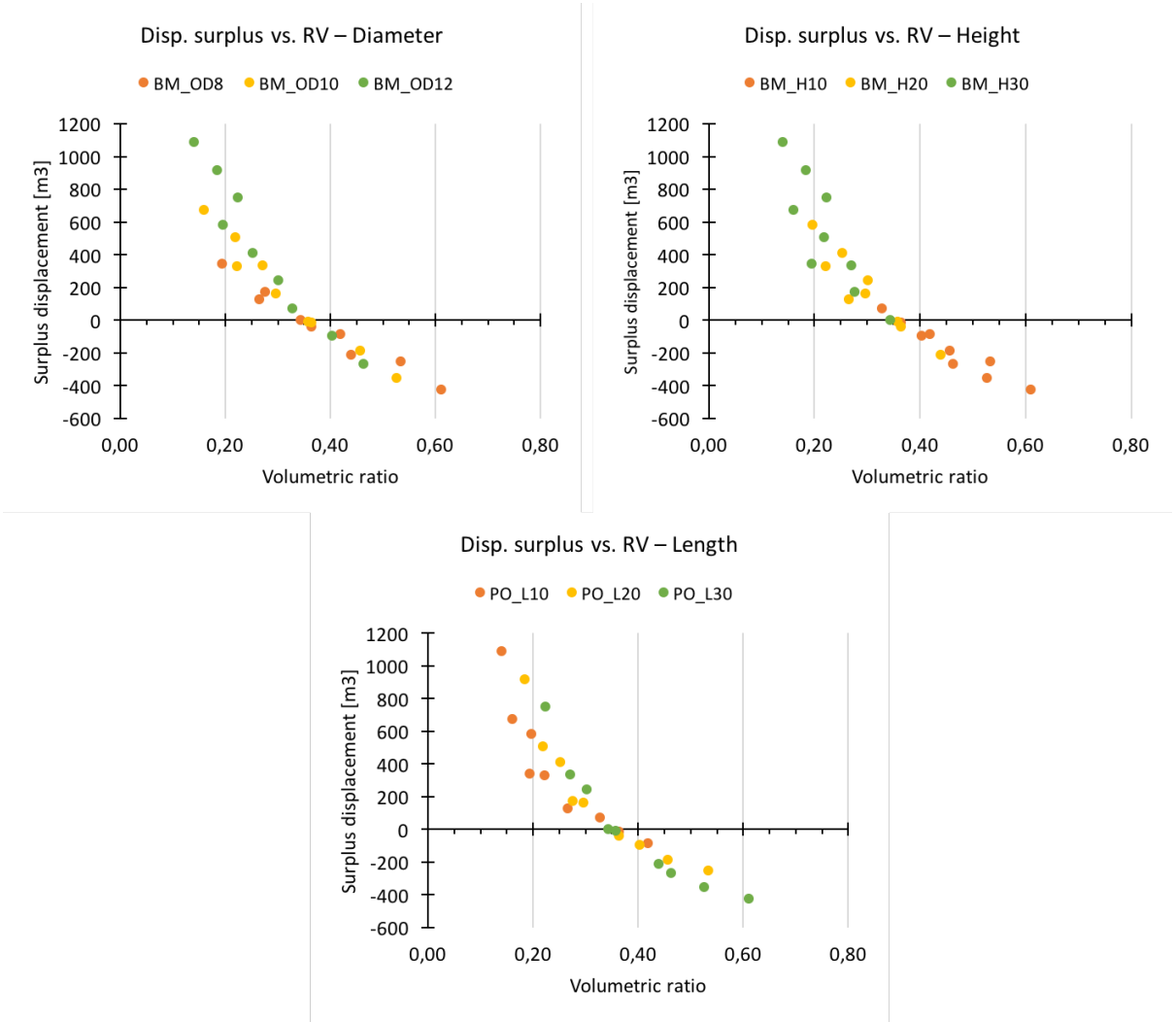

Figure 10-9: Surplus displacement vs. volumetric ratio at PBF50%

From the figure above it is apparent that there are, approximately, linear relationships between the diameter and the surplus displacement (top plot on the left) in the design space. The slope is largest for the larger diameter, and

smallest for the small diameter. There also seems to be a pivot point at the volumetric ratio of 0.35, which is approximately the same for all three diameters. Another key observation from this data set is that the number of data points with negative surplus displacement increases with decrease in BM diameter. This follows the expectation as the total volume of the BM is expected to decrease as the diameter is reduced.

A similar trend is found for the surplus displacement figure where the BM height is highlighted. The general trend is that the surplus displacement increases with a following decrease in volumetric ratio, which follows the expectation as the volume of the BM becomes larger leading to a reduction in the volumetric ratio. For the pontoon length, the effect of an increase has adverse effects on the surplus displacement. As can be observed from the sub-figure on the bottom in Figure 10-9, 67% of the generated data yield negative (or zero) surplus displacement for a pontoon length of 30 m. Typically a short pontoon length will yield greater surplus displacement, but will have a negative effect on the yaw stiffness in tethered condition [29].

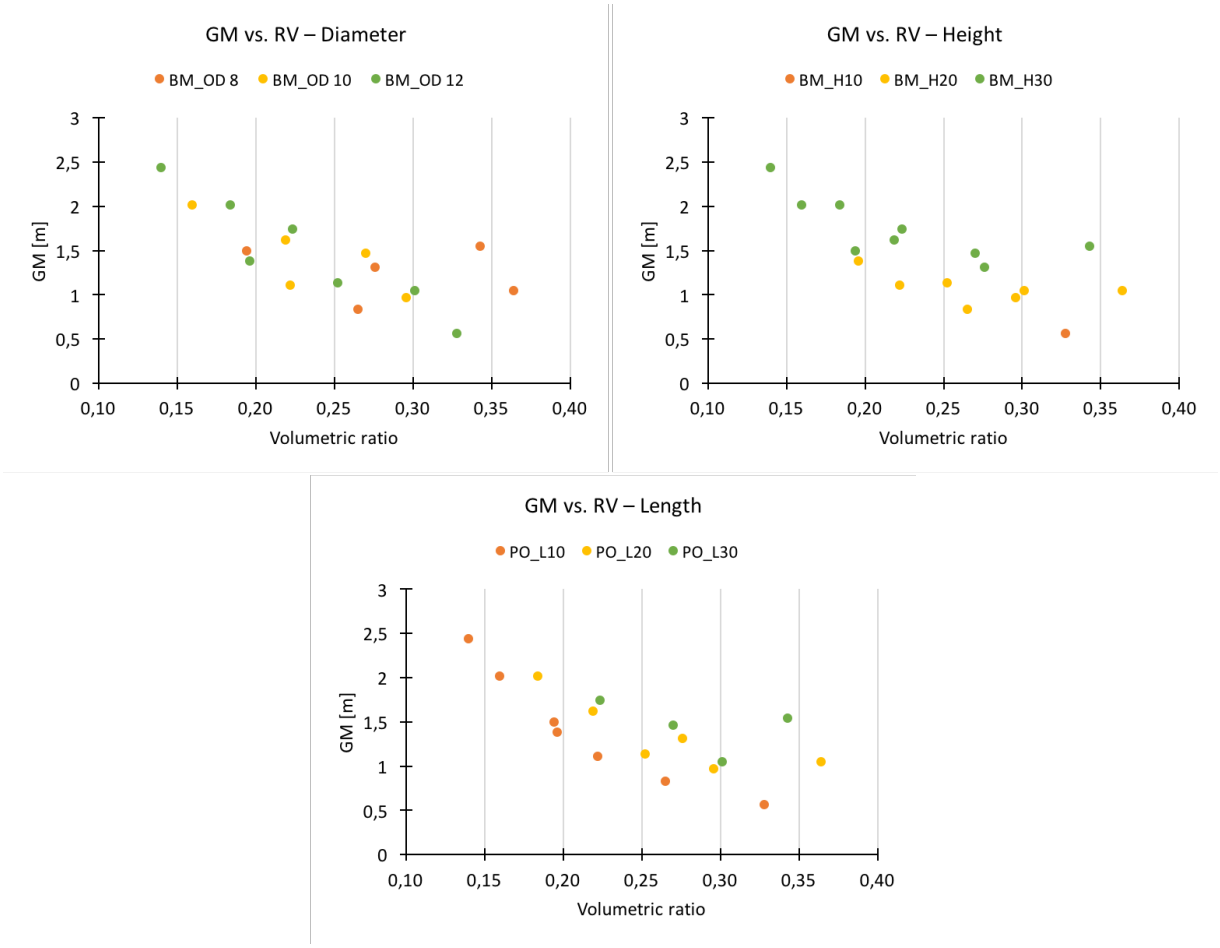

Figure 10-10: Effects on stability in float out at PBF50%

From initial evaluations of the surplus displacement data it was found that most of the parameter combinations resulting in a volumetric ratio in excess of 0.35 resulted in negative surplus displacement and were therefore deemed inappropriate for further analysis. The corresponding data points have been removed from the stability calculations in float out conditions (Figure 10-10). The general trend to be observed from the data is that increased volumetric ratio leads to a decrease in the metacentric height, as is expected as the centre of gravity will tend to increase with more weight added to the top of the structure. The most consistent method of improvement is to increase the height of the buoyancy module as can be observed in the top right sub-figure in the figure above. Again, longer pontoon lengths are tolerated by increasing the BM height. It is worth noting that the PBF was set to 50% for the isolated assessment of structural changes in line with what has been stated in the previous section.

The table below presents the matrix experiment results with reference to BM freeboard (analogous to surplus displaced volume for BM) and the stability in float. Note that the colour coding stated earlier is maintained for ease of parameter identification.

Table 10-10: Matrix experiment results at PBF50%

ID	POL	BMOD	BMH	FREE-BOARD	$\overline{GM}$ FLOAT
1	10	8	10	-1.65	NA
2	10	8	20	2.59	0.83
3	10	8	30	6.83	1.49
4	20	8	10	-502	NA
5	20	8	20	-0.78	NA
6	20	8	30	3.45	1.31
7	30	8	10	-8.40	NA
8	30	8	20	-4.16	NA
9	30	8	30	0.08	1.55
10	10	10	10	-0.17	NA
11	10	10	20	4.22	1.11
12	10	10	30	8.61	2.02
13	20	10	10	-2.33	NA
14	20	10	20	2.06	0.97
15	20	10	30	6.45	1.62
16	30	10	10	-4.49	NA
17	30	10	20	-0.10	NA
18	30	10	30	4.29	1.47
19	10	12	10	0.65	0.57
20	10	12	20	5.15	1.38
21	10	12	30	9.64	2.44
22	20	12	10	-0.85	NA
23	20	12	20	3.64	1.13
24	20	12	30	8.14	2.02
25	30	12	10	-2.35	NA
26	30	12	20	2.14	1.05
27	30	12	30	6.64	1.74

As can be observed from the table above the following combinations, listed with ID, are not to be evaluated for stability in submerged state; 1, 4, 5, 7, 8, 10, 13, 16, 17, 22 and 25 due to the lack of sufficient freeboard. ID 9 and 19 are also rejected due to the fact that the associated freeboard is relatively close to zero, i.e. pontoons are almost in the water. The number of experiments to be completed for the stability in submerged state is 14 out of the 27 conducted for float out stability. Note that deviations from this may occur, as there are possible alternatives (complete submergence tow) for the tow-out procedure, hence the float-out stability (elevated pontoons) may be regarded as non-critical. This is reflected in some of the results presented in Sections 10.3.5, 10.3.6 and 10.3.7.

10.3.5 Stability in submerged state

The criteria for stability in this case is that $\overline{GM} > 0$ to prevent the vessel from rotating during the submergence stage. There are several variables that affect the stability in its submerged state such as the length and diameter of the pontoons, the wall thicknesses for each respective component, ballast density, PBF, etc. In general, the stability of a certain combination of structural parameters (diameters, length and wall thickness) is adjusted by the permanent ballast fraction because the densities of the two ballast types are assumed to be fixed in this analysis. An increase in PBF will have a beneficial effect on $\overline{KG}$ but will adversely affect the tension capacity of the system. In the spreadsheet the mass of total ballast is handled by equating the total displaced mass of water to the mass of the structure, which means that whenever a change is made to the dimensions, a change in ballast will follow based on Archimedes' principle.

A pre-requisite for assessing the stability in the submerged state is that one can achieve submergence for the given parameter combination. As mentioned under the design criteria for the buoyant docking station the system must be sinkable, i.e. there must be sufficient ballasting space in the buoyancy module to achieve at least neutral buoyancy. The volumetric ratio is used here to express, in essence, the ratio of non-ballast-able volume to the total volume, i.e. the volume of the central column plus the volume of all three pontoons relative to the total volume.

10.3.5.1 Achieving submergence for various PBFs

In this section the submergence criterion is evaluated for PBFs ranging between 40 and 60%.

In order to achieve submergence there must be available space in the BM to add sufficient temporary ballast such that the mass of the vessel exceeds that of the displaced mass of water. It is worth noting that there is no ballast in the pontoons or the central column, which means that a significant change in the dimensions of these components will require more ballast in the buoyancy module to counteract the increase in buoyancy. As such there is an imposed structural limitation on the relative dimensions of CC and PO for certain BM dimensions due to the available ballasting column. This is illustrated in the figure below, using the volumetric ratio. The generated results are based on the same matrix experiment presented earlier. The plot below shows the results obtained for the available ballast column where the total mass equals that of the displaced water.

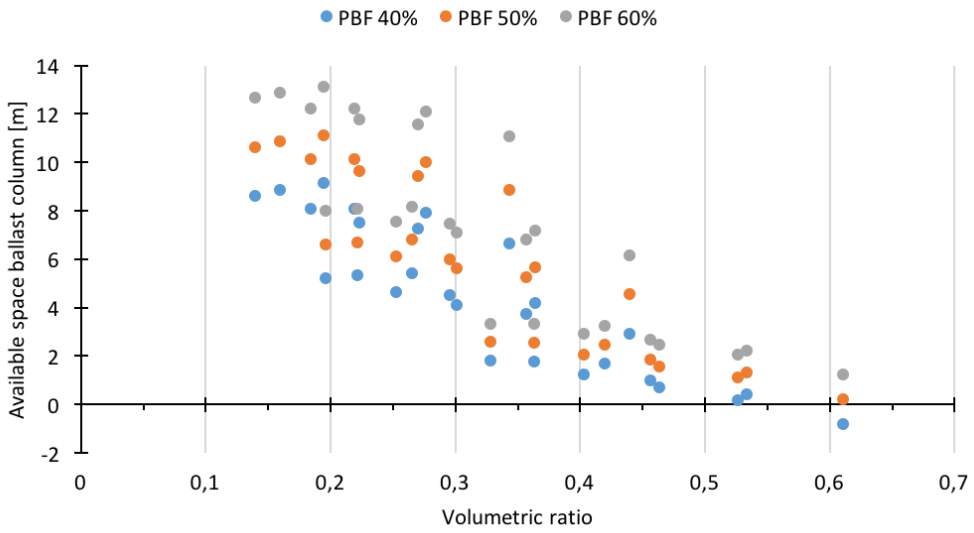

Figure 10-11: Volumetric ratio to available ballast column for several PBFs

The numerical value of available ballast column represents the clearance between the top of the internal column and the top of the temporary ballast column. As can be observed from this figure, there is a clear negative trend associated with increasing the pontoon length on the available ballast column, where an increase in volumetric ratio tends to decrease the available ballast column. For a PBF of 40% the vessel is not submergible when the volumetric ratio exceeds 0.53 because the internal ballasting space in the buoyancy module is completely filled. It can be observed that if the PBF is increased to 50% the volumetric ratio limit increases to around 0.61. This limit is extended further for a PBF of 60%. It is worth noting that although there is a positive relationship between increasing the PBF and the tolerated volumetric fraction, there is an adverse impact on the tension capacity per tendon as the amount of temporary ballast is significantly reduced when increasing the PBF. It should be noted that an increase in BM height will lead to a reduction in the volumetric ratio if all else is held constant. An increase in BM height will also have a direct effect on the amount of ballast-able internal volume.

The conclusions to be drawn from the figure above is that there is a possibility of tolerating larger volumetric ratios by adjusting permanent ballast fraction, but at a potential cost of pre-tension capacity due to the loss of temporary ballast. This is as expected due to the increased density of the permanent ballast resulting in more efficient use of internal volume with respect to the required temporary ballast column. Unlike float-out stability, achieving submergence is regarded as a highly critical aspect of this design.

10.3.5.2 Achieving submergence for various structural alterations at constant PBF

Similarly to that which was presented in the previous section, the submergence criterion is evaluated for structural alterations at constant PBF. The same matrix experiment approach has been implemented here for consistency. The underlying data is identical to that of the previous section, but the focus in this section is to assess the effect each of the three structural variables have on the available ballast column. This is presented in Figure 10-12.

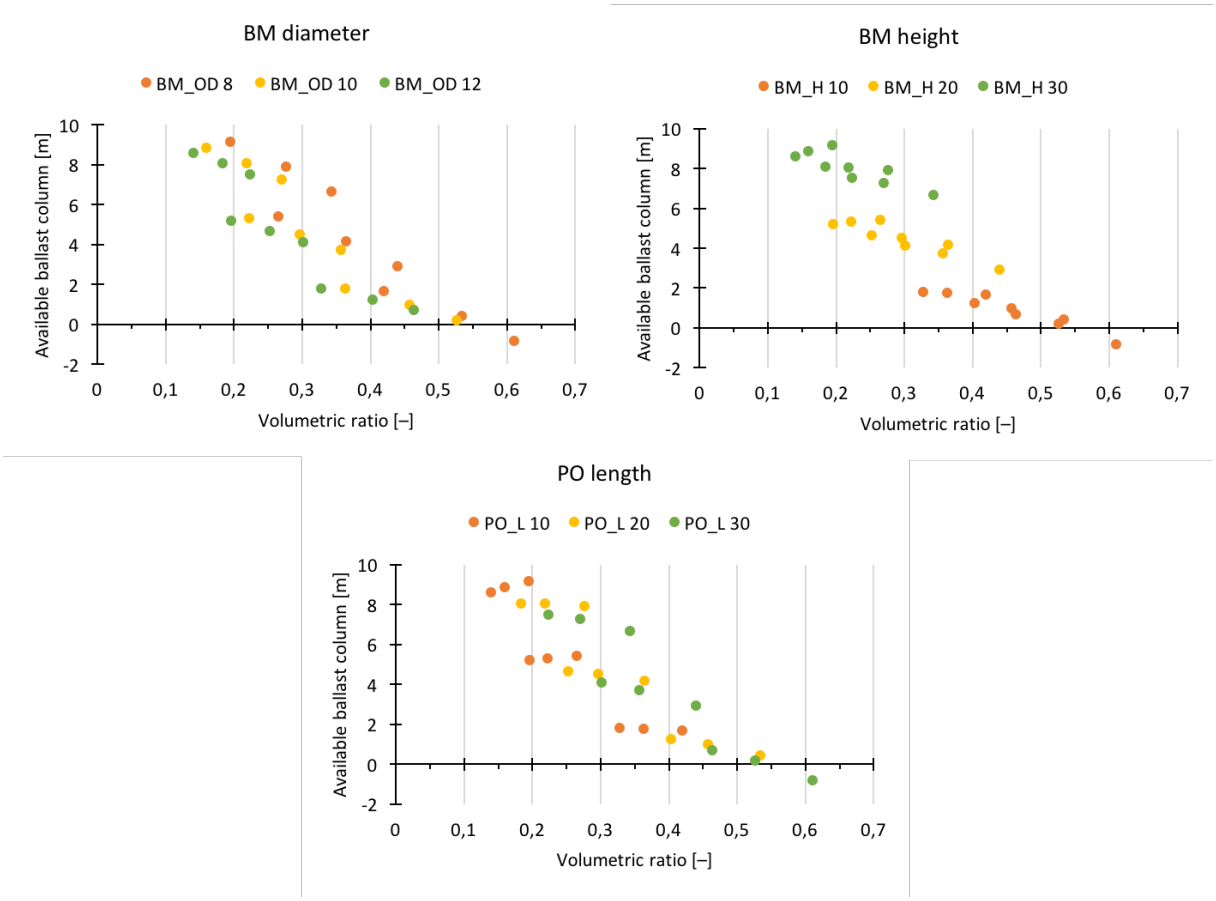

Figure 10-12: Effect of structural alterations on available ballast column for PBF40%

As one would expect, it is clear that the BM height is the most consistent method of improving the available ballast column (upper right hand corner). The diameter of the buoyancy module does not appear to have a significant effect on the available space, but will affect the volumetric ratio. The reason being that one observes a horizontal translation of data parallel to the abscissa, without a significant vertical shift. Changes in the pontoon length typically tends to have a slight effect on the available ballast column and a relatively significant effect on the volumetric ratio. In this case one can observe that the available ballast column reduces with increase in pontoon length.

The data indicates that it is not possible to submerge the structure if the volumetric ratio exceeds 0.55, i.e. there exists a limit to the relative size of the pontoons for this PBF. From these results it is clear that optimization of the structure will generally be linked to the reduction of BM height (for fixed PBF), as a lower available ballast column is considered optimal in regards to resource utilization. However, resource utilization is not the main priority in this design, where focus is directed towards establishing an array of BDS's with suitable pre-tension capacities and stiffness characteristics. By stiffness characteristics it is meant that the pontoon radii shall be sufficient according to the pre-determined design criteria. Further discussion of resource utilization is presented in Section 10.3.8).

10.3.5.3 Effect of altering PBF on submerged stability

Prior to presenting the isolated assessment of structural alterations for the submerged stability it was deemed necessary to present the effect of PBF. In this section the same matrix experiment has been conducted for PBFs ranging between 40 and 60%.

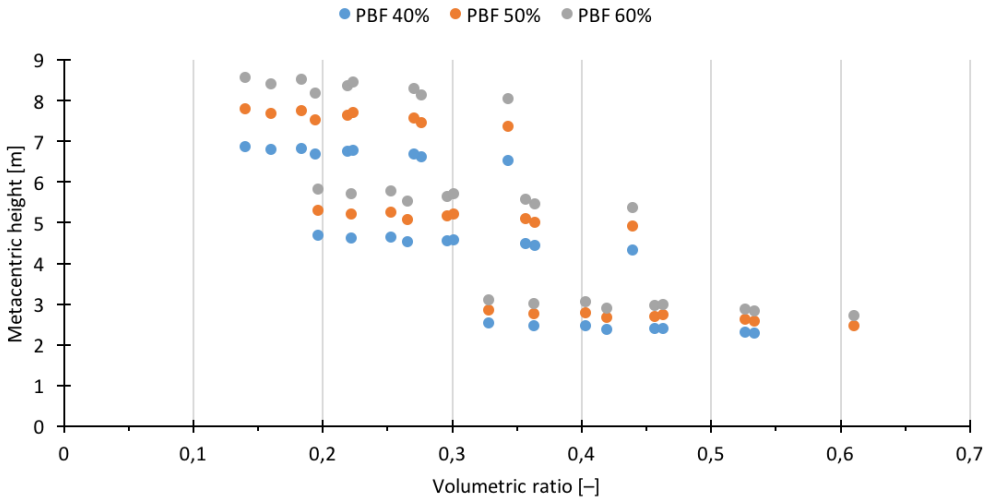

Figure 10-13: Effect of PBF on submerged stability

As expected, increasing the PBF yields improved results for the metacentric height. There seems to be a 1 m reduction in $\overline{GM}$ associated with a 10 percentage point reduction in PBF. Based on the presented results it is clear that all combinations in the design space yield sufficient stability in the submerged state. Increase in volumetric ratio does however, seem to have a negative effect as expected based on the float out stability results. This is largely due to the increase in weight at the top of the structure (pontoon weight). Note that a volumetric ratio of 0.61 at a PBF of 40% resulted in negative available ballast column (as observed in Figure 10-11), which means that it could not be evaluated for stability. In conclusion it is clear that submerged stability is not critical in the pre-defined design space as it is satisfied for all combinations.

10.3.5.4 Isolated assessment of structural alterations for submerged stability

A similar matrix experiment was conducted for the submerged stability calculation. The isolated assessment of structural changes is solely conducted for submerged stability in this section, tension capacities are assessed at a later stage. Note that the structural assessment for submerged stability was conducted for structures that yielded sufficient float out stability, i.e. structures that were stable relying solely on the buoyancy from the BM.

In Figure 10-14 the submerged stability vs. volumetric ratio is presented for the identified cases from the floating stability analysis. As can be observed from the results, there are relatively insignificant changes to submerged stability with increase in volumetric ratio. Changes in the diameter of the BM does not have significant effect on the stability in this case and the relationship is somewhat unclear. Increase in pontoon length only affects the volumetric ratio, but has negligible effect on the stability by itself, when assessing floating stability. The only clear indication to draw from these results is that an increase in the height of the BM leads to an increase in metacentric height. On a general note, the stability is well above the requirement $\overline{GM} > 0$, which is an indication that this requirement is generally satisfied for the submerged state.

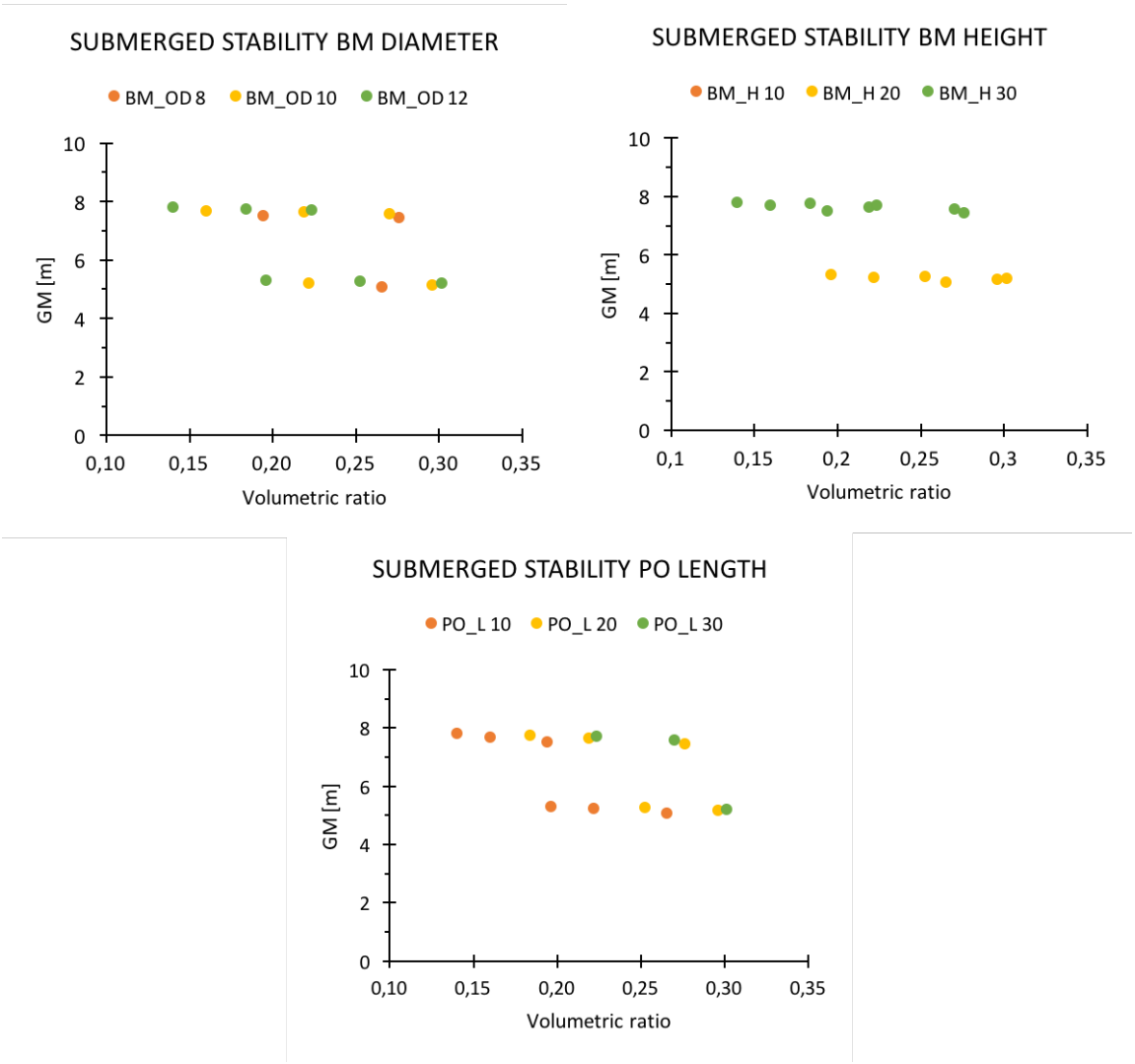

Figure 10-14: Submerged stability vs. volumetric ratio at PBF 50%

10.3.6 Tension capacity

The tension capacity is a critical parameter to consider during the case selection phase for the BDS. In this section the matrix experiment is taken further for comparison with stability and surplus displacement. The tension capacity is calculated based on the total displaceable volume vs. the displacement required for the vessel to remain buoyant with no temporary ballast added; i.e. the temporary ballast is a direct indication of the total tension capacity.

As can be observed from Figure 10-15, the tension capacities for the data set vary between 1.8 and 5.8 MN per tendon. In general, there is little change in the tension capacity when altering the pontoon length (figure labelled PO Length); i.e. a similar tension capacity is found, but with an associated shift along the abscissa. The BM diameter leads to a general increase in the tension capacity, which is reasonable considering its effect on the total displaced volume. The BM height does not seem to have a significant effect in this context, as the results seem to yield a coupled effect with BM diameter. It is clear from Figure 10-15 that the largest BDS (diameter 12, height 30 and length 30) results in the highest tension capacity overall as is expected due to increased amount of temporary ballast mass required to submerge the vessel.

Figure 10-16 presents a comparison of data sets with varying the PBF between 40 and 50%. Note that floating stability is not verified for this data set, the only requirement was achievable submergence. The reason for this adjustment is to cover a larger range of data sets, with possible optimization of PBF.

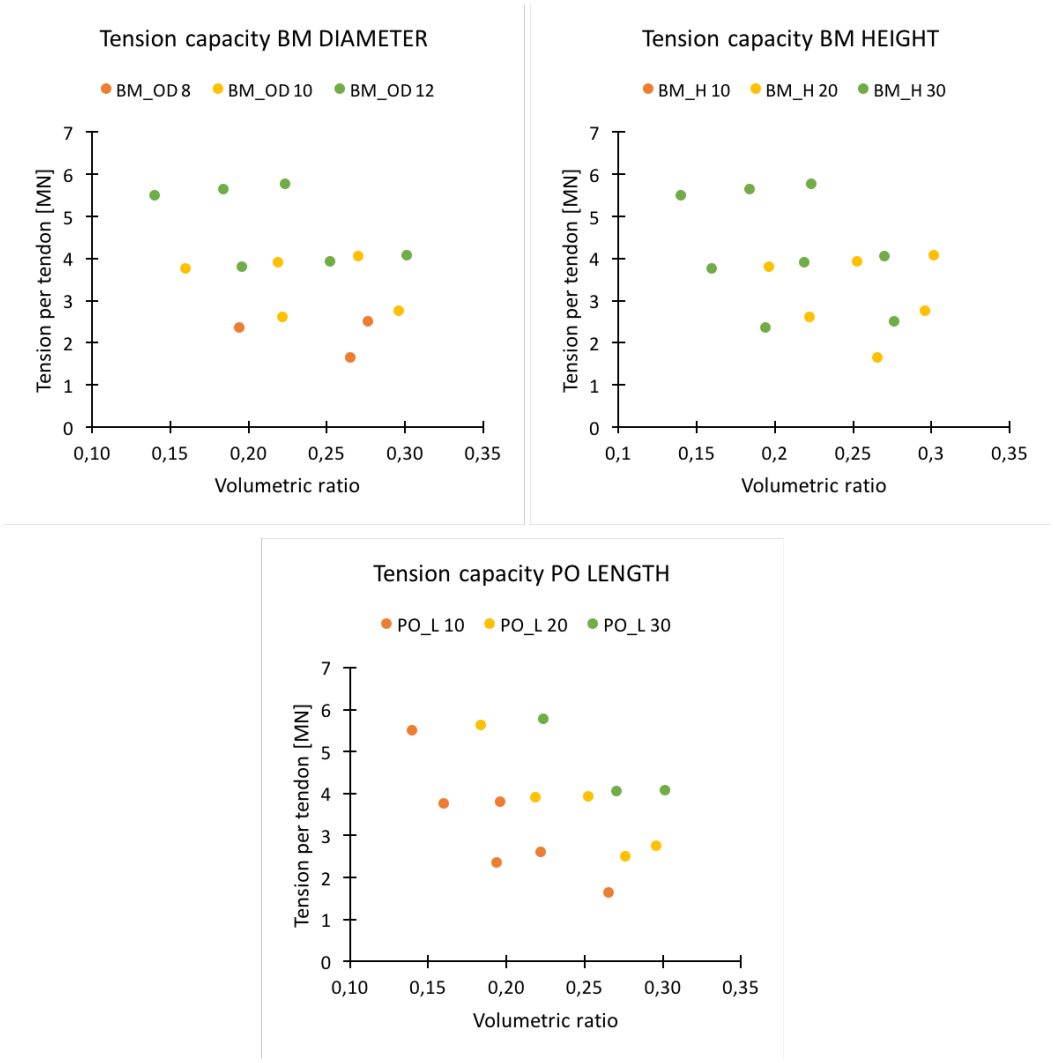

Figure 10-15: Tension capacities at PBF 50%

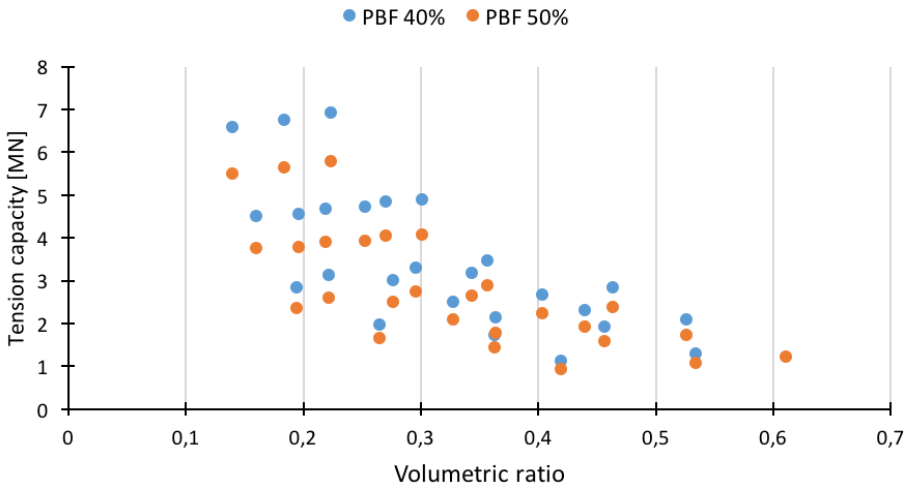

Figure 10-16: Effect of changing PBF on the tension capacity

As can be observed from the figure above, the general trend for increasing the PBF is loss of tension capacity. The effect seems to be more pronounced for lower volumetric ratios as can be observed in the range 0.1-0.3 where the

difference between the data points indicate a decrease in 1 MN per tendon as a result of an increase in PBF from 40 to 50%.

10.3.7 Angle of rotation (66)

The selection of cases requires information about the yaw stiffness of the system, which is highly dependent on the radial distance from the centre-line to the tether connection point (pontoon radius) [29]. The objective here is to assess the angle of rotation associated with the input torque from the turbine. The generated torque is assumed to be 1800 kNm (Section 7.3.1.2). The data series are generated by assuming a tendon length of 150 m, which represents an initial tendon length slightly larger than the achievable tendon length at minimum draft of the identified substructure cases in the previous section. Note that this is conservative as tendon stiffness is dependent upon the length of the tendon, as stiffness reduces with length (ref. equation (5.34) on page 24).

The structural assessment for angle of rotation in yaw is presented in Figure 10-17. The data used for generating this plot are based on combinations that yield sufficient float-out stability (Section 10.3.4). As can be observed from this figure the general tendency for change in diameter is that the angle of rotation is reduced. This is most likely due to the fact that the tension capacity of the vessel is significantly increased for the larger diameters, which has a direct effect on the stiffness of the mooring system in k_{11}, leading to an increased stiffness in k_{66}. The most consistent improvement for angle of rotation is observed for increasing the pontoon length. It is worth noting that the effect is more pronounced for the transition from 10 to 20 m pontoon length. The effect observed in the transition from 20 to 30 m is not as significant, where the improvement ranges between 1-2 degrees.

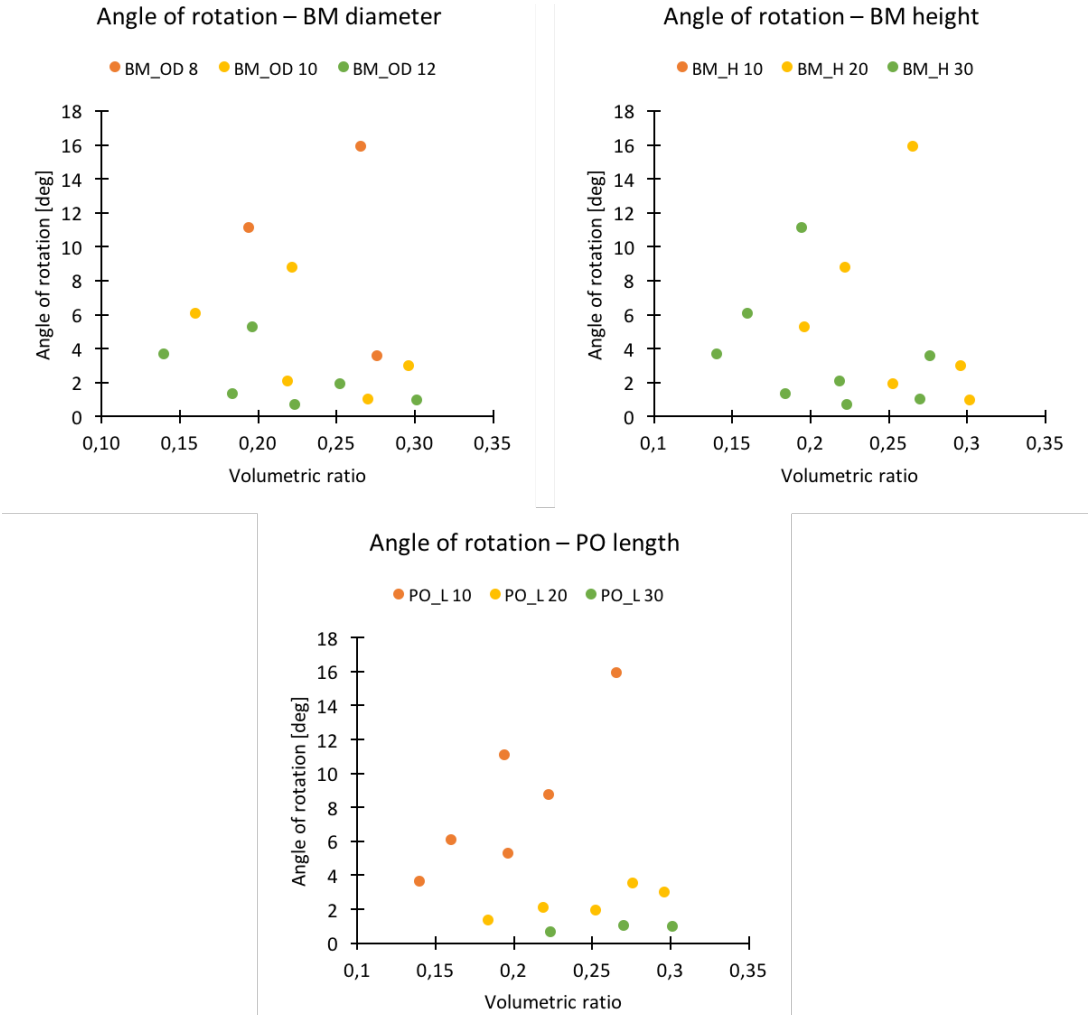

Figure 10-17: Angle of rotation vs. volumetric ratio at PBF 50%

The effect on angle of rotation for a reduction of the PBF to 40% from 50% is presented in Figure 10-18. As can be observed from Figure 10-18, the general trend associated with a reduction in PBF is a reduction in the angle of rotation for the given loading condition. The trends observed earlier for structural changes, i.e. diameter, height

and lengths, are identical in this case and are not repeated here. This is likely due to the increased pre-tension capacity associated with an increase in the total temporary ballast mass.

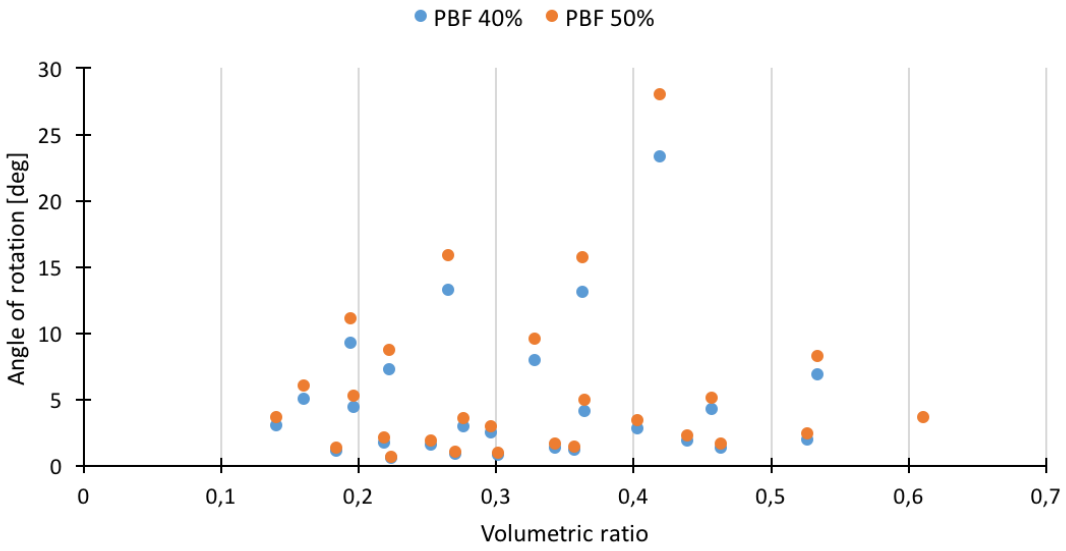

Figure 10-18: Effect of changing PBF on angle of rotation at 1800 kNm, length 150 m

10.3.8 Note on resource utilization

Resource utilization is not a central part of the scope of work, but it should be considered when deciding the optimum combination of parameters. At the preliminary stage it was proposed to express resource utilization in terms of available space above the total ballast column, where a large value indicates poor resource utilization and zero would represent the ideal resource utilization. With 0 m clearance above the total ballast column, the hull is believed to be optimized as it fulfils the minimum requirement for submergence.

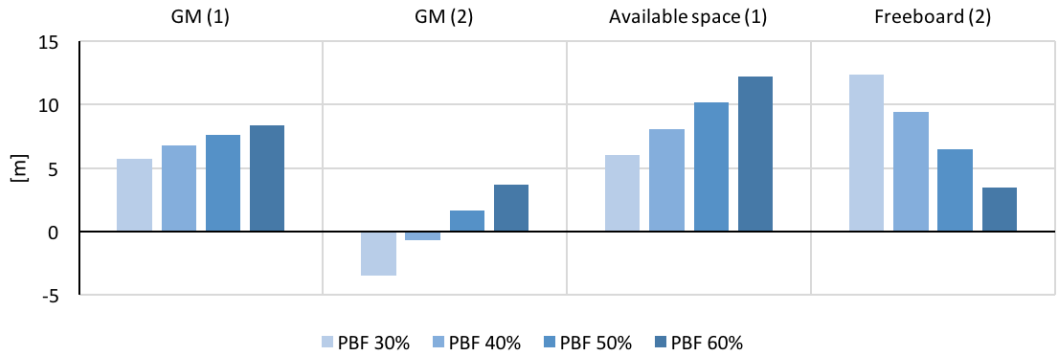

Figure 10-19: Resource utilization for BM(OD, H) = (10, 30) and PO(L) = (20)

The figure above shows a comparison of resource utilization with reference to stability and freeboard characteristics for the stated combination of parameters. The independent variable in this data set was the permanent ballast fraction, set to a range between 30 and 60%. The numbering system used in this context is as follows: (1) includes temporary ballast and (2) excludes temporary ballast. In general, stability improves with increase in PBF however, the available space also increases which is an indication of poor resource utilization. In addition to increased available space, there will also be a significant reduction in tension capacity due to a lower fraction of temporary ballast. The limiting factor above is the stability in float (GM (2)) as this becomes negative for PBF 30-40%. This can however, be remediated by including temporary ballast during the tow-out phase, but this is not included in the spreadsheet as the temporary ballast is assigned in a binary manner, i.e. either there is temporary ballast or there is not. In future work this should be included by, for example, including a temporary ballast filling fraction, which would allow for optimized design and improved resource utilization.

10.3.9 Concluding remarks

As can be observed from the obtained results for the spreadsheet analysis of the buoyant docking station, there are several variables to consider simultaneously; where structural adjustments and ballast modifications have different effects on stability, pre-tension, and angle of rotation. One example is the permanent ballast fraction, where an increase may result in improvements to stability characteristics, but will in turn have adverse effects in angle of yaw and pre-tension capacity. Another example is increasing the pontoon lengths, which yields significant improvement to angle of rotation, but may in turn reduce the stability-in-float characteristics of the structure as a greater proportion of mass is concentrated at the top of the structure. An increase in volumetric ratio, also has a seemingly negative effect on the pre-tension capacity as observed in Figure 10-16 where there is a general trend for reduction in tension capacity with increasing volumetric ratio. However, this effect is believed to be a result of a change in buoyancy module dimensions for constant pontoon length, which is supported by the data obtained in Figure 10-15, where the isolated effect of increasing pontoon length does not result in a significant change in tension capacity.

Another factor that affects the selection of suitable cases is resource utilization. This is, as previously mentioned, important to reduce costs as one can express the "structural waste" in terms of the available space above the total ballast column during the submergence stage. However, this is not evaluated as a critical consideration in this thesis.

From the results, it is clear that there must be a compromise between the tension capacity, pontoon length and stability in float. The submerged stability seemed to be relatively unaffected by changes in pontoon length and buoyancy module diameter, but was sensitive to buoyancy module height. Based on the recommendations provided in [29] regarding pontoon lengths, it is believed that the pontoon lengths must be as large as possible considering the defined design space. In addition to this, it was believed necessary to maintain larger values of pre-tensioning capacity, aiming at the pre-tensions presented in [8], [29]. Since focus will be on maintaining larger pontoon lengths and higher tension capacities, this means that a reduced permanent ballast fraction is beneficial, which will sacrifice some of the float-out stability characteristics, i.e. float out stability is not a critical criterion. Note that the submerged stability was ensured for the three PBFs analysed in this section, which means that the vessel will be stable in a submerged state, regardless of insufficient float-out stability. The reason for this is that the stability-in-float is somewhat conservative considering the fact that there are possibilities to add a fraction of temporary ballast to improve stability characteristics, if necessary. Modifications to the tow-out procedure may also be carried out, but this is not analysed in detail here. In regards to the tow-out procedure, it may be suitable to tow the system out in a submerged state to reduce the amount of permanent ballast, while still maintaining a positive GM. The tow-out procedure, is as previously stated, not analysed in this work.

10.3.10 Case selection

Several performance indicators are required in order to make sound case selections for further analysis. One of the more important factors to consider is the pre-tension capacity of the BDS structure, as this needs to be significantly large to prevent slack [8]. As mentioned during the TLP background study, Bachynski and Moan conducted a number of hydrodynamic analyses of several different 5 MW HAWT TLP systems with pre-tensions ranging between 5-8 MN for a range of displacements between 4000-11000 m^3. In light of this research, it was found reasonable to assume that similar values are required for the total system. The figure below shows the complete data set with two PBFs at 40 and 50%, and labelled acceptance criteria. Results are presented in Appendix A, found on the attached CD.

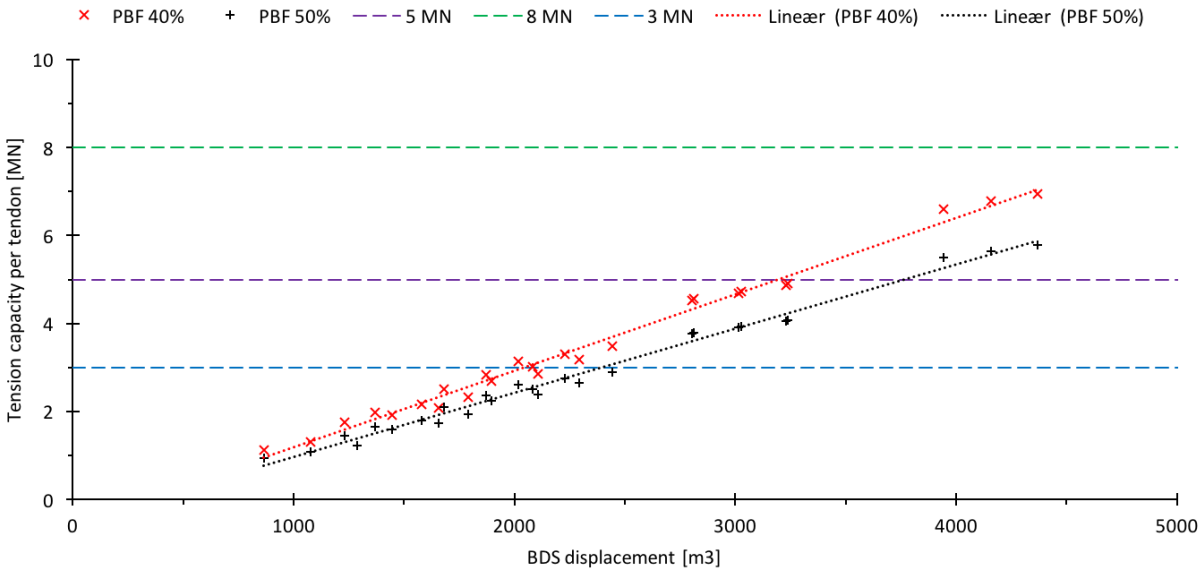

Figure 10-20: BDS displacement vs. tension capacity per tendon

The figure above shows tension capacities for different BDS displacements with the range of pre-tensions from [8] labelled (5 MN and 8 MN dashed lines). A third criterion was added to this figure, labelled 3 MN as this represents the lower limit in terms of tolerable pre-tension from the BDS. The reason for implementing this criterion is that the pre-tension is likely sufficient when the substructure is disconnected from the docking station, as the expected loading; even in severe sea states should not lead to slack tendons. This assumption builds on linear wave theory, where there is insignificant wave excitation at depths of 50-70 meters below sea level due to the exponential depth decay of wave particle acceleration [9]. The 3 MN limit is utilized because of the potential pre-tension contribution from the substructure in mated condition. From the initial spreadsheet study of the substructure (ref. Section 10.2.6) it was found that the additional pre-tension capacity ranges between 2 and 3 MN per tendon. This means that the most unfavourable combination of an accepted BDS and substructure will be within the lower limit of 5 MN.

Based on the underlying data used to generate the plot above, it is concluded that a PBF of 50% is rejected in its entirety. The reason for this is that the improvement in pre-tension capacity is significant for displacements above 2000 m^3, equating to a minimum improvement of ~0.8 MN (approximately 30% improvement in the lower tier) as can be observed from the figure above. This decision was also backed up by the fact that modifications to the tow-out procedure are possible; where one may opt for the submerged tow method, which has more favourable stability characteristics compared to the elevated pontoon method at PBF 40% (refer to Figure 10-8 on page 86).

The table below shows the parameter combinations resulting in a displacement of at least 2000 m^3 at a PBF of 40%.

Table 10-11: Parameter combinations with displacement above 2000 m^3

BM H [m]	BM OD [m]	PO L [m]	∇_{BDS} [m^3]	Available space [m]	Tension capacity [MN]	Yaw [deg]	Comment
20	10	10	2018	5.32	3.13	7.31	Rejected based on angle
30	8	20	2082	7.91	3.01	2.97	

BM H [m]	BM OD [m]	PO L [m]	∇_{BDS} [m^3]	Available space [m]	Tension capacity [MN]	Yaw [deg]	Comment
20	10	20	2230	4.53	3.30	2.50	Accepted
30	8	30	2294	6.67	3.18	1.40	
20	10	30	2442	3.73	3.47	1.21	
30	10	10	2803	8.86	4.52	5.07	Rejected based on angle
20	12	10	2813	5.21	4.56	4.42	Rejected based on angle
30	10	20	3015	8.06	4.69	1.76	
20	12	20	3025	4.66	4.73	1.61	
30	10	30	3227	7.27	4.86	0.87	Accepted
20	12	30	3237	4.11	4.90	0.81	
30	12	10	3944	8.62	6.60	3.05	Rejected based on angle
30	12	20	4156	8.07	6.77	1.13	Accepted
30	12	30	4368	7.52	6.94	0.57	

The table above shows the 14 cases with a tension capacity, per tendon, above the 3 MN acceptance criteria. Additional information about the available space at full ballast and the angle of rotation at 1800 kNm torque is included here. As can be observed from the table above there are several parameter combinations that, even though they have satisfied the acceptance criteria in terms of tension capacity, the angle of rotation exceeds 3°. Although there is no specific numeric criterion used here, a smaller-the-better based approach was used. The typical range of the angles of rotation excluding the aforementioned outliers was found to be (0.57, 2.97).

Another criterion that can be used for selection of potential parameter combinations for dynamic analysis is the available space in the BM. As mentioned in the section on resource utilization, a significant surplus of available space is an indication of a sub-optimal combination of PBF and buoyancy module dimensions. However, this may be required for temporary ballasting during the float-out phase to adjust stability characteristics because of the reduced PBF in the selected cases above compared to the PBF previously studied (50%). As mentioned earlier adjustment of the ballast column to include a fraction of temporary ballast has not been included as part of the analysis.

The rejected combinations, based on angle of rotation, are labelled in the table above. The general trend was that these combinations featured pontoon lengths of 10 m, hence the selected cases for the BDS will not include pontoon lengths in this region.

The three selected cases are presented in the table below. These were selected in order to cover a wider range of tension capacities and displacements based on the potential structures presented in Table 10-11. The table below also presents the ballast column heights for reference when modelling the vessels in Autodesk Inventor.

Table 10-12: Selected cases

Case ID	BM H	BM OD	PO L	∇_{BDS}	Tension capacity	Height of temporary ballast	Height of permanent ballast	Internal diameter
B1	20	10	20	2230	3.30	12.75	2.64	9.92
B2	30	10	30	3227	4.86	18.76	3.88	9.92
B3	30	12	20	4156	6.77	18.10	3.75	11.92
Units	m	m	m	m^3	MN	m	m	m^2

11 Identification of cases

In this section the cases to be analysed are presented with reference to the structural dimensions and information regarding the ballast properties used in each case. In order to have a consistent method of reference to a certain combination of floater and buoyant docking station it was necessary to adopt a numbering system for the selected cases. This is presented below with an explanation of the setup of this system, with reference to the systems used during the hydrodynamic modelling and the dynamic simulation.

11.1 Numbering system

The numbering system used to identify the individual cases consists of an alphanumeric identity string as illustrated below. The figure below shows the identity string for a mated system with substructure A1 and buoyant docking station B1 with specific mesh setting Ms1 (a). Note that the mesh setting is used in conjunction with hydrodynamic analysis in HydroD (refer to section on hydrodynamic modelling).

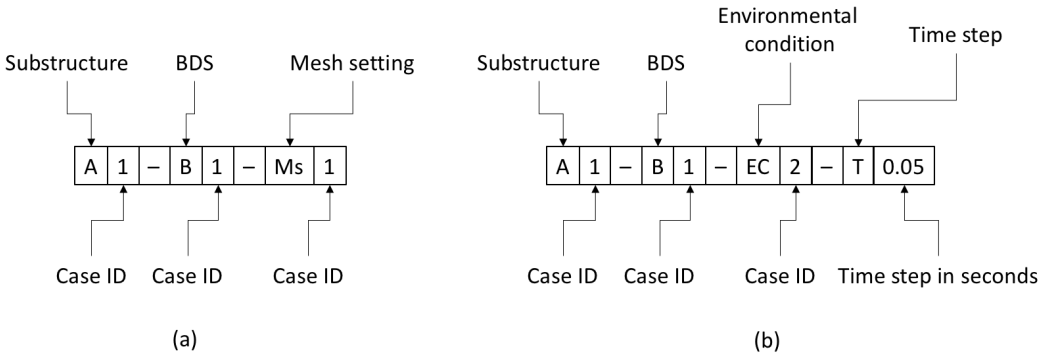

Figure 11-1: Alphanumeric case numbering system

The mesh setting case numbering system depend on the system in question. In general, the mesh settings are to be numbered with increasing mesh density, but deviations from this rule may occur depending on the case at hand. In addition to this there may be slight adjustments in the mesh, where there is only a small difference between the number of elements present in the mesh model, for example Ms2.1 may be used to identify this small step. The alphanumeric case numbering system for mesh model is always used with reference to the number of elements and nodes in the specific mesh model, with reference to the mesh identities presented in Table 9-2.

The numbering system is modified for the dynamic simulation section of this thesis where the mesh setting is replaced with the environmental condition, i.e. EC#. In addition to this a fourth step was added to represent the time step used designated by T0.05 (for a time step of 0.05 seconds). This can be observed in Figure 11-1 (b).

11.2 Summary of individual cases

The following section is a summary of the individual cases selected from the spreadsheet results. The structural dimensions and inertial properties for each case are presented here for clarity.

11.2.1 External structural dimensions

The nomenclature presented in the two tables below are as follows: outer diameter (OD), wall thickness (WT), height (H), permanent ballast fraction (PBF), permanent ballast density (ρ), length (L). Units are given at the bottom of each table. Input and output values are separated, but are identified by a common Case ID for reference purposes.

Table 11-1: Structural dimensions for substructure cases

Case ID	OD	WT	H	PBF	ρ
A1	9	25	70	80 %	3300
A2	10	25	70	80 %	3300
A3	12	25	60	80 %	3300
Units	m	mm	m	–	kg/m^3

Table 11-2: Structural dimensions for buoyant docking station cases

Case ID	Central column			Buoyancy module			Pontoons			Ballast	
	OD	WT	H	OD	WT	H	OD	WT	L	PBF	ρ
B1	10	40	3	10	40	20	3	60	20	40%	3300
B2	10	40	3	10	40	30	3	60	30	40%	3300
B3	12	40	3	12	40	30	3	60	20	40%	3300
Units	m	mm	m	m	mm	m	m	mm	m	–	kg/m^3

The inertial properties, displaced volume, stability and available pre-tension for the identified cases are presented in the tables below. Note that these are determined based on 3-D generated models in Autodesk Inventor.

11.2.2 Inertial properties <u>including</u> temporary ballast

Table 11-3: Inertial properties, stability and static pitch for cases A1-3

Case ID	Total mass	Perm. Ballast mass	Temp. Ballast mass	R1 & R2	R3	KG	KB	GM	∇	Pitch
A1	3.91E+06	2.41E+06	6.04E+05	39.65	5.95	24.22	30	5.87	3817	5
A2	4.83E+06	3.11E+06	7.77E+05	36.34	5.74	21.67	30	8.44	4712	4
A3	5.80E+06	3.86E+06	9.66E+05	31.21	5.92	17.35	25	7.83	5655	4
Units	kg	kg	kg	m	m	m	m	m	m^3	°

Table 11-4: Inertial properties, stability, pre-tension capacity for cases B1-3

Case ID	Total mass	Perm. Ballast mass	Temp. Ballast mass	R1 & R2	R3	KG	KB	GM*	∇
B1	2.28E+06	6.74E+05	1.01E+06	8.67	6.65	8.8	13.4	4.6	2230
B2	3.31E+06	9.91E+05	1.49E+06	12.12	8.47	12.8	19.5	6.7	3227
B3	4.26E+06	1.38E+06	2.07E+06	10.51	6.13	11.2	18.0	6.8	4156
Units	kg	kg	kg	m	m	m	m	m	m^3

*GM calculated in complete submergence. Total mass and radii of gyration (R1, R2 and R3) include temporary ballast.

11.2.3 Inertial properties <u>excluding</u> temporary ballast

The following inertial properties excludes the temporary ballast. It is worth noting that the centres of buoyancy and displacements are the same as presented in the previous section, thus the displacements represent the displacement in tethered condition. The un-ballasted inertial properties are important for the dynamic simulation stage as these represent the mated state with the tendons attached. The tension capacity per tendon T is presented for each individual case.

Table 11-5: Inertial properties, stability, displacement , pre-tension for cases A1-3

Case ID	Total mass	Perm. Ballast mass	R1 & R2	R3	KG	KB	∇	T
A1	3.30E+06	2.41E+06	42.94	6.33	25.65	30	3817	1.97
A2	4.05E+06	3.11E+06	39.59	6.08	22.55	30	4712	2.54
A3	4.83E+06	3.86E+06	34.12	6.20	17.88	25	5655	3.16
Units	kg	kg	m	m	m	m	m^3	MN

Table 11-6: Inertial properties, stability, displacement, and pre-tension capacity for cases B1-3

Case ID	Total mass	Perm. Ballast mass	R1 & R2	R3	KG	KB	∇	T
B1	1.28E+06	6.74E+05	10.91	8.34	8.7	13.4	2230	3.3
B2	1.82E+06	9.91E+05	15.40	10.97	12.3	19.5	3227	4.9
B3	2.19E+06	1.38E+06	13.25	7.50	9.6	18.0	4156	6.8
Units	kg	kg	m	m	m	m	m^3	MN

11.3 Combined cases

Prior to establishing the hydrodynamic models, it was deemed necessary to limit the number of combined cases to a representative set of three, based on the individually selected cases presented earlier. The selection was based on total pre-tension capacity and displacement. The figure below presents the pre-tension and displacement for the 9 possible combinations.

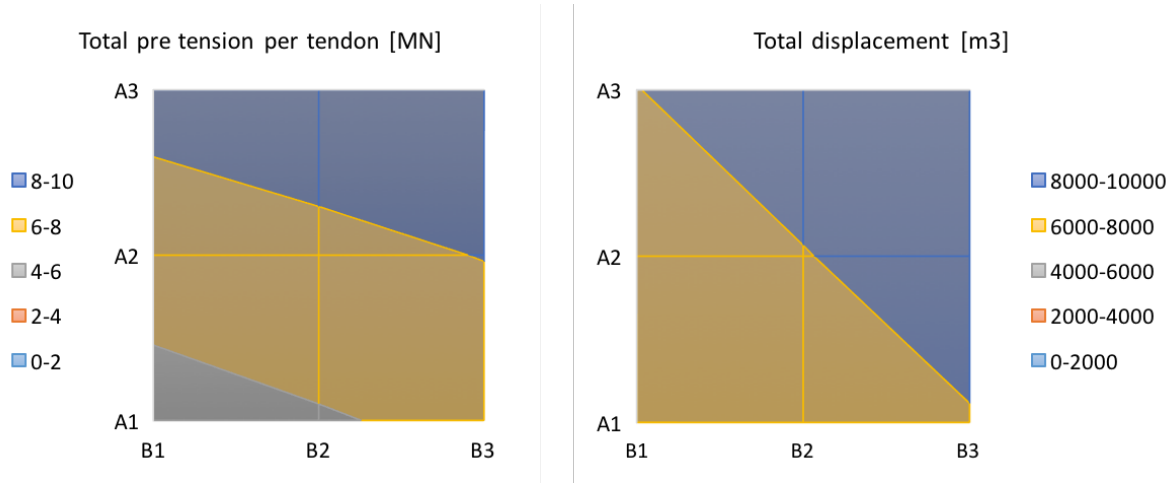

Figure 11-2: Pre-tension and total displacement combinations of A1-3 and B1-3

The figure above shows contour plots for the possible combinations. The total pre-tension capacities range between 4 and 10 MN, where the combination A1-B1 results in the lowest total pre-tension value. A3-B3 results in the largest pre-tension. The total displacement follows a similar trend where A1-B1 has the lowest displacement of 6000 m^3 and A3-B3 results in a total displacement of 9800 m^3. In order to capture the effects of low, medium, high pre-tension it was found that the cases A1-B1, A2-B2 and A3-B3 should be taken further for hydrodynamic analysis and dynamic simulation. In addition to observing the effect of change in pre-tension, one is also able to obtain some data on the effect of increasing the total displacement. This is significant with respect to the wave load as larger structures should generally experience an increase in wave load. The properties of these vessels are presented in Section 12, with reference to external structural properties and inertial properties for the two states where temporary ballast is included and excluded.

12 Results

In this section the results for A1-B1, A2-B2, and A3-B3 are presented. The results for each case are divided into their respective subchapters, with reference to model inputs, mesh models, environmental conditions used etc. Some tables are repeated here for ease of reference. Note that the results are presented on a **case-by-case basis**[14], where the hydrodynamic analysis results are presented prior to the dynamic simulation results. The discussion and interpretation of these results are left to the discussion chapter (Section 13). This means that the interpretation of results in the following sub-sections are limited to the convergence and time step sensitivity studies, as these are not comparable across the different cases.

The results chapter is structured in the following manner:

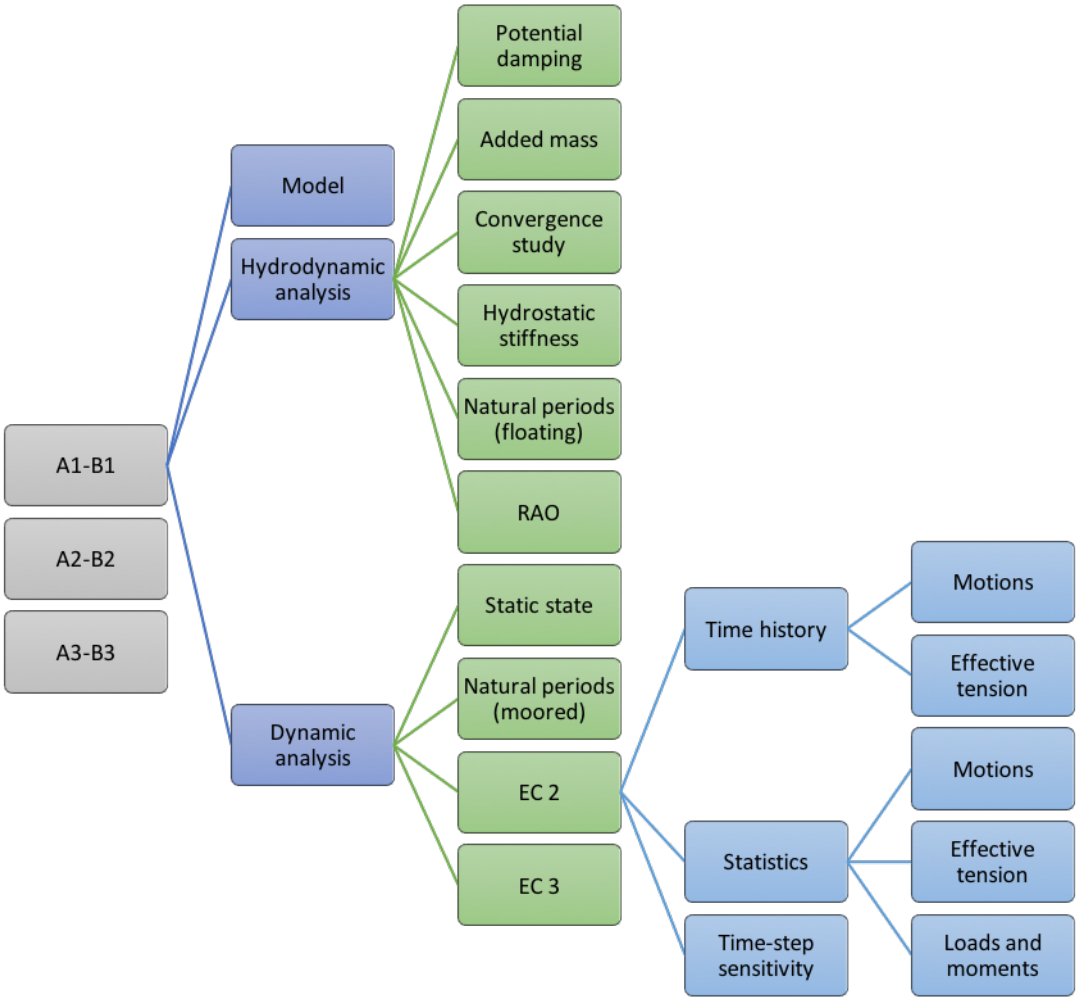

Figure 12-1: Structure of results chapter

An overview of the different cases, with reference to structural and inertial properties, is presented prior to the presentation of the results. As can be observed from the figure above, time histories are provided here to illustrate the variation with time. For further case-by-case comparison, statistical data in the form of standard deviations and average values are provided, forming the basis for the discussion chapter following these results.

[14] This approach has been selected as the main interest in this work is to compare the three cases, and the case-by-case presentation of results makes such a case comparison somewhat inefficient if it were to be conducted in the results chapter.

12.1 Overview of inputs/case

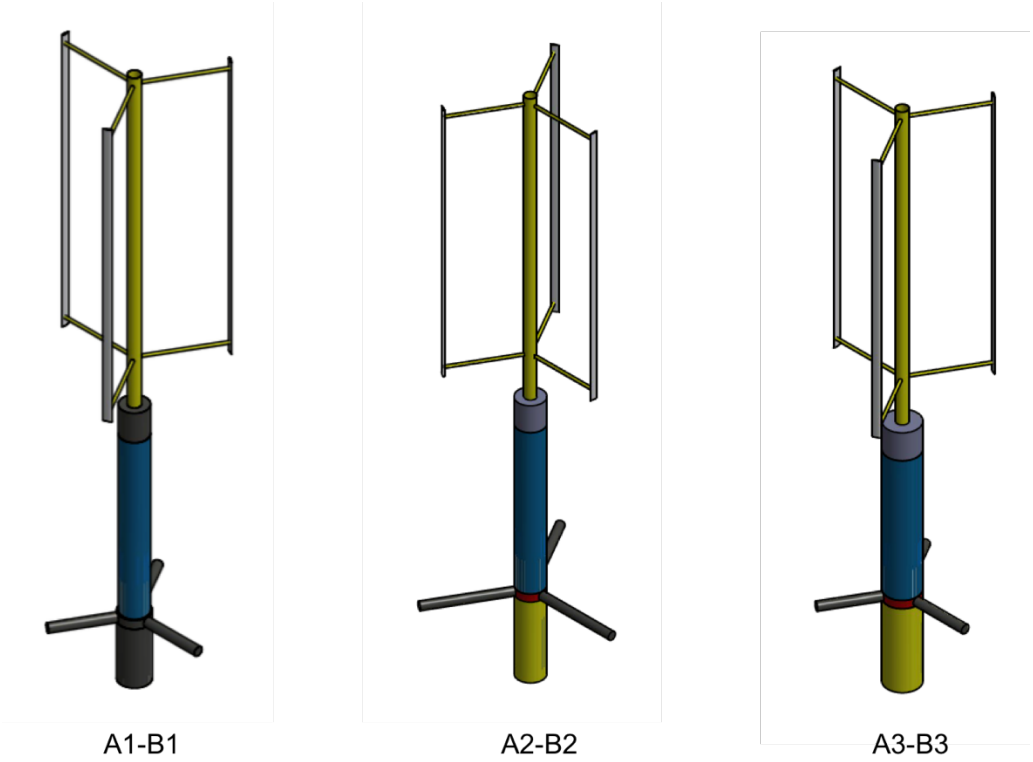

Figure 12-2: 3-D views of the three model cases

The figure above shows the three selected cases in 3-D view exported from Autodesk Inventor. Structural data, inertial properties, and stability properties are presented below for the three cases illustrated in Figure 12-2. For more detailed data, refer to Appendix B.

The following tables provide information about the various cases to be analysed in HydroD and OrcaFlex. The data is presented here for ease of reference. The external structural data table presented below shows the total height of the floating structure with reference to the outer diameters, heights and lengths that define the model cases.

Table 12-1: External structural data

Case ID	Total height	Section A		Section B		
		OD	H	BM OD	BM H	PO L
A1-B1	93	9	70	10	20	20
A2-B2	103	10	70	10	30	30
A3-B3	93	12	60	12	30	20
Units	m	m	m	m	m	m

Table 12-2 shows the inertial properties of the vessel with temporary ballast included. The data provided are used for the hydrodynamic modelling process to determine the damping and added mass values, as well as displacement and load RAOs. The moments of inertia (I) and radii of gyration (R) are defined about the principal axes of the structure as determined in Autodesk Inventor. Note that this corresponds to the centre of gravity of the mated structure.

Table 12-2: Inertial properties with temporary ballast

Case ID	Total mass	KG	I1 & I2	I3	R1 & R2	R3
A1-B1	6.195E6	33.05	8.44E9	2.40E8	36.93	6.22
A2-B2	8.134E6	39.16	10.31E9	3.96E8	35.59	6.99
A3-B3	1.005E7	33.76	9.88E9	3.63E8	31.34	6.01
Units	kg	m	$kg \cdot m^2$	$kg \cdot m^2$	m	m

Table 12-3 shows the inertial properties of the vessel without temporary ballast. The data provided in this table are of particular relevance to the dynamic simulation section as the un-ballasted condition is used in OrcaFlex to generate the required pre-tension in the tendons. Note that the centre of gravity with respect to keel is specified for the un-ballasted state.

Table 12-3: Inertial properties without temporary ballast

Case ID	Total mass	KG	I1 & I2	I3	R1 & R2	R3	T*
A1-B1	4.580E6	37.51	7.718E9	2.212E8	41.05	6.95	5.27
A2-B2	5.871E6	42.14	9.124E9	3.691E8	39.42	7.93	7.44
A3-B3	7.018E6	38.01	8.568E9	3.091E8	34.94	6.64	9.96
Units	kg	m	$kg \cdot m^2$	$kg \cdot m^2$	m	m	MN

*Tension is specified for each tendon, for total tension the value presented in the table above must be multiplied by three (number of tendons).

The table below presents the stability properties of the ballasted structure, with reference to total displacement, centre of buoyancy and metacentric height. Note that the centre of buoyancy and total displacement are also valid for the structure in the un-ballasted condition when the tendons are attached.

Table 12-4: Stability properties in temporary ballasted condition

Case ID	∇	KB	GM
A1-B1	6 047	38.40	5.35
A2-B2	7 939	45.32	6.16
A3-B3	9 811	41.06	7.30
Units	m^3	m	m

Additional data such as added mass, damping, RAOs and hydrostatic stiffness are provided under each respective case, as part of the hydrodynamic analysis section for each case. Comparisons of the hydrodynamic properties across each of the three cases are presented in Section 13.1.5.

12.2 Case A1-B1

12.2.1 Model

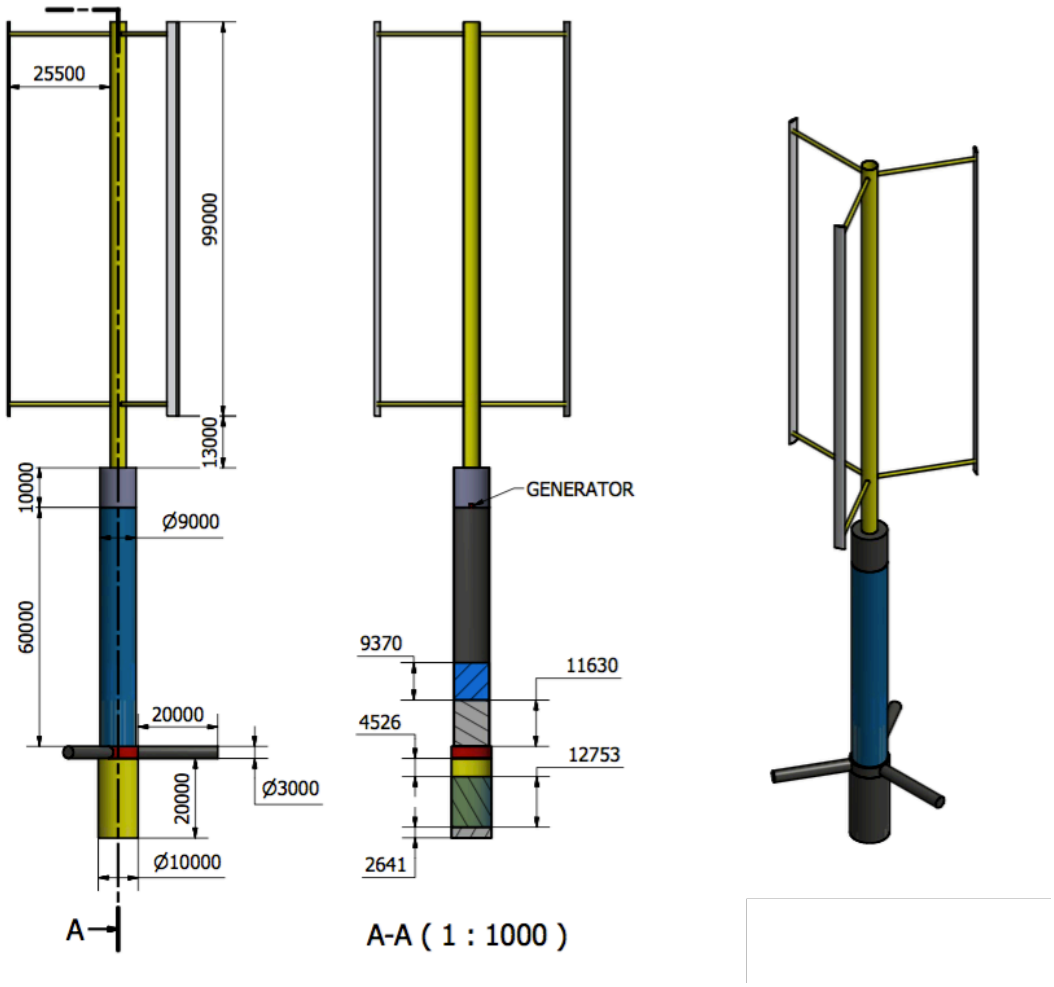

Figure 12-3: Model dimensions illustrated for A1-B1

12.2.2 Hydrodynamic analysis

12.2.2.1 Mass model

Table 12-5: Mass model A1-B1

Property	Value	Property	Value	Property	Value
Total mass [kg]	6.195E6	Buoyancy vol. [m^3]	6047		
COG X [m]	0	COG Y [m]	0	COG Z [m]	-49.95
COB X [m]	0	COB Y [m]	0	COB Z [m]	-44.60
RX [m]	36.93	RY [m]	36.93	RZ [m]	6.22

The table above presents the specified mass model in HydroD. The total mass has been presented with more significant figures here in order to keep the error margin as low as possible when computing the hydrodynamic coefficients. This number is based on the generated Inventor model, with high accuracy specified for the computation of the inertial properties of the total system with temporary ballast. See appendix for details regarding the physical properties generated in Autodesk Inventor.

12.2.2.2 Mesh models

The figure below presents the assigned mesh properties for A1-B1-Ms(1-4).

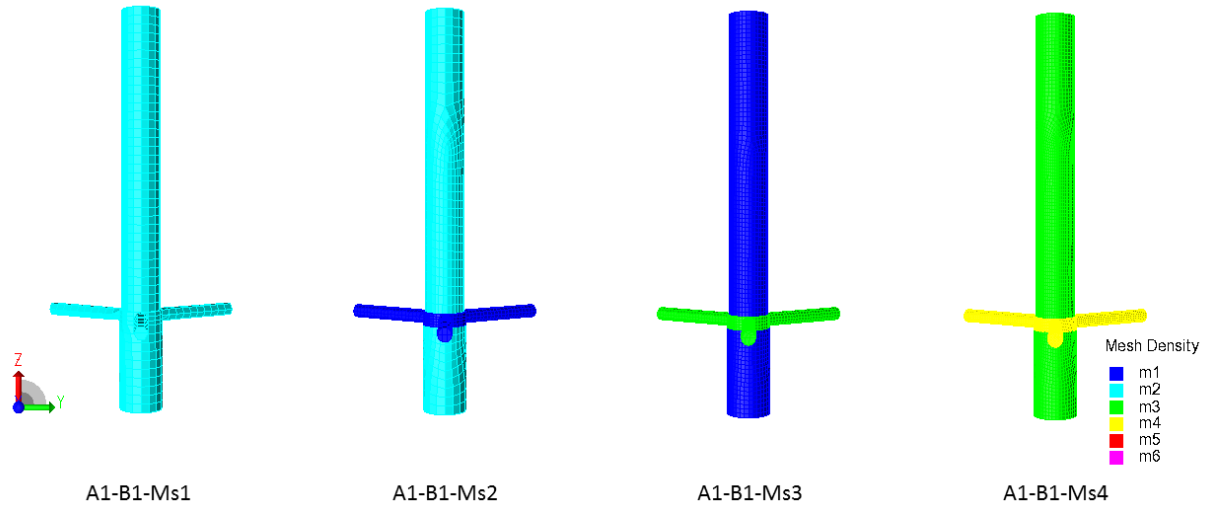

Figure 12-4: Mesh refinements for convergence study A1-B1

The four main steps in the mesh refinement process for A1-B1 are presented in the figure above. Due to an issue occurring in the potential damping in yaw (D66) for A1-B1-Ms2, three additional mesh models were generated. These are presented in the figure below. However, only plots for damping in yaw (D66) were generated for these mesh models, and these figures can be found in Appendix C.

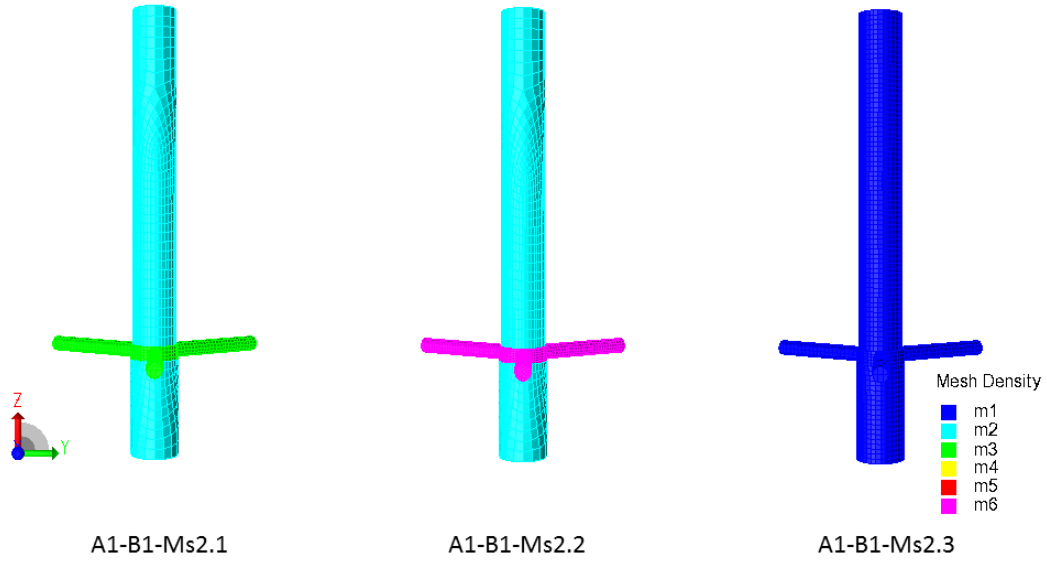

Figure 12-5: Mesh refinements of A1-B1-Ms2

The associated number of nodes and elements for each of these mesh settings are presented in the table below.

Table 12-6: A1-B1 Mesh properties and computed values

Case	Nodes	Elements	*t*	ΔZ	*d*	Computed GM	Δ GM	A W_{PL}	RUN
A1-B1-Ms1	1051	1064	38	3.39	86.39	7.14	1.79	62.0	YES
A1-B1-Ms2	2055	2072	102	1.49	84.49	6.11	0.76	62.0	YES
A1-B1-Ms2.1*	2618	2635	155	1.18	84.18	5.96	0.61	62.0	YES
A1-B1-Ms2.2*	3361	3384	279	0.97	83.97	5.84	0.49	62.0	YES
A1-B1-Ms2.3*	3795	3811	342	1.01	84.01	5.93	0.58	63.1	YES
A1-B1-Ms3	4450	4468	479	0.74	83.74	5.77	0.42	63.2	YES
A1-B1-Ms4	9287	9311	20597	0.22	83.22	5.51	0.16	63.3	ERROR
Units	–	–	s	m	m	m	m	m^2	–

Where *t* is the associated computing time in WADAM. ΔZ is the change in z-water line (positive values indicates decreased freeboard), *d* is the computed draft, computed $\overline{GM}$ is the metacentric height for the given floater calculated by HydroD, $\Delta\overline{GM}$ is the difference between the established $\overline{GM}$ from manual calculation and the computed $\overline{GM}$. "A W_{PL}" is the water plane area.

As can be observed from the table above, the difference in number elements between two subsequent mesh models in the original mesh setup equates to a factor of 2, i.e. the number of elements in Ms3 is double that of Ms2 (excluding mesh models 2.1, 2.2 and 2.3). The first mesh settings with elements ranging between 1064 and 4468 ran without issues in HydroD. Ms4 resulted in an error, which means that the number of elements were most likely too large, or caused by an unknown error.

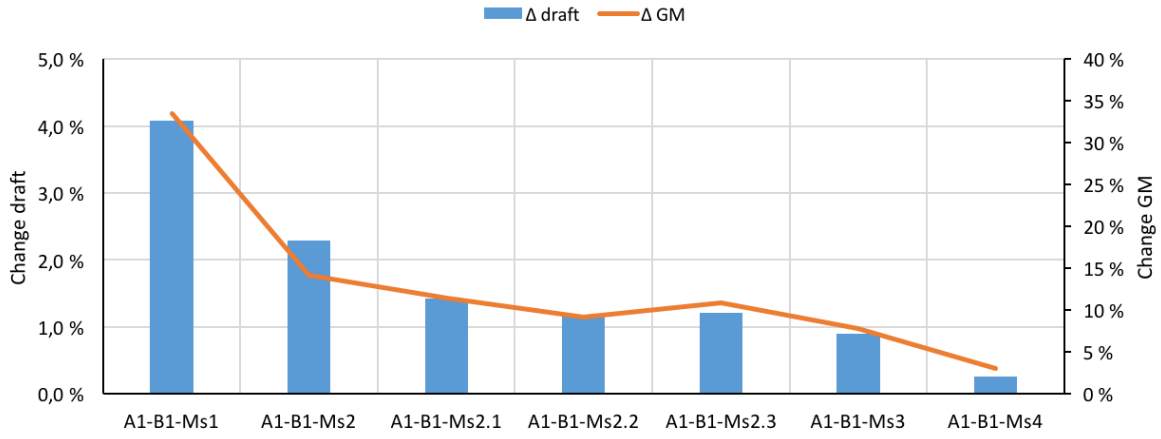

Figure 12-6: Percentage change in draft and GM relative to estimate A1-B1

The figure above shows the percentage change in draft and $\overline{GM}$ relative to the estimated values based on spreadsheet calculations for case A1-B1. As can be observed from this figure, the change in draft and change in $\overline{GM}$ decreases with increase in mesh refinement, as is expected since the mesh model gradually approaches the theoretical shape of the structure.

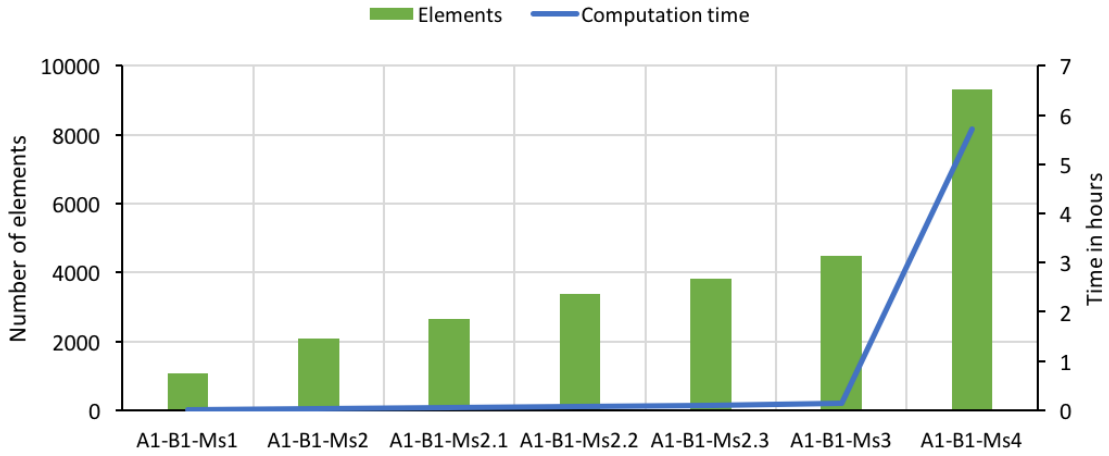

Figure 12-7: Computation time and number of elements A1-B1

The figure above shows the computation time vs number of elements for each of the mesh settings analysed for case A1-B1. As can be observed, the number of elements follow a gradual increase in value with each step in the mesh refinement process, except for Ms4 where a significant increase in number of elements is observed. The computation time does not seem to increase significantly for elements below 4500 but a significant peak is observed for Ms4.

Note that cases A1-B1-Ms2.1-3 were run as an additional set of cases to observe the effect of a slight increase in mesh refinement to verify whether or not the mesh setting Ms2 was an error in the system when calculating the potential damping in D66 (Section 12.2.2.3). A1-B1-Ms2.1 featured m2 density at the same location as A1-B1-

Ms2, with the only exception being a refined mesh on the pontoons and central column corresponding to mesh identity m3. A1-B1-Ms2.2 features the same main column mesh but a further refinement of pontoon and CC mesh to m6 density. A1-B1-Ms2.3 featured a uniform mesh density across the structure corresponding to m1. The potential damping in 66 for cases designated with * are found in Appendix C.

12.2.2.3 Frequency dependent potential damping

The following figures present the frequency dependent potential damping for 11, 33, 55, 66, 24 and 51.

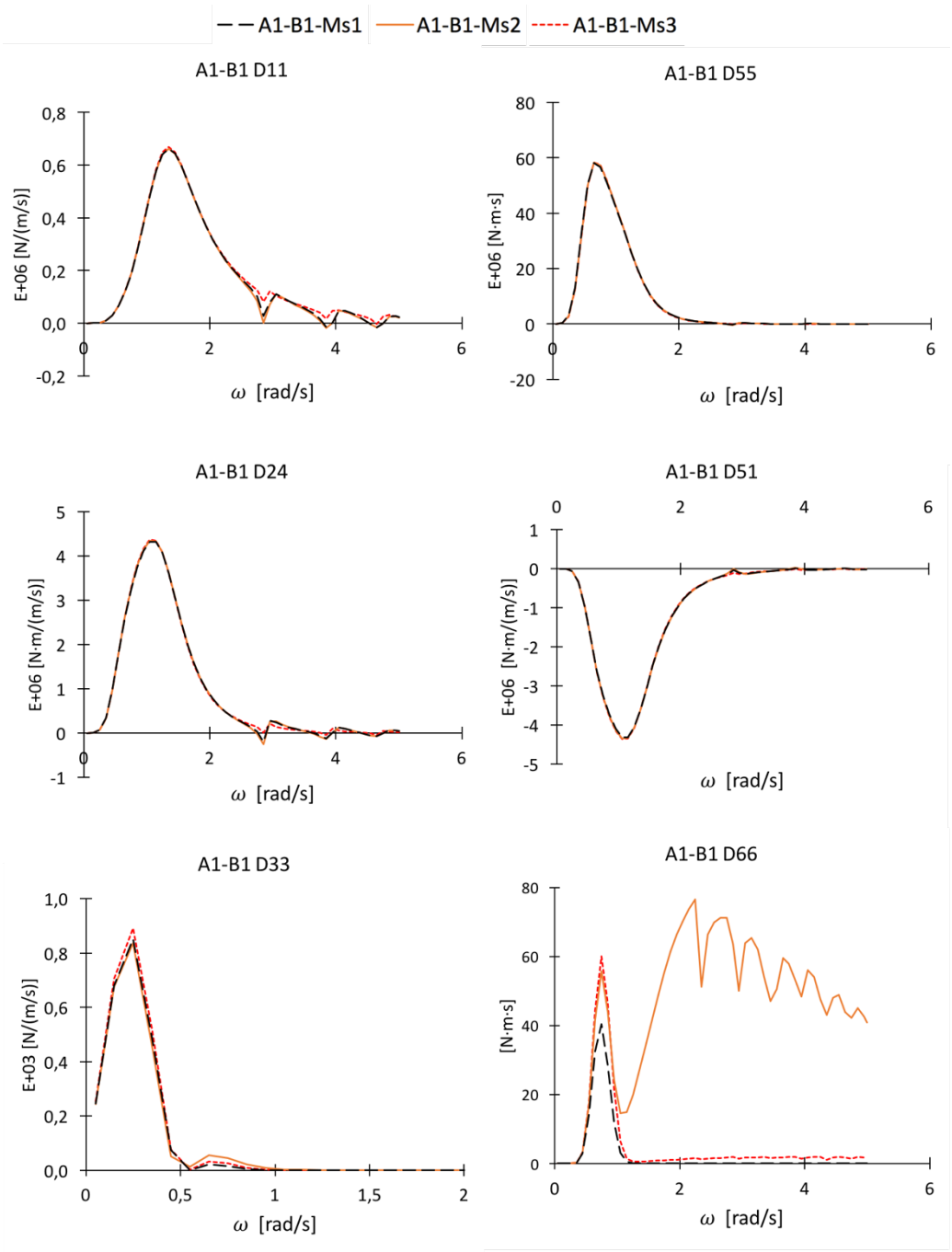

Figure 12-8: Frequency dependent potential damping A1-B1

As can be observed from the frequency dependent potential damping in 66 there seems to be some erratic results associated with mesh setting 2. As previously stated, several slight refinements of the mesh were carried out to determine if the results in potential damping for D66 occurred due to a numerical error. It was initially believed to be a numerical error as the values are in the order of 1E-06 compared to the values in most of the other degrees of freedom. After testing the three refinements of the mesh with somewhat similar number of nodes and elements, it was found that the difference in the potential damping in D66 was due to a numerical error. See the Appendix C.

12.2.2.4 Frequency dependent added mass

The following figures present the frequency dependent added mass for A11, A33, A55, A66, A24 and A51.

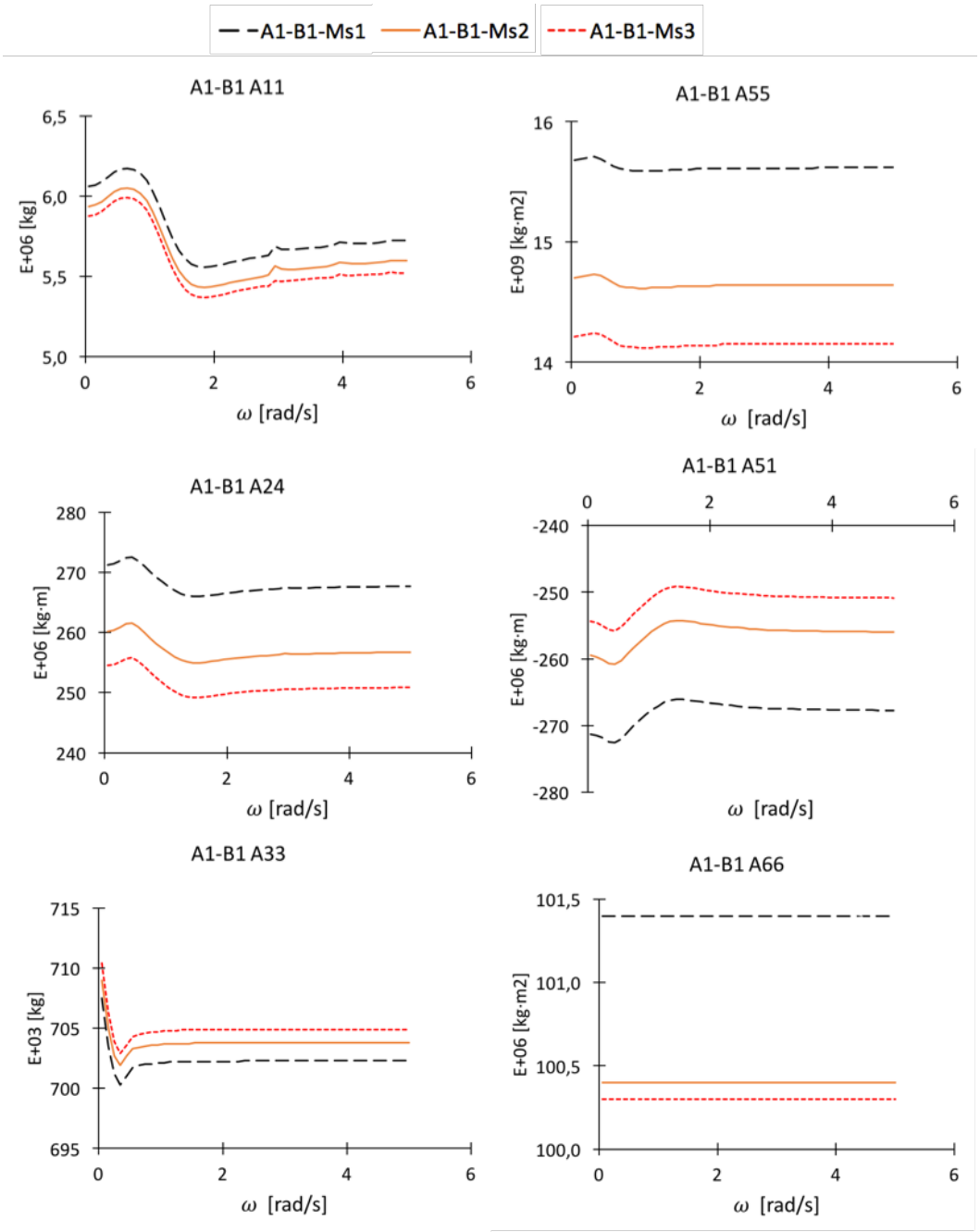

Figure 12-9: Frequency dependent added mass A1-B1

Note that there is a variation in the axes for these graphs, where the added mass in for example A55 is given in terms of E+09. The general observation from these results are that there is relatively little difference between the three mesh cases for the obtained results in added mass. The differences are only apparent by adjustment of the y-axis to reflect the values between a relatively small range. It is thus concluded that the three mesh settings yield fairly accurate results for the added mass. The largest variation between mesh setting 1 and 3 was found for A55, but the differences between mesh setting 2 and 3 were within reason for convergence.

12.2.2.5 Convergence and selection of results

As can be observed from the figures on frequency dependent damping and added mass, it was found that mesh setting Ms3 was sufficiently refined for the solution to converge. This is particularly evident for the potential damping values as the difference between the three mesh settings were relatively small. The only observable change was the irregularities occurring at higher frequencies, which tended to become less pronounced with increasing fineness of the mesh. The differences between the frequency dependent added masses are relatively small across all the degrees of freedom.

Referring to Figure 12-8 the potential damping in D66 (yaw) exhibited some erratic values for mesh setting 2. The values for mesh settings 1 and 3 seemed to coincide, which may indicate that there is a problem with mesh setting 2 in HydroD (refer to Appendix C). The solutions for potential damping in the other degrees of freedom seemed to follow the expected values, since the curves more or less coincide. The values in 66 are however relatively insignificant compared to the damping in the other degrees of freedom. It is therefore assumed that the values are representative of the actual structure and will be deemed useable for the dynamic simulation stage.

The RAOs are exported from the model featuring mesh setting 3 (Ms3), as this is the converged solution, with the finest mesh out of the three main runnable settings. This mesh setting was also selected because of the lower loss in draft due to change in the Z-water line as indicated in Table 12-6.

12.2.2.6 Hydrostatic stiffness matrix

The following hydrostatic stiffness matrix is exported from HydroD for case A1-B1-Ms3.

$$\mathbf{C}_{\mathrm{A1-B1}} = \begin{bmatrix} 0 & 0 & 0 & 0 & 0 & 0 \\ 0 & 0 & 0 & 0 & 0 & 0 \\ 0 & 0 & 6.35 \cdot 10^{5} & 4.41 \cdot 10^{2} & 2.34 \cdot 10^{1} & 0 \\ 0 & 0 & 4.41 \cdot 10^{2} & 3.51 \cdot 10^{8} & -2.52 \cdot 10^{2} & 4.85 \cdot 10^{3} \\ 0 & 0 & 2.34 \cdot 10^{1} & -2.52 \cdot 10^{2} & 6.42 \cdot 10^{8} & -2.89 \cdot 10^{3} \\ 0 & 0 & 0 & 0 & 0 & 0 \end{bmatrix}$$

As can be observed from the matrix above, there is a concentration of larger values along the diagonal of the matrix where the orders of magnitude range between 10^5 and 10^8. The matrix is mostly symmetric with smaller values occurring off the diagonal, as is expected from theory. However, there are two relatively large values (order 10^3) observed in the sixth column, which were initially expected to be zero based on the aforementioned theory. In addition to this, these values also violate the symmetric property of the hydrostatic stiffness matrix. However, these values are believed to occur due to a slight offset in COB_X, COB_Y, COG_X, and COG_Y observed in the WADAM.LIS file associated with this model. If one observes the magnitude of the shift in COB_Y and COG_Y, amounting to $1.7 \cdot 10^{-4}$ and $-2 \cdot 10^{-11}$ m respectively, which equates to a fraction of a millimetre, the hydrostatic stiffness matrix can give readings of magnitude in the range of 10^3 N·m. The significance of this is that a shift in position of the centre of gravity by less than a millimetre will result in a non-zero value in column 6 of the hydrostatic stiffness matrix. In conclusion the hydrostatic stiffness is sufficient for use as OrcaFlex only requires information about the matrix values in columns 3-5 and rows 3-5.

The hydrostatic stiffness is, as previously mentioned under the background theory section, insignificant relative to the restoring stiffness contribution from the mooring system and the relatively small values observed in the off-diagonal points should not have a significant effect on the results as a whole.

12.2.2.7 Natural periods

The natural periods for the floating system, as determined in HydroD, is presented in the table below (A1-B1-Ms3).

Table 12-7: Natural periods A1-B1 in floating condition

Degree of freedom	Natural period [s]	Natural frequency [rad/s]	Degree of freedom	Natural period [s]	Natural frequency [rad/s]
Surge	∞	0	Roll	36.55	0.172
Sway	∞	0	Pitch	36.55	0.172
Heave	20.71	0.303	Yaw	∞	0

As one can observe the natural period in surge, sway, and yaw is infinite; as there is no hydrostatic stiffness in these degrees of freedom.

12.2.2.8 Displacement RAOs

The displacement RAOs are defined for angular frequencies corresponding to periods ranging between 0.5 and 24 seconds. The displacement RAOs were exported, from the HydroD POSTRESP software, and plotted in Excel as presented below. Note that the displacement RAOs are defined with respect to the centre line of the vessel at sea level.

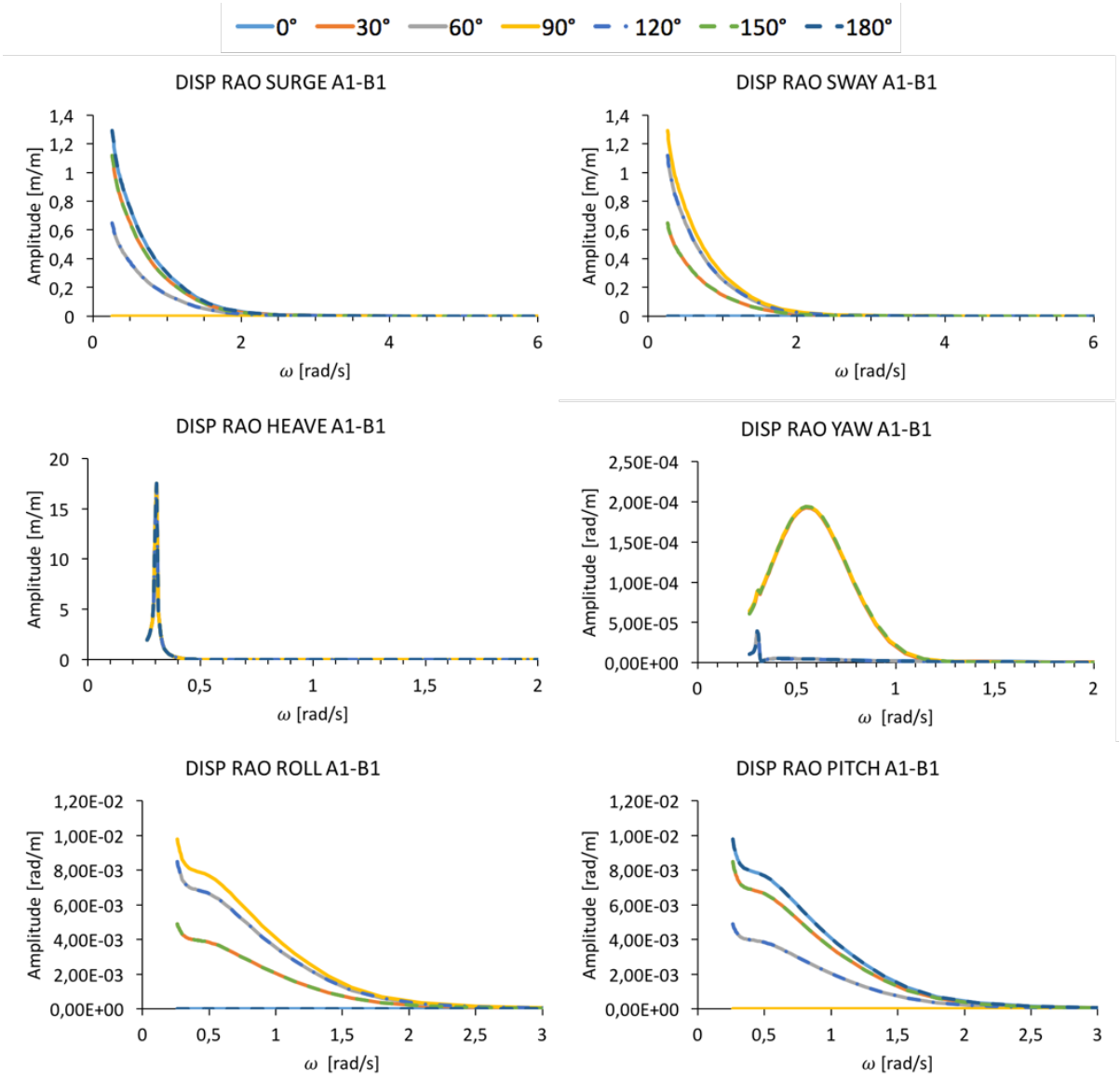

Figure 12-10: Displacement RAOs for A1-B1

The displacement RAOs are given for each of the 7 directions analysed in HydroD. The surge and sway displacement RAOs are equal in magnitude but vary with direction, as can be observed for surge, where 0 and 180° yield the largest amplitudes. This is expected, since the wave direction coincides with the direction of movement defined by this degree of freedom. Sway sees its maximum value at 90°, which is expected for the same reasons as discussed for surge. As can be observed for heave, the displacement RAO is independent of direction, which follows the expectation, since heave is a vertical motion. Roll and pitch are also equal in magnitude but follow the same dependence on direction as surge and sway. The displacement RAO for yaw sees its maximum value for 30 and 150° directions. In general, the displacement RAOs tend to have maximum values centred around the lower frequencies, corresponding to the longer periods, as is expected from the natural periods in the respective degrees of freedom presented earlier. Since the structure is symmetric about the XZ plane, it is sufficient to only analyse the directions ranging between 0 and 180°.

12.2.2.9 Load RAOs

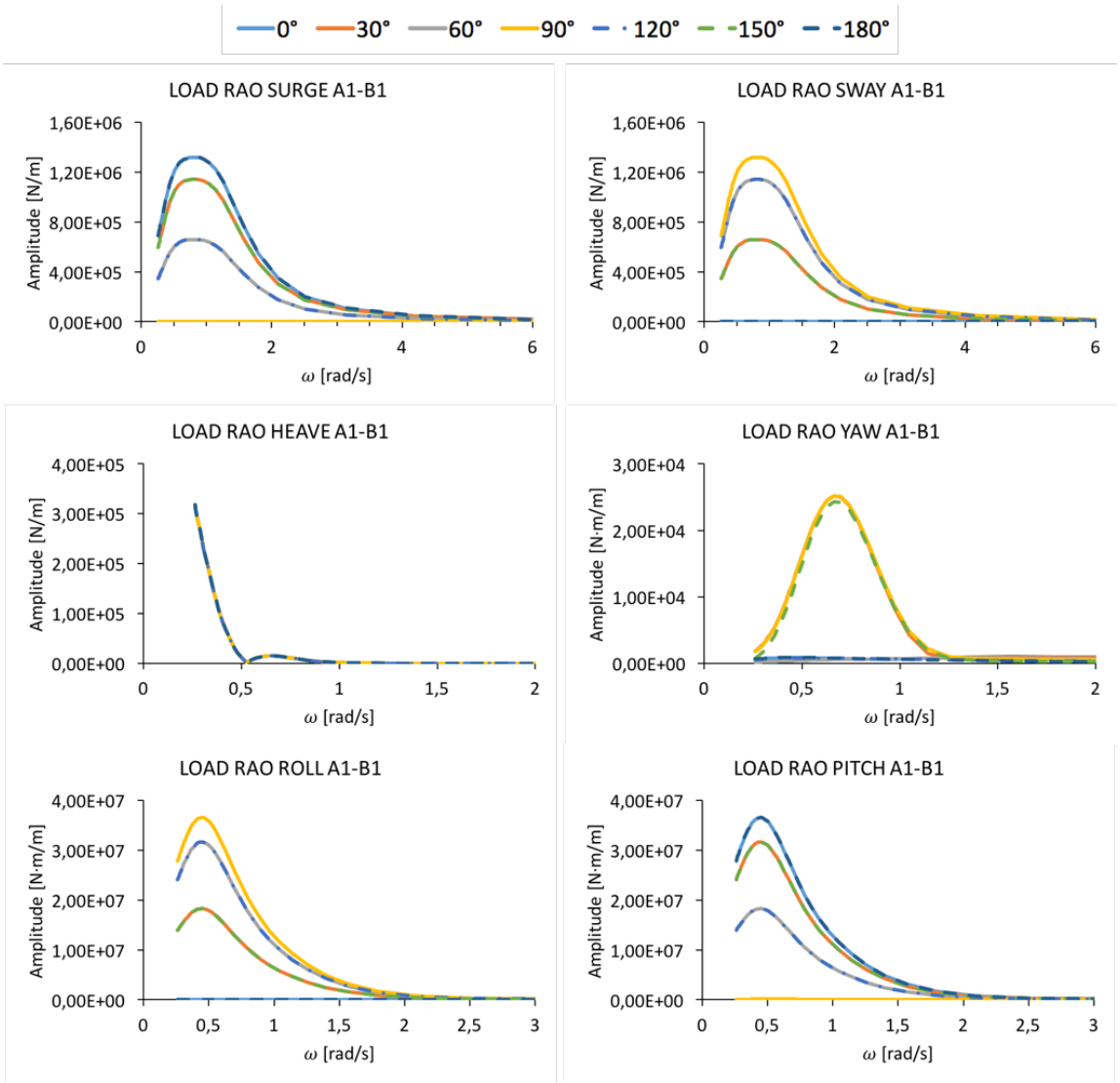

Figure 12-11: Load RAOs for A1-B1

As can be observed from the figure above, the same trends in direction dependence are observed for the displacement RAOs in surge and sway. This is as expected based on the definition of the coordinate system of these two degrees of freedom. This is also similar for roll and pitch. The largest values for the load RAOs were found for roll and pitch followed by the two translational motions surge and sway. The load RAO in heave also gave a significant magnitude, similar to that of surge and sway. The lowest magnitude was observed for yaw, which is expected based on the dimension of the pontoons and their depth relative to the RAO origin at the still water line.

From the load RAO in yaw it is clear that there is little effect for the 0°, 60°, 120° and 180° wave headings. This is reasonable as the vessel is symmetric in the vertical planes following these directions. This implies that the there is no net moment about the vessels centreline for these headings, as an incident wave will excite both sides of this plane equally. Directions of 60° and 180° refer to incident waves acting parallel to one of the extruded pontoons with the wave propagating towards the central column. The other two directions represent the intersection between two adjacent pontoons.

12.2.3 Dynamic simulation

12.2.3.1 Tendon properties and arrangement

The tendon properties used for this case in OrcaFlex are presented in the tables below. The initial lengths are determined based on the predefined freeboard (10 m) and draft of Section A, for the specific case. The submerged depth of the structure is 83 m, based on the output from spreadsheet calculations.

Table 12-8: Tendon properties and arrangement A1-B1

Tendon	Line type	Section length	Segment length	End A			End B		
				R*	θ*	Z*	R**	θ**	Z**
1	Tendon_1m	138.50	0.5	25	0	-1.5	0	0	-138.50
2	Tendon_1m	138.50	0.5	25	120	-1.5	0	0	-138.50
3	Tendon_1m	138.50	0.5	25	240	-1.5	0	0	-138.50
Units	–	m	m	m	°	m	m	°	m
* Defined relative to vessel coordinates									
** Defined relative to End A coordinates (End A of the line)									

Note that the locations of End A and End B are given in polar coordinates.

12.2.3.2 Static results

Table 12-9: Output from the static state calculation A1-B1

	Value static state	Target	Difference
Vessel Z-position [m]	-59.97	-60.00	0.05 %
Pre-tension 1 [N]	5.28E6	5.28E6	0 %
Pre-tension 2 [N]	5.28E6	5.28E6	0 %
Pre-tension 3 [N]	5.28E6	5.28E6	0 %

The table above presents, for each variable, the calculated static value by OrcaFlex, the target value and the computed difference between the two. As can be observed from these results the static state is sufficiently close to the target values and a dynamic simulation of the given system is approved based on this correspondence. Note that the static values presented above exclude effects from externally applied loads.

The natural periods of the vessel in its six DOFs were determined using OrcaFlex Modal Analysis by identifying the mode shapes and associated periods, resulting in an amplitude of ± 1 in the respective degree of freedom. Note that the mode shapes are listed in decreasing order for periods, i.e. longer periods correspond to the primary mode shapes. The results are presented below.

Table 12-10: Natural periods for 6 DOFs A1-B1

Degree of freedom	Mode	Amplitude	Period [s]	Frequency [rad/s]
Surge (η_1)	1	1 m	40.73	0.154
Sway (η_2)	2	1 m	40.73	0.154
Heave (η_3)	24	1 m	0.625	10.053
Roll (η_4)	10	-1 deg	2.13	2.950
Pitch (η_5)	11	1 deg	2.13	2.950
Yaw (η_6)	3	1 deg	14.29	0.440

Note that the natural periods for the different mode shapes of tendons are not to be analysed as part of this system, as this exceeds the scope of work. The roll amplitude, when determining the natural periods from the modal analysis, yielded a negative angle, which is assumed valid due to symmetry. As expected the natural period in roll and pitch are identical. If one observes the amplitudes presented above, roll yields a negative value and pitch a positive value. This backs up the previous assumption that the periods are identical for ± amplitudes in a certain degree of freedom (as long as the vessel is symmetric).

12.2.3.3 Results EC2

Table 12-11: Input information A1-B1 EC2

	Value	Location relative to local axis
Applied load	365 kN	132.5 m
Applied torque	1800 kNm	60 m
JONSWAP (H_s, T_p, γ)	(3.10 m, 10.1 s, 3.3)	NA
Water depth	200 m	NA
Simulation duration	3600 s	NA

The time histories for surge, heave, pitch, and yaw are presented in the figures below.

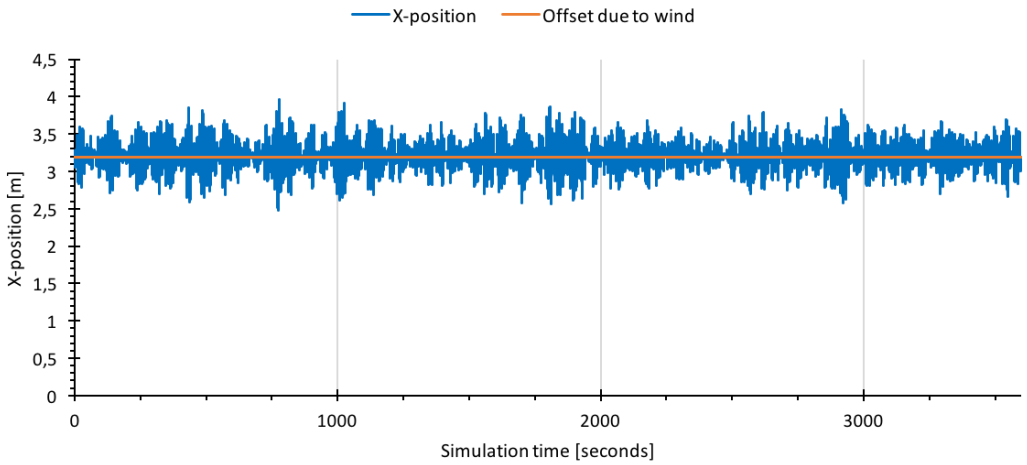

Figure 12-12: Time history surge (0, 0, 60 m) A1-B1-EC2-T0.05

As can be observed from the figure above, the mean position of the vessel in surge corresponds to the static offset due to wind. The variation is limited to around ± 1 m, which is reasonably small considering a depth of 200 m.

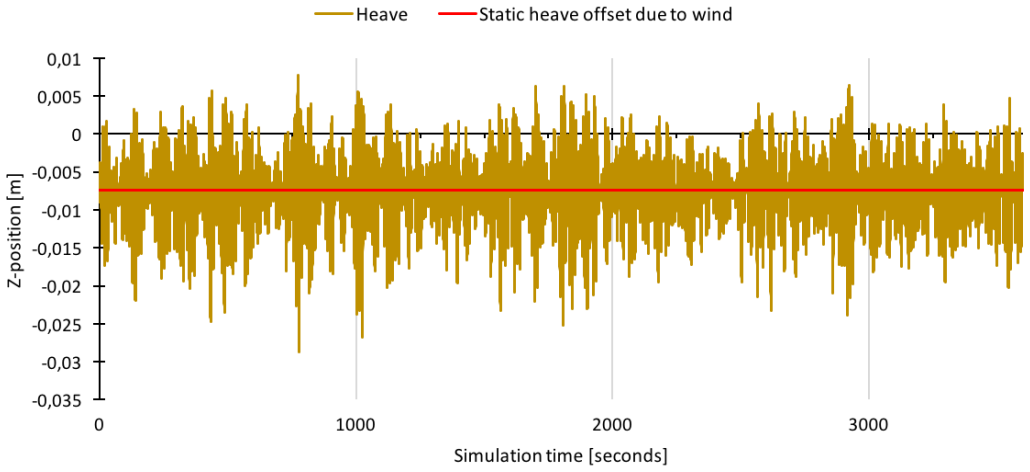

Figure 12-13: Time history heave (0, 0, 60 m) A1-B1-EC2-T0.05

The time history in heave oscillates around the static heave offset due to wind. Note that this offset is largely due to the set-down effect in the static state. The point of reference is specified at the initial water line, i.e. 60 m above the local axis coordinate system. This corresponds to the draft of section A. For this reason, the time history in heave is also to some degree affected by the pitching angle, although this is sufficiently small here and should not have a significant effect on the overall result. Another observation, for this time history, is that the deviations below the static offset tend to be slightly larger than the vertical motions upward.

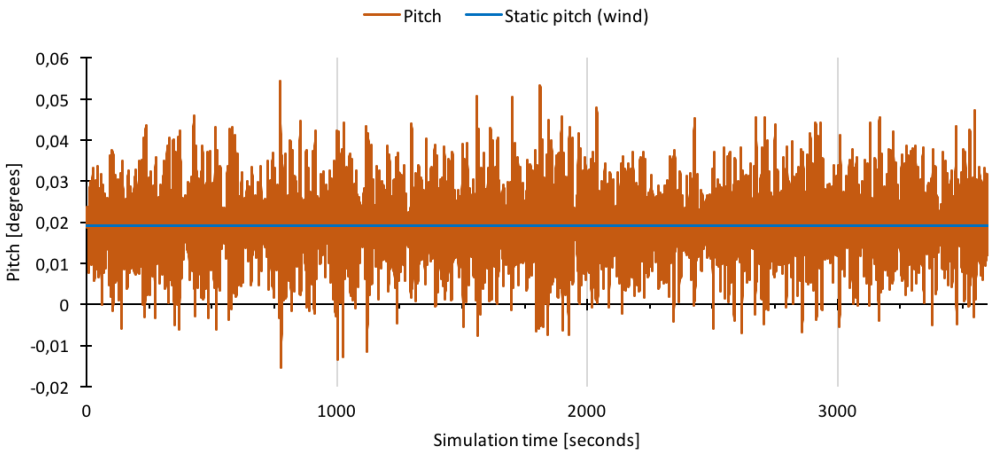

Figure 12-14: Time history pitch (0, 0, 0 m) A1-B1-EC2-T0.05

The time history in pitch is presented relative to the origin of the vessel. Here the values also tend to oscillate around the pitch angle induced by the statically applied wind. The range is limited to ±0.03 degrees relative to the mean position, which can be regarded as relatively small, and illustrates the restraint in pitch, inherent to this type of station keeping principle.

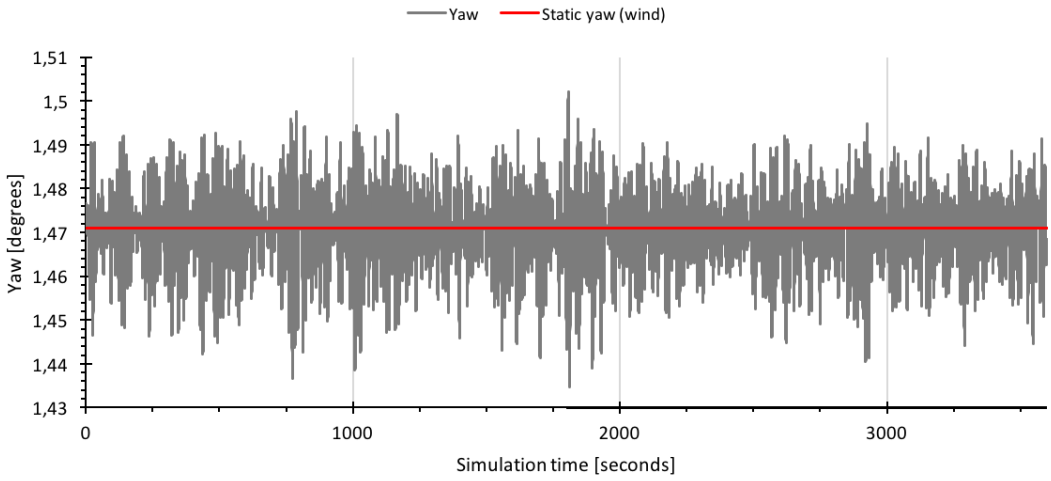

Figure 12-15: Time history pitch (0, 0, 0 m) A1-B1-EC2-T0.05

The yaw angle, similarly to the previously presented time histories, also tends to oscillate about the statically induced yaw angle by the input torque. The oscillations induced by the wave action, are relatively insignificant compared to the torque-induced angle, where variations are limited ± 0.03 degrees, which corresponds to 2% of the static angle. This is in line with what was observed from the RAOs in yaw, which featured small amplitudes due to incident waves (0° wave direction).

The figure below shows the time history for the effective tendons at End A (vessel connection).

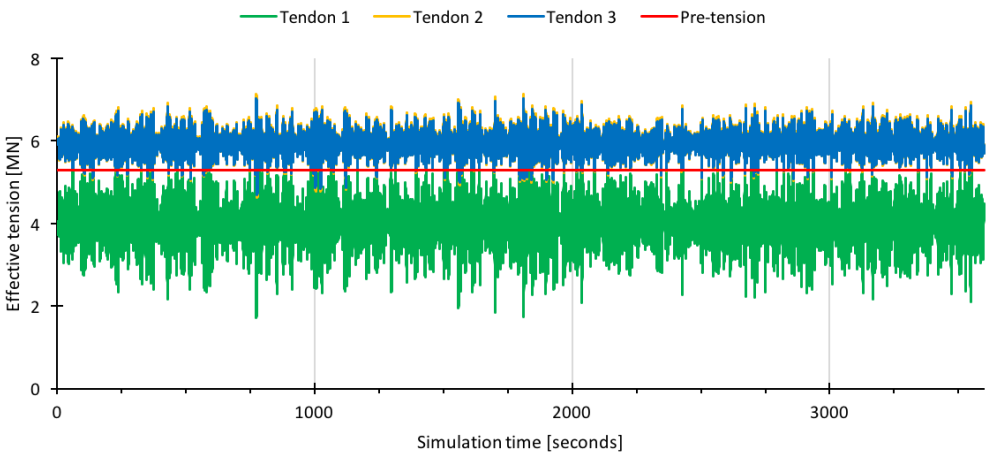

Figure 12-16: Time history effective tension A1-B1-EC2-T0.05

As can be observed from the time history of effective tension there is a significant variation in tension for the downwind tendon (Tendon 1), which may have implications for fatigue although this is not analysed in this thesis. As one would expect, the variation in tendon 2 and tendon 3 are not as severe compared to tendon 1, which is reasonable considering the fact that these two tendons are upwind and the total variation is divided on two tendons. One additional concern to be observed from this time history is that there is a significant initial loss in tension in tendon 1 associated with the statically applied wind load. The pre-tension line is presented in this figure for reference purposes. Tendon 2 and 3 obtain a mean tension larger than the initial pre-tension, which is reasonable considering the direction of wind and wave loading (0°).

The following table shows the statistical results obtained from the simulation for each of the result categories.

Table 12-12: Summary of statistical results for A1-B1-EC2-T0.05

Variable	Min.	Max.	μ	σ	Units
Motion					
Surge (0, 0, 60 m)	2.474	3.966	3.208	0.216	m
Heave (0, 0, 60 m)	-0.029	0.008	-0.008	0.005	m
Pitch (0, 0, 0 m)	-0.015	0.054	0.019	0.010	degrees
Yaw (0,0, 0 m)	1.435	1.502	1.470	0.010	degrees
Sea surface clearance (0, 0, 83 m)	19.81	25.65	22.98	0.77	m
Tendons					
Effective tension – tendon 1	1.72E+06	6.51E+06	4.00E+06	6.61E+05	N
Effective tension – tendon 2	4.62E+06	7.13E+06	5.95E+06	3.47E+05	N
Effective tension – tendon 3	4.70E+06	7.03E+06	5.93E+06	3.22E+05	N
Declination – tendon 1	178.24	178.99	178.64	0.11	degrees
Declination – tendon 2	178.68	179.16	178.91	0.07	degrees
Declination – tendon 3	178.22	178.71	178.45	0.07	degrees
Local axis dynamic loads and moments*					
Total Lx-force	-1.63E+06	1.54E+06	1.76E+02	4.20E+05	N
Total Lz-force	-2.69E+04	5.47E+04	6.32E+01	9.99E+03	N
Total Ly-moment	-2.33E+07	2.11E+07	2.44E+03	5.40E+06	Nm
Local axis static loads and moments**					
Total Lx-force	–	–	3.65E+05	1.62E+00	N
Total Lz-force	–	–	1.77E+07	–	N
Total Ly-moment	–	–	4.83+07	2.15E+02	Nm

* Only includes the dynamic results computed by OrcaFlex, i.e. the static loading is not included. This note is valid for all cases and environmental conditions in this analysis.

** The Lx-force and Ly-moment are obtained from the static load in OrcaFlex (wind load). The total Lz-force is obtained from the spreadsheet calculations, which is added to give an indication of the loading at the connection point between A1 and B1. This value represents the total load acting on the connection (i.e. tension capcity per

tendon multiplied by number of tendons). This note is valid for all cases and environmental conditions in this analysis.

12.2.3.4 Results EC3

Table 12-13: Input information A1-B1 EC3

	Value	Location relative to local axis
Applied load	1200 kN	132.5 m
Applied torque	0 kNm	60 m
JONSWAP (H_s, T_p, γ)	(12.70 m, 14.1 s, 3.3)	NA
Water depth	200 m	NA
Simulation duration	3600 s	NA

The time histories for surge, heave, pitch, yaw, and sea surface clearance relative to blades are presented in the figures below.

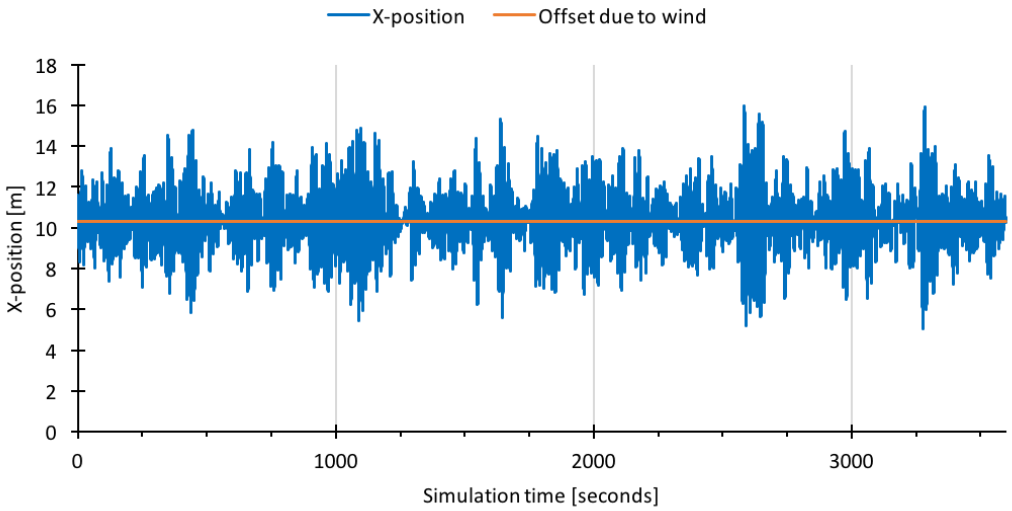

Figure 12-17: Time history surge (0, 0, 60 m) A1-B1-EC3-T0.05

The time history for surge in EC3, yields significantly larger variation in surge compared to EC2, as one would expect considering the severity of the sea state. The variation is limited to around ±5 m for the maximum values, but the variation seems to exhibit more erratic behaviour compared to EC2. Similarly to EC2, the mean position in surge corresponds to the static surge offset due to wind.

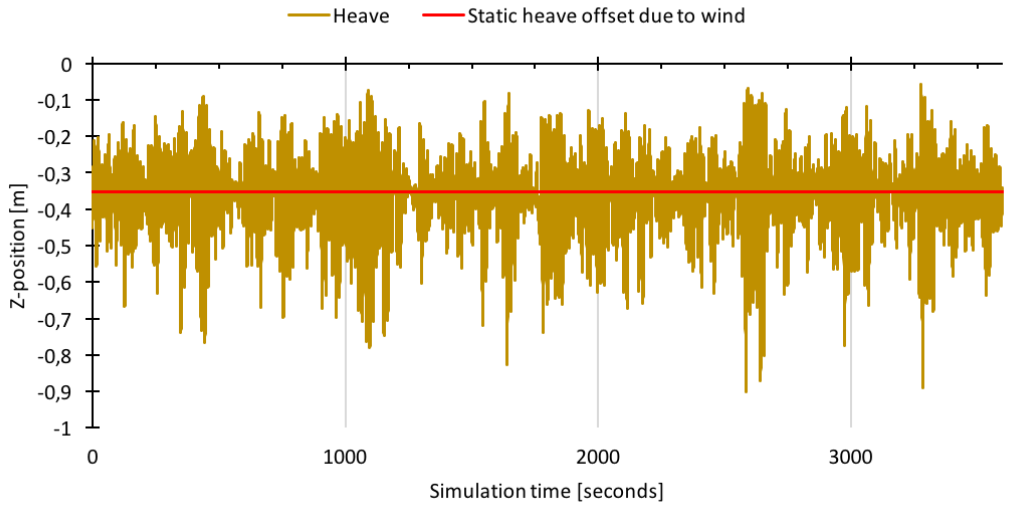

Figure 12-18: Time history heave (0, 0, 60 m) A1-B1-EC3-T0.05

In general terms the vessel experiences a significantly more severe motion in heave, than what was observed for the operational condition. It is worth noting that the heave motion here to some extent affected by the pitch motion, as this rotation was more severe in this sea state, with a probable cause being the increased load and overturning moment, which led to significant slack in the downwind tendon.

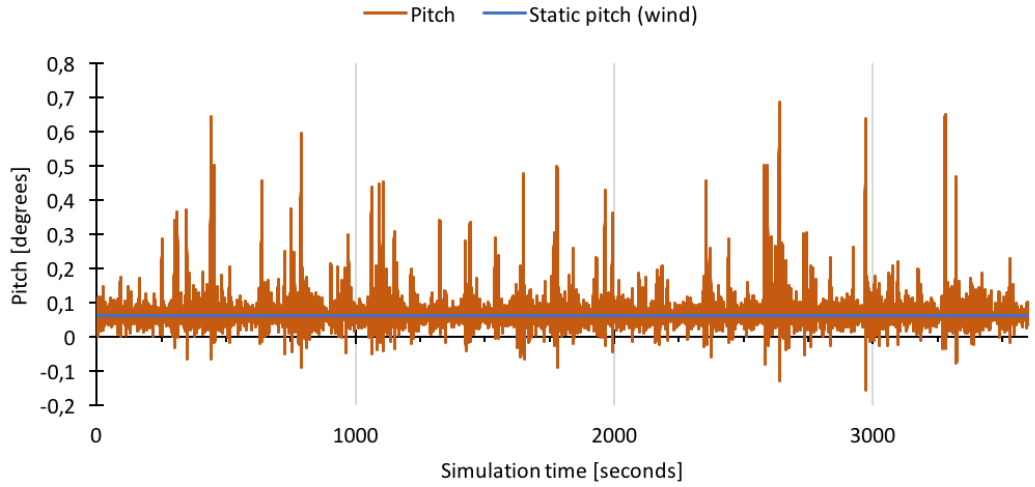

Figure 12-19: Time history pitch (0, 0, 0 m) A1-B1-EC3-T0.05

The pitch motion time history above, indicates that the vessel intermittently reaches relatively large pitch angles as can be observed from the large peaks throughout the simulation time. The effects are more pronounced for positive rotation (pitching with the waves) than for the negative rotation. This is obviously due to the fact that the wind and wave loads coincide, generating a larger pitching moment and subsequently forces the vessel to rotate significantly. The maximum peak results in a pitch rotation corresponding to a 736% increase relative to the mean position (induced by the wind only). This shows that the wave induces significant pitch moment for this vessel.

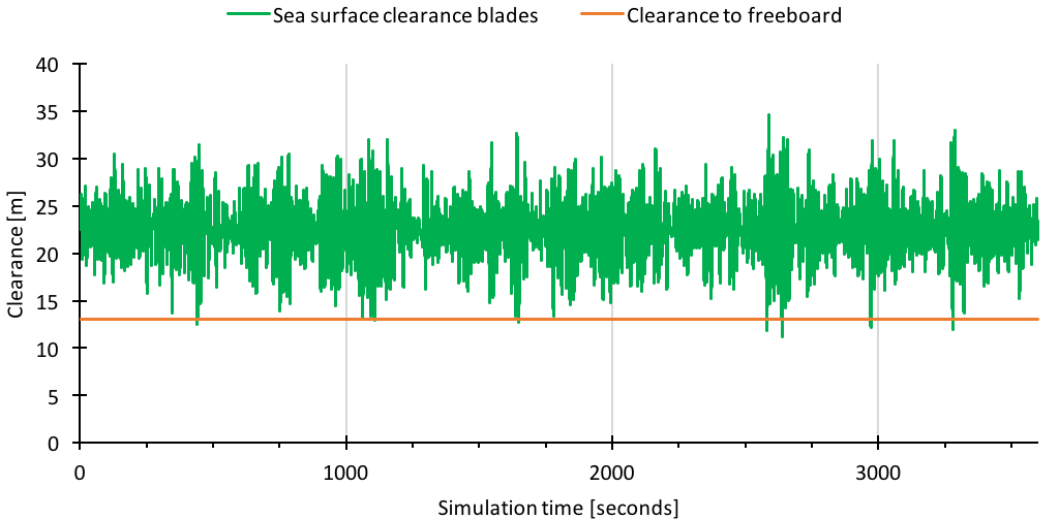

Figure 12-20: Time history sea surface clearance to bottom of blades A1-B1-EC3-T0.05

The figure above shows the sea surface clearance to the bottom of the blades and the clearance to freeboard. The sea surface clearance is an important aspect to consider, with particular focus on the air gap to the blades. As can be observed there is sufficient clearance to the turbine blades, where the lowest clearance is slightly lower than 13 m. Note that there are incidents in this simulation where the entire hull of the structure is submerged, i.e. zero freeboard. This may not necessarily be a threat to system as long as the hull-turbine shaft connection is watertight to avoid water ingress. The situation of loss of freeboard is not ideal, but as stated previously, the most critical aspect is that the blades come into contact with the water. Remediation of freeboard may be required.

The figure below shows the time history for the effective tendons at End A (vessel connection).

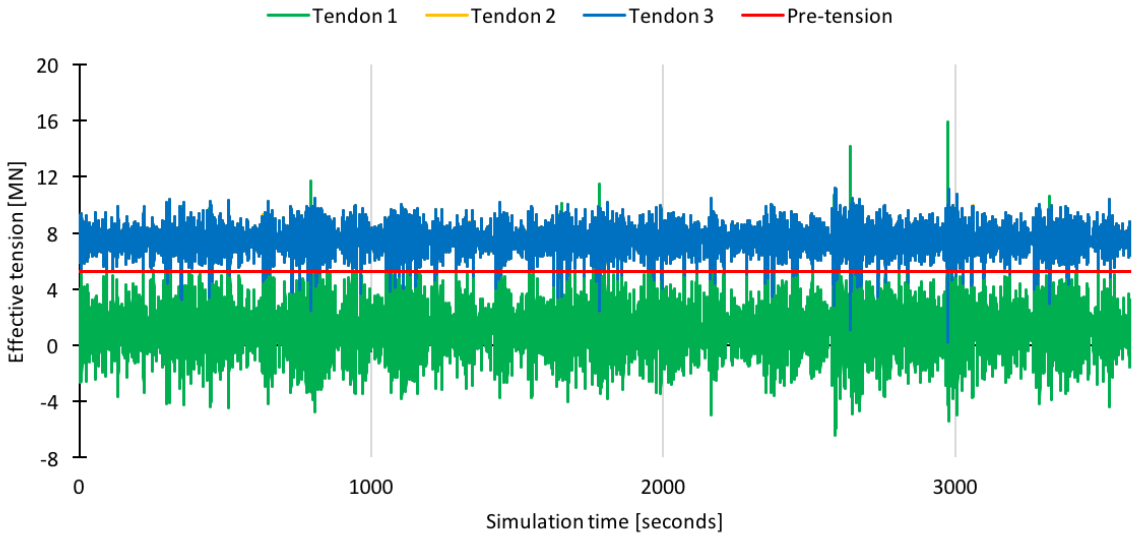

Figure 12-21: Time history effective tension A1-B1-EC3-T0.05

As can be observed from the time history presented above, Tendon 1 is slack for a significant portion of the simulation time. This is critical for the structure and cannot be accepted to the extent presented above. It is safe to conclude that A1-B1, in its current configuration, is not suitable for the survival of the studied storm condition. Note that there are four pronounced peaks in the tension of tendon 1, with varying magnitude. One of these resulted in a 16 MN tensile load at the connection, which seems to follow a time step in which there is significant loss of tension. This may be attributed to a snap load, where the tendon is suddenly loaded from its slack state. Also observe the significant reduction in tension for tendon 3 coinciding with the peak in tendon 1 near 3000 seconds.

The following table shows the statistical results obtained from the simulation for each of the result categories.

Table 12-14: Summary of statistical results for A1-B1-EC3-T0.05

Variable	Min.	Max.	μ	σ	Units
Motion					
Surge (0, 0, 60 m)	5.028	15.989	10.373	1.623	m
Heave (0, 0, 60 m)	-0.902	-0.058	-0.365	0.124	m
Pitch (0, 0, 0 m)	-0.156	0.686	0.082	0.059	degrees
Sea surface clearance (0, 0, 83 m)	11.16	34.60	22.52	3.24	m
Tendons					
Effective tension – tendon 1	-6.40E+06	1.59E+07	1.13E+06	1.92E+06	N
Effective tension – tendon 2	1.41E+05	1.12E+07	7.51E+06	9.97E+05	N
Effective tension – tendon 3	1.42E+05	1.12E+07	7.51E+06	9.97E+05	N
Declination – tendon 1	168.35	178.40	175.47	1.09	degrees
Declination – tendon 2	173.67	177.86	175.76	0.60	degrees
Declination – tendon 3	173.67	177.86	175.76	0.60	degrees
Local axis dynamic loads and moments					
Total Lx-force	-6.11E+06	6.09E+06	7.59E+02	1.66E+06	N
Total Lz-force	-1.06E+06	1.35E+06	5.35E+02	1.57E+05	N
Total Ly-moment	-2.83E+08	1.60E+08	9.52E+03	3.36E+07	Nm
Local axis static loads and moments					
Total Lx-force	–	–	1.20E+06	4.62E+00	N
Total Lz-force	–	–	1.77E+07	–	N
Total Ly-moment	–	–	1.59E+08	6.12E+02	Nm

The local axis static loads and moments do not have max and min values, as these are not varying loads. Note that some variation in the total Lx-force and Ly moment are present (as observed from the standard deviations) but these are negligible as one would expect for the static state.

12.2.3.5 Time step sensitivity

In order to verify if the time step is sufficiently small to produce accurate results it was, as previously mentioned, necessary to conduct a time step sensitivity analysis. The starting time step was set to the OrcaFlex standard value, corresponding to 0.1 seconds. To assess the effect of increasing the time step resolution, it was proposed to conduct a dynamic simulation for each environmental condition using a modified time step of 0.05 seconds, which corresponds to a halving of the OrcaFlex standard value. The selected variables for this sensitivity study include the mean and standard deviations in effective tension for all three tendons, and the primary degrees of freedom of the vessel (η_1, η_3, η_5). Yaw was not included because the time step sensitivity study was conducted for EC3 only. The results are presented with calculated differences in the table below.

Table 12-15: Time step sensitivity for T0.1 and T0.05 – A1-B1-EC3

Variable	Difference μ	Difference σ
η_1 [m]	-0.0025%	0.0473%
η_3 [m]	-0.0065%	0.0456%
η_5 [degrees]	-0.1250%	0.1154%
Effective tension T1	-0.0169%	1.1956%
Effective tension T2	0.0008%	1.1956%
Effective tension T3	0.0009%	1.2110%

As can be observed from the table above, there is relatively little difference between the results obtained for time step 0.1 and 0.05 seconds. Note that the difference between the time step is 50%, which is a significant refinement. The largest variation in results tend to fall under the standard deviation, however the maximum difference is 1.2110%, which is small enough to assume that the time step, 0.05, is sufficient for the accuracy in simulation results.

12.3 Case A2-B2

12.3.1 Model

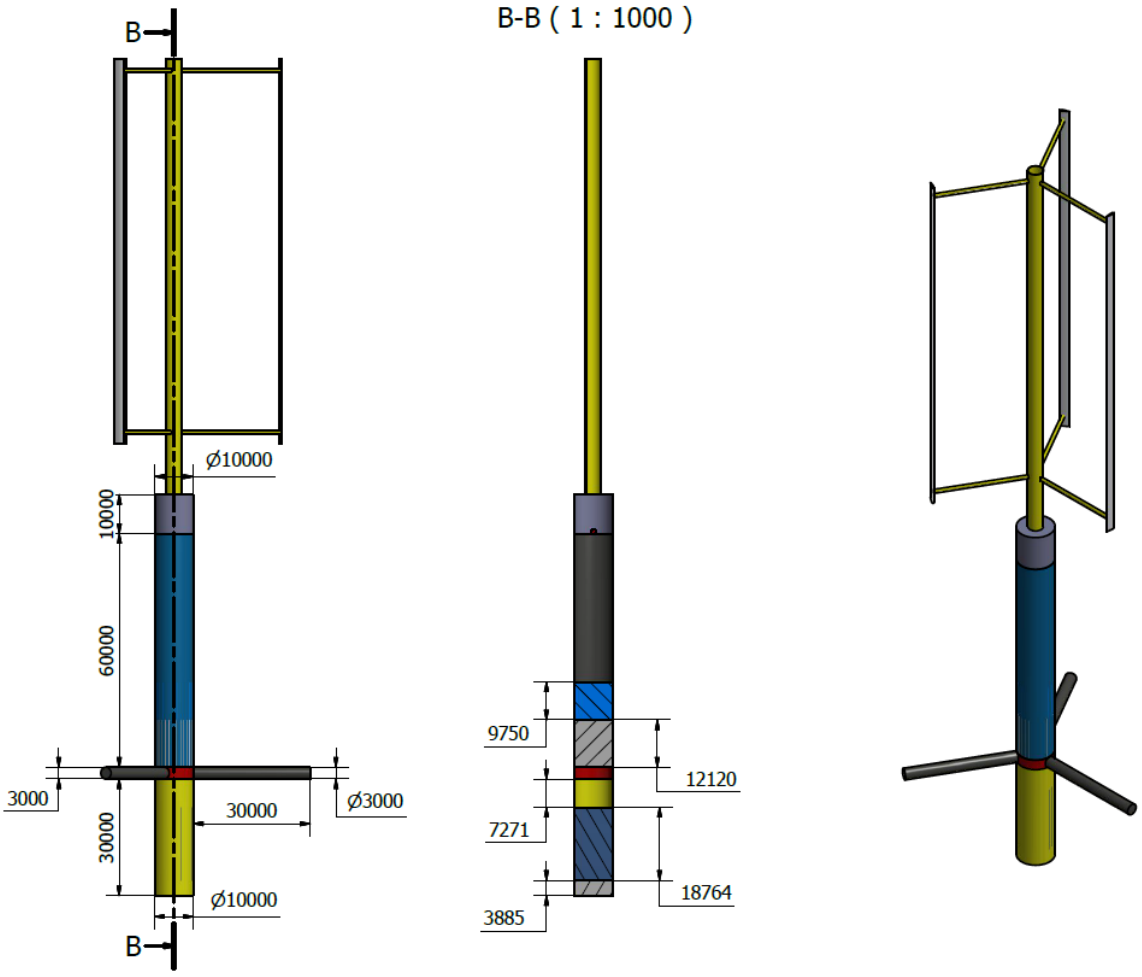

Figure 12-22: Model dimensions illustrated for A2-B2

The figure above shows the relevant model dimensions for case A2-B2. The turbine properties are identical across each cases, hence the dimensions are not repeated here.

12.3.2 Hydrodynamic analysis

12.3.2.1 Mass model

Table 12-16: Mass model A3-B3

Property	Value	Property	Value	Property	Value
Total mass [kg]	8.134E6	Buoyancy vol. [m^3]	7939		
COG X [m]	0	COG Y [m]	0	COG Z [m]	-55.38
COB X [m]	0	COB Y [m]	0	COB Z [m]	-47.68
RX [m]	35.56	RY [m]	35.56	RZ [m]	6.99

The radii of gyration are defined about the centre of gravity, and the centres of buoyancy and gravity are both defined with respect to the sea surface. The mass model used in the hydrodynamic analysis represents the ballasted case (including temporary ballast).

12.3.2.2 Mesh models

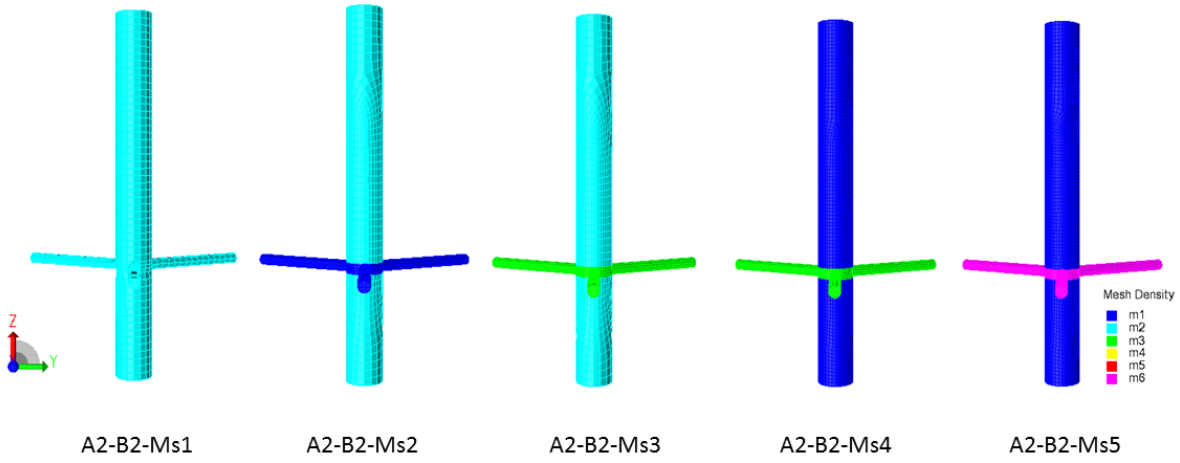

Figure 12-23: Mesh models A2-B2

The figure above is an illustration of the exported mesh models for A2-B2, with colour coded mesh densities, according to the table presented earlier for the mesh identity cases. The associated mesh properties for the FEM files are presented in the table below.

Table 12-17: Mesh properties for the mesh models A2-B2

Case	Nodes	Elements	*t*	ΔZ	*d*	Computed GM	Δ GM	A W_{PL}	RUN
A2-B2-Ms1	1245	1257	43	3.65	96.65	9.62	56 %	76.54	YES
A2-B2-Ms2	2549	2565	149	1.60	94.60	8.55	38 %	76.54	YES
A2-B2-Ms3	3317	3332	391	1.27	94.27	8.37	36 %	76.53	YES
A2-B2-Ms3WS	3317	3332	380	0.83	93.83	8.35	36 %	76.54	YES
A2-B2-Ms4	5580	5595	13814	0.75	93.75	8.13	32 %	78.04	YES
A2-B2-Ms5	6628	6650	23342	0.61	93.61	8.05	31 %	78.04	YES
Units	–	–	s	m	m	m	m	m^2	–

The following figures present selected values from the table above in a set of bar graphs and line plots. The differences observed are computed relative to the manual calculations.

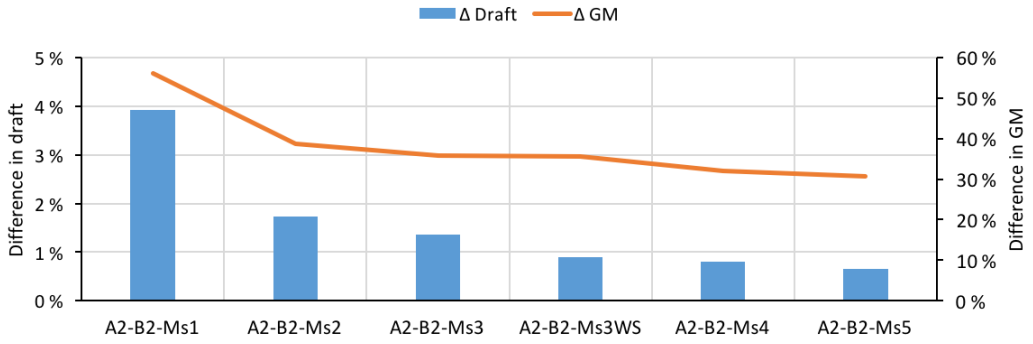

Figure 12-24: Percentage difference in draft and GM relative to spreadsheet A2-B2

As can be observed from the figure above, the differences in draft reduce significantly with increased refinement of the less dense mesh models (A2-B2-Ms1 to A2-B2-Ms2). The difference in draft becomes less pronounced for the increasing mesh densities following A2-B2-Ms3. One issue observed, for this case, in regards to the computed $\overline{GM}$, is that there seems to be a systematic over-prediction in $\overline{GM}$ of 30% (corresponding to 2 m) relative to the manually calculated value. The values seem to converge to a value 30% larger than what was predicted in the manual calculations. As these values seem to converge with increasing mesh density, there may be an underlying error either in this model or in the manual calculations. This source of error is discussed in the sources of error chapter at the end of this thesis. Note that convergence is established hence any errors are likely not due to the mesh model or the imported FEM model, but may be due to an error in input.

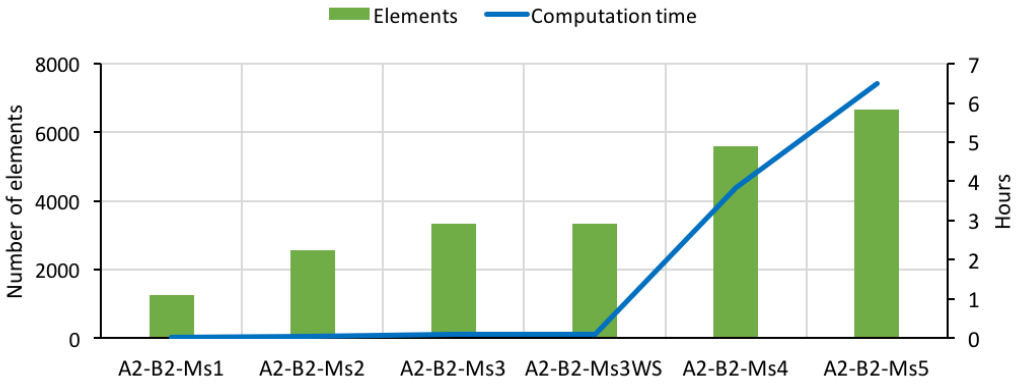

Figure 12-25: Number of elements vs. computation time for A2-B2

The figure above shows the general increase in mesh density for each step in the mesh modelling sequence, with lower number of elements typically observed for Ms1 and Ms2. The computation time is low for the first four mesh models, but increase significantly for Ms4 and Ms5. The mesh densities for Ms4 and Ms5 are significantly finer than what is observed for Ms1-Ms3. Ms3 and Ms3WS have identical mesh densities as the only difference here is the differences in application of the wet surface.

A2-B2-Ms3WS is a modified version of A2-B2-Ms3 where the wet surface has been removed from the inner plate of the pontoons nearest to the contact point with the central column. This was selected to observe the effect on the results if there is no wet surface applied to this region. The reason for this is that this surface would normally not come into contact with the water as it is welded to the central column. The initial hypothesis here was that there would be no or little effect. The results did indicate that this did not have a significant effect on the results.

12.3.2.3 Frequency dependent potential damping

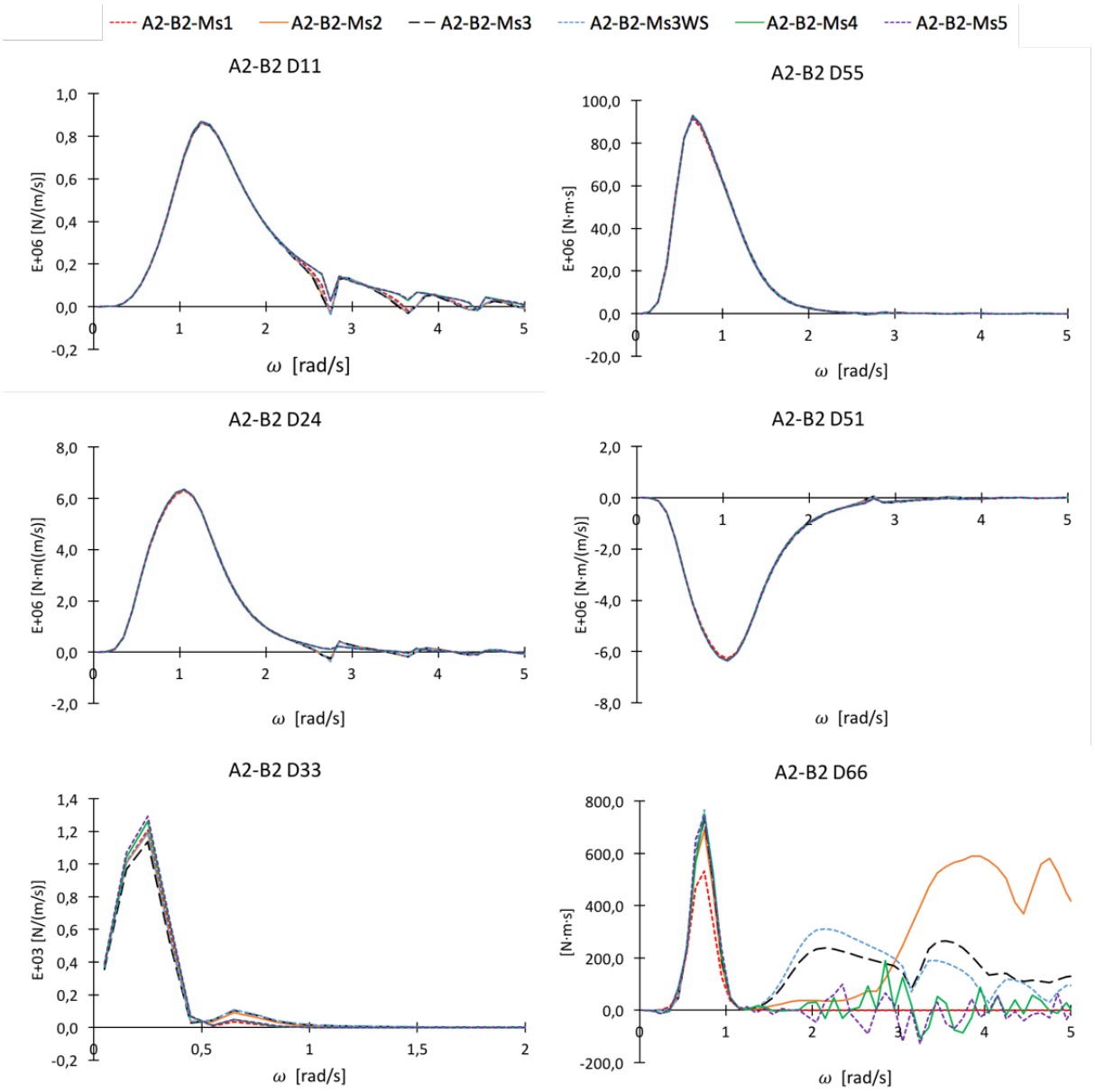

Figure 12-26: Frequency dependent potential damping A2-B2

As can be observed in the figure above, the frequency dependent potential damping values seem to coincide for all mesh settings in D11, D55, D24, D51 and to some extent D33. Typical to most of these results is that there is a tendency for some erratic behaviour in the tail end of the data (i.e. higher frequencies), which is most noticeable in D66, D11 and D24. For D66, the coarser mesh model resulted in a lower damping value at the low frequency peak than what was observed for the other mesh models. The coarse model did not exhibit the same erratic behaviour at the higher frequencies. The high frequency behaviour in D66 was somewhat more erratic than what was observed for A1-B1, but the trend was that, with increased mesh refinement, the peaks reduced in magnitude. This is discussed further in Section 12.3.2.5.

The damping values are in a general sense similar to that which was observed for case A1-B1 with respect to the peak regions and overall shape of the curves, which is reasonable considering the fact that the designs are similar in terms of overall geometry.

12.3.2.4 Frequency dependent added mass

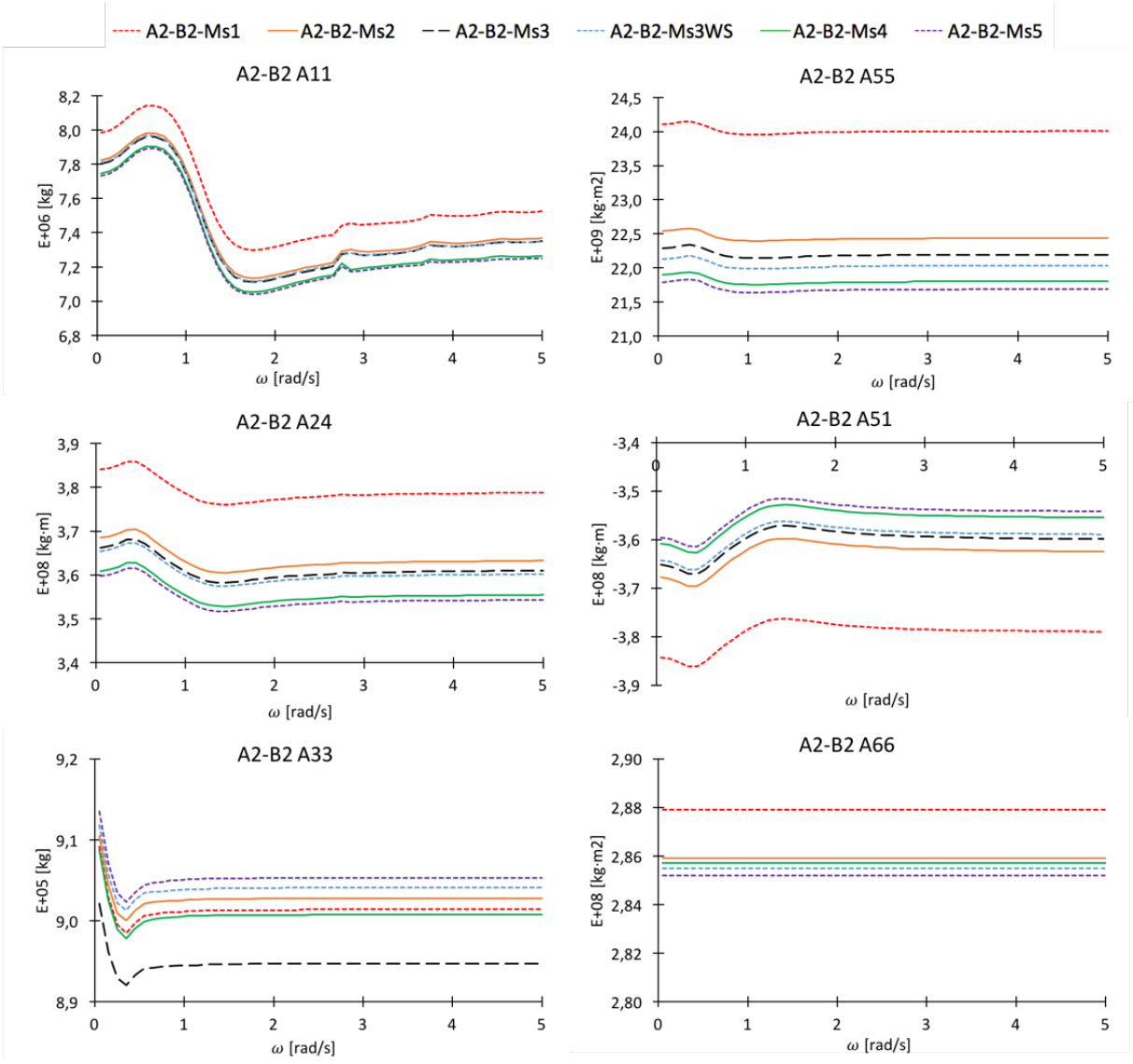

Figure 12-27: Frequency dependent added mass A2-B2

As can be observed from the figure above there seems to be a general trend for A11, A55, A24, A51, and A66; where an increase in mesh density results in less added mass, in the respective degree of freedom. One exception to this trend is that which can be observed for A33, where the value seems to increase with mesh density. This can be explained by the increase in area at the bottom of the structure as the mesh at the bottom plate approaches the shape of the actual structure (circular shape is more accurately modelled with increase in mesh density). However, as presented in the figure above, mesh density Ms3 seems to give the lowest value in A33. This may be due to an interaction between the heave added mass contribution from the pontoons, which are more refined for this mesh setting than, for example, Ms1.

There also seems to be some oscillatory behaviour in the results for heave when considering the different mesh settings, as can be observed by the fact that Ms3 yields minimum values and Ms5 results in the overall maximum value, i.e. the added mass in heave does not follow a clear pattern with increase in mesh density. One potential culprit for this unexpected behaviour in A33 may be the fact that the magnitude of added mass in this DOF is relatively small compared to the other DOF's, which makes it more susceptible to minor variations. By this it is meant that a slight error in the calculation process will give a larger effect on the output, since the added mass value is relatively small. This is discussed in more detail under the sources of error chapter.

12.3.2.5 Convergence and selection of results

By observation of the frequency dependent added mass results, it seems that the values have sufficiently converged for Ms5 as the differences in values between Ms4 and Ms5, corresponding to the two mesh settings with the largest number of elements, yield only slight changes in the added mass. Note that the step in number of elements in the transition from Ms4 to Ms5 corresponds to an increase of 18%, where the general effect on the results vary with less than 0.5%.

As can be observed from the frequency dependent potential damping for A2-B2, there seems to be good correspondence between the different mesh settings for D11, D24, D33, D55 and D51. However, there is considerable erratic behaviour in D66. The erratic behaviour observed for D66 was the main reason for establishing extra mesh models from the original 3-4 mesh settings. For the two data sets with finer mesh, Ms4 and Ms5, there is a tendency for slight oscillatory behaviour about 0 N·m·s with amplitudes peaking at 100 to -100 N·m·s in the frequency interval 2-5 rad/s. The fact that the values tend to oscillate about zero indicates that the theoretical value should be in this region. However, this conclusion is somewhat speculative as finer mesh studies exceeding those that have been defined have not been conducted.

It is known from previous cases studied that the frequency set; used to generate RAOs, damping and added mass matrices to be exported to OrcaFlex, has a different resolution for frequencies above 3 rad/s. In light of this, the frequency dependent damping values in D66 has been exported for A2-B2-Ms5 in order to compare the values obtained from frequency sets 1 and 2 (refer to Section 9.3.3.2 on page 67). The results are presented graphically below.

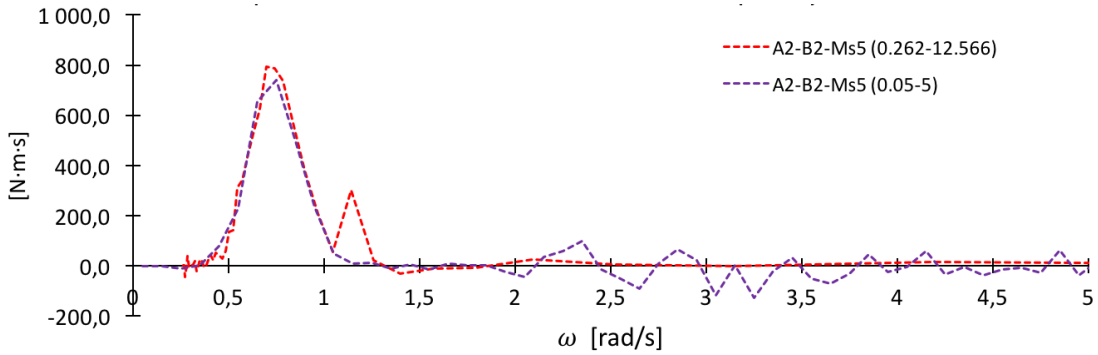

Figure 12-28: Comparison of D66 A2-B2-Ms5 at (0.262-12.566 rad/s) and (0.05-5 rad/s)

As can be observed from the figure above, the peak in the range [0.5, 1] rad/s yields similar results for both of these frequency sets. The effect of changing the frequency set is not easily observed in the lower frequency ranges, as the resolution in this region is somewhat similar, but the effect becomes apparent after 1.5 rad/s. Frequency set 2 shows that the damping in 66 is approximately zero in the interval [1.5, 5] rad/s as is expected based on previous results. One can also observe the additional peak at 1.2 rad/s for frequency set 2; which is likely due to a numerical error, but this peak should not affect the results in the dynamic simulation. The reason for this is that the damping values in this degree of freedom are relatively small compared to other degrees of freedom.

D66 has a track record here of being susceptible to, what is believed to be, a numerical error associated with the fact that the values generated by the program are relatively small in magnitude. Hence the significance of a slight error or noise in the generated results will tend to have a larger effect on the results than, for example, a comparable error in D55, where the values are much larger in magnitude than the potential noise. Note that an illustrative example is presented in Section 13.1.8.2, covering the sources of error for further clarification.

For the reasons presented above, and the fact that the values are comparatively insignificant to the damping in the other degrees of freedom, it is believed that the solution for Ms5 seems to have suitably converged.

12.3.2.6 Hydrostatic stiffness matrix

$$\mathbf{C}_{\mathrm{A2-B2}} = \begin{bmatrix} 0 & 0 & 0 & 0 & 0 & 0 \\ 0 & 0 & 0 & 0 & 0 & 0 \\ 0 & 0 & 7.84 \cdot 10^5 & -1.35 \cdot 10^2 & 6.18 \cdot 10^2 & 0 \\ 0 & 0 & -1.35 \cdot 10^2 & 6.42 \cdot 10^8 & 2.73 \cdot 10^2 & -1.48 \cdot 10^4 \\ 0 & 0 & 6.18 \cdot 10^2 & 2.73 \cdot 10^2 & 6.42 \cdot 10^8 & 1.28 \cdot 10^4 \\ 0 & 0 & 0 & 0 & 0 & 0 \end{bmatrix}$$

The hydrostatic stiffness matrix presented above was exported from HydroD. The values follow the expectation to some degree as the largest values are centred around the diagonal, where magnitudes between 10^5 and 10^8 are observed. The off-diagonal values, which are expected to be zero generally have a magnitude of 10^2, which is relatively insignificant compared to the aforementioned values. However, there are significant values occurring at matrix positions C_{46} and C_{56}. The value in C_{46} was found to be a result of a slight offset in COB_X corresponding to $1.09 \cdot 10^{-4}$ m (i.e. 0.1 mm), and an offset in COG_X corresponding to $6.46 \cdot 10^{-11}$ m. From the hydrostatic stiffness matrix reported in DNV-RP-C205 Section 7.2.1.4, the value in C_{46} is estimated by the following expression.

$$C_{46} = -\rho g \nabla x_B + M g x_G$$

Since the displaced volume is 7939 m^3, and the density of water is given as 1025 kg/m^3 the effect of this slight change in COB_X results in a value of -8701 N·m in the hydrostatic stiffness matrix, excluding the effect of the horizontal shift in COG_X. This calculated value does not match the value given in the hydrostatic stiffness matrix above, but gives an indication of the potential cause for the appearance of a non-zero value in position C_{46}. The same explanation applies for C_{56}.

Another cause for concern was the non-symmetric properties of the hydrostatic stiffness matrix. Based on the background theory provided earlier in this thesis, it was found that the hydrostatic stiffness matrix should be symmetric for a symmetric floater. Since the non-zero values in C_{46} and C_{56} were not observed in C_{64} and C_{65} this violates the assumption of a symmetric hydrostatic stiffness matrix. The reason for this is unknown, but it is speculated that this may be an assumption from the software, where it does not expect a coupled hydrostatic stiffness value for yaw, hence it assumes zero values in row 6.

It is worth noting that only the values in rows 3-5 and columns 3-5 are exported into OrcaFlex as this software assumes that the other values are zero. Since the symmetry condition is satisfied for the values in the aforementioned matrix positions it is believed that the hydrostatic stiffness matrix is valid for use and should not impose any significant errors in the simulation. The hydrostatic stiffness contribution is relatively small compared to the mooring stiffness, thus it should not have a significant effect on the results overall.

12.3.2.7 Natural periods

The natural periods in each degree of freedom for the vessel, without the mooring system attached, are presented in the table below for mesh A2-B2-Ms5.

Table 12-18: Natural periods A2-B2 in floating condition

Degree of freedom	Natural period [s]	Natural frequency [rad/s]	Degree of freedom	Natural period [s]	Natural frequency [rad/s]
Surge	∞	0	Roll	30.38	0.207
Sway	∞	0	Pitch	30.34	0.207
Heave	21.33	0.295	Yaw	∞	0

The results presented above follow the expectation of the natural periods as surge, sway, and yaw with zero hydrostatic stiffness have undefined (infinite) natural periods. One should note that resonant behaviour in heave, will be, to some extent, covered by the frequency set used to develop the RAOs, as the lowest frequency is 0.261 rad/s. The natural periods in roll and pitch are not captured by this frequency set as these are lower than the lowest frequency. This means that the peak displacement RAO will not be determined for roll and pitch.

12.3.2.8 Displacement RAOs

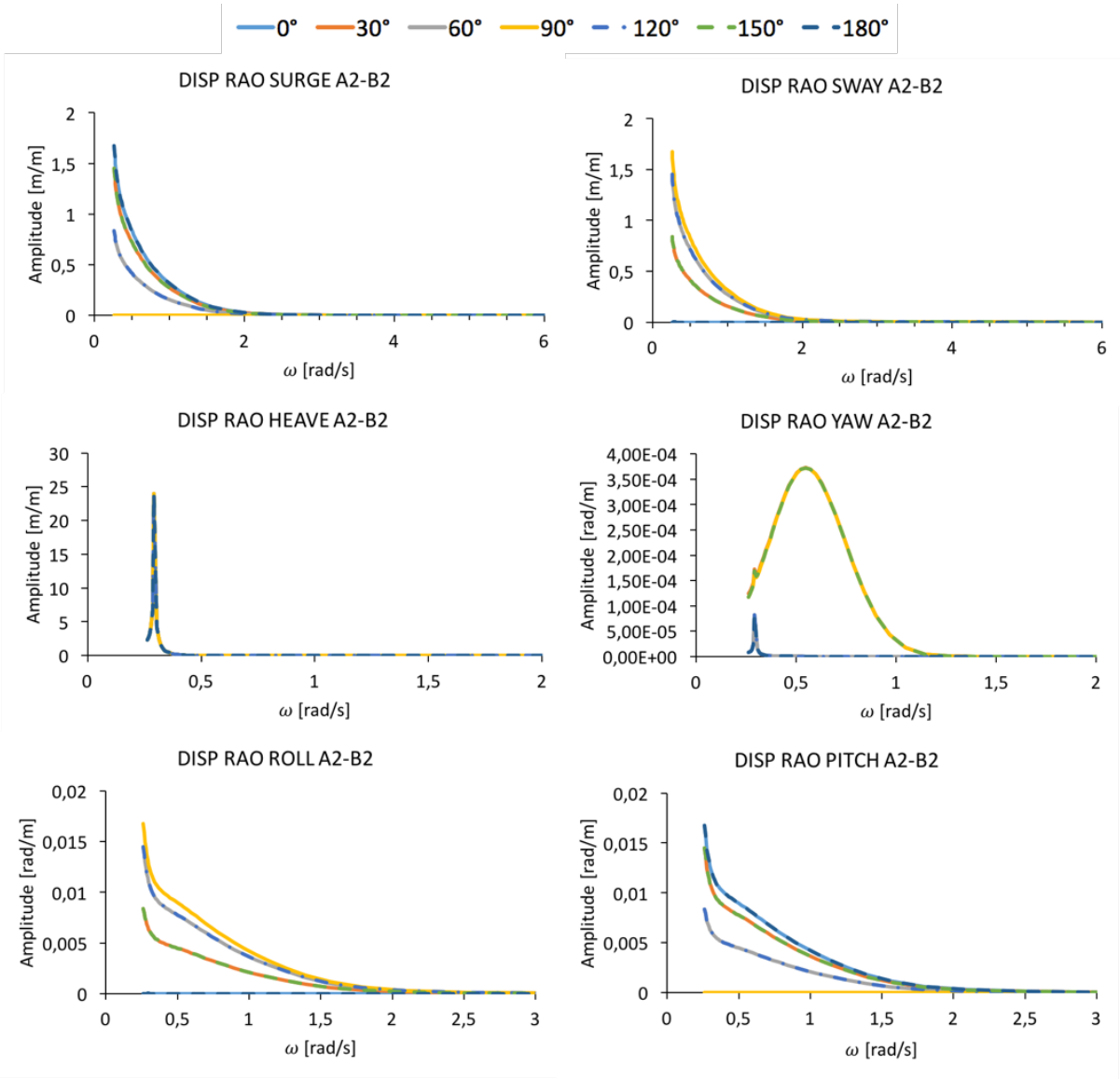

Figure 12-29: Displacement RAOs for A2-B2

As can be observed from the figure above, the displacement RAOs for A2-B2 seem to follow the same type of behaviour as that which was observed for A1-B1. As can be observed for the displacement RAO in heave, there is a significant peak in the data set below 0.5 rad/s, around 0.3 rad/s. This is due to resonance, as the natural frequency of the vessel in heave was found to be 0.295 rad/s. The amplitude of the resonant motion in this set approaches 25 m/m. There seems to be a similar peak in the yaw displacement RAO near the natural frequency in heave, but the reason for this is uncertain. One explanation for this, although speculative in nature, is that there may be an overlap of resonant behaviour from the heave motion in yaw causing this disturbance in the displacement RAO.

12.3.2.9 Load RAOs

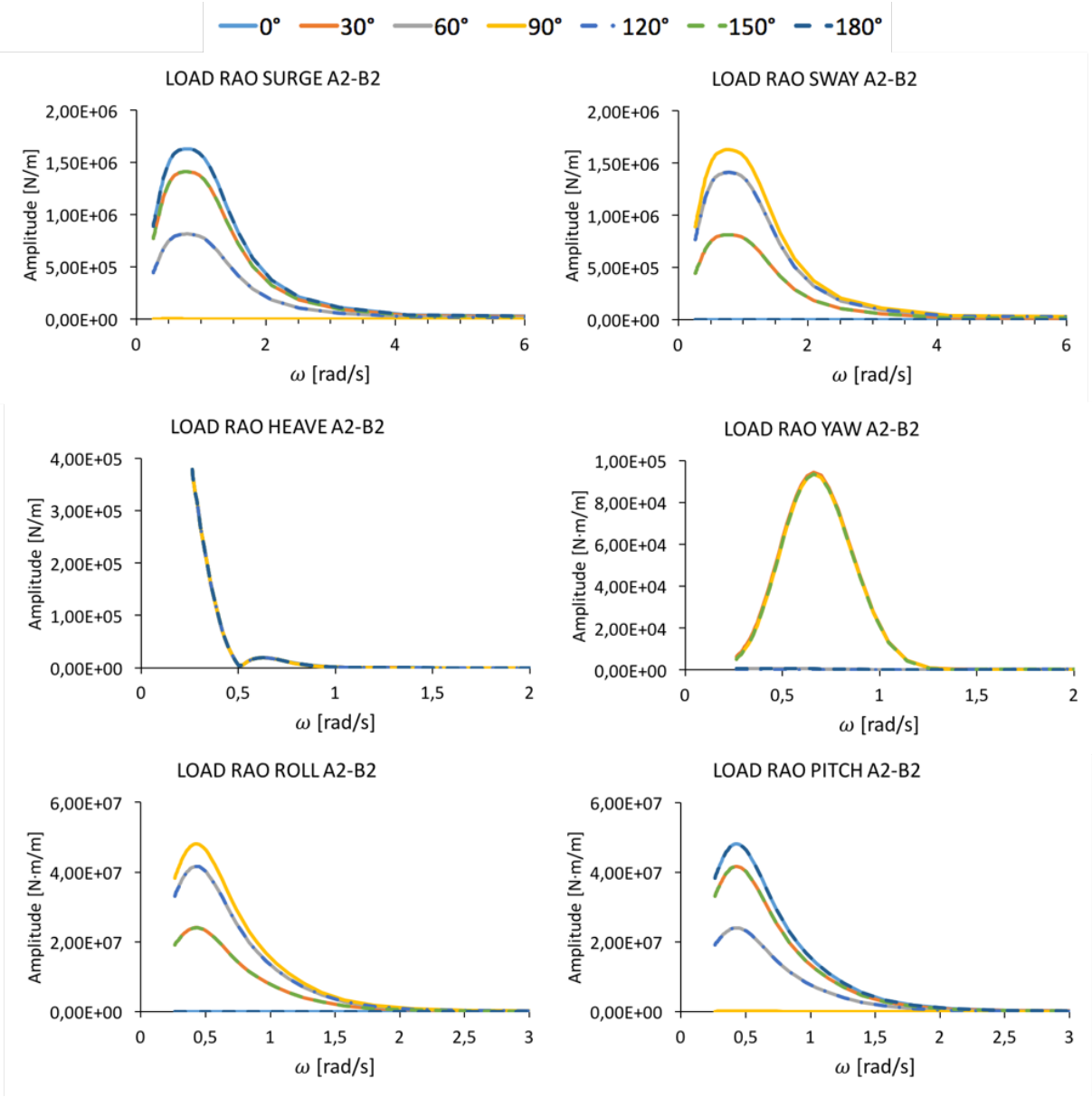

Figure 12-30: Load RAOs for A2-B2

The load RAOs follow a similar pattern as was observed for A1-B1. The surge and sway components show the same direction dependence, as observed for A1-B1, but with greater amplitudes. The similarity between these two sets of load RAOs is a reasonably good indicator that the coordinate system has been appropriately defined in line with the recommendations presented under the hydrodynamic modelling chapter. By this it is meant that the coordinate system used in the Inventor model coincides with the coordinate system in HydroD, which is necessary in order to give the correct value for the direction that is analysed.

The load RAOs in pitch and roll tend to give the largest amplitudes, captured by the frequency set, overall; followed by surge and sway. In comparison to A1-B1, the load RAO in yaw has increased significantly. This is likely due to the increased pontoon radius for A2-B2.

In general terms, which has also been observed from the previous set of load RAOs (A1-B1), the dominant region of excitation occurs for the lower frequencies. This is particularly evident in the interval 0.5-1.5 rad/s. Further comparison of the load RAOs, across the three cases, is presented in Section 13.1.5.

12.3.3 Dynamic simulation

12.3.3.1 Tendon properties and arrangement

Table 12-19: Tendon properties and arrangement A2-B2

Tendon	Line type	Section length	Segment length	End A			End B		
				R*	θ*	Z*	R**	θ**	Z**
1	Tendon_1m	138.50	0.5	25	0	-1.5	0	0	-138.50
2	Tendon_1m	138.50	0.5	25	120	-1.5	0	0	-138.50
3	Tendon_1m	138.50	0.5	25	240	-1.5	0	0	-138.50
Units	–	m	m	m	°	m	m	°	m
* Defined relative to vessel coordinates									
** Defined relative to End A coordinates									

12.3.3.2 Static results

The following table presents the static results without the application of wind load. This is conducted to uncover any discrepancies between the target value and the calculated value from OrcaFlex. Large deviations here should indicate that there are some underlying issues with the inputs. For this reason, a relative difference has been presented to give an indication of the percentage differences between the target and the calculated value, from OrcaFlex.

Table 12-20: Output from the static state calculation A2-B2

	Value static state	Target	Difference
Vessel Z-position [m]	-59.95	-60	0.08 %
Pre-tension 1 [N]	7.397E6	7.44E6	−0.58 %
Pre-tension 2 [N]	7.397E6	7.44E6	−0.58 %
Pre-tension 3 [N]	7.397E6	7.44E6	−0.58 %

The vessel Z-position is specified with reference to the local coordinate of the vessel relative to the global axis at the still water line. The target value is equal to the draft of the mono-hull floater. As can be observed from the data above, there is relatively little difference between the target values and the static state calculations conducted in OrcaFlex. This is a good indication that the model is representative of its target value in the static state.

The natural periods of the whole system, as calculated in OrcaFlex, are presented in the table below.

Table 12-21: Natural periods for 6 DOFs A2-B2

Degree of freedom	Mode	Amplitude	Period [s]	Frequency [rad/s]
Surge (η_1)	2	1 m	38.772	0.162
Sway (η_2)	1	1 m	38.772	0.162
Heave (η_3)	24	1 m	0.706	8.900
Roll (η_4)	16	-1 deg	1.115	5.635
Pitch (η_5)	17	-1 deg	1.115	5.635
Yaw (η_6)	3	1 deg	11.560	0.544

As can be observed from the table above, the natural periods and frequencies of the system follow, in a general sense, the basic characteristics of the TLP system, with long periods observed in the horizontal degrees of freedom (surge, sway and yaw) and short periods in the restrained degrees of freedom, roll, pitch and heave. Similarly, to that which was observed for case A1-B1, the amplitude in roll (and pitch here) yielded a negative value. This is assumed valid, as a negative amplitude should yield the same natural period as positive value, for a symmetric system.

12.3.3.3 Results EC2

Table 12-22: Input information A2-B2 EC2

	Value	Location relative to local axis
Applied load	365 kN	132.5 m
Applied torque	1800 kNm	60 m
JONSWAP (H_s, T_p, γ)	(3.10 m, 10.1 s, 3.3)	NA
Water depth	200 m	NA
Simulation duration	3600 s	NA

The time histories for surge, heave, pitch, and yaw are presented in the figures below.

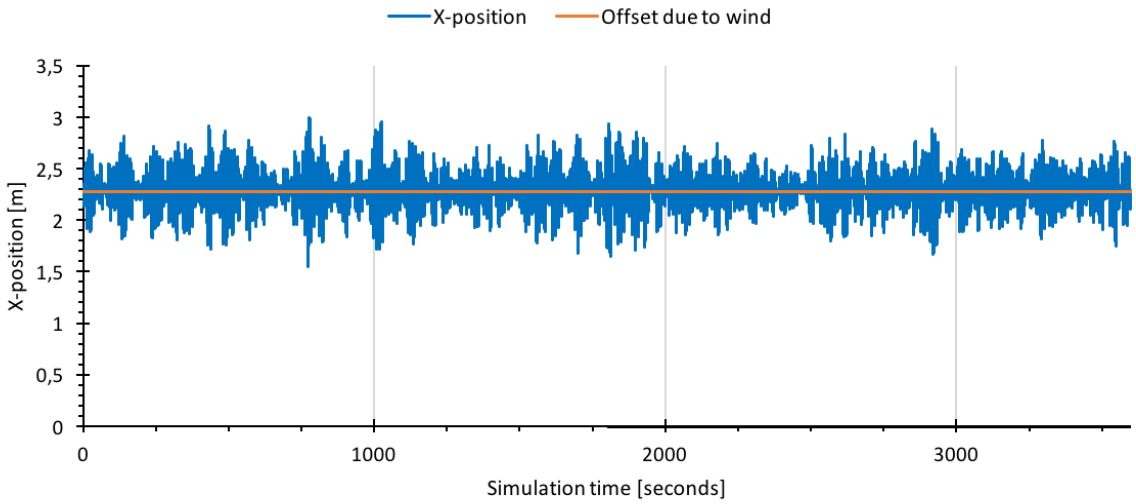

Figure 12-31: Time history surge (0, 0, 60 m) A2-B2-EC2-T0.05

Similar to past time histories, the mean oscillating position of the system in this environmental condition is equivalent to the static offset due to wind. The mean position in surge equates to roughly 1.7% of the observed water depth (length of tendons).

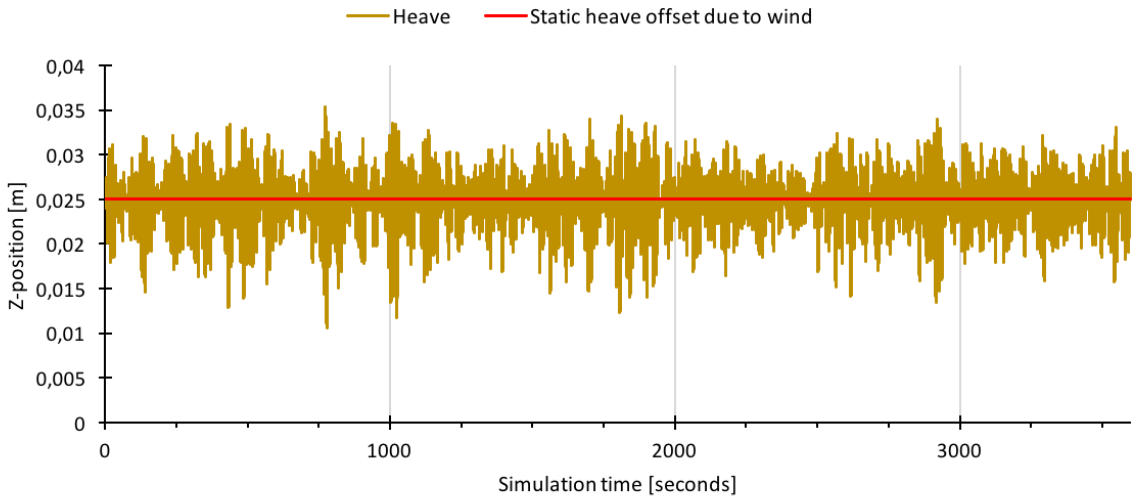

Figure 12-32: Time history heave (0, 0, 60 m) A2-B2-EC2-T0.05

As can be observed from the figure above, the heave of the vessel tends to oscillate about a value larger than zero. This differs from the previous case, where the mean offset in heave was negative. This is likely attributed to the fact that the pre-tension of A2-B2 is significantly larger than that of A1-B1, where the increased pre-tension leads to an increased strain of the tendons. This means that the elongation of the tendons, results in static offset in heave in the positive direction (upwards). The static offset with wind applied (as illustrated in Figure 12-32) results in a set down relative to the static z-position obtained in Table 12-20. The variations in heave are limited to ±1 cm,

which are representative for the TLP system (DNV states that the translation in heave is usually in the range of cm [21] as presented in the vessel motions chapter earlier).

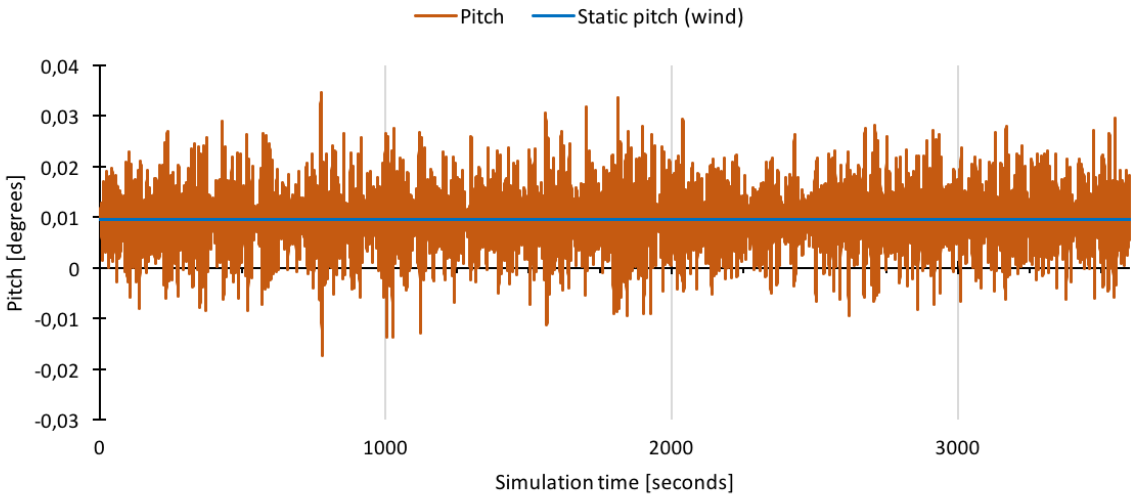

Figure 12-33: Time history pitch (0, 0, 0 m) A2-B2-EC2-T0.05

The pitch motions are typically limited to ± 0.025 degrees relative to the static pitch rotation induced by the applied wind load. Note that this is lower than what was observed for A1-B1. This is likely attributed to the increase in pontoon radius [29].

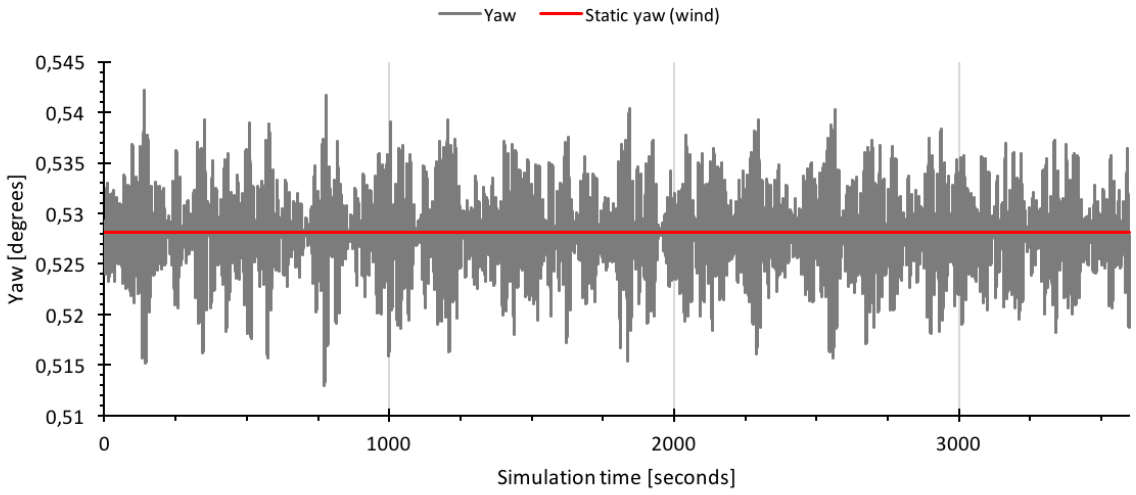

Figure 12-34: Time history yaw (0, 0, 0 m) A2-B2-EC2-T0.05

Similar to what has been discussed earlier, the wave-induced yaw motions experience relatively little variation as can be observed above. This is more or less expected based on the presented load and displacement RAO amplitudes for this wave direction.

The figure below shows the time history for the effective tendons at End A (vessel connection).

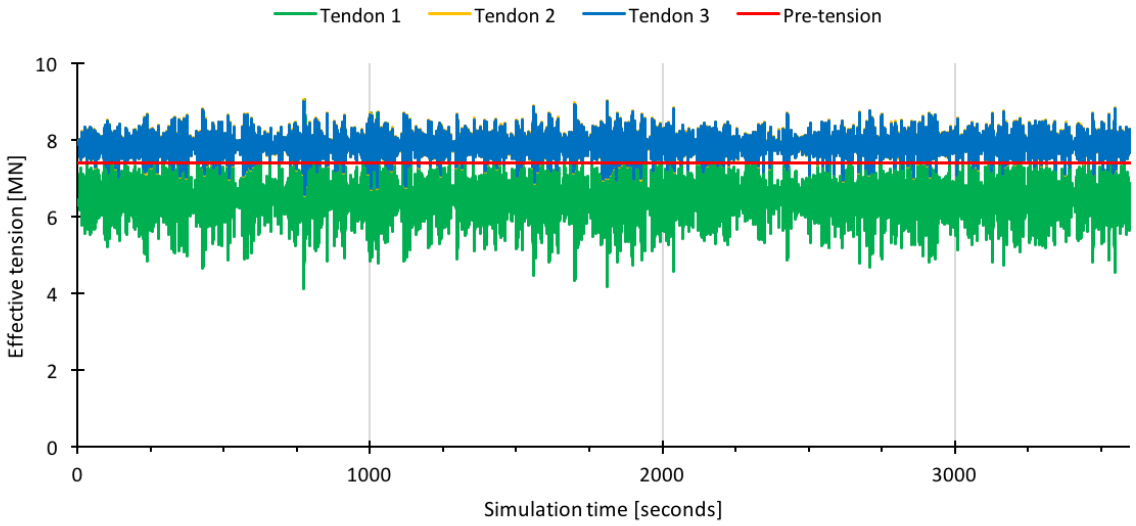

Figure 12-35: Time history effective tension A2-B2-EC2-T0.05

As can be observed from the effective tension time history above, the variation in tendon 1 is not as severe as what was observed for A1-B1. Similar to what has been observed earlier, tendon 1 experiences a larger variation in load compared to tendons 2 and 3. The variation in tendon 1 is however, less pronounced for this case (in this sea state) if one compares the obtained results in A1-B1 for EC2, relative to the initial pre-tension. Comparisons of these are presented in 13.1.6

The following table shows the statistical results obtained from the simulation for each of the relevant result categories.

Table 12-23: Summary of statistical results for A2-B2-EC2-T0.05

Variable	Min.	Max.	μ	σ	Units
Motion					
Surge (0, 0, 60 m)	1.550	2.996	2.288	0.210	m
Heave (0, 0, 60 m)	0.011	0.035	0.025	0.004	m
Pitch (0, 0, 0 m)	-0.017	0.035	0.010	0.007	degrees
Yaw (0,0, 0 m)	0.513	0.542	0.528	0.004	degrees
Sea surface clearance (0, 0, 83 m)	19.82	25.67	23.02	0.77	m
Tendons					
Effective tension – tendon 1	4.10E+06	9.06E+06	6.48E+06	6.54E+05	N
Effective tension – tendon 2	6.54E+06	9.07E+06	7.87E+06	3.34E+05	N
Effective tension – tendon 3	6.57E+06	9.03E+06	7.86E+06	3.25E+05	N
Declination – tendon 1	178.79	179.25	179.04	0.06	degrees
Declination – tendon 2	178.93	179.40	179.17	0.07	degrees
Declination – tendon 3	178.70	179.17	178.94	0.07	degrees
Local axis dynamic loads and moments*					
Total Lx-force	-2.01E+06	1.94E+06	2.13E+02	5.19E+05	N
Total Lz-force	-2.32E+04	4.96E+04	5.60E+01	8.78E+03	N
Total Ly-moment	-1.53E+07	1.60E+07	1.83E+03	4.16E+06	Nm
Local axis static loads and moments**					
Total Lx-force	–	–	3.65E+05	2.48E-01	N
Total Lz-force	–	–	2.29E+07	–	N
Total Ly-moment	–	–	4.84E+07	3.29E+01	Nm

As can be observed from the presented results for A2-B2-EC2, it is clear that there are limited motions in surge, heave, pitch and yaw for this operational sea state. The effective tension in all tendons are sufficiently large to avoid slack in this environmental condition. There is however a significant variation in the tensile load in tendon 1, where the standard deviation is doubled compared to the values for tendons 2 and 3. The angles at the tendon connection points are sufficiently small as they do not exceed more than 1.3 degrees from the static state (180°).

12.3.3.4 Results EC3

Table 12-24: Input information A2-B2 EC3

	Value	Location relative to local axis
Applied load	1200 kN	132.5 m
Applied torque	0 kNm	60 m
JONSWAP (H_s, T_p, γ)	(12.70 m, 14.1 s, 3.3)	NA
Water depth	200 m	NA
Simulation duration	3600 s	NA

The time histories for surge, heave, pitch, yaw and sea surface clearance relative to blades are presented in the figures below.

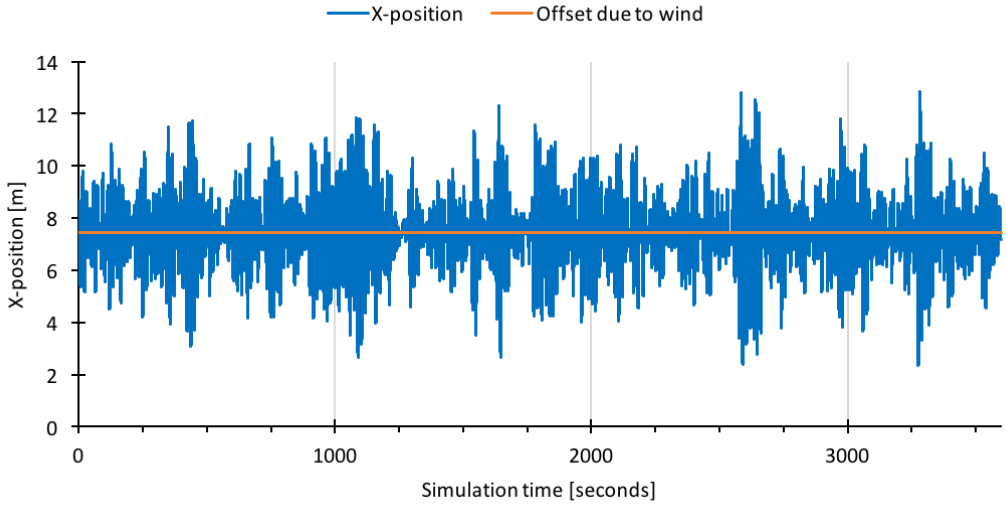

Figure 12-36: Time history surge (0, 0, 60 m) A2-B2-EC3-T0.05

Similar to what has been observed earlier, the time history in surge for EC3 indicates larger variations in surge motions than what is observed for EC2, as expected. The largest variation occurs around 2500-2750 seconds in the simulation time. Note that comparisons between the motions in this sea state across the cases is presented in the discussion chapter and will not be drafted here.

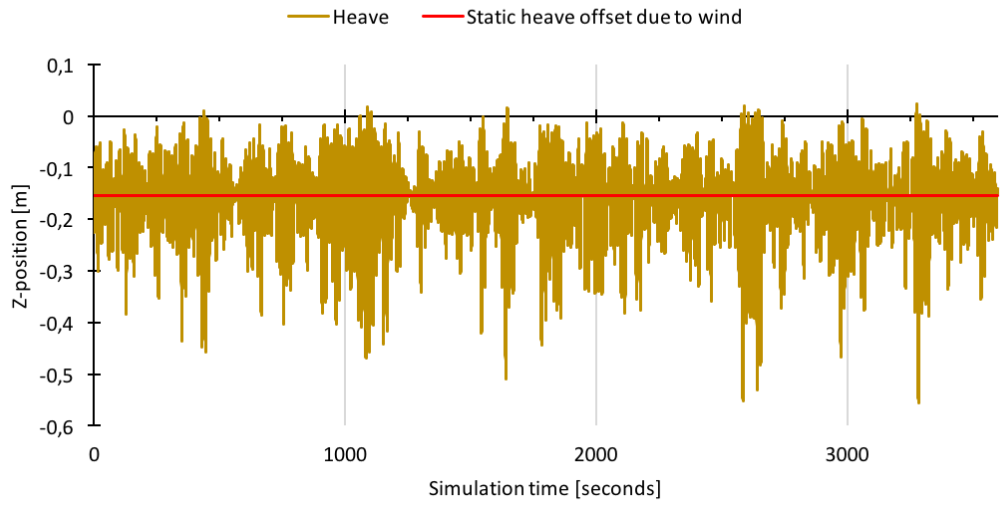

Figure 12-37: Time history heave (0, 0, 60 m) A2-B2-EC3-T0.05

As can be observed the mean offset in heave has transitioned from a positive value to a negative value for this sea state (if one compares the time history in EC2 for this case). Note that the z-position is affected by the translation in surge as presented under the TLP principles and design considerations chapter earlier (set down effect). One

can also observe significant spikes in this data set as well, which may be attributed to loss of tension in the downwind tendon, but is also likely due to the presence of a large wave in the wave record. Similar to what has been stated before, this motion is also affected by the pitch rotation (presented below).

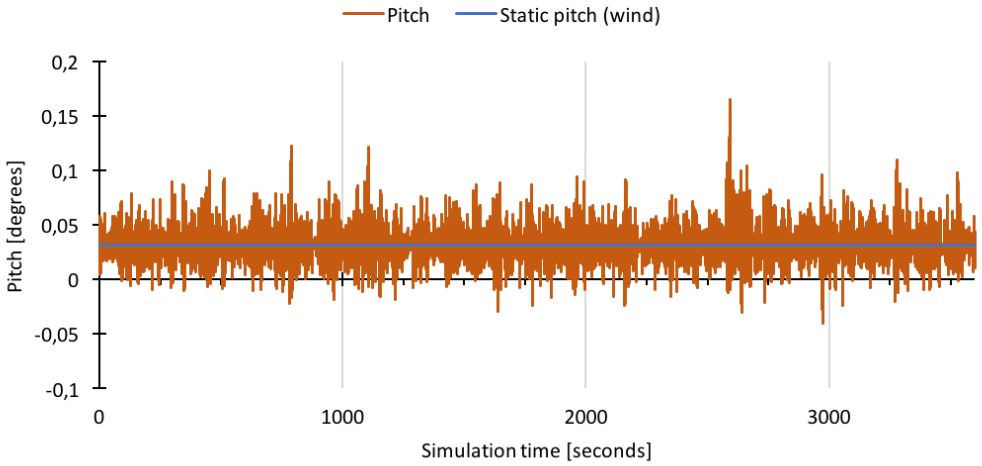

Figure 12-38: Time history pitch (0, 0, 0 m) A2-B2-EC3-T0.05

Although the main discussion of motions across the three cases are left to the discussion chapter in this thesis, one may notice the reduction in pitch rotation for this case, relative to that which was observed for A1-B1. The variation in pitch rotation is significantly lower here, as is clear from the reduced number of "spikes" in this time record. The maximum value occurs after 2500 seconds in the simulation time, where the system experiences a 0.15-degree rotation. This is significant relative to the other peaks present in this data set.

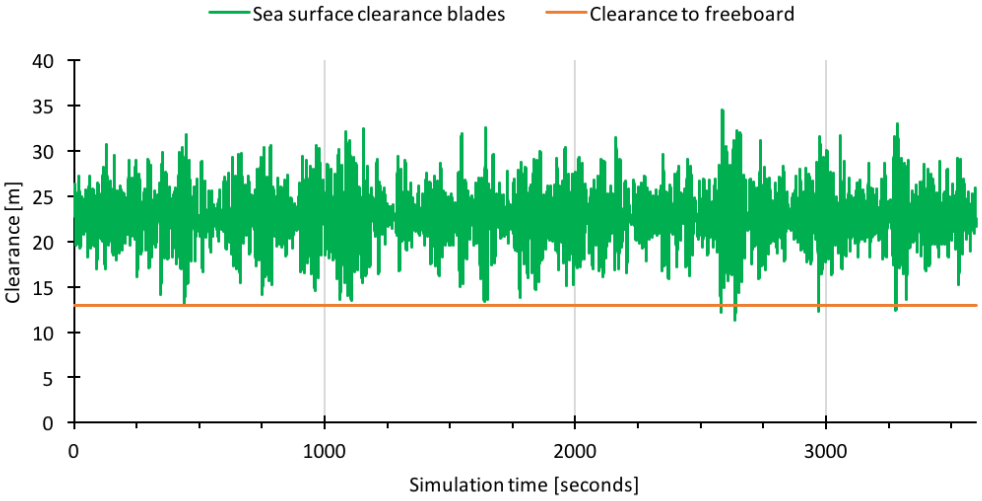

Figure 12-39: Time history sea surface clearance to bottom of blade A2-B2-EC3-T0.05

The sea surface clearance time history above indicates that there is sufficient air gap between the blades and the sea surface in this sea state. The freeboard, similarly to case A1-B1 is insufficient here as there are a number of waves that exceed the designated freeboard. However, as previously stated, this may not necessarily pose a significant threat to the system if the hull-turbine shaft connection interface is watertight, but this occurance is not ideal and may require an increased freeboard.

The figure below shows the time history for the effective tendons at End A (vessel connection).

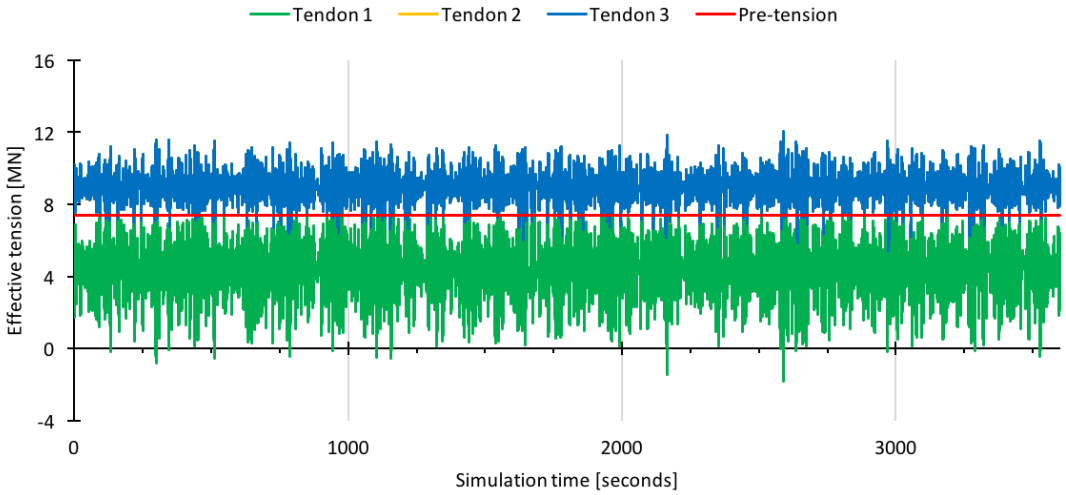

Figure 12-40: Time history effective tension A2-B2-EC3-T0.05

As can be observed from the figure above, there is a significant reduction in the occurrence of slack in tendon 1 for this case. The tension in tendon 1 seems to oscillate around 4 MN with around 13 slack states appearing in the simulation time. Although this case yields significant improvement, to the tension in tendon 1, compared to A1-B1, the occurrence of slack is an indication that the vessel cannot survive this sea state, as there is a potential for loss of platform associated with slack tendons [8].

The following table shows the statistical results obtained from the simulation for each of the result categories

Table 12-25: Summary of statistical results for A2-B2-EC3-T0.05

Variable	Min.	Max.	μ	σ	Units
Motion					
Surge (0, 0, 60 m)	2.335	12.872	7.462	1.579	m
Heave (0, 0, 60 m)	-0.557	0.025	-0.164	0.087	m
Pitch (0, 0, 0 m)	-0.040	0.165	0.033	0.020	degrees
Sea surface clearance (0, 0, 83 m)	11.24	34.59	22.72	3.23	m
Tendons					
Effective tension – tendon 1	-1.88E+06	1.11E+07	4.42E+06	1.77E+06	N
Effective tension – tendon 2	5.40E+06	1.20E+07	8.99E+06	9.18E+05	N
Effective tension – tendon 3	5.39E+06	1.20E+07	8.99E+06	9.18E+05	N
Declination – tendon 1	174.69	178.66	176.85	0.55	degrees
Declination – tendon 2	174.98	178.89	176.94	0.59	degrees
Declination – tendon 3	174.98	178.89	176.94	0.59	degrees
Local axis dynamic loads and moments					
Total Lx-force	-7.31E+06	7.46E+06	9.02E+02	2.06E+06	N
Total Lz-force	-4.70E+05	6.87E+05	5.90E+02	1.21E+05	N
Total Ly-moment	-7.73E+07	7.16E+07	6.53E+03	1.81E+07	Nm
Local axis static loads and moments					
Total Lx-force	–	–	1.20E+06	2.97E-01	N
Total Lz-force	–	–	2.29E+07	–	N
Total Ly-moment	–	–	1.59E+08	3.99E+01	Nm

As can be observed from the results in this environmental condition, the pre-tension is insufficient as slack condition is observed in tendon 1 at several points throughout the duration of the simulation. The motions in heave and pitch experience intermittent peaks that exceed the general variation significantly. This is likely explained by sudden loss of tension in tendon 1 and lowered tension values for tendons 2 and 3 which means that the vessel is to some extent free to rotate. Since the heave motion is specified in the still water line, some additional contribution from the increased pitching is observed for this heave motion.

From the table above it is also clear that there is an excessive Ly-moment on the connection point, which by summation of the dynamic load and the statically applied load, leads to a value of 230 MNm. If one observes the

range in the moment at the connection point (82 to 230 MNm) it is clear that there is relatively large variation in loading, which may have implications for fatigue although this is not analysed further. Further discussion and comparison for the cases is presented under the discussion chapter.

12.3.3.5 Time step sensitivity analysis

The time step analysis results are presented in the table below. The same variables are used here as presented for A1-B1.

Table 12-26: Time step sensitivity for T0.1 and T0.05 – A2-B2-EC3

Variable	Difference μ	Difference σ
η_1 [m]	0.000%	-0.044%
η_3 [m]	-0.004%	-0.044%
η_5 [degrees]	0.004%	-0.017%
Effective tension T1	0.000%	-0.027%
Effective tension T2	0.000%	-0.025%
Effective tension T3	0.000%	-0.025%

As can be observed from the results above, there is little change difference between the two time steps and it is thus possible to assume that the time step is sufficient for T0.05.

12.4 Case A3-B3

12.4.1 Model

12.4.1.1 Dimensions

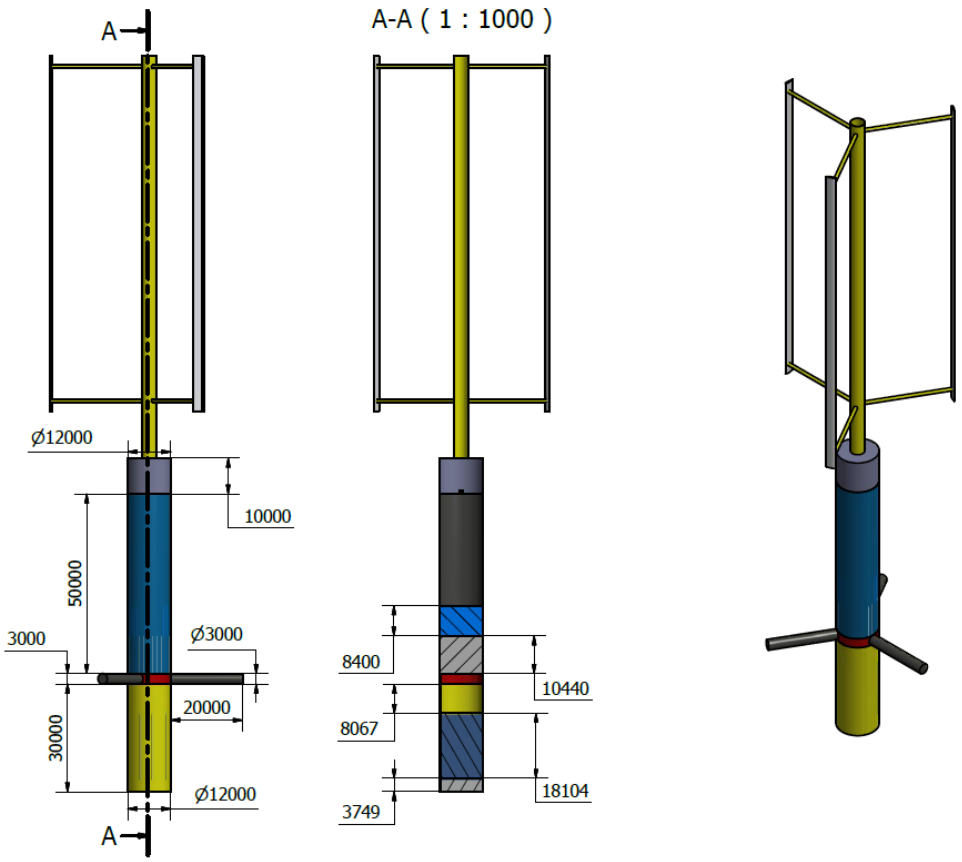

Figure 12-41: Illustrated dimensions for A3-B3

The dimensions presented in the figure above are given in mm. The blue-shaded internals represent the temporary ballast, with dimensions specified in terms of ballast column heights.

12.4.2 Hydrodynamic analysis

12.4.2.1 Mass model

Table 12-27: Mass model A3-B3

Property	Value	Property	Value	Property	Value
Total mass [kg]	1.005E7	Buoyancy vol. [m^3]	9811		
COG X [m]	0	COG Y [m]	0	COG Z [m]	-49.24
COB X [m]	0	COB Y [m]	0	COB Z [m]	-41.94
RX [m]	31.34	RY [m]	31.34	RZ [m]	6.01

The radii of gyration are defined about the centre of gravity, and the centres of buoyancy and gravity are both defined with respect to the sea surface.

12.4.2.2 Mesh models

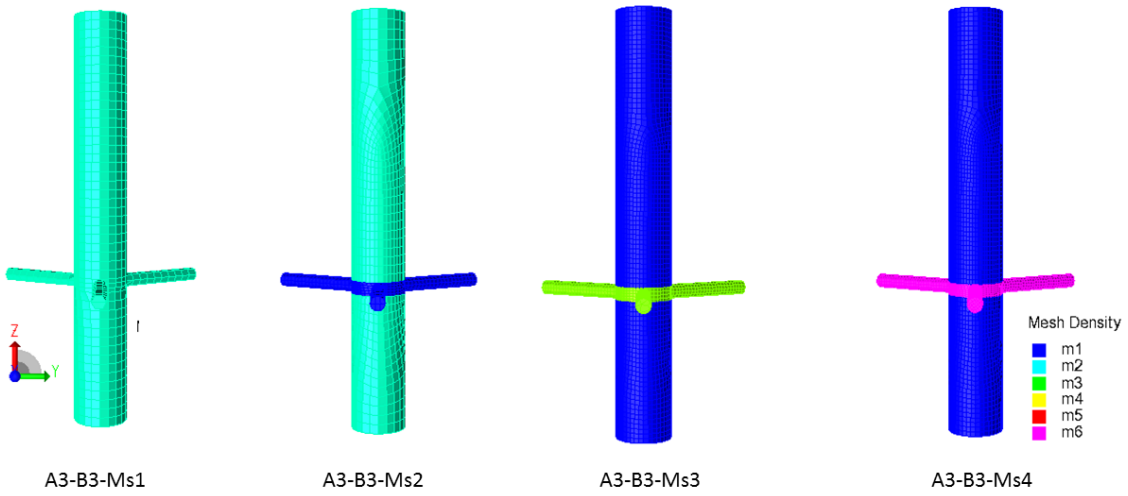

Figure 12-42: Mesh models A3-B3

The figure above presents the mesh models used for A3-B3, and the table below presents the number of nodes, elements, computation time etc. for these mesh models.

Table 12-28: Mesh results A3-B3

Case	Nodes	Elements	*t*	ΔZ	*d*	Computed GM	Δ GM	A W_{PL}	RUN
A3-B3-Ms1	1283	1295	45	1.926	84.93	8.396	1.09	111.2	YES
A3-B3-Ms2	2434	2449	131	0.879	83.88	7.86	0.56	111.2	YES
A3-B3-Ms3	5331	5345	734	0.409	83.41	7.62	0.32	112.6	YES
A3-B3-Ms4	6377	6399	22324	0.325	83.33	7.57	0.27	112.6	YES
Units	–	–	s	m	m	m	m	m^2	–

Some of the key values presented in the table above are illustrated graphically below.

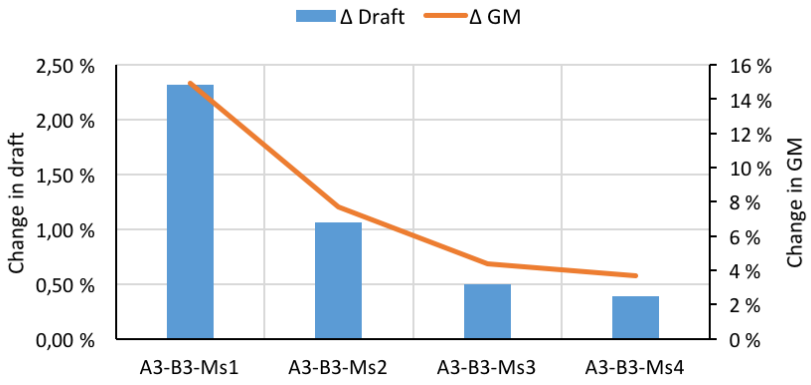

Figure 12-43: Change in draft and GM with reference to mesh setting A3-B3

The figure above shows the change in draft as a percentage of the estimated draft from manual calculations, and the change in metacentric height as a percentage of the estimated value from manual calculations. As can be observed from this figure, the difference in draft reduces with each mesh case. Mesh setting 3 boasts a relative increase in draft by 0.5% which is within reason for this application. The change in metacentric height remains somewhat larger compared to that of the draft, as can be observed for mesh setting 1, where $\overline{GM}$ is over-estimated by around 16%. This value decreases significantly with increase in number of elements, but the effect seems to diminish with each increment. This is noticeable between Ms3 and Ms4, where the difference between the two is around 1% (relative to the target value based on spreadsheet calculations). One possible reason for the over-estimate in $\overline{GM}$ is that the centre of gravity is positioned further below the SWL and the centre of buoyancy is positioned further up the vessel due to the increase draft. It may also be a result of rounding errors in the total mass

of the system, when generating the mass model in HydroD. It is also worth mentioning that, since there is little effect between Ms3 and Ms4 on both draft and $\overline{GM}$ it may be assumed that the solution has sufficiently converged. However, conclusions regarding convergence are determined based on frequency dependent potential damping and added mass and not the change in draft or $\overline{GM}$.

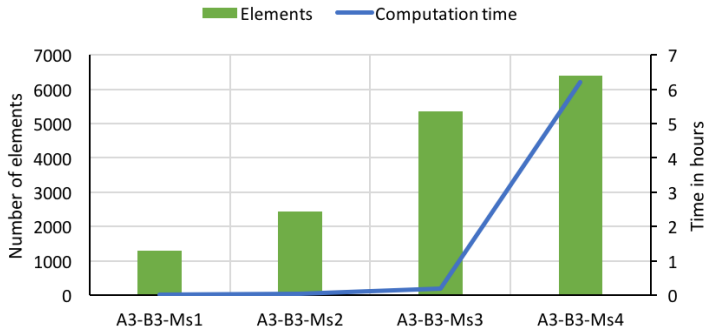

Figure 12-44: Computation time and number of elements A3-B3

The figure above shows the number of elements for each mesh case with the associated computation time in HydroD. As can be observed, the computation time increases exponentially with increase in number of elements, which is especially apparent between Ms3 and Ms4 where the computation time increases by a factor of 30.4.

12.4.2.3 Frequency dependent potential damping

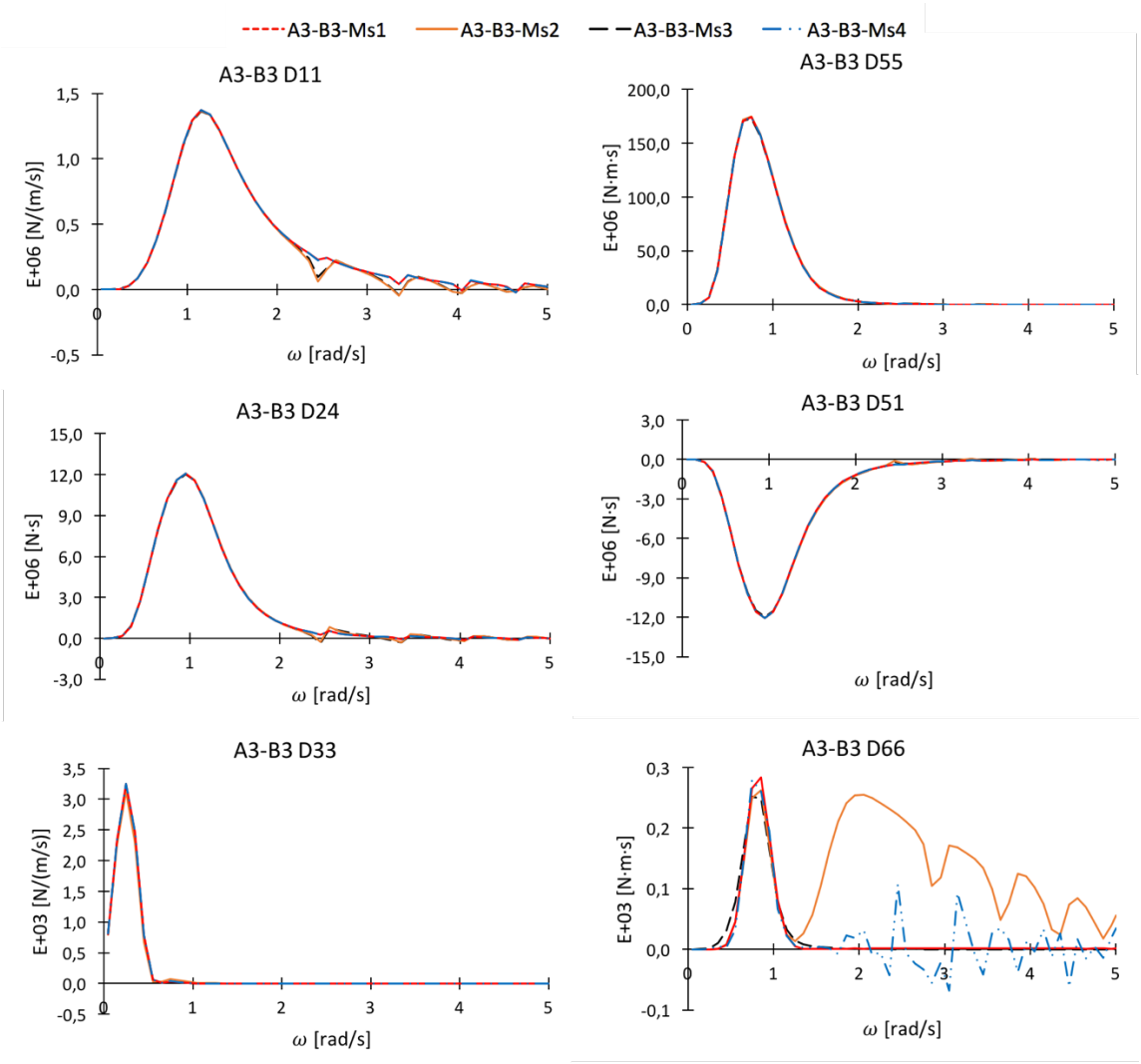

Figure 12-45: Frequency dependent potential damping for A3-B3

Figure 12-45 shows the frequency dependent potential damping for case A3-B3 with the four data-series representing each of the mesh models presented earlier. As can be observed from these values there is a relatively good correspondence between the values in D11, D55, D24, D33 and D51. The coarse mesh models had a significant erratic behaviour in the tail end of D11 and D24 as can be observed from the figure above. This erratic behaviour became less pronounced, although still present for the finer mesh models Ms3 and Ms4.

One noticeable difference was observed for the values obtained D66 (potential damping in yaw). The erratic behaviour in this degree of freedom was more pronounced for mesh setting 2 (Ms2), containing 2449 elements in the mesh model. The erratic behaviour seems to reduce with increasing angular frequency but the peak at 2 rad/s was in the same order of magnitude as the peak around 1 rad/s, which was common to all mesh models. This erratic behaviour was also observed for case A1-B1-Ms2 in D66 with 2072 elements, but for this case the magnitude exceeded that of the first peak. The behaviour disappears for mesh setting three (A3-B3-Ms3), which had a finer mesh with 5435 elements, but reappears with smaller magnitude and oscillating values about zero for the finest mesh setting (A3-B3-Ms4). The damping in the other degrees of freedom seem to directly coincide for Ms3 and Ms4, which may suggest that the behaviour observed in D66 is a result of a numerical error in the program. This is further backed up by the fact that the overall order of magnitude of the damping in D66 is 10 times smaller than that of D33, and 1 000 000 times smaller than that of D55, which again means that any numerical error will have a significant effect on the values in D66. This effect is discussed under the sources of error chapter, with an accompanying illustrative example.

12.4.2.4 Frequency dependent added mass

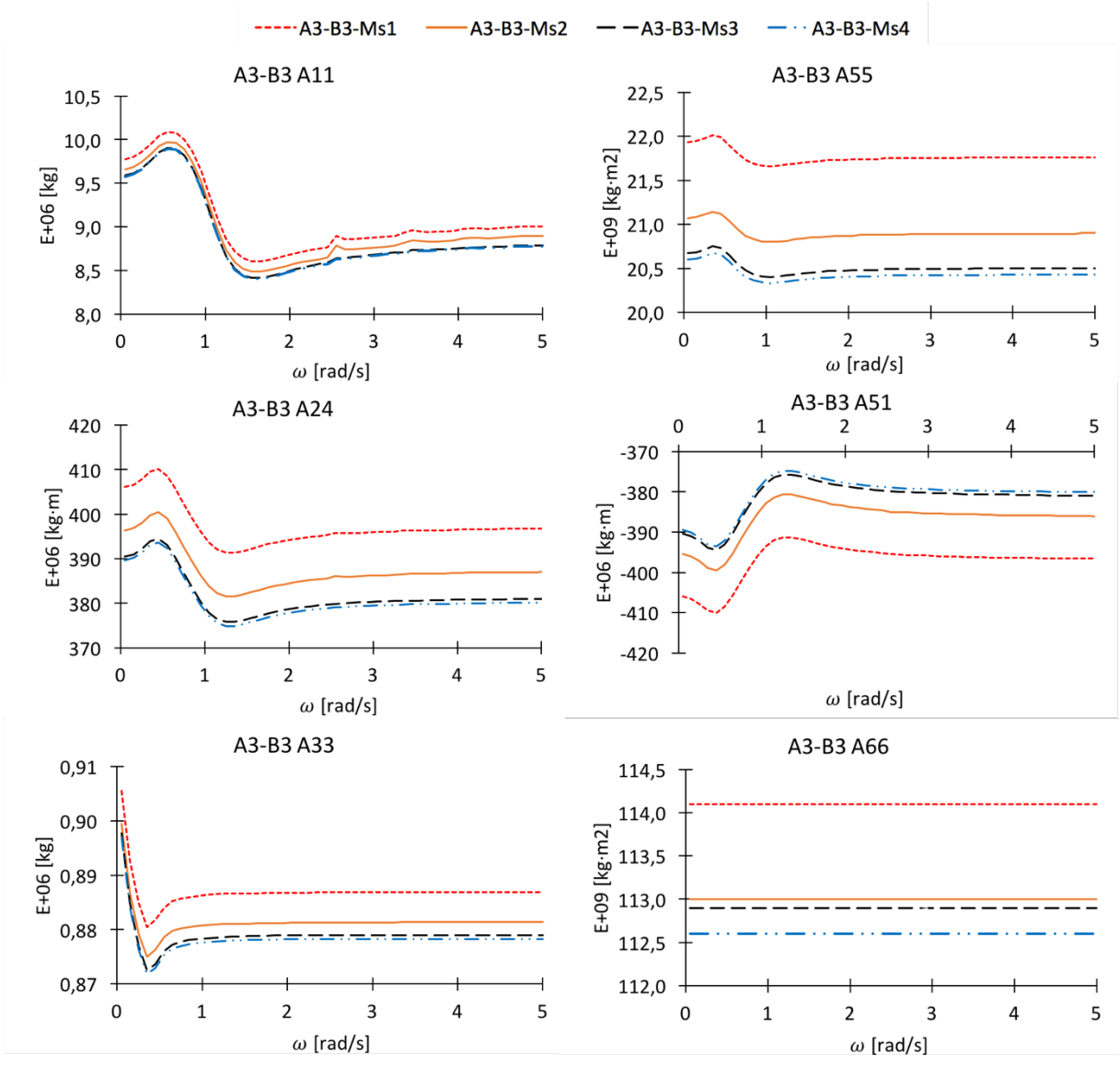

Figure 12-46: Frequency dependent added mass A3-B3

Figure 12-46 shows the frequency dependent added mass for case A3-B3 for the four mesh models presented earlier. As can be observed from these figures, the added mass for A3-B3-Ms1 tends to be over-predicted for all the added mass matrix values presented above. There seems to be relatively good agreement between mesh settings three and four in this case, even though the number of elements in the mesh has increased by approximately 20%. This suggests that convergence has been established at Ms3, with 5345 elements. The values seem to agree for A11, A55, A51, A33 and A24, but there is some difference in A66. This difference however, equates to a reduction in added mass by 0.4%, which is well within reason for this application.

12.4.2.5 Convergence and selection of results

As stated in the two sub-chapters above, the solution seems to have converged at A3-B3-Ms3, which is evident from both the potential damping values and the added mass. For this reason, case A3-B3-Ms3 has been selected for further generation of displacement and load RAOs, for importing into OrcaFlex. The reason for not selecting the finest generated mesh in the mesh model array, is that the generation of RAOs requires more frequencies in the tail end of the data set, which demands an additional run in HydroD, but also the fact that there was some erratic behaviour in Ms4 D66, which was not observed for Ms3. The increased computation time for Ms4 (6.2 hours) also aided in the decision to opt for mesh setting three, which had a significantly lower associated computation time without a significant effect on the results.

12.4.2.6 Hydrostatic stiffness matrix

The hydrostatic stiffness matrix for case A3-B3-Ms3 is presented below.

$$\mathbf{C}_{\mathrm{A3-B3}} = \begin{bmatrix} 0 & 0 & 0 & 0 & 0 & 0 \\ 0 & 0 & 0 & 0 & 0 & 0 \\ 0 & 0 & 1.13 \cdot 10^{6} & 8.91 \cdot 10^{2} & 7.11 \cdot 10^{2} & 0 \\ 0 & 0 & 8.91 \cdot 10^{2} & 7.51 \cdot 10^{8} & -2.09 & 8.77 \cdot 10^{3} \\ 0 & 0 & 6.18 \cdot 10^{2} & -2.09 & 7.51 \cdot 10^{8} & 8.43 \cdot 10^{3} \\ 0 & 0 & 0 & 0 & 0 & 0 \end{bmatrix}$$

As can be observed from the hydrostatic stiffness matrix above the values are symmetrical in rows 3-5 and columns 3-5. Values are observed in column 6, similarly to the other two cases analysed in this thesis. The values in column 6 are relatively small in magnitude compared to the values in the diagonal, corresponding to at most ~0.1%. Since OrcaFlex only requires information about rows 3-5 and columns 3-5, the symmetry condition is satisfied for this matrix and is deemed fit for use. The reader is referred back to the discussion on the hydrostatic stiffness matrix in Section 12.2.2.6 on page 111 as the same reasoning can be applied for this case.

12.4.2.7 Natural period

The natural periods in each degree of freedom for the vessel, without the mooring system attached, are presented in the table below for mesh A3-B3-Ms3.

Table 12-29: Natural periods A3-B3 in floating condition

Degree of freedom	Natural period [s]	Natural frequency [rad/s]	Degree of freedom	Natural period [s]	Natural frequency [rad/s]
Surge	∞	0	Roll	27.29	0.230
Sway	∞	0	Pitch	27.29	0.230
Heave	19.53	0.322	Yaw	∞	0

The natural periods presented above are based on the Eigen solutions to the rigid body motion specified in the HydroD WADAM.LIS file for the respective case.

12.4.2.8 Displacement RAOs

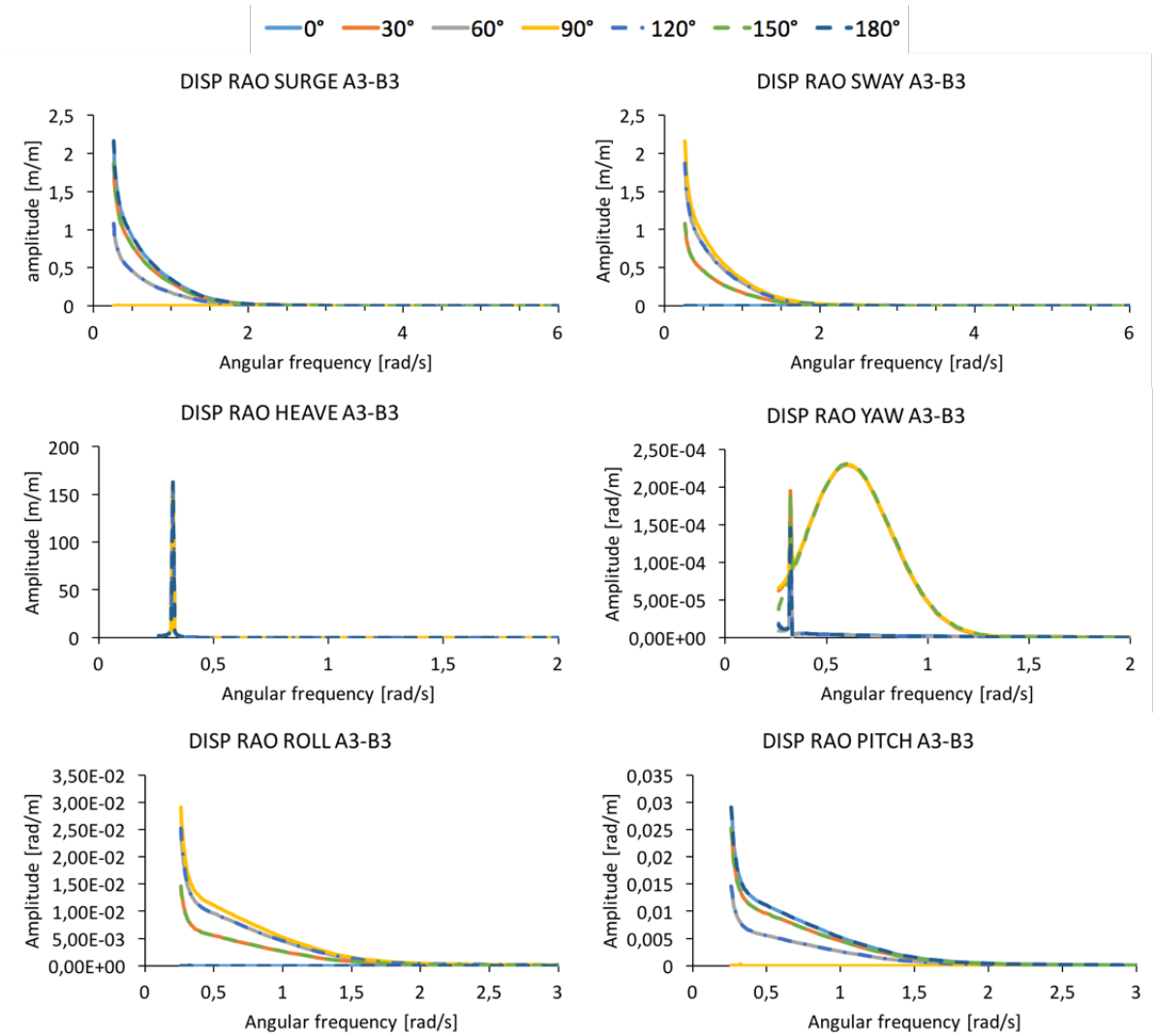

Figure 12-47: Displacement RAOs for A3-B3

Figure 12-47 shows the displacement RAOs for case A3-B3 exported from mesh setting 3 (Ms3). The directions presented above range between 0° and 180° with an interval step of 30°. As can be observed from these figures, the surge and sway displacement RAOs are equal in magnitude but the maximum values are at 0° and 90° directions respectively. This follows the expectation for the RAOs in these degrees of freedom because of how these degrees of freedom are defined relative to direction 0°, corresponding to the x-axis of the vessel. The maximum values in surge and sway do not seem to be captured by the frequency range used to generate these figures, but this follows the expectation since the value will continue to increase with longer wave periods (corresponding to lower frequencies), because of the infinite natural period in this degree of freedom.

The heave displacement RAO has a significant peak at around 0.3-0.4 rad/s where the amplitude approaches 170 m/m. This is due to resonance, where the natural frequency matches that of the wave frequency [9]. The natural frequency in heave was determined to be 0.322 rad/s, which matches that of the peak in the aforementioned frequency range. By chance there was a value in the input frequency set at 0.322 rad/s, which is the reason why there is significant peak in this RAO compared to the other cases discussed earlier. The displacement RAO in heave exhibits direction independence, meaning that the RAO is unaffected by direction, which follows the expectation since heave is, by definition, a pure vertical motion.

The pitch and roll displacement RAOs exhibit the same type of direction relationship as discussed for surge and sway. The natural period in these degrees of freedom are not captured by the frequency set specified above.

One noticeable difference in the presented set of RAOs above is yaw. There seems to be a double peaked relationship dependent on direction, where the directions 30°, 90° and 150° seem to produce a clear bell-shaped

curve with the amplitude peaking at around 0.6 rad/s, and a narrow spike is produced for 0°, 30°, 60°, 180° at around 0.4 rad/s. The low frequency peak corresponds to the natural frequency in heave, which may have had an effect due to potential overlap.

12.4.2.9 Load RAOs

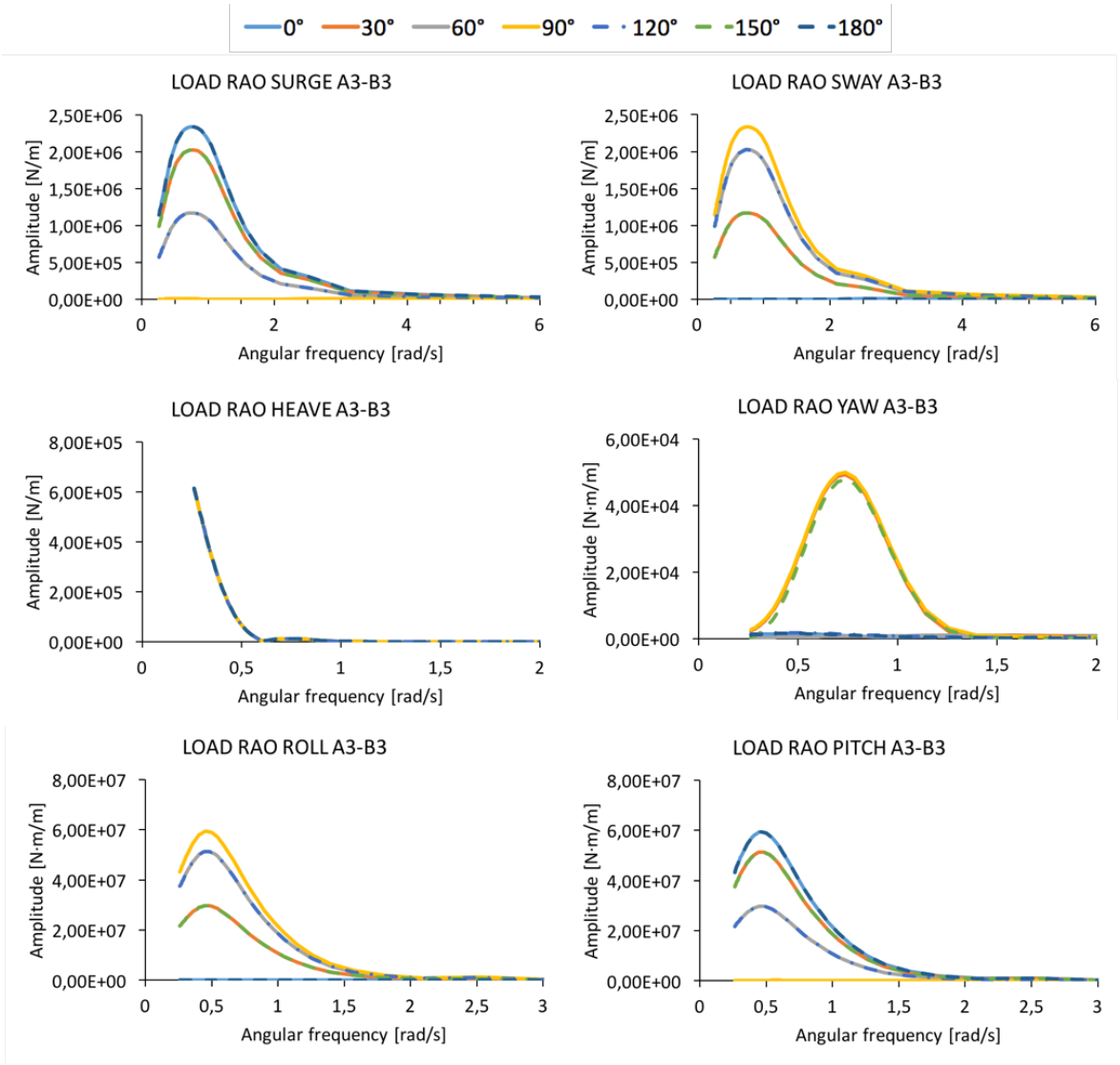

Figure 12-48: Load RAOs A3-B3

The load RAOs for case A3-B3 are presented in the figure above. The colour coding of series follow the same system as presented for the displacement RAOs, for simpler comparison. As can be observed from the figures above the maximum amplitudes in load are found for frequencies around 0.8 rad/s for both surge and sway. A similar relationship with the directions are found here as for the displacement RAOs, as expected.

As can be observed for heave, the load RAO seems to peak in the lower frequencies, but the peak is not defined in the given frequency set. This should not pose a problem in the dynamic simulation stage as waves with high energy in this frequency region are not likely to occur. The load RAO in yaw seems to follow a similar pattern to that of the displacement RAO, however there is no sudden peak at around 0.4 rad/s associated with the 0°, 60°, 120° and 180° directions. The load RAO in yaw is slightly larger, in amplitude, than what was observed for A1-B1, which may be attribute to the increase in diameter of the buoyancy module, which affects the pontoon radius. Further comparison of the load RAOs are found in the discussion chapter in this document.

12.4.3 Dynamic simulation

The following sub-chapters present the tendon properties and arrangement along with a presentation of static state results with no wind applied. Natural periods for the moored configuration are also presented in this section. The results from the dynamic simulations are presented in the form of time histories (consistent with the results presented for the previous cases) and statistics. This section is concluded with a time-step sensitivity analysis for the selected indicators, with emphasis on EC3.

12.4.3.1 Tendon properties and arrangement

Table 12-30: Tendon properties and arrangement A3-B3

Tendon	Line type	Section length	Segment length	End A			End B		
				R*	θ*	Z*	R**	θ**	Z**
1	Tendon_1m	148.50	0.5	26	0	-1.5	0	0	-148.50
2	Tendon_1m	148.50	0.5	26	120	-1.5	0	0	-148.50
3	Tendon_1m	148.50	0.5	26	240	-1.5	0	0	-148.50
Units	–	m	m	m	°	m	m	°	m
* Defined relative to vessel coordinates									
** Defined relative to End A coordinates									

Note that the tendons, for this case, are 10 m longer than what was specified for the two previous cases. This is due to the reduced draft of A3, while maintaining constant water depth.

12.4.3.2 Static results

The following static results were obtained, excluding any applied wind load or torque.

Table 12-31: Static results A3-B3

	Value static state	Target	Difference
Vessel Z-position [m]	-49.94	-50	0.01 %
Pre-tension 1 [N]	9.91E6	9.96E6	-0.5 %
Pre-tension 2 [N]	9.91E6	9.96E6	-0.5 %
Pre-tension 3 [N]	9.91E6	9.96E6	-0.5 %

As can be observed from the table above, the initial z-position of the vessel is slightly higher than the predicted value, but the difference is sufficiently small for this to be accepted. One plausible explanation for this is the elongation of the tethers due to the applied load. The pre-tension values are 0.5% lower than the target value, which is deemed sufficiently accurate for this purpose. The difference here is most likely due to the number of significant figures given for the total mass of the vessel, which may have been rounded up.

The natural periods of the system obtained by modal analysis, in OrcaFlex, are presented in the table below. Note that the natural periods presented below are calculated for an adjusted tendon segment length of 0.25 m (down from 0.5 m), due to an issue encountered with the associated mode shapes in roll and pitch. The associated natural periods where identical for segment lengths 0.5 m and 0.25 m, but differences motion were observed. This occurred because the vessel rolled about the axis running through pontoon 3 instead of the positive x-axis (pontoon 1). It should be noted that the magnitude of the motion did not change, but the motion was presented with values less than 1 in the Cartesian coordinate system, which amount to the same amplitude.

Table 12-32: Natural periods by modal analysis A3-B3

Degree of freedom	Mode	Amplitude	Period [s]	Frequency [rad/s]
Surge (η_1)	2	1 m	37.86	0.166
Sway (η_2)	1	1 m	37.86	0.166
Heave (η_3)	24	1 m	0.797	7.884
Roll (η_4)	17	-1 deg	1.496	4.200
Pitch (η_5)	16	-1 deg	1.496	4.200
Yaw (η_6)	3	1 deg	11.86	0.530

The natural periods match the expectation for a typical TLP structure as longer natural periods are observed for the compliant degrees of freedom (surge, sway and yaw), and shorter natural periods are observed for heave, roll and pitch.

12.4.3.3 Results EC2

Table 12-33: Input information A3-B3 EC2

	Value	Location relative to local axis
Applied load	365 kN	122.5 m
Applied torque	1800 kNm	50 m
JONSWAP (H_s, T_p, γ)	(3.10 m, 10.1 s, 3.3)	NA
Water depth	200 m	NA
Simulation duration	3600 s	NA

The time histories for surge, heave, pitch and yaw are presented in the figures below.

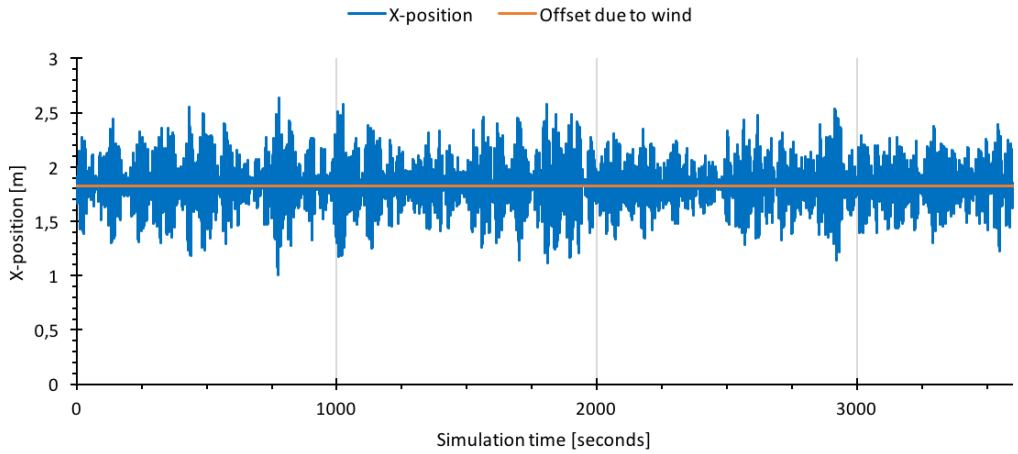

Figure 12-49: Time history surge (0, 0, 50 m) A3-B3-EC2-T0.05

Similar to what has been observed for the other cases, the surge motion oscillates about the offset due to the static wind load. The oscillation is limited to approximately ± 0.75 m, which for the given water depth is relatively small.

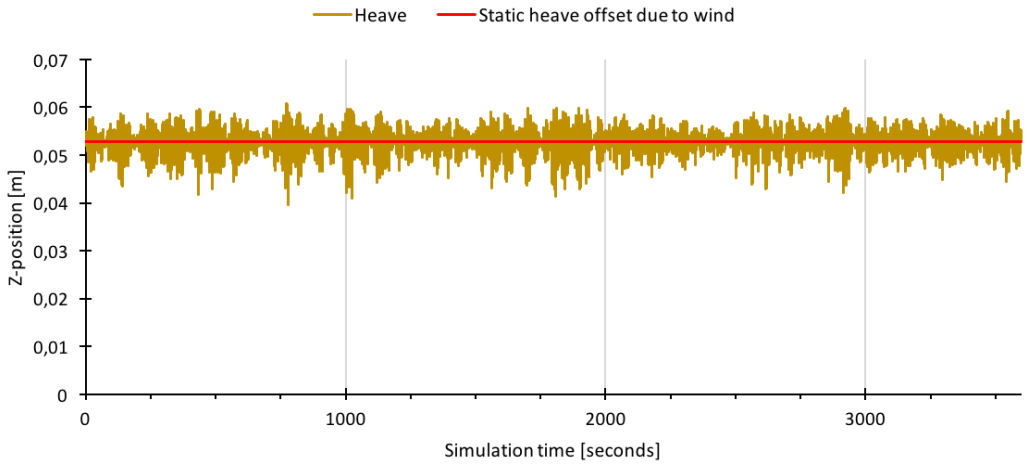

Figure 12-50: Time history heave (0, 0, 50 m) A3-B3-EC2-T0.05

The oscillatory behaviour of the heave motion for this case is limited to ±0.01 m, which is an improvement compared to that of A1-B1, where heave motion was found to oscillate in the interval ± 0.015 m (approximately). Motion in this degree of freedom is sufficiently suppressed in-line with the characteristics of this type of station keeping concept. Comparisons between the cases are discussed in greater detail in the discussion section following the presentation of results. Note that some of the oscillatory behaviour in heave is due to the pitch motion, although this is negligible when pitch is limited/restrained.

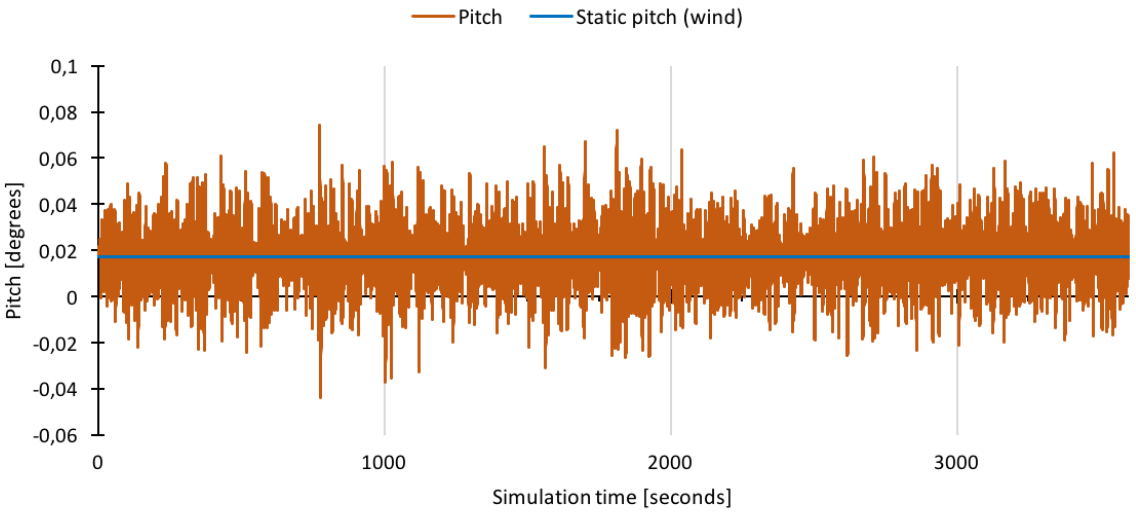

Figure 12-51: Time history pitch (0, 0, 0 m) A3-B3-EC2-T0.05

As can be observed from this time history there seems to be an increase in the variation in pitch compared to the previously presented case (A2-B2). This is likely due to the reduced pontoon radius, as the pre-tension in the case presented above is larger than for A2-B2. This pitch rotation in A3-B3 has also increased relative to A1-B1, which boasts a lower pre-tension. Increased pitch is an indication of greater wave load for this case, as this leads to a greater pitch moment. It should be noted that the pitch angle is limited to relatively small values, which is a characteristic of this type of station keeping concept, largely due to its restraint against rotation.

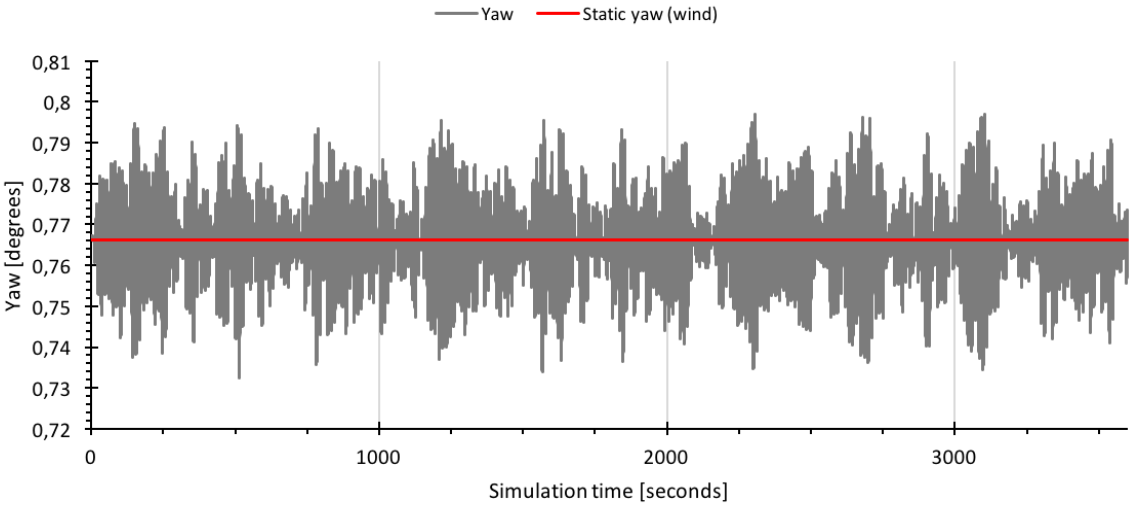

Figure 12-52: Time history yaw (0, 0, 0 m) A3-B3-EC3-T0.05

Similar to what has been observed for this environmental condition from the previous cases, the wave induced yaw motion is insignificant relative to the operational torque contribution. This follows the expectation considering the low values observed in the load and displacement RAO for this wave heading, i.e. the wave acton does not induce significant rotation. The maximum yaw in this time history deviates from the mean by approximately 4%, relative to the operational torque induced yaw (mean).

The figure below shows the time history for the effective tendons at End A (vessel connection).

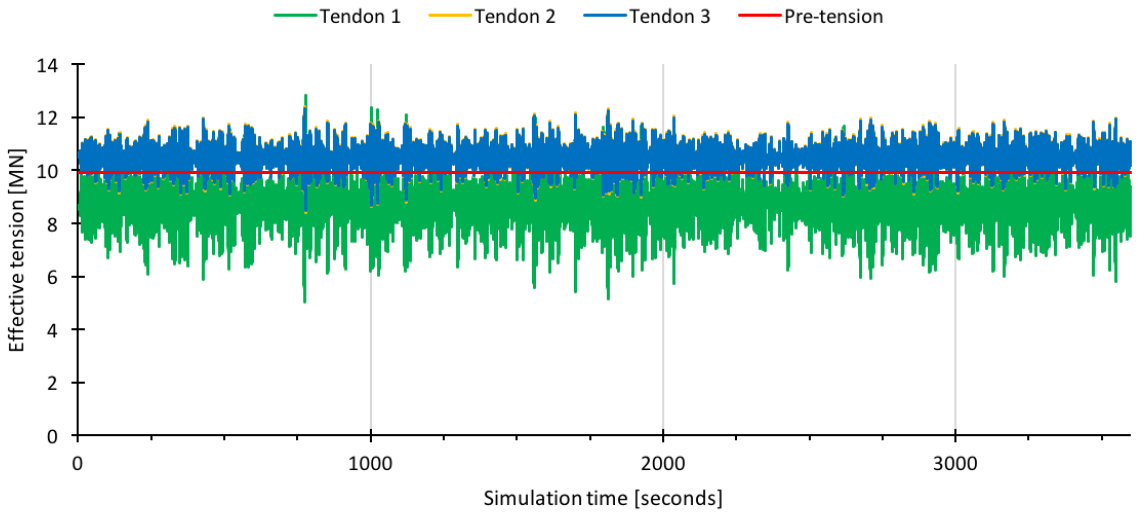

Figure 12-53: Time history effective tension A3-B3-EC2-T0.05

As can be observed from the time history above, the average effective tension in tendon 1 experiences a reduction of around 1 MN relative to the initial pre-tension. This effect is attributed to the moment of the wind force acting at the connection base, which results in a compressive force being applied to the downwind tendon. This also results in an increase in tension on the upwind tendons. This effect is similar to that which was found for the previous cases. No slack occurred in this environmental condition as there is a minimum 5 MN of surplus tension in the downwind tendon, which is sufficient. However, it should be noted that slack tendons were not expected for this sea state, considering the relatively mild condition analysed.

The following table shows the statistical results obtained from the simulation for each of the result categories.

Table 12-34: Summary of statistical results for A3-B3-EC2-T0.05

Variable	Min.	Max.	μ	σ	Units
Motion					
Surge (0, 0, 50 m)	1.006	2.640	1.840	0.238	m
Heave (0, 0, 50 m)	0.040	0.061	0.053	0.003	m
Pitch (0, 0, 0 m)	-0.044	0.074	0.017	0.015	degrees
Yaw (0,0, 0 m)	0.732	0.797	0.766	0.012	degrees
Sea surface clearance (0, 0, 73 m)	19.84	25.69	23.05	0.77	m
Tendons					
Effective tension – tendon 1	4.99E+06	1.28E+07	8.77E+06	1.03E+06	N
Effective tension – tendon 2	8.40E+06	1.24E+07	1.05E+07	5.29E+05	N
Effective tension – tendon 3	8.47E+06	1.23E+07	1.05E+07	5.09E+05	N
Declination – tendon 1	178.99	179.51	179.28	0.07	degrees
Declination – tendon 2	179.18	179.64	179.41	0.07	degrees
Declination – tendon 3	178.95	179.42	179.18	0.07	degrees
Local axis dynamic loads and moments*					
Total Lx-force	-2.78E+06	2.70E+06	2.93E+02	7.17E+05	N
Total Lz-force	-2.52E+04	5.33E+04	1.82E+02	9.18E+03	N
Total Ly-moment	-1.04E+07	1.01E+07	1.22E+03	2.88E+06	Nm
Local axis static loads and moments**					
Total Lx-force	–	–	3.65E+05	9.78E-01	N
Total Lz-force	–	–	2.84E+07	–	N
Total Ly-moment	–	–	4.47E+07	1.20E+02	Nm

As can be observed from the statistical results above, there is no slack observed for this setup, which is an indication of sufficient performance in the operational condition. This is in-line with what was observed for the time history presented earlier. Further comparisons are made in Section 13.1.6.

12.4.3.4 Results EC3

Table 12-35: Input information A3-B3 EC3

	Value	Location relative to local axis
Applied load	1200 kN	122.5 m
Applied torque	0 kNm	50 m
JONSWAP (H_s, T_p, γ)	(12.70 m, 14.1 s, 3.3)	NA
Water depth	200 m	NA
Simulation duration	3600 s	NA

The time histories for surge, heave, pitch and sea surface clearance are presented in the figures below.

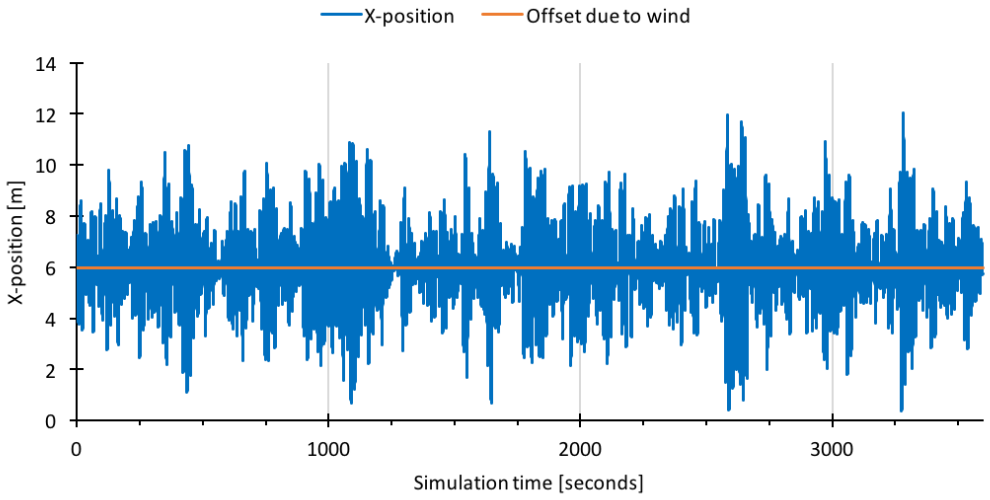

Figure 12-54: Time history surge (0, 0, 50 m) A3-B3-EC3-T0.05

As can be observed in the figure above, the surge component oscillates about the mean offset due to wind. There seems to be significant variation in the surge motion in this sea state, particularly in the interval 2500-2750 seconds.

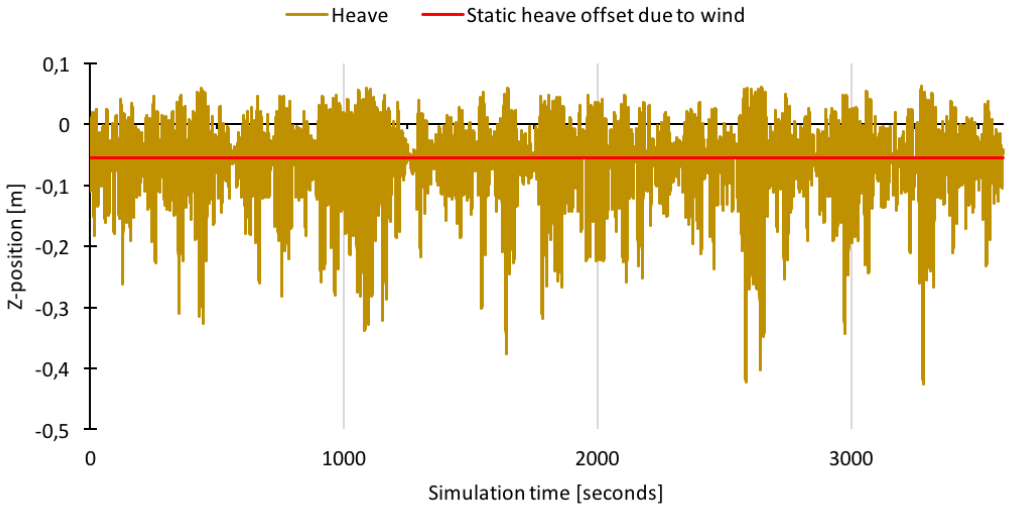

Figure 12-55: Time history heave (0, 0, 50 m) A3-B3-EC3-T0.05

The time history of the heave motion shows a tendency for significant downward translation in the vertical plane during the simulation after 2000 seconds. This is most likely due to loss of tension in the downwind tendon in conjunction with a large wave (the wave records are presented in intervals corresponding to 10% of the simulation time in Appendix D). The motions are typically restrained against large translations in the upwards direction, as these seem to have limited peaks (relative to the static offset due to wind). Again, note that this degree of freedom, at the specified reference point, is to some extent affected by the pitch rotation.

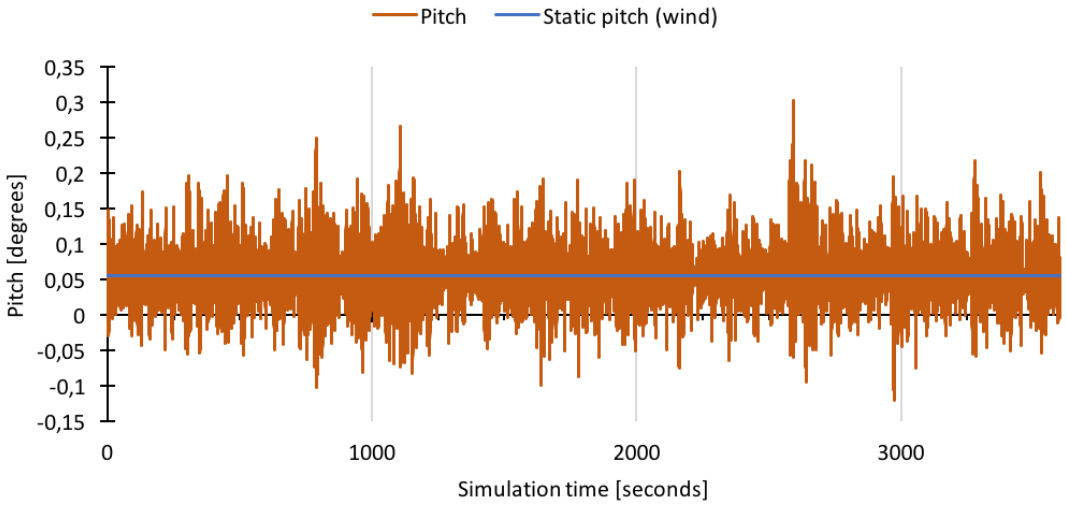

Figure 12-56: Time history pitch (0, 0, 0 m) A3-B3-EC3-T0.05

As can be observed from the figure above, there is significant variation in pitch, which is most likely due to the loss of tension in the downwind tendon as observed in Figure 12-58 (time history of effective tension). Intermittent peaks are observed around 1000 seconds and 2750 seconds.

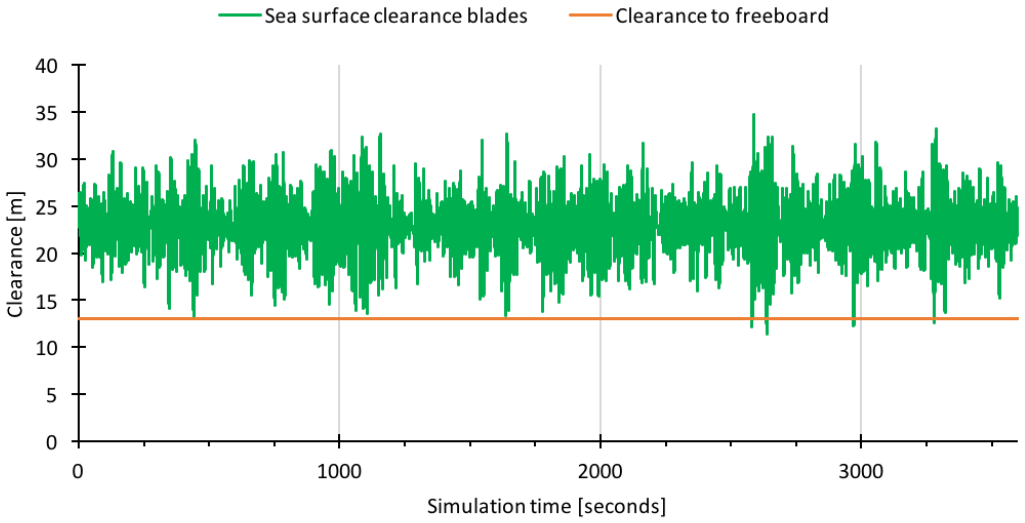

Figure 12-57: Time history sea surface clearance (0, 0, 73 m) A3-B3-EC3-T0.05

As can be observed from the figure above, the air gap between the blades and the sea surface is sufficient at all times throughout this simulation period. However, there are several regions where there is a loss of freeboard, which means that the sea surface extends above the 10 m freeboard set in the analysis. This should however, not be a problem if the hull-turbine connection is watertight, but the loss of freeboard is not ideal. Loss of freeboard may require modifications to the hull.

The figure below shows the time history for the effective tendons at End A (vessel connection).

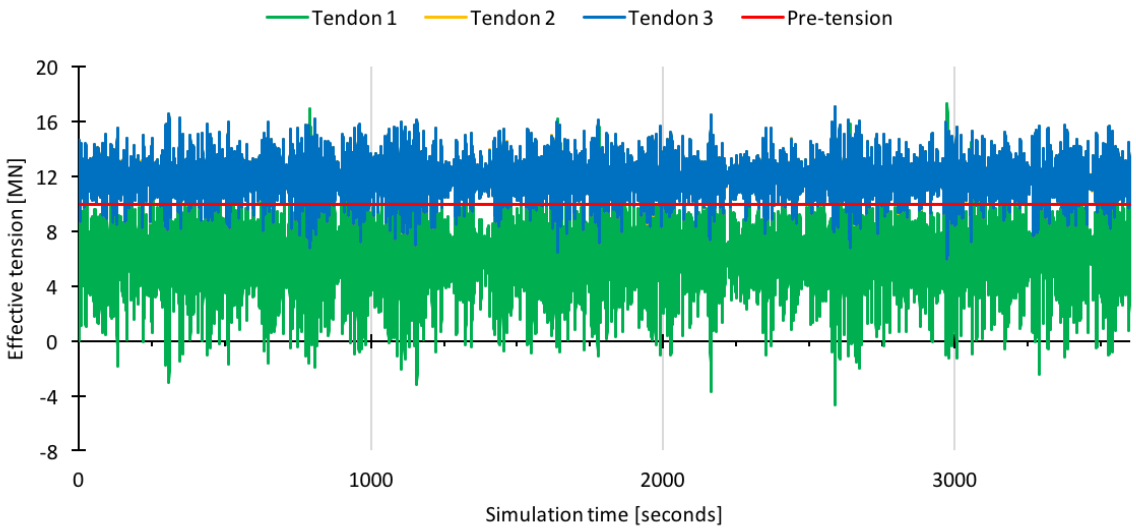

Figure 12-58: Time history effective tension A3-B3-EC3-T0.05

As can be observed from the figure above there is significant variation in the effective tension in all three tendons, where tendon 1 is, as expected, experiencing the most variation in tension. As can be observed from this data there is a significant loss of tension (slack) in tendon 1, which is unacceptable. The variation in general is also deemed too large for this setup because of problems associated with fatigue. Intermittent peaks are also observed for tendon 1 where the instantaneous tension exceeds 16 MN.

The following table shows the statistical results obtained from the simulation for each of the result categories.

Table 12-36: Summary of statistical results for A3-B3-EC3-T0.05

Variable	Min.	Max.	μ	σ	Units
Motion					
Surge (0, 0, 50 m)	0.354	12.038	6.014	1.746	m
Heave (0, 0, 50 m)	-0.426	0.064	-0.066	0.073	m
Pitch (0, 0, 0 m)	-0.119	0.303	0.059	0.046	degrees
Sea surface clearance (0, 0, 73 m)	11.31	34.73	22.81	3.23	m
Tendons					
Effective tension – tendon 1	-4.70E+06	1.73E+07	6.21E+06	2.90E+06	N
Effective tension – tendon 2	5.97E+06	1.71E+07	1.18E+07	1.48E+06	N
Effective tension – tendon 3	5.97E+06	1.71E+07	1.18E+07	1.48E+06	N
Declination – tendon 1	174.94	179.54	177.61	0.60	degrees
Declination – tendon 2	175.68	179.72	177.71	0.62	degrees
Declination – tendon 3	175.68	179.72	177.71	0.62	degrees
Local axis dynamic loads and moments					
Total Lx-force	-9.82E+06	9.97E+06	1.20E+03	2.78E+06	N
Total Lz-force	-1.11E+06	9.79E+05	1.86E+03	1.46E+05	N
Total Ly-moment	-1.43E+08	1.25E+08	8.35E+03	2.72E+07	Nm
Local axis static loads and moments					
Total Lx-force	–	–	1.20E+06	1.24E+00	N
Total Lz-force	–	–	2.84E+07	–	N
Total Ly-moment	–	–	1.47E+08	1.52E+02	Nm

As can be observed from the table above, there is significant variation in tension in tendon 1, where slack state was observed. This is consistent with what was observed in the time history presented earlier, hence this case is not sufficient to withstand the storm condition analysed in this section. Another observation from the data, is the large variation in Ly-moment, where the standard deviation indicates a variation in bending moment of 27 MNm with relatively large probability of occurrence. The static Ly-moment of 147 MNm is also of concern in regards to the envisioned collet connector interface.

12.4.3.5 Time step sensitivity analysis

The time step analysis results are presented in the table below. The same variables are used here as for A1-B1 and A2-B2.

Table 12-37: Time step sensitivity for T0.1 and T0.05 – A3-B3-EC3

Variable	Difference μ	Difference σ
η_1 [m]	0.000%	-0.041%
η_3 [m]	-0.017%	-0.040%
η_5 [degrees]	-0.004%	-0.380%
Effective tension T1	-0.006%	-0.455%
Effective tension T2	0.002%	-0.446%
Effective tension T3	0.002%	-0.456%

As can be observed from the results above, there is little change difference between the two time steps and it is thus concluded that the time step is sufficiently fine for T0.05.

13 Discussion

This section will primarily cover a general comparison of the three cases analysed in this thesis with intermittent reference to values obtained by Bachynski and Moan in [8] and [29] where relevant. The reason for this comparison is that the pre-tension and displacement ranges are to some extent based on the results obtained in the aforementioned articles. Note that there are some fundamental differences between the analyses conducted here and those presented in [8], [29] and [11], especially in terms of turbine type and dimensions, but also the structural dimensions of the TLP's. The comparison with the 5 MW HAWT-TLP is merely used to check if there is a significant difference in results based on an overall engineering judgment rather than direct comparison of values.

13.1 Comparison of vessel properties

13.1.1 Summary of properties

Table 13-1: Vessel properties for moored system (no temporary ballast)

Variable	A1-B1	A2-B2	A3-B3	Units
Section A				
Structural properties				
Outer diameter	9	10	12	m
Draft	60	60	50	m
Displacement	3817	4712	5655	m^3
Inertial properties				
Turbine and generator mass	4.80E+05	4.80E+05	4.80E+05	kg
Steel mass	4.10E+05	4.59E+05	4.84E+05	kg
Permanent ballast mass	2.41E+06	3.11E+06	3.86E+06	kg
Temporary ballast mass	6.04E+05	7.77E+05	9.66E+05	kg
Section B				
Structural properties				
Outer diameter BM	10	10	12	m
Height BM	20	30	30	m
Outer diameter PO	3	3	3	m
Length PO	20	30	20	m
Displacement	2230	3227	4156	m^3
Inertial properties				
Steel mass	6.02E+05	8.31E+05	8.09E+05	kg
Permanent ballast mass	6.74E+05	9.91E+05	1.38E+06	kg
Temporary ballast mass	1.01E+06	1.49E+06	2.07E+06	kg
Mated vessel (moored)				
Total Draft	83	93	83	m
Displacement	6047	7939	9811	m^3
Inertial properties				
Structural mass (incl. VAWT)	1.49E+06	1.77E+06	1.77E+06	kg
Permanent ballast mass	3.09E+06	4.10E+06	5.24E+06	kg
Moment of inertia 1 & 2	7.72E+09	9.12E+09	8.57E+09	$kg \cdot m^2$
Moment of inertia 3	2.21E+08	3.69E+08	3.09E+08	$kg \cdot m^2$
Radius of gyration 1 & 2	41.05	39.42	34.94	m
Radius of gyration 3	6.95	7.93	6.64	m
Centre of gravity and buoyancy				
KG (z)	37.51	42.14	38.01	m
KB (z)	38.40	45.32	41.06	m
Tension capacity				
Pre-tensioning capacity	5.27E+06	7.44E+06	9.96E+06	N
Locked pre-tension capacity*	1.01E+07	1.34E+07	1.71E+07	N
Utilization of total capacity**	34 %	36%	37%	–

*The amount of pre-tension capacity locked in the permanent ballast column

**Assumes that all permanent ballast can be removed to generate extra tension capacity. This may not be the case for several combinations, due to the lack of internal space for temporary ballast only. Stability characteristics will also be affected by this.

13.1.2 Relative differences between the cases for selected values

Selected variables from the table presented in the previous section are presented here in terms of percentage difference relative to the reference case A1-B1. The variables are selected for the discussion of probable trends in the results obtained from the dynamic simulation.

Table 13-2: Relative differences between the cases for selected values

Variable	Units	Reference (A1-B1)	A1-B1	A2-B2	A3-B3
Structural mass	kg	1.49E+06	0 %	+ 19 %	+ 19 %
Permanent ballast mass	kg	3.09E+06	0 %	+ 33 %	+ 70 %
Total draft	m	83	0 %	+ 12 %	+ 0 %
Draft of A	m	60	0 %	+ 0 %	- 17 %
Diameter of A	m	9	0 %	+ 11 %	+ 33 %
Diameter of B	m	10	0 %	+ 0 %	+ 20 %
Displacement	m^3	6047	0 %	+ 31 %	+ 62 %
Tether radius	m	25	0 %	+ 40 %	+ 4 %
Pre-tension	N	5.27E+06	0 %	+ 41 %	+ 89 %

As can be observed from this table, case A2-B2 represents a slight general increase in all of the variables specified above whereas case A3-B3 represents a significant increase relative to A1-B1. This is particularly evident in variables such as the pre-tension per tendon, displacement and permanent ballast mass. Note that this table is presented for later reference when discussing the effective tension in the tendons and motions of the vessel across each case.

13.1.3 Comparison of cost performance

Although cost efficiency was not a central part of this thesis, it will have a clear effect on the selection of a potential design. The cost performance is based on the total mass of ballast and steel, where the tendons are included. This comparison will be of a qualitative nature, where a relative comparison of the aforementioned variables will provide the basis or evaluating the cost performance. The qualitative measures are presented under the cost effect column in the table below, where steel mass of the hull is expected to have the most significant effect on cost increase, followed by steel mass in the tendons. The hull is believed to be the dominant factor in costs, due to manufacturing complexity and needed equipment. The case values are presented as percentages relative to a source of reference (which in this case corresponds to case A1-B1).

Table 13-3: Qualitative cost comparison for the three cases.

	Cost effect	Reference	A1-B1	A2-B2	A3-B3
Steel mass (hull)	+ + +	1.01E+06	+ 0 %	+ 28 %	+ 28 %
Steel mass (tendon)	+ +	3.37E+05	+ 0 %	+ 0 %	+ 7 %
Permanent ballast mass	+	3.09E+06	+ 0 %	+ 33 %	+ 70 %
Cost performance	N/A	0	0	+ +	+ + +

As can be observed from the table above, it is clear that the cost performance is affected for each case step. Note that the permanent ballast mass has been assumed to contribute slightly to an increase in costs, but due to the significant difference between A1-B1 and A3-B3, this is believed to have a significant effect on the cost performance. The cost performance of A1-B1 is set to 0 as this is the reference case. Note that (+) in cost performance means that there are increased costs associated with this case relative to A1-B1. For detailed information about the associated steel mass for each case refer to Table 13-1.

13.1.4 Comparison of natural periods in moored/floating condition

Table 13-4: Natural periods for each case (free)

Degree of freedom	A1-B1	A2-B2	A3-B3		Reference	A1-B1	A2-B2	A3-B3
Surge (η_1)	∞	∞	∞		∞	0 %	0 %	0 %
Sway (η_2)	∞	∞	∞		∞	0 %	0 %	0 %
Heave (η_3)	20.71	21.33	19.53		20.71	0 %	+ 3%	– 6 %
Roll (η_4)	36.55	30.38	27.29		36.55	0 %	– 17 %	– 25 %
Pitch (η_5)	36.55	30.34	27.29		36.55	0 %	– 17 %	– 25 %
Yaw (η_6)	∞	∞	∞		∞	0 %	0 %	0 %

As can be observed from the natural periods in the floating condition (in ballasted state, and no tendons attached), there are relatively small differences between the natural periods in heave. The natural periods in roll and pitch observe larger variations across the cases. These natural periods are only applicable for discussion of the load and displacement RAOs and do not apply to the moored state. The natural periods for the moored state are presented below.

Table 13-5: Natural periods for each case (moored)

Degree of freedom	A1-B1	A2-B2	A3-B3		Reference	A1-B1	A2-B2	A3-B3
Surge (η_1)	40.73	38.772	37.86		40.73	0 %	– 5 %	– 7 %
Sway (η_2)	40.73	38.772	37.86		40.73	0 %	– 5 %	– 7 %
Heave (η_3)	0.625	0.706	0.797		0.625	0 %	+ 13 %	+ 28 %
Roll (η_4)	2.13	1.115	1.496		2.13	0 %	– 48 %	– 30 %
Pitch (η_5)	2.13	1.115	1.496		2.13	0 %	– 48 %	– 30 %
Yaw (η_6)	14.29	11.560	11.86		14.29	0 %	– 19 %	– 17 %

As can be observed from the table above the natural periods in surge, sway, roll, pitch and yaw are largest for case A1-B1. This follows the expectation since this case featured the lowest total pre-tension, which is a key factor affecting the natural period of the system due to the reduced stiffness (refer to background theory). As can be observed from the relative differences in natural periods (to target A1-B1), there is a general trend in reduction in the natural periods, with heave being the exception. The heave natural periods tend to increase with mass for systems with equal number of tendons and identical tendon properties (refer to equation (6.4)). The difference in total mass (considering structural/ballast mass only[15]) of the system is significant (comparing A3-B3 and A1-B1) as there is a 19% increase in structural mass and a 70% increase in permanent ballast mass. In addition, there is an increase in tendon length for A3-B3 of 7% relative to A1-B1. The natural periods in surge (and sway) experience a reduction with each case, which is most likely attributed to the increase in pre-tension, refer to equation (6.5).

As has been discussed above, the reductions in natural periods for surge and sway are attributed to differences in pre-tension (the mass of the system has an increasing effect here, but the increase in mass was counteracted and exceeded by the increase in pre-tension), whereas heave is attributed to mass/displacement. The rotational degrees of freedom do not exhibit a clear relationship as there are no identifiable trends in terms of a change in one variable (i.e. pre-tension or mass/displacement) as for the three translational DOFs. For pitch/roll and yaw, the effect seems to be dependent on both the pontoon radius and pre-tension. The reasoning behind this is that there is no significant difference in pontoon radius for A1-B1 and A3-B3 (4%), which on its own cannot explain the 30% and 17% difference between the natural periods in the rotational DOFs. This is most likely attributed to the difference in pre-tension of 89% when comparing A1-B1 and A3-B3. For A2-B2 the pre-tension is 41% larger than for A1-B1 with an associated reduction of 48% in the natural period for roll and pitch. This means that there is a significant contribution from the extended pontoon radius in A2-B2 (40%). This follows the expectation as the structure is stiffer against pitching as the moment arm is significantly larger with increase in pontoon radius. The same reasoning can be applied to explain the differences in natural periods in yaw.

To summarize, case A1-B1 seems to be, on average, a less stiff system compared to the other two cases. Referring back to the initial design criteria presented in Table 6-2 on page 39, each system satisfies the natural period requirement in surge/sway (> 25 s), heave (< 3.5 s), and roll/pitch (< 3.5 s). However, as stated in [29], it was recommended that the natural periods in surge/sway be larger than 45 seconds for improved characteristics in a storm scenario. The natural periods of the floaters above, did not satisfy this criterion, which may be an explanation

[15] The added mass will also have a considerable effect here if one observes the general equation for the natural period presented in the background theory of this thesis.

of the consistent appearance of slack in tendon 1 (EC3) for each of the studied cases, as the natural period in surge were likely too short.

As the natural periods in surge and sway were most significantly affected by pre-tension, it is not possible to adjust the natural period, to fit this criterion, by a reduction in permanent ballast fraction. Doing so would lead to an increase in pre-tension, which would, in line with what has been discussed previously, not allow for an increase in natural period. Improvements may only be found by increasing the length of the tendons, which for constant vessel geometry means that the system must be installed in deeper waters to achieve the desired effect, but this is not discussed further in the present work.

Note that the following discussions will typically be expressed in terms of angular frequencies, hence conversions of the natural periods for the floating and moored state to natural frequencies in rad/s is provided in the tables below for clarity.

Table 13-6: Natural frequencies (rad/s) for each case (floating)

Degree of freedom	A1-B1	A2-B2	A3-B3
Surge (η_1)	0	0	0
Sway (η_2)	0	0	0
Heave (η_3)	0.303	0.295	0.322
Roll (η_4)	0.172	0.207	0.230
Pitch (η_5)	0.172	0.207	0.230
Yaw (η_6)	0	0	0

Table 13-7: Natural frequencies (rad/s) for each case (moored)

Degree of freedom	A1-B1	A2-B2	A3-B3
Surge (η_1)	0.154	0.162	0.166
Sway (η_2)	0.154	0.162	0.166
Heave (η_3)	10.053	8.900	7.884
Roll (η_4)	2.950	5.635	4.200
Pitch (η_5)	2.950	5.635	4.200
Yaw (η_6)	0.439	0.544	0.530

13.1.5 Comparison of hydrodynamic properties

The following section presents a comparison of the frequency dependent potential damping and added mass for each respective case. In addition to this comparisons of the displacement RAOs and load RAOs for the wave heading analysed in the dynamic simulation are presented. This corresponds to a wave heading of 0°.

13.1.5.1 Frequency dependent potential damping

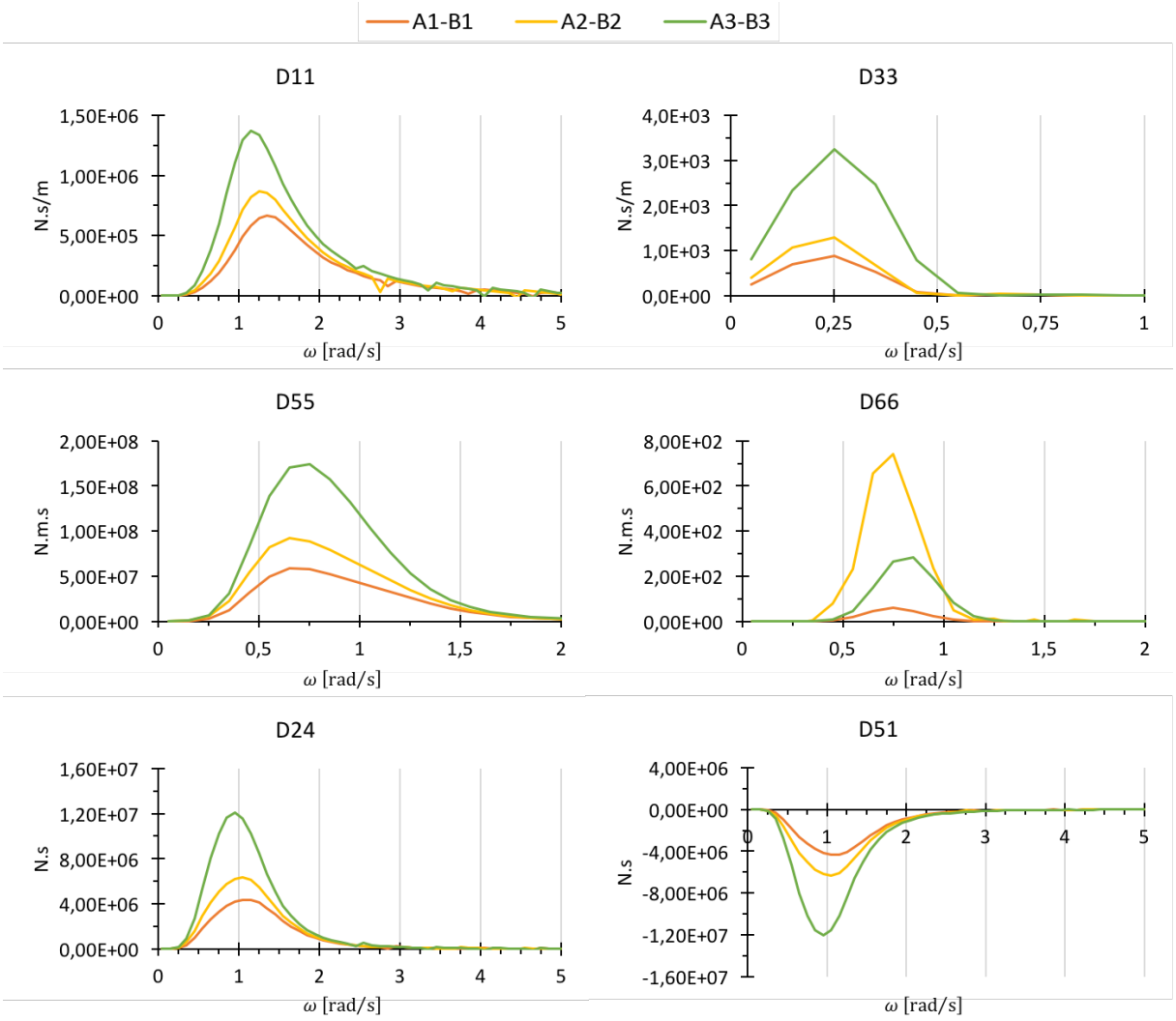

Figure 13-1: Comparison of potential damping across cases

As can be observed from the figures above, there is a significant difference between the cases regarding the potential damping values in each matrix position. In general terms the damping values for case A3-B3 tends to be larger than for cases A1-B1 and A2-B2. Note that all cases tend to have zero damping for higher frequencies.

As observed in D11, the peak is largest for A3-B3 with a slight shift in peak frequency towards the lower frequency range. The differences in D11 are most likely explained by reference to the relative difference in the diameter of section A and B, which are 33% and 20 % larger than A1-B1 respectively, but also the general increase in displacement (62%). The difference between A1-B1 and A2-B2 is less pronounced than the previously discussed case (A3-B3).

For D55 the change in peak frequency is the opposite of what was observed for D11, where A3-B3 had a peak frequency around 0.75 rad/s compared to the other two cases which had similar peak frequencies at around 0.60 rad/s, i.e. there was a slight transition towards the higher frequency ranges. The difference between the magnitude of the peaks seems to follow a similar pattern as observed for D11.

One observation made from this set of figures is that there seems to be relatively little effect on the damping in D33, with reference to the pontoon radius. Based on the geometric properties of the three vessels analysed in this

thesis, it was initially expected that the difference in D33 would be significantly larger between A1-B1 and A2-B2 as these have the same BM diameter of 10 m, but A2-B2 has 40% larger pontoon radius. Since the pontoons are extrusions from the main body in the horizontal plane it was expected that these would yield a greater effect than what was observed. If one observes the difference between A1-B1 and A3-B3, it is clear that there is a significant effect on D33 as a result of a 2 m increase in diameter. One explanation for this phenomena here is that the potential damping contribution of the pontoons tend to decrease with depth[16], because there is limited surface wave generation from the deeper sections of the structure. This is clearly observed for A3-B3, where the draft is reduced by 17% compared to the other two cases, which means that the pontoons are closer to the surface, and hence will have a greater effect on the overall generation of surface waves, in line with the theory presented in Section 5.5.1.3 on page 26. The effect is still limited due to this decrease in draft, as the magnitude of damping in this DOF is 0.23% relative to the magnitude in D11 (by comparison of peaks).

The only exception is D66, where A2-B2 yields the largest peak in the data set. This is likely attributed to the fact that the pontoons are longer for this case. The difference in pontoon radius is more pronounced for this case where a relative difference of 40% is observed based on the pontoon radius of A1-B1. The increase in the peak of D66 from A1-B1 to A2-B2 is approximately 700%, which is significant. However, the general magnitude of damping in D66 is small compared to the damping observed in D11, D55 etc., which is related to the fact that the pontoons are situated far below the water [22]. The peak frequency (approx. 0.75 rad/s) seems to be the same for A2-B2 and A1-B1, but does not apply to case A3-B3. The differences between the peak frequencies are not particularly significant, and the difference for A3-B3 may be due to the resolution of the frequency set.

13.1.5.2 Frequency dependent added mass

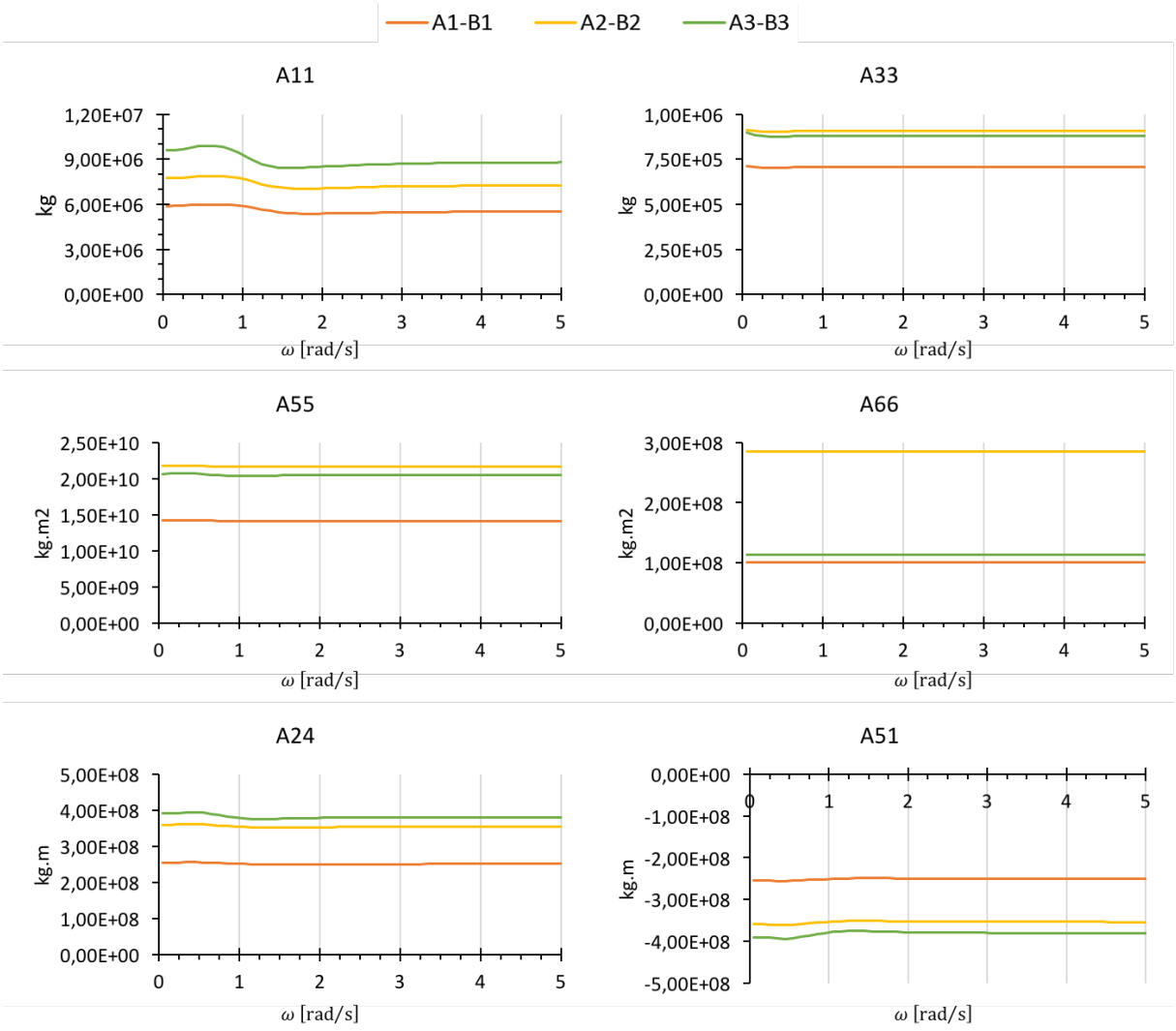

Figure 13-2: Comparison of added mass across cases

[16] The reader is directed to the potential damping chapter, in the background theory, for more detail on this.

The figure above shows the added mass values for A11, A33, A55, A66, A24 and A51 for each of three cases studied. The general trends observed for added mass are somewhat different to what was found for the potential damping values discussed in the previous section, as A2-B2 seemed to yield larger values than case A3-B3, which tended to have significantly greater damping values than the other two cases.

As previously presented in Table 13-2, the difference between the displacements of A1-B1 and A3-B3 amounts to 62%, where the difference in added mass for A11 at ~0 rad/s amounts to approximately 50% increase. The relative differences between the cases, with regards to added mass in A11, seems to approximately follow the relative difference in displacements (50% change in displacement ≈ 50 % change in added mass in A11). This does follow the expectation based on the transverse added mass equation for a cylindrical structure as presented in Section 5.5.1.2. The reason being that the transverse added mass in surge is equivalent to the displaced mass of water, from equation (5.39) on page 24.

The added mass in A33 does not follow the typical trend observed from the damping values as A3-B3, being the largest vessel, tends to yield the largest values. This is explained by the extension of pontoon radius in A2-B2 relative to A1-B1 (+40%) as these two cases both feature a buoyancy module diameter of 10 m, which is the only other contributor to added mass in heave for these cases. The expectation was that longer pontoons would, indeed, increase the heave added mass as confirmed based on these results. A plausible explanation for the inconsistency for which case yields the maximum value in added mass vs. the case in damping is that the effect of added mass in heave does not decay with depth in a similar manner to what is observed for potential damping. An increase in pontoon length of 40% vs. a change in buoyancy module diameter of 20% seems to give the same added mass in heave, i.e. the heave added mass is more sensitive to the increase in BM diameter (raised to the third power when using the hemi-spherical added mass approximation) than an equal, relative increase in pontoon length. Although not assessed here, an increase in pontoon diameter will likely have a significant effect on the added mass in heave, if one takes into account the transverse added mass equation (5.39), in which the diameter is raised to the second power.

For A55, A2-B2 also seems to yield the largest overall value in added mass, however the difference between this case and A3-B3 is relatively small. One reason for this may be the fact that the total draft of vessel A2-B2 is 10 m larger (12% relative increase) than the other two cases, in addition to an increase in pontoon radius of 40% (relative to A1-B1).

The most significant difference between the three cases is observed for A66, where A2-B2 yields a stable added mass in yaw approximately 3 times larger than that for A1-B1 and A3-B3. There is a slight difference between A1-B1 and A3-B3, which is likely due to the increase in pontoon radius (4%) due to the 20% increase in BM diameter for A3-B3. From this set it is clear that the added mass in yaw is significantly affected by the pontoon radius, which is expected as a cylindrical vessel without pontoons is expected to yield no added mass in yaw [8], due to the lack of eccentricity.

A24 and A51 show similar trends to that which was observed for A55 except A3-B3 yields larger values than A2-B2, but these are not discussed in further detail.

13.1.5.3 Displacement RAOs

The following figure shows a comparison of the displacement RAOs for the selected structures with focus on the analysed wave direction (0°) in each relevant degree of freedom.

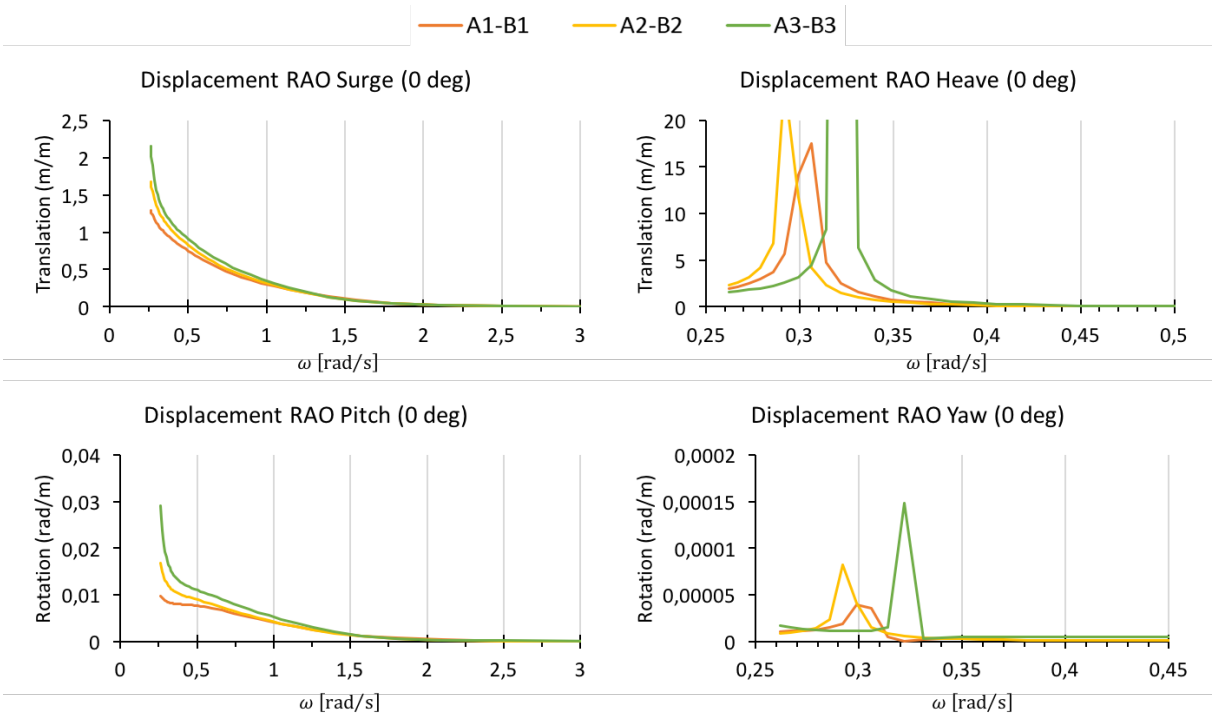

Figure 13-3: Comparison of displacement RAOs in 0° wave heading

As can be observed from the figure above, there are some fundamental differences between the displacement RAOs for the different cases. The surge displacement RAO seems to more or less coincide for the three cases, but with more pronounced differences occurring at the lower frequencies. The amplitude of surge per meter doubled for case A3-B3 compared to A1-B1. This is likely due to the increase in diameter of section A for A3-B3, which again leads to a more significant "catching" of the wave, leading to a larger displacement as the natural frequency for this degree of freedom is undefined.

The heave displacement RAO exhibits clear resonance peaks for each of the three cases, but with varying magnitudes. This is because of the fact that case A3-B3 had a natural period in heave which, by chance, was matched in the frequency set to three significant figures. The figure was cut-off at 20 m/m amplitude as the values for the amplitude at the resonance frequency is not of particular interest in this context. Peak frequencies differ for the three cases, as is expected due to the differences in natural period in heave, presented in Table 13-4, where A3-B3 had the lowest natural period (highest frequency).

The displacement RAO in yaw results in relatively low values in terms of the rotation amplitude for the presented wave heading. This is in line with the expectation as the specified direction does not induce particularly significant rotations due to the XZ plane symmetry of these structures. By this it is meant that an incident wave will provide a positive rotation on the positive side of the XZ plane (following the direction of the positive y-axis), but an equal but opposite rotation on the negative side. This means that, ideally, the vessel yields no net rotation for this wave direction. Although there are three distinct peaks present, these peaks occur at frequencies coinciding with the heave natural frequencies (observed in the heave displacement RAOs), which means that the induced motions in yaw may be due to some overlapping of heave motion, but it is worth noting that this reasoning is somewhat speculative.

13.1.5.4 Load RAOs

The following figure shows a comparison of the load RAOs for the selected structures at a direction of 0°, corresponding to the wave heading analysed during the dynamic simulation phase.

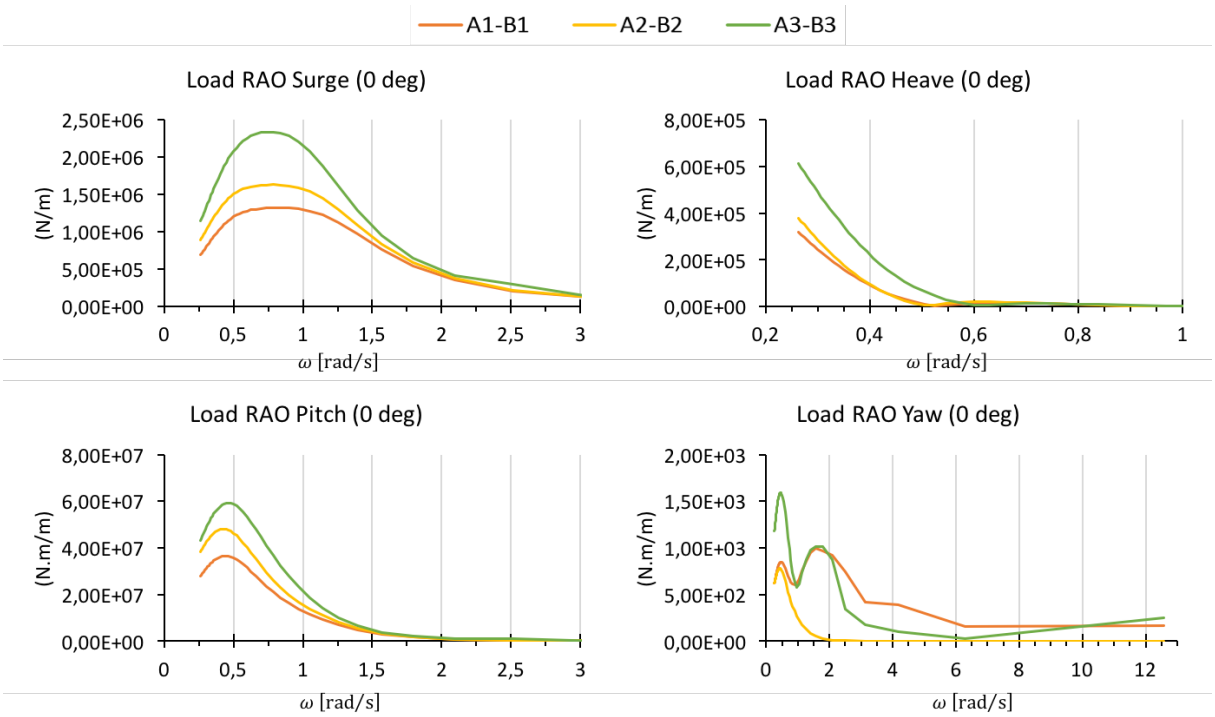

Figure 13-4: Comparison of the load RAOs for a wave heading 0°

The load RAOs presented above do not follow the same behaviour as observed for the displacement RAOs. Non-zero amplitudes are found across a much wider spectrum of frequencies than that which was found for the displacement RAOs. This is particularly evident for heave and surge, as non-zero values are obtained near 0.5-0.6 rad/s and 3.5 rad/s respectively, but does not apply to the pitch load RAO. In terms of general magnitude pitch and surge experience the largest values across each case. Yaw is, relative to the other DOFs, insignificant as one would expect based on the overall geometry of these vessels (with particular reference to pontoon depth) and the presented wave heading.

There seems to be a general trend where case A3-B3 yields the largest magnitude across all DOFs. This is likely related to the overall displacement for this case, as this is 62% larger than the reference case A1-B1. The surge load RAO is significantly larger than the other two cases, which may be explained by the 33% increase in diameter of section A, but also due to the reduction in draft of A. The added mass in surge (linked to displacement) is significantly larger for A3-B3 compared to A2-B2 and A1-B1, which may also help to explain this significant increase in load RAO. The reduction in draft means that the pontoons are closer to the water line, which may cause the pontoons to experience a greater wave load at the lower frequencies. The lower frequencies result in increased wave length, which in turn leads to more significant wave action at lower depths; in line with linear wave theory and the principle of depth decay. In relation to the peak frequency, there seems to be little difference between the three cases in surge.

The load RAO in pitch sees a slight shift towards the higher frequencies for case A3-B3 relative to the other two cases. The general observation in terms of magnitudes, for the pitch load RAO, is that there seems to be an equal difference between two subsequent cases, i.e. the difference between A1-B1 and A2-B2 matches the difference between A2-B2 and A3-B3. The exception to this observation is that A3-B3 seems to retain significant pitch load for higher frequencies than the other two cases (evident at a frequency of 1 rad/s). The pitch load RAO does not follow the same excessive difference between A2-B2 and A3-B3, which may be attributed to the somewhat similar added mass for the aforementioned cases (refer to Figure 13-2). The radii of gyration for the three cases are 36.93 m, 35.56 m, and 31.34 m for cases A1-B1, A2-B2 and A3-B3 respectively (ballasted condition). The difference in radii of gyration correspond to reductions of 4 and 15% relative to A1-B1 respectively. The reason for the difference in the pitch load RAO is unclear due to the complexity of the underlying expression, which makes it difficult to pinpoint which variable(s) causes this difference. Based on the information available, it seems that the pitch load RAO may express a certain sensitivity to the total displacement.

The load RAO in yaw seems to exhibit some degree of irregular behaviour, but since this load RAO yields relatively low amplitudes this is not deemed particularly important for the system as a whole. Note that pontoon depth is likely the root cause for the low load RAOs in yaw, due to reduced wave action with depth.

13.1.5.5 General remarks

All in all, there seems to be a consistent relationship between an increase in vessel displacement (increased dimeter at the water line) and the overall hydrodynamic properties. This is particularly evident for the potential damping coefficients, where A3-B3 (boasting the largest overall displacement and diameter in the water line) seems to yield the largest values in general terms. The effects seem to vary with the degrees of freedom, as A2-B2 yields larger values in pitch/heave/yaw added mass and potential damping in yaw. It is worth noting that the hydrodynamic properties of the selected cases are somewhat misleading as the mated condition is only valid for the moored state. The hydrodynamic properties were evaluated for an un-moored mated case, with significant differences in inertial properties in the free floating state compared to the moored state. In other words, the evaluation of hydrodynamic properties are based on an un-coupled system (no tendons attached).

The hydrodynamic properties do seem to follow a certain trend with displacement as the geometrical properties of the three cases are, to some extent, identical; i.e. the structures exhibit similarities in the overall shape. By this it is meant that all three cases feature one surface-piercing column, with three pontoons of similar cross sectional properties, and have the same total operating draft (with A2-B2 being one exception to this rule). Since the cases are similar in terms of overall vessel properties it is clear from the hydrodynamic properties that they follow more or less the same type of trends, where larger values are usually observed for the lower frequency ranges. This is particularly evident for the displacement RAOs.

13.1.6 Comparison of simulation results

As can be observed from the simulation results presented under each case (Section 12) there are several differences observed in the variation in motions and effective tension between the analysed cases in this thesis. In the following section a comparison between the three cases, with focus on the aforementioned variables and environmental conditions, is presented. Comparisons are made in terms of mean and standard deviations with reference to maximum values where relevant. The spectral density of the effective tension in tendon 1 under the two environmental conditions is also presented in this section. In addition to the effective tension and general motions of the system, comparisons of the A-B connection load and moments are also included.

13.1.6.1 Motions

The motions of the system are an important segment of this analysis, with particular focus on the surge and pitch motions. Some discussion of the yaw motion is also included, since the VAWT power generation results in a net torque being applied about the local z-axis of the system. Large rotations in yaw are unfavourable[17] to the connection system. The motion results are presented below for each case and environmental condition.

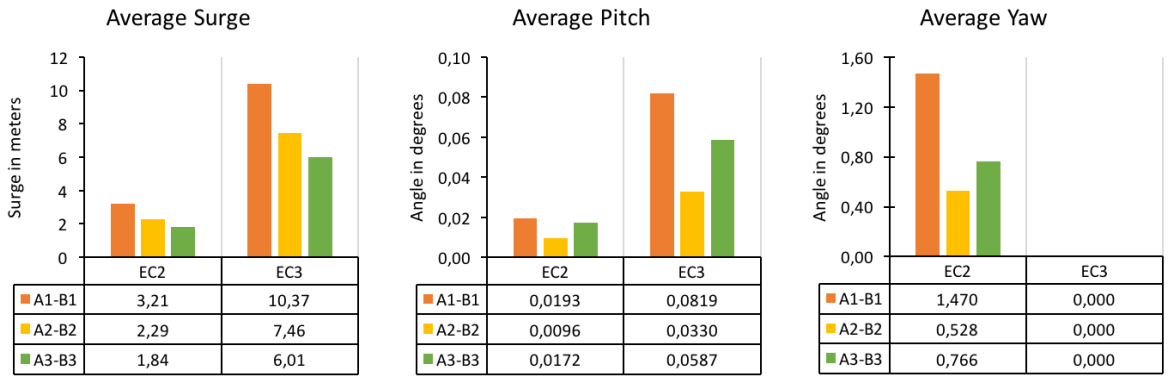

	EC2	EC3
A1-B1	3,21	10,37
A2-B2	2,29	7,46
A3-B3	1,84	6,01

	EC2	EC3
A1-B1	0,0193	0,0819
A2-B2	0,0096	0,0330
A3-B3	0,0172	0,0587

	EC2	EC3
A1-B1	1,470	0,000
A2-B2	0,528	0,000
A3-B3	0,766	0,000

Figure 13-5: Comparison of average motions for the three cases

[17] As drafted in the TLP considerations chapter, the angle at the connection point should be limited to small values corresponding to roughly 5% of the water depth [29], which implies a 10 m offset in surge.

As can be observed from the figure above, the average surge motion decreases from A1-B1 to A3-B3, which may be attributed to the increase in pre-tension as suggested by Equation (6.1). The same trend is observed in both environmental conditions, but the differences between the cases seems to be more pronounced for EC3. For pitch the behaviour is different, as A2-B2 yields a significantly lower average pitch angle compared to the other cases. EC2 seems to result in similar characteristics for A1-B1 and A3-B3, which is an indication that the pontoon radius is critical for motion in this DOF. The reason being that the pre-tension of A3-B3 is larger than A1-B1 by a factor of 1.63, which if pre-tension was critical, should yield a more pronounced difference. For the average yaw motion it is clear that A2-B2 has the most favourable characteristic as it achieves a lower angle of rotation at a reduced pre-tension relative to A3-B3. This follows the initial expectation, as the restoring moment in yaw is dependent on the pontoon radius to the second power and pre-tension to the first power (refer to equation (6.2)). Note that the mean yaw angle is zero in the storm state, as there is no applied torque in this environmental condition (i.e. the VAWT is parked), and the waves are not able to induce a significant yaw motion. This is also observable from the displacement and load RAOs presented earlier in this discussion.

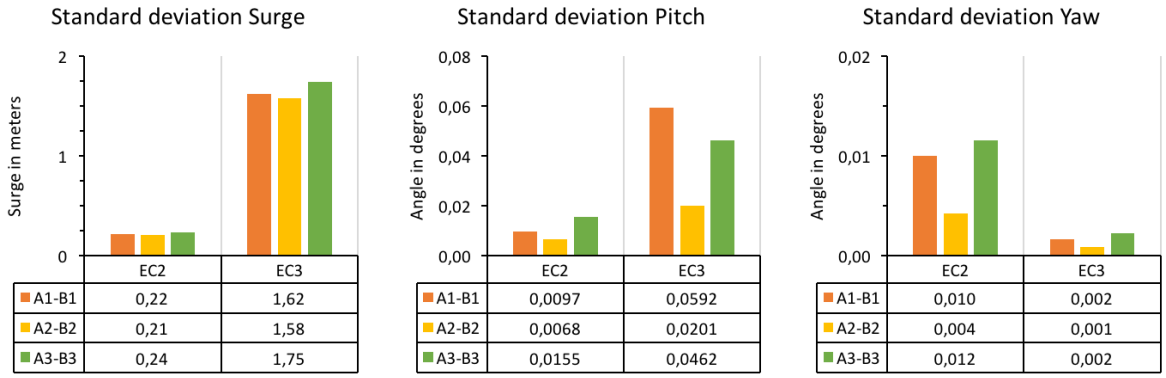

	EC2	EC3
A1-B1	0,22	1,62
A2-B2	0,21	1,58
A3-B3	0,24	1,75

	EC2	EC3
A1-B1	0,0097	0,0592
A2-B2	0,0068	0,0201
A3-B3	0,0155	0,0462

	EC2	EC3
A1-B1	0,010	0,002
A2-B2	0,004	0,001
A3-B3	0,012	0,002

Figure 13-6: Standard deviation of surge, pitch and yaw

The surge motions exhibit slightly different behaviour across the cases compared to the average values (which correspond to the translations/rotations associated with the static wind load). The standard deviation in surge for A3-B3 is slightly larger than the other two cases, which is likely due to the increased surge load for this case (refer to Figure 13-14 pp. 170). This effect may, to some extent, also be attributed to the slightly longer tendons for this case due to the reduction in draft of Section A. This has an adverse effect on the stiffness in surge given by equation (5.34), but it should be noted that increased pre-tension results in a subsequent increase in stiffness. However, an increase in tendon length cannot explain this increase in surge as the difference in pre-tension is greater, percentagewise, compared to the increase in tendon length. The increased wave load excitation is likely the underlying for the increase in standard deviation.

In pitch, case A2-B2 boasts the lowest standard deviation in both EC2 and EC3. For A1-B1 and A3-B3 the standard deviation in pitch seems to vary with EC2 and EC3. A1-B1 has the greatest standard deviation in EC3, which is most likely a result of the increased severity of the slack condition observed for tendon 1. In the operational condition A3-B3 seems to experience the greatest variation in pitch angle, which again may be explained by the increased surge load for this structure, due to increased diameter in the waterline, but may also be affected by the slightly shallower depth of the pontoons. Note that the variations in yaw are typically low, for similar reasons as previously discussed regarding balance of load across the XZ plane. The variation is slightly larger for EC2 because of the induced angle of the vessel as a result of the input torque, which means that the vessel is no longer laterally symmetric relative to the incoming wave. As presented under the results chapter, the yaw displacement and load RAOs are sensitive to wave direction. However, one should note that the induced mean angle in yaw is less than 1.5° (for all cases), which is not a large enough angle to have a significant effect on the observed wave direction of the vessel.

On a general case-by-case basis, it is clear that the motions are most severe for A1-B1, and A2-B2 has the most favourable motion characteristics overall. Note that slack tendons were observed for all cases, which has an effect on the output results in regards to the motions, particularly in EC3. The slack condition was less pronounced for A2-B2, which has likely had an effect on the motion characteristics as well.

13.1.6.2 Spectral density of effective tension in tendon 1

The following figure presents the spectral density of effective tension in tendon 1 for cases A1-B1, A2-B2 and A3-B3 for environmental condition 2 and 3. These plots were generated by Fourier analysis of the time histories in OrcaFlex with a frequency interval of 0.02 Hz.

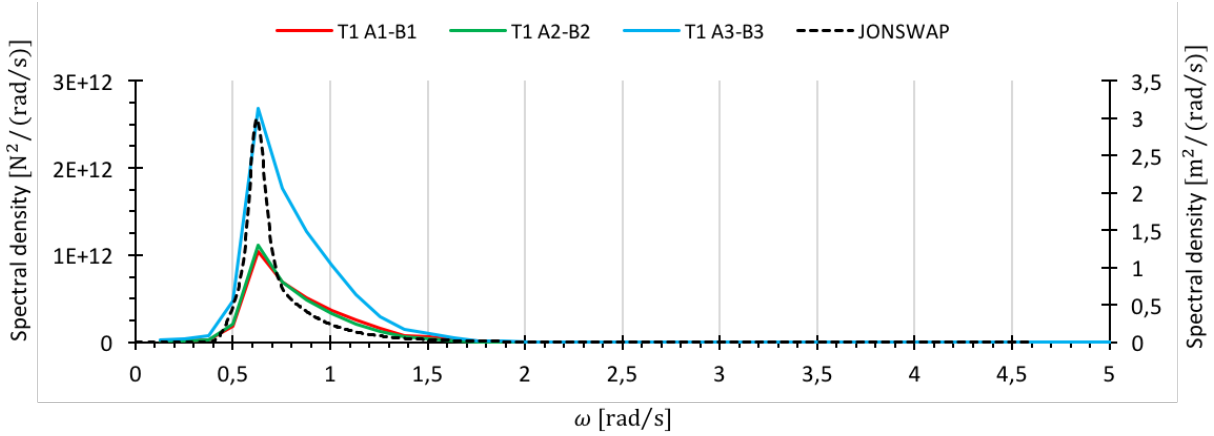

Figure 13-7: Spectral densities for tendon 1 in EC2

The figure above shows the three spectral densities for each case with the JONSWAP spectra for the specified environmental condition (values on the secondary axis). In general, the peaks for each spectral density (effective tension in tendon 1) coincide with the peak of the JONSWAP spectra. As can be observed from this figure the peaks for A1-B1 and A2-B2 yield similar values at around $1 \cdot 10^{12}$ N^2/s, whereas A3-B3 gives a significantly larger value at $2.75 \cdot 10^{12}$ N^2/s. The tension spectra seem to have a more pronounced envelope of frequencies with significant values observed from 0.5 to 1.2 rad/s. No effects are observed in frequencies exceeding 2 rad/s, which is reasonable considering the fact that there are no significant concentrations of energy in this region (if one observes the wave spectra). The peak values that coincide with the peak frequency of the wave spectra are due to first order wave excitation [8].

As observed from the figure above, it is clear that there is a significant difference in the broadness of the tension spectra in comparison to the JONSWAP spectra. This is likely a result of, for example, the surge load RAO presented in Section 13.1.5.4, as significant load amplitudes are observed between 0.7 and 1.5 rad/s. In this frequency interval one observes values (for the JONSWAP spectra) between 1 and 0 $m^2 \cdot s$, which by cross reference with the the load RAO gives significant values in surge load. The tendon load however, is not only dependent on the surge load, but also loads in heave (loss or increase in submerged volume due to passing waves), set down effects etc. as discussed under the TLP principles chapter earlier on.

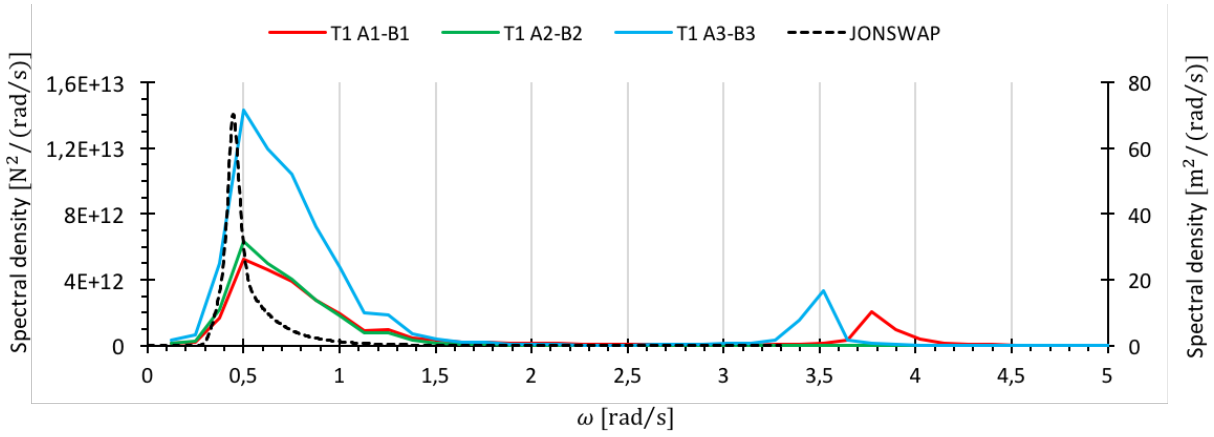

Figure 13-8: Spectral densities for tendon 1 in EC3

The figure above shows the spectral densities (tension in tendon 1) for cases A1-B1, A2-B2 and A3-B3 in EC3. As can be observed from this figure, there seems to be a slight difference in the peak frequency of the wave spectra compared to the peak frequencies for the tension spectra for each of the three cases, but these differences are relatively small. This difference in peak frequency may be due to the selected frequency interval, as the difference corresponds roughly to one interval (0.02 Hz ≈ 0.12 rad/s). The low frequency peaks are, similarly to EC2,

determined to be a result of 1st order wave excitation, similarly to [8]. These peaks have a similar relationship between the three cases as was observed from the operational environmental condition.

One notable difference in this environmental condition is the observation of two pronounced peaks at higher frequencies for A1-B1 and A3-B3. These peaks are likely due to resonant excitation of one of the components in the system. Similar high frequency peaks were found by Bachynski, E. E. in [8]. The explanation for the rise of these peaks in [8] was that they coincided with the 1st pitch frequency. In the figure above these peaks do not coincide directly with the natural frequency in pitch determined by modal analysis in OrcaFlex. These natural frequencies (for pitch) were 2.95 and 4.19 rad/s for A1-B1 and A3-B3 respectively. The higher frequency peaks occurred at 3.7 and 3.5 rad/s for A1-B1 and A3-B3 respectively. This means that the peak in A1-B1 occurs at a frequency larger than the pitch natural frequency with a difference of +0.75 rad/s, and for A3-B3 this difference is -0.69 rad/s. This may be an indication of some erratic behaviour, which may be due to the resolution of the logging intervals in the obtained result or that that these peaks are not in fact due to some resonant behaviour with the natural frequency in pitch, as one would expect from comparison with [8].

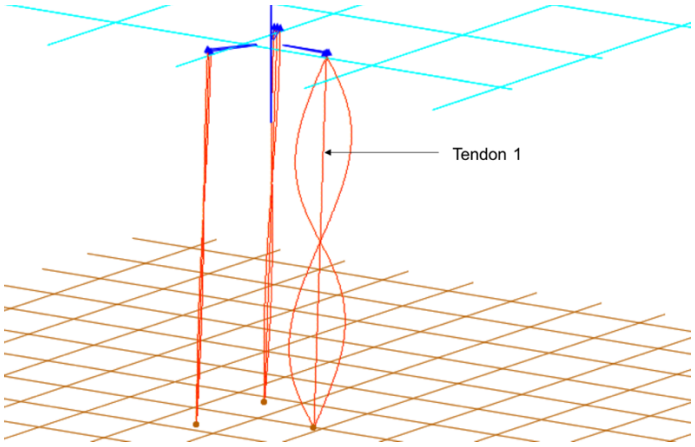

Figure 13-9: Tendon mode shape for A3-B3

For A3-B3 it was found that there is a corresponding mode shape that fits the high frequency peak observed in the spectral density for the tension in tendon 1 (EC3). This mode shape corresponds to mode 11 from the modal analysis conducted in OrcaFlex. As previously stated, which is in line with the pre-defined scope of work, tendon modes are not analysed in this thesis hence these are not discussed in detail. The tendon mode shape is presented graphically from the static-modal analysis in OrcaFlex above. The frequency of this mode corresponds to 3.50 rad/s (identical to the high frequency peak in Figure 13-8). By similar reasoning one can also explain the high frequency peak for A1-B1, as a result of a particular mode shape in the tendons.

The broad span of the tension spectra may also be an indication of somewhat coarse resolution in the logging interval. Note that the fundamental frequency of 0.02 Hz was selected as values lower than this resulted in an incoherent spectral density curve. Slightly larger values for the fundamental frequency tended to yield similar results, but with less detail in the lower frequency areas. If the values were increased by a factor of 10 (i.e. fundamental frequency of 0.2 Hz) the results did not give meaningful results based on the initial prediction of the curves based on what was found in [8]. All in all, one can observe that the linear analysis conducted here results in tension spectra that generally follow the wave spectra, which is in line with what one would expect considering the underlying limitation of this analysis to linear first order wave excitation. Note that the broader span of the tension spectra are likely a result of the load RAOs, maintain a relatively large amplitude for frequencies between 0.25 and 1.5 rad/s.

If one observes the line tension spectra obtained by Bachynski, E. E. (who included non-linear effects in the analyses) in [8], it is clear that there are some differences between these and the results obtained here. Some of the TLPWTs analysed by Bachynski in [8] featured multiple peaks (TLPWT 2) in the tension spectra, corresponding to wave frequency, 2x wave frequency and the pitch bending frequency of the system. Although these two analyses are not directly comparable, one would expect to observe at least some element of similarity, which has been observed to some extent as two separate low and high frequency peaks in the line tension spectra were found here similarly to [8], but occurring for different resonant phenomena. One fundamental difference was evident for EC2 (operational), which expressed significant differences in these results compared to [8]. This is more or less

expected considering the differences in turbine type and dimensions, but also the extent of the dynamic analysis (inclusion of non-linear effects).

Again one should exercise caution when reading further into this comparison (with [8]) considering the fact that the dynamic simulation in this thesis features a statically applied wind load for a 2.3 MW VAWT with significantly different characteristics than the 5 MW HAWT analysed by Bachynski, E. E., who also focused on non-linearity's and dynamic wind conditions. The hulls presented in [8] also differ from the those analysed in this thesis. The comparison is only made to observe any similarities in the results, which may be attributed to the overall characteristic of the tension leg platform principle.

To summarize, the tension spectra typically follow that of the first order wave excitation, which is reasonable considering the limitations to the dynamic simulation conducted in this thesis. The limitations of the analysis are discussed further under the limitations chapter further on in the text.

13.1.6.3 Statistical perspective on effective tension in tendons 1-3

In addition to the tension spectra in tendon 1, it is useful to compare the mean and standard deviations in the effective tension across all tendons for each case under both operational and storm conditions. The mean and standard deviations in effective tension for tendons 1-3 are presented in a similar manner to that observed in [8]. The mean and standard deviations have been divided by the respective pre-tensions from each case based on the values obtained from the static state with no loads applied in OrcaFlex. Note that all these cases feature identical tendon cross-sectional and material properties, but one should keep in mind the increase in tendon length (10 m) for case A3-B3.

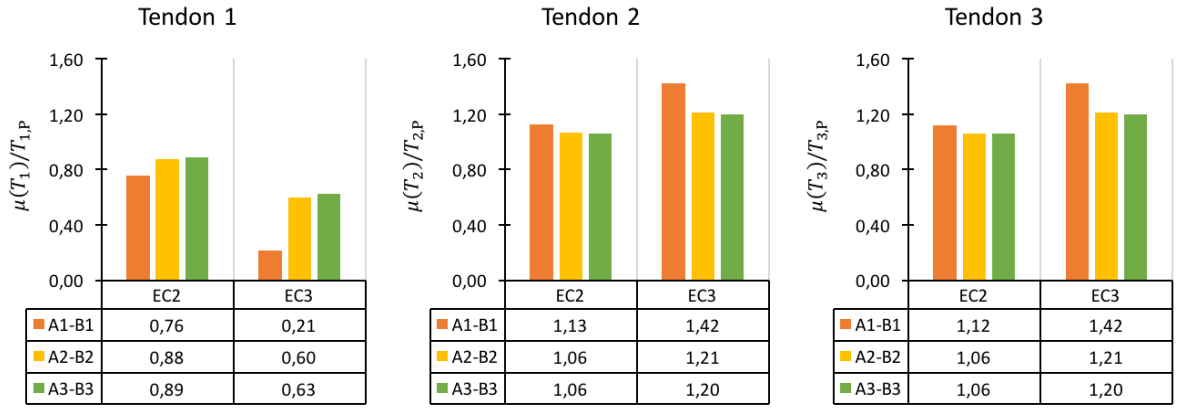

	EC2	EC3
A1-B1	0,76	0,21
A2-B2	0,88	0,60
A3-B3	0,89	0,63

	EC2	EC3
A1-B1	1,13	1,42
A2-B2	1,06	1,21
A3-B3	1,06	1,20

	EC2	EC3
A1-B1	1,12	1,42
A2-B2	1,06	1,21
A3-B3	1,06	1,20

Figure 13-10: Average effective tension for tendons 1-3

As can be observed from the figure above, each mean tension value has been normalized with the initial pre-tension from the static state (excluding wind effects). Tendon 1 features, on average, a lower mean tension value for both the operational and storm conditions (EC2 and EC3 respectively). For tendon 1 it is clear that case A1-B1 has the lowest mean value relative to initial pre-tension. Out of the three cases, lower values were expected for this case (A1-B1) because it featured the smallest pontoon radius and lowest initial pre-tension. Lower initial pre-tension was found in [29] to generally lead to greater tension variation. Case A1-B1 had significantly lower mean values in tendon 1 for both EC2 and EC3 compared to the other two cases. In EC3 the mean value amounted to a value of 0.21, which is consistent with the time history presented earlier where tendon 1 experiences significant slack throughout the simulation period. The differences between the mean values for A2-B2 and A3-B3 were found to be relatively small even though the pre-tension is 34% larger for A3-B3 relative to A2-B2. The pontoon radius of A2-B2 is 34.6% larger than A3-B3, which may explain the reduced effect on the mean effective tension in tendon 1.

On average the tension in tendons 2 and 3, tend to yield larger values than the initial pre-tension, which is expected since these are positioned upwind and are resisting the pitch motion of the vessel due to the imposed loading. In EC3 the mean tension for case A1-B1 yields significantly larger values than what is observed for cases A2-B2 and A3-B3. This also follows the expectation as the net buoyancy force does not vary significantly (some variation is present due to the varying surface profile), meaning that equilibrium between the restoring force and the buoyancy force must be satisfied in the vertical direction in order to prevent large motions in heave. This is backed up by the relatively small variability in the heave motion as presented in the time histories for each case in Section 12.

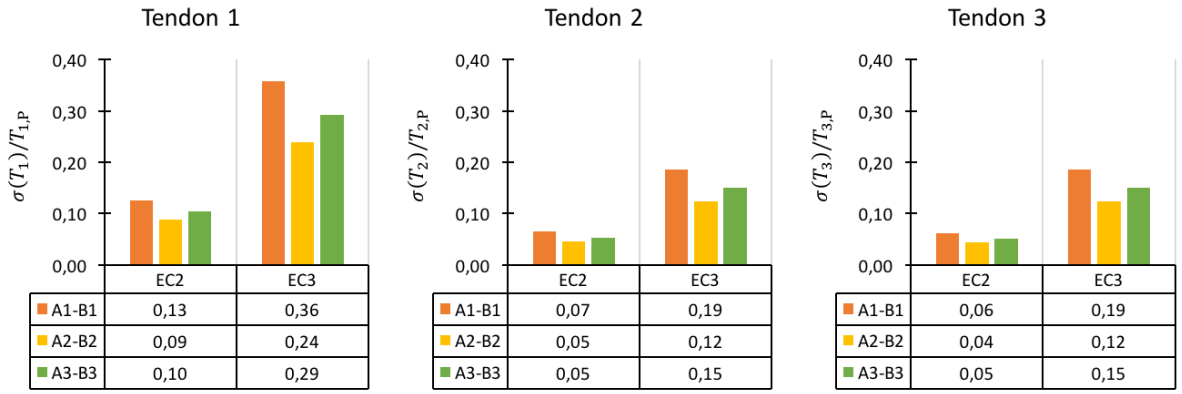

Figure 13-11: Standard deviation of effective tension for tendons 1-3

The figure above shows the standard deviations for the tension in tendons 1-3. The data are separated into their respective environmental conditions where the coloured series represent the different cases studied similarly to that which was presented for the average values earlier. As can be observed from the figure above, it is clear that tendon 1 experiences the largest individual variation in tension compared to the other two tendons. In addition to this the standard deviation tends to be larger in EC3 than for EC2 as is expected considering the fact that these represent a severe storm and operational conditions respectively.

In line with what was discussed for the average values, higher pre-tension tends to result in lower variation in tensile load [29], which is evident from the results as cases A2-B2 and A3-B3 tend to yield lower standard deviations compared to A1-B1, which boasts the lowest amount of pre-tension. However, there is evidence of an additional factor that affects these results, since A2-B2 (with medium pre-tension) yields the lowest standard deviation. This is attributed to the increase in pontoon radius (40% larger compared to A1-B1), which confirms the conclusions made by Bachynski, E. E. in [29], where an increased pontoon radius would result in beneficial tendon characteristics (tension).

If one compares the associated standard deviation in EC3 for tendon 1 and the mean values presented earlier it is clear that there is a relatively large probability of observing slack in this environmental condition, particularly for case A1-B1. This is clear from these two sets of data, since the mean normalized tension in tendon 1 is 0.21 and the standard deviation is 0.36. This implies that tendon 1 will remain slack within the first standard deviation relative to the mean. For case A2-B2, tendon 1 is still in tension at two times the standard deviation, which is an indication of a significant reduction in the probability of occurrence. The same applies to case A3-B3. It should however, be noted that a probability corresponding to two standard deviations from the mean is not sufficient to conclude that the specified case, in its current configuration, is sufficient to survive an environmental condition similar to EC3.

As is clear from these results, the standard deviations in tendon 1 are generally large across all cases, which may have an implication for fatigue. Considering the fact that the tension variation in tendon 1, observed in the time histories presented earlier, was significant for both operational and storm conditions, it is clear that these cases are not suitable to achieve adequate design life in regards to fatigue. This can however, be remediated by altering the tendon cross sectional properties, e.g. material area, to increase the tolerated stress levels. Tendon optimisations are however, not part of the scope as the primary focus in this study is the vessel properties.

It should also be noted that the total initial pre-tension capabilities of this set of cases are significantly greater than what has been analysed, where the theoretical utilization of the total capacity[18] ranges between 34 and 37%. By this it is meant that there are possibilities to remediate the occurrence of slack tendons, as well as improving the overall variation in tension through an increase in pre-tension by replacing some of the permanent ballast with temporary ballast. This will again have a negative effect on the natural periods in surge and sway discussed earlier, effectively creating a larger gap between the target of 45 seconds and the natural periods of each case. Tendon yielding will also likely be an issue for the selected tendon type Tendon_1m. However, increased pre-tension in the tendons only remediate the problem of slack, as there are other underlying issues with the design to be covered,

[18] Under the assumption that all permanent ballast may be replaced by temporary ballast. As discussed earlier (particularly under the spreadsheet results chapter), this is probably not possible as there are limitations with respect to the ballast volumes. These limitations include: available space in the hull internals, as well as ensuring stability in float out. The theoretical utilization capacity is presented for discussion purposes only.

with particular reference to the loading of the connection point between section A and B as discussed in the following section.

13.1.6.4 Connection load

Since the main characteristic of the concept, analysed in this thesis, is the ability to remotely connect a floating offshore wind turbine to a submerged docking station it is necessary to consider the loads in this area. During the early design phase, it was found that the bending moment at the connection is a central issue that must be addressed due to the overall build-up of this concept. The method of establishing the connection between sections A and B was not analysed in this thesis other than a qualitative assessment of the underlying benefits of utilizing a method similar to that of the collet connector, which has a widespread use and considerable track record in many offshore oil and gas projects. The benefit of this collet-type-connector is that it boasts a simple method of establishing a connection without the need for human intervention at the connection area.

Even though these types of connectors typically have a large pre-load capacity in tension, it may not be suitable for absorbing large load variations in the axial direction or in bending. The initial dimensions in [45] are limited to hub ODs ranging between 1.5 and 1.9 m, with bending moment capacities between 4 and 14.9 MNm and associated preloads of 1 to 53.6 MN. A simplified illustration of the imposed loads in this region has been provided below (illustrated for the envisioned collet connector at the mated connection area between A and B).

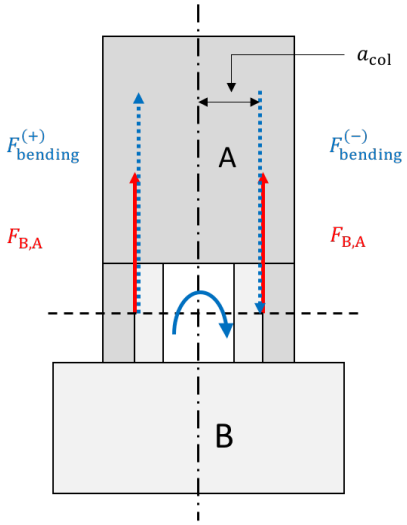

Figure 13-12: Illustration of forces at connection (collet)

As can be observed from this simplified illustration, the bending moment can be transferred to a tensile and a compressive contribution at the outer diameter of the collet connector. The bending moment is illustrated in blue, with the aforementioned force contributions located at a distance a_{COL} away from the centre line. For excessive bending moments the stresses at the connection will become significantly high, and may induce tensile yielding or buckling (compression) of the cross section. Although not directly linked to the scope, it is necessary to evaluate the magnitude of this bending moment as this is likely the region of greatest stress, hence considerations must be made to this region, for this concept to perform as intended. The point to be made from this figure is that an increase in the outer diameter of the collet will lead to a reduction in magnitude of the equivalent vertical forces arising due to this bending moment as a result of the increased moment arm.

As previously mentioned, the vessels used in OrcaFlex during the dynamic simulation phase of this thesis, were built with the local axes positioned at the connection interface between the two structures in order to obtain the local axis pitch moments and vertical loads. The dynamic loads are assessed separately from the statically applied loads (wind load) in OrcaFlex, hence the results presented in the figures below represents the super-positioned static and dynamic load contributions (note that the mean value is affected by the addition of static loads, but the standard deviation is unaffected).

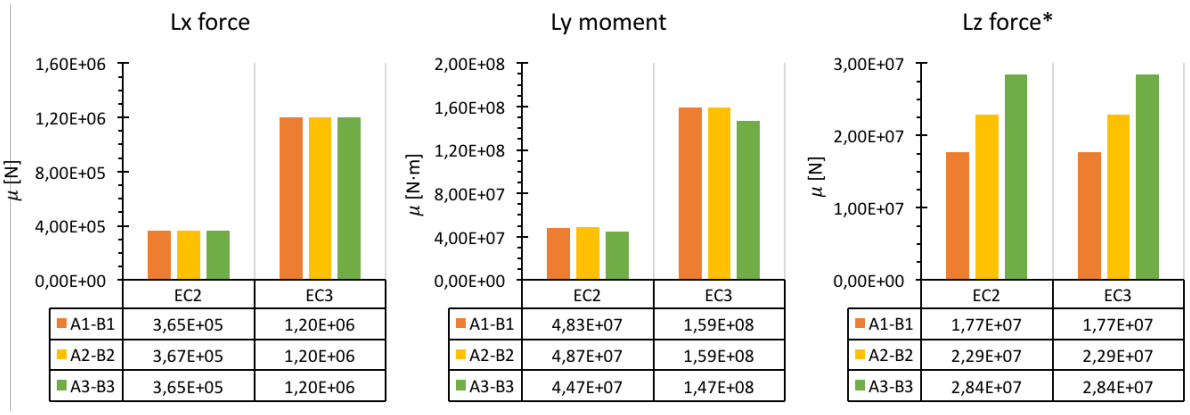

Figure 13-13: Mean connection loads

As can be observed from Figure 13-13, the mean Lx load at the connection coincides with the statically applied wind load for each environmental condition and is identical across each of the three cases. This follows the expectation based on the oscillatory nature of the waves, with zero (or near zero) contribution to the mean in this model. The mean Ly moment is approximately identical to the calculated moment based on the statically applied wind load at the centre of the turbine blades. In contrast to the Lx force, there are some differences between the three cases. This is observed for A3-B3, boasting a shallower draft for section A, which effectively means that the moment arm is reduced by 10 m since the connection point is closer to the sea surface than for the other two cases. A 16% reduction in draft results in a 7.5% reduction in mean Ly moment. The other two cases have identical moment arms, i.e. the drafts of A1 and A2 are identical. This means that there is a reduction in the bending moment at the connection, which is a beneficial trait of A3-B3 compared to the other two cases (in light of mean moment only). The Lz force contribution at the connection point has a mean value identical to the pre-tension capacity of section A for each mated case. The differences observed in this case are due to the varying pre-tension capacities of A1, A2 and A3.

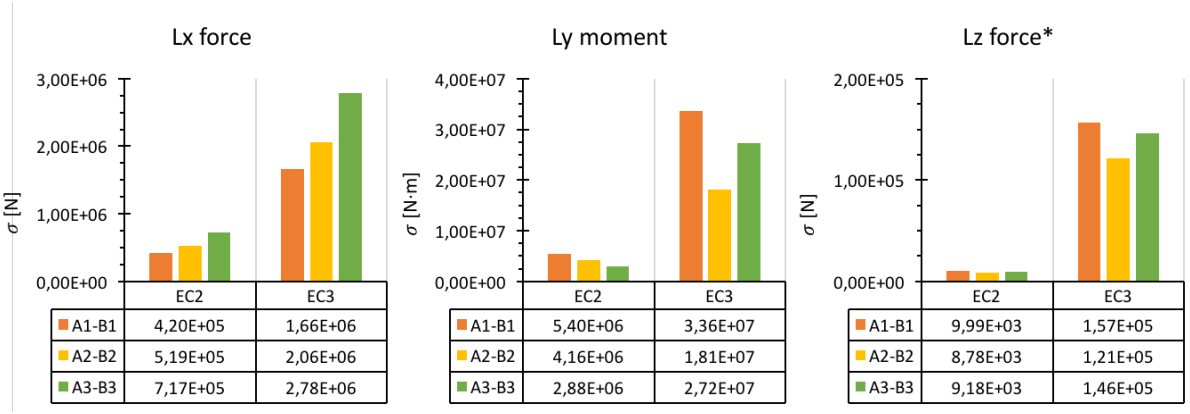

Figure 13-14: Standard deviation of connection loads

Figure 13-14 shows the standard deviation of the connection loads, which are based on the dynamic results only (due to zero variation in the static load). As can be observed from the figure above, there is a clear pattern in the total Lx force, where a subsequent increase is found for each case relative to the previous case. The difference between the two environmental conditions is as expected considering the severity of the sea state in EC3 compared to EC2.

The Ly moment exhibits a different trend than what was observed for the Lx force. In EC2 the standard deviation reduced with each transition from one case to another. This is explainable with reference to the tendons, as these did not enter the slack region in this sea state, and as previously discussed, increased pre-tension gave less variation in the tension in the tendons [29], which again has an effect on the variability of the pitch moment. For EC3 this was not the case, as A2-B2 yielded the lowest standard deviation among the three cases. This is likely attributed to the fact that A1-B1 and A3-B3 experience more frequent occurrences of slack in this sea state. The increased pontoon length may, as such, contribute to a reduction in the variability of the pitch moment, which is beneficial for the studied concept. The Lz force experiences relatively low values in the standard deviation (10^5) compared to the mean value (10^7). This is as expected because this force arises due to hydrostatic stiffness in passing waves, which is relatively insignificant compared to the initial pre-load of this connection in Z.

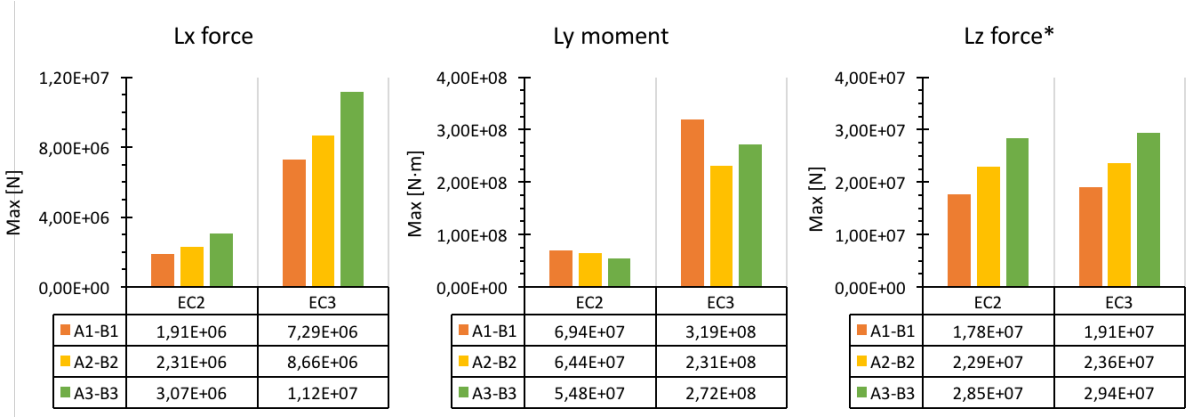

Figure 13-15: Maximum connection loads and moments

The maximum force and bending moment at the connection is also of interest in this context (results in Figure 13-15). The maximum Lx force increases with each case as is generally expected considering the increase in total displacement (reflected by load RAO in surge). The maximum Ly moment is obtained for A1-B1 amounting to a 319 MNm, which is considerably larger than what was obtained for A2-B2 and A3-B3. If one refers back to the collet connector capacities presented earlier, it is clear that the capacity of a "standard" collet is not sufficient to resist the imposed loading, as expected. This means that, even for the operational condition the bending moments (70 MNm) exceed the capacity of the standard connectors. Adjustments must therefore be made to the connection interface to increase bending moment capacity of the collet or by further optimization of the vessel. It is worth noting that the cases analysed all resulted in slack tendons, which means that improvements must be made to the vessels regardless of the connection load/moments.

One such improvement, which will have significant effect in the static state (wind load only) is to reduce the draft of section A. This reduces the moment arm for the wind load, but will likely lead to a significant increase in the wave load (in surge) for the system and subsequently the moment at the connection. The reason for this being the requirement for increased diameter leading to an increase in surge load. The Lz forces are, for an isolated perspective of the vertical load only, likely within spec as the total Lz force ≤ 50 MN for all cases. However, as is clear from the results, the bending moment is critical to the functionality of the system. It is also worth noting that the Lz force is not particularly sensitive to the sea state as is clear from the figure above. Note that shearing effects are not discussed, but may be of importance in this context.

Table 13-8: Performance indicators connection loads

Variable	A1-B1	A2-B2	A3-B3
Displacement	0	+ +	+ + +
Section A draft	0	0	–
Pontoon radius	0	+ +	0*
Pre-tension	0	+ +	+ + + +
Standard deviations of connection loads			
Lx-force	0	+ +	+ + +
Ly-moment	0	– –	–

Since the mean values for the connection loads and moments more or less coincide with the statically applied wind load, it was deemed necessary to evaluate the effect of selected variables on the standard deviation for the two categories of connection loads that were significantly affected by the wave action (Lx force and Ly moment). The table above presents a performance indicator chart based on similar approach observed in [29]. An increase in value relative to case A1-B1 is presented with (+), where each (+) represents an increase between 0–20%. If the result yields a negative value relative to A1-B1 then (–) is used with the same relationship, in terms of percentages, as presented for (+). Note that the pontoon radius for A3-B3 is only slightly different compared to A1-B1 (4%), which corresponds to 1 m and as such the difference is deemed negligible for the purposes of this comparison.

As one can observe from the table above, the increase in the variation of Lx force seems to more or less follow the increase in diameter in the water lien (also linked to displacement). There may also be a correlation with the reduction in Section A draft, as the pontoons are brought further into the wave action zone if this is reduced. This was only the case for A3-B3 as A1-B1 and A2-B2 have identical drafts (for section A).

The Ly moment experiences the greatest difference in A2-B2, which has a significant increase in pontoon radius and only a slight increase in pre-tension. The increase in pre-tension has only a slight effect on the variation in Ly-moment as is apparent from the table above. Note again that the increased severity in slack (for A3-B3 and A1-B1) may have clouded these results significantly, making the comparison somewhat more difficult. A similar method of comparison is advised for further work with cases yielding adequate performance in the storm condition.

Overall, in order to reduce the bending moment at the connector, it seems to be necessary to reduce the draft of Section A, while increasing the pontoon radius. Note that an adjustment of the pre-tension to higher values may also be useful to reduce the variability of the bending moment, although this will not have an effect on the mean value (as this is mostly dependent on the statically applied wind in this thesis). Concluding remarks are presented in Section 14, following the discussion of limitations and sources of error.

13.1.7 Limitations

The scope of work induced several limitations to the overall span of this analysis, along with the given time frame, which has led to some segments of this analysis to become somewhat limited in, for example, the capturing of all relevant effects. In this section the limitations to the analysis are discussed with particular reference to the wind component, and the neglecting of higher order effects.

The main limitation to this analysis, in terms of capturing all relevant effects, is that higher order effects have been neglected despite the fact that these are typically important for TLP systems [26]. As mentioned before, these effects were neglected in order to limit the analysis to first order excitations (linear). Since the model is linearized, effects such as drift, ringing and springing are not captured by the simulations. These effects may have significant effects on the performance of the concept. This limitation was imposed by the scope of work, as the main objective was to conduct a somewhat simplified feasibility study of the concept defined at the start of the project. The idea was that if the system showed sufficient characteristics under a linearized analysis, it would be deemed sufficient for further analysis taking into account these higher order effects (perhaps in future work). It should be noted that the vessel-tendon connections were pin-jointed with zero stiffness. This may not necessarily be the case for the actual construction and should be assessed in future work.

Another main limitation to this analysis is the use of a simplified model to represent the wind contributions. As stated in DNV-RP-C205, the wind speed varies time and height above sea level, and dynamic wind aspects should be considered [25]. In this thesis the wind force has been established from a 1-hour mean wind speed and applied in the form of a point load at the centre of the turbine blades. This means that the representation of the height variation is somewhat limited in addition to neglecting transient effects such as gusts or extreme changes in wind direction [25]. The variation in wind speed about the mean (turbulence) has also not been taken into account. The issue with the approach used in this thesis is that it does not take into account any variations in wind, which means that the true maximum force has, likely, not been captured in the simulation.

Another limiting factor in the analysis is the limited simulation duration of 1-hour. This was specified because the averaging period of the wind velocity was one hour. There are some uncertainties regarding the selected sea state, as mentioned earlier, in terms of simulation period as this was not directly specified in [11]. Hence, it was assumed that these environmental conditions were in-fact representative of a 1-hour sea state. However, one may state that this should not have a direct effect on the comparison of cases, as all of these are subjected to the same environmental condition. This means that if there is an error in the specification of simulation period, this would result in a systematic error, which would have no effect on the basis of comparison.

In contrast to what was analysed in [11], the work in this thesis also assumed full rigidity between the turbine and the hull structure. This means that no tower flexibility was assessed, but this is in-line with the scope of work as the turbine was not modelled in the dynamic simulation phase.

Although the transfer of electricity is critical to this type of system, no power cable was implemented in the model. This may have some effect on the response of the structure, but this was not analysed in this thesis. For future work, this should be included, along with possible design proposals.

As stated in [29] issues with fatigue are important for this type of structure as significant load variations occur in the tendons throughout the operational life of the TLP. The cyclic nature of the pitch and surge loads will induce fatigue and should be assessed in order to find a system, which will have adequate fatigue life. Focus areas for

fatigue include: tendons, connection point between the pontoons and the BDS central column, and the connection interface between the floater and the docking station (Section A and B respectively).

Although some elements of the tow-out operation have been covered in this thesis, with particular reference to intial stability and angle of pitch due to incident wind and waves, this was limited in scope. The tow-out operation was not part of the scope of work other than the intial stability criteria in the un-mated condition.

In regards to the establishment of the hydrodynamic properties of the system, there were some limitations regarding the implementation of the mooring system. The RAOs and potential damping coefficients were established for a free floating condition in the mated state, without including the contribution from the tendons. Since the behaviour of the vessel is altered significantly with the mooring system attached, both in terms of reduced mass (no temporary ballast), and the restraint of motions in certain degrees of freedom, this may have impacted the usefulness of the determined hydrodynamic properties. This may also have imposed some significant effects on the simulation in OrcaFlex as the inertial properties of the vessel is different for these two analyses. In OrcaFlex, the inertial properties were adjusted to reflect the un-ballasted condition. The effects of using this approach vs. the moored model in HydroD has not been covered in this thesis. Another issue with this approach is also the limitation of the analysis to the linear domain, where second order effects were neglected. The hydrodynamic properties of the vessel in the un-moored state has been assumed valid for dynamic simulation of the moored state in this thesis.

13.1.8 Sources of error

13.1.8.1 General discussion of errors

As with most engineering work, there are a number of sources of error to consider for these analyses. In this chapter a general discussion of these are provided with reference to some specific observations made during the course of the presented work.

First and foremost, there may be some underlying errors regarding the spreadsheet stage in this analysis due to the number of variables present as well as the overall complexity of the system at hand. The spreadsheet was programmed in such a manner that output results were generated based on the pre-defined input variables, without having to perform any adjustments to the intermediate calculations. Due to the vast number of calculations leading up to the establishment of, for example, the metacentric height or the static pitch angle, it is not unlikely that there may have been errors in some of the equations. The spreadsheets were checked against the physical properties calculated by Autodesk Inventor to determine whether or not the manually calculated values were accurate or not. This verification approach was limited as not all the manual calculations could be verified against the Inventor model. Overall there has been good agreement between the manual calculations and the values obtained in the external software used to develop the 3-D model and calculation of hydrodynamic properties.

One issue that was encountered during preliminary work on the programming of the spreadsheet was that certain spreadsheets failed to communicate with sufficient accuracy, which required some modifications to be made. Some of these include the grouping of data, which intermittently led to data being collected from the other cells than what was intended. This was fixed prior to the exportation of data, and should not have had any effect on the outgoing results. It is worth noting that the calculations made in the spreadsheet analysis are subject to engineering assumptions, which will have an effect on the overall accuracy of the results. This is particularly evident for the wind model and force calculation used to establish the static pitch angle. Rounding errors may also have been present in this stage, which may have had an effect on the modelling in HydroD, with particular reference to the masses of the system.

The mass models in HydroD were generated with a general accuracy down to the nearest ten tonnes, which is one explanation for the discrepancy between target draft and the calculated draft by HydroD. One particular case that yielded some erratic results in this regard was that of case A2-B2. Cases A1-B1 and A3-B3 were in agreement with the manually calculated values, as there were no significant differences between, for example, the metacentric heights. This was not the case for A2-B2, where a 30% deviation from the estimated metacentric height was found from the results. During the modelling work this was accepted as the actual value, which means that it was initially believed that there may have been some errors in the calculation of $\overline{GM}$ in the spreadsheet as the hydrodynamic model was based on the physical properties of the vessel determined in Inventor (which is largely independent of the spreadsheet). However, it was later found (at the end of the allocated time frame for this thesis) that there may have been an issue in the conversion of the location of centre of gravity, leading to an error in the mass model input. This conversion error is the likely cause of the issue observed with the calculated $\overline{GM}$, because the mesh models for A2-B2 had a consistent over-prediction of $\overline{GM}$ while reaching the target draft. The mass model was

unchanged for the mesh-convergence study, hence the presence of this systematic error. The reason for this error was that, for the manual calculations, the centre of gravity was determined relative to the keel of the vessel, whereas the software (HydroD) specified COG relative to sea level. Manual conversion of this was necessary to specify COG in accordance with the convention in HydroD, and this conversion was subject to human error (in this case).

It is however, not believed that this over-prediction in $\overline{GM}$ will have a significant effect on the results as a whole, as the stability characteristics are altered significantly with the attachment of tendons regardless of this outcome in HydroD. In line with the previous recommendations, attempts should be made to model the entire system in HydroD to observe the effect of including the tendons on the system in addition to including second order effects. This however, requires the generation of a composite model taking into account the panel model (used in this thesis), but also the implementation of a Morison model [33].

As previously stated, human error may also have had an effect on the results as a whole, but this has been limited by double checking the inputs to the software based on the calculated inputs. Double checking inputs will however, not eradicate all errors as evident from the previous discussion regarding the conversion from keel to COG to the conventions used in HydroD for case A2-B2.

Another source of error present in this work is linked to the mesh setup in HydroD. The mesh models generated in this thesis were checked visually for any significantly warped elements, which may affect the results. There seems to be good consensus between the finer mesh models in general, which is a good indicator of a satisfactory mesh model. Errors in this regard are difficult to uncover without generating several mesh models, which was to some extent sufficiently covered in this work.

Last, but not least there is also an inherent risk of numerical error as much of the work in this thesis was conducted using numerical software to determine the hydrodynamic properties of the selected cases, as well as performing the dynamic simulation in OrcaFlex. There was one noticeable presence of numerical error that was observed during the hydrodynamic modelling phase, with particular reference to the development of frequency dependent potential damping matrices in HydroD. Erratic behaviour for damping in yaw (D66) was observed for all three cases, which were likely attributed to numerical noise/numerical errors. Although the software is capable of handling this type of error, through the employment of numerical damping tools, these methods were not used due to lack of experience with such approaches and improper use may adversely affect the other results (e.g. D11). A discussion of this numerical error is discussed in greater detail in the following section with an illustrative example.

13.1.8.2 Discussion on noise

In the hydrodynamic analysis section in this thesis there were some erratic observations in the results regarding the damping coefficients in yaw (D66) across all three of the cases analysed. As discussed under each of these respective cases, the behaviour was likely due noise in the results. The potential damping in this degree of freedom tended to yield significantly lower magnitudes than observed in the other degrees of freedom. For the purpose of discussion, it is assumed that the generated noise is approximated by a sinusoidal function with a certain frequency and amplitude. The point being that if the relative magnitude of the noise is high compared to the output results the effect is more pronounced.

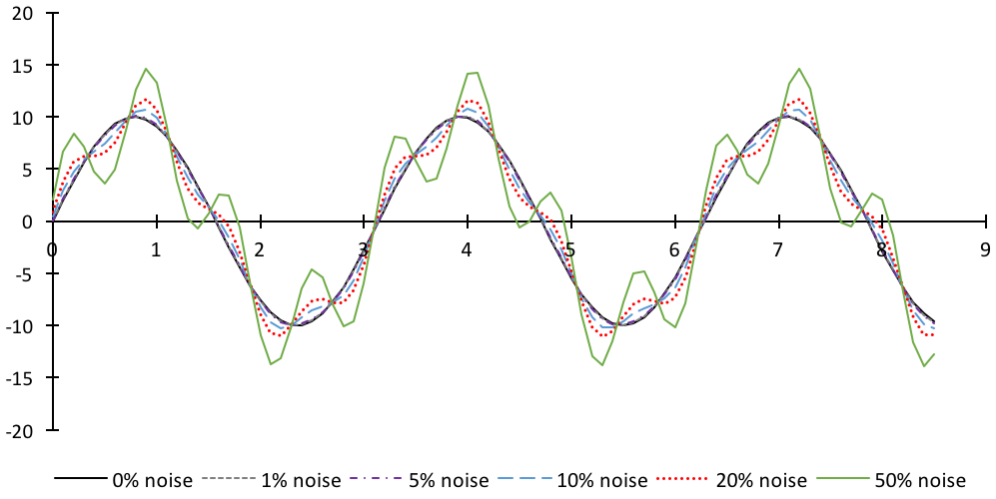

Figure 13-16: Illustration of noise-signal for a sinusoidal profile

This has been attempted illustrated in Figure 13-16 by adopting a fictive sinusoidal signal with an amplitude 10, a frequency of 2 Hz and a phase angle 0°. A set of noise functions are added with relative amplitudes of 0%, 1%, 5%, 10%, 20%, and 50%, a frequency of 8 Hz and a phase angle of 25°. The noise functions have higher frequency than the signal function frequency to present the effect of high frequency noise [58]. The noise function is a fictive representation of what the WADAM user manual refers to as irregular frequencies/numerical problems [30], but reference is also made to Orcina Ltd.'s mention of high frequency responses inherent to the finite element method [58]. High frequency noise can typically be filtered out by employing what is referred to as numerical damping, where the non-physical high frequency responses are damped out [58]. Figure 13-16 presents the sum of the signal and noise for each of these relative amplitudes, the y-axis represents a unit value and the x-axis is the time axis.

As can be observed from Figure 13-16, at 0% noise the signal follows the target sinusoidal profile. Keeping in line with the previous discussion, 0% noise indicates that the magnitude of the signal is significantly larger than that of the associated noise, which is analogous to, for example, D55. On the other end of the spectrum one can observe the effect where a noise/signal ratio of 0.5 (i.e. noise amplitude is 50% of the signal), analogous to D66, is present, where the erratic behaviour is clearly visible in the figure with peaks in the vicinity of 15. This means that if the target is 10, and the output gives 15, then there is a sizeable error inherent in the output results. Although the figure above, has no direct relation with the data collected for the cases analysed in this thesis, it is used to illustrate the reason for the author's belief that the erratic results observed for D66 are, indeed, due to noise associated with the small relative magnitude of damping in yaw.

14 Conclusion

As evident from the presented work, there are many considerations that need to be made in order to make a sound engineering judgment about the overall feasibility of the station keeping solution for this type of structure. In this section some concluding remarks are made on the overall performance of the selected cases in the two environmental conditions, with emphasis on tension in the tendons, motions and connector loads. In addition to this some conclusions are also drawn from the spreadsheet analysis with focus on the initial stability characteristics of the two structures, i.e. stability in float for the floater and the buoyant docking station (BDS).

In general terms the best performance characteristics were found for A2-B2, which featured medium pre-tension and large pontoon radius. For this case the average surge motions were significantly improved relative to the lowest performing case out of the three (A1-B1). The variation in surge due to the wave action was somewhat similar in this regard compared to the other two cases, but yielded slightly lower values. The most significant improvements in motion characteristics of this platform was observed in pitch and yaw. This was found to be attributed to the lower amount of slack observed in EC3, but also to some extent the variation in tendon tension partly due to the increase pre-tension. Although the overall performance in the operational condition (EC2) are somewhat similar across the cases in terms of platform motions, case A1-B1 experienced significant variation in tension for the downwind tendon, which is undesirable in terms of fatigue. Although fatigue elements have not been assessed here, cyclic loads of significant magnitude will have adverse effects on the fatigue life.

For the tension in tendon 1, there was negligible difference between cases A2-B2 and A3-B3 in terms of the normalized mean tension. Case A1-B1 experienced a significant reduction here compared to the other two cases. The variation in tension was however, significantly improved for case A2-B2, which was found to be a result of the increase pontoon radius and pre-tension relative to A1-B1. The data suggest that an increase in pontoon radius significantly reduces the variation in tension, which is in consensus with the discoveries made in [29]. It should be noted however, that all of the selected cases resulted in slack for tendon 1 at some point during the simulation time. Out of the three cases, A2-B2 experienced the least frequent observation of slack.

The loads at the connection point between section A and B was also an important performance indicator to consider. As was discussed earlier, the mean Ly-moment (primarily due to the static wind load) was relatively similar for each of the three cases, except for a slight difference in A3-B3. This was attributed to the reduced draft of section A, which reduced the moment arm for the imposed wind load. The bending moment due to wind exceeded the capacity of the standard collet connectors mentioned earlier, which means that significant improvements must be made in this area. Ideally one should reduce the draft of the vessel to obtain a lower bending moment at the connector, but this would require an increase in diameter. This was done for A3-B3, but because of the increased diameter, the wave load also increased on the structure, which led to an increase in the variation of Ly-moment. However, some of this variation is attributed to the increased occurrence of slack tendons.

In terms of stability for the assessed floaters, it seems plausible that the structure will be possible to mate offshore in line with the envisioned concept. This is based on the fact that float out stability was ensured for the individual components for several combinations of diameters and drafts for the floater (section A), based on the manual calculations. However, if the drafts are to be reduced (to reduce the connection moment), then the design space for the diameters must be increased in order to provide sufficient stability characteristics. The design space for the floater diameters in this thesis were limited to values between 8 and 12 m. It may be beneficial to maintain a larger diameter to draft combination than what has been presented in this thesis. One issue with reduced draft and diameter is that the wave loading in surge will experience a significant increase in magnitude consistent with the observations made to the load RAO in surge for the three cases.

For the BDS there were two plausible methods identified for the tow-out procedure: tow-out with pontoons elevated from the sea surface (float-out) and submerged tow-out. The stability characteristics were evaluated for this structure in both of the aforementioned tow-out methods. However, the float-out method imposed limitations on the dimensions of the pontoons relative to the docking station as a whole. This was due to the binary activation of temporary ballast, where the structure relies entirely on the permanent ballast for stability in float. By activating the temporary ballast, the structure was ballasted to complete submergence, i.e. no freeboard. Therefore, the float-out method imposed restrictions on the permanent ballast fraction (PBF), which had to be relatively large to satisfy the stability criterion. This had adverse effects on the pre-tensioning capacity of the structure, as an increase in PBF led to a reduction in the volume of temporary ballast (used for pre-tensioning). In regards to the tow-out procedure it may therefore be required that the structure be towed to location in a submerged state, unless modifications to the procedures are made.

One should also note that the utilization factor (in terms of total available pre-tension) of the tested cases was somewhat low, meaning that the vessels are likely larger than what is required to achieve the desired pre-tension. This has an effect on the overall loading on the vessel and subsequently the variation in tension. The displacements of the mated vessels are not optimized and further work should be conducted to find vessels that have lower displacement to reduce the wave load on the structure. In this thesis relatively deep drafts were used, which had adverse effects on the moment at the connection and also the mean tension in the downwind tendon.

In conclusion none of the selected cases in this thesis were adequate with respect to fulfilling the no-slack criterion in the extreme environmental condition, which means that more work must be conducted in order to find a suitable combination of cases. The author proposes that the utilization of the total pre-tension capacity be increased in order to maintain similar pre-tension for smaller vessels, i.e. reduce the amount of permanent ballast in favour of more temporary ballast. Floaters with shallower drafts are recommended in order to reduce the initial loss in tension for the downwind tendon due to the imposed wind loading. Shallower drafts will also be beneficial to reduce the bending moment at the connection interface. For further work it is recommended that drafts between 20 and 30 m should be used as a starting point. Note that work must also be done on establishing a proper estimate for the bending moment capacity of the connection system. In line with the recommendations in [29] the pontoon radius should be larger than 30 m in order to reduce the variation in tension, which would be beneficial for enhanced fatigue life and also fulfilling the no-slack criterion.

Although it was not the primary focus of this thesis to provide a cost estimate for the identified structures, some remarks were made regarding the overall cost performance for each of the three cases. This comparative cost performance was limited to a simplified qualitative analysis of the volume of steel required for both the hull structure and the tendons. This analysis was limited to the assumption that a greater volume of steel would lead to increased manufacturing costs, but also increased material costs.

In terms of the concept in general, the results did not indicate that the concept would perform as intended/required with the cases identified in this thesis, but there are several improvements that may be made to find a plausible design, some of which have been discussed earlier. As a general conclusion the loads at the connector are currently too large for the collet type connector with dimensions presented in [45], but improvements in this regard, along with a reduction in the moment arm (draft of section A) should be sufficient to improve the overall performance.

15 Recommendations for future work

The no-slack criterion was violated for all the selected cases analysed in this thesis, hence improvements must be made to remediate the significant variation in tendon tension. As previously discussed there are several means of achieving this, namely reduce the draft of the floater, increase the pontoon radius or increase pre-tension. Combinations of these three methods may also yield improved results. Establishing a more suitable wind model may also improve the results, as the wind loads used in this thesis may have been over conservative. It should be noted that the wind model did not include gust effects or any variation with time. This may, in contrast to the previous statement, indicate that the wind load may be underestimated. Further research on this is advised.

Establishing a dynamic wind model and including the VAWT turbine in the analysis should also be conducted in order to obtain a more complete model of the total system. Implementing a turbine model will require more insight into plausible dimensions of the turbine exceeding the estimations used in this thesis. This should however, be done after establishing a floater-docking station concept that yields sufficient performance in the storm state.

The design of a suitable connector with high bending capacity is another area that needs work as the bending moments that act at the connection area are, based on the results obtained in this thesis, relatively large in magnitude. In order to fulfil the “connect-disconnect” requirement inherent to this concept, it is necessary for this design to be remotely operated, which may impose some restrictions on the design.

A TLP model that takes into account second order effects should also be conducted in order to observe the non-linear behaviour of this station keeping concept. This has been done for HAWT TLPs in [11], but due to the differences in the design, it should also be conducted for this concept.

An analysis of the marine operations aspect of this concept should also be conducted. This must also build on a floater-docking station combination that has sufficient performance in the storm state.

16 References

[1] European Commission, “Climate Action - Paris Agreement,” 5 February 2016. [Online]. Available: http://ec.europa.eu/clima/policies/international/negotiations/future/index_en.htm. [Accessed 8 February 2016].

[2] European Union, “Energy statistical pocketbook 2015,” 8 February 2016. [Online]. Available: https://ec.europa.eu/energy/sites/ener/files/documents/PocketBook_ENERGY_2015%20PDF%20final.pdf. [Accessed 8 February 2016].

[3] European Wind Energy Association, “Wind in power - 2015 European statistics,” European Wind Energy Association, 2016.

[4] European Wind Energy Association, “The European offshore wind industry - key trends and statistics 2015,” European Wind Energy Association, 2016.

[5] Statoil, “Hywind - The floating wind turbine - Fact Sheet,” Stavanger.

[6] European Wind Energy Association, “Deep water - The next step for offshore wind energy,” European Wind Energy Association, 2013.

[7] A. Nergaard, “Fremgangsmåte for forankring av flytende vindturbin samt system for anvendelse ved utøvelse av fremgangsmåten”. Norway Patent 329254, 31 July 2009.

[8] E. E. Bachynski and T. Moan, “Hydrodynamic modeling of tension leg platform wind turbines,” in *ASME International conference on Ocean, Offshore and Arctic Engineering*, Nantes, 2013.

[9] O. T. Gudmestad, Marine Technology and Operations - Theory & Practice, First ed., Southampton: WIT Press, 2015.

[10] J. Odland, “Tension leg platforms and deep draft floaters,” in *OFF515 Offshore Field Development Compendium*, Stavanger, 2014.

[11] E. E. Bachynski, Design and Dynamic Analysis of Tension Leg Platform Wind Turbines, Trondheim: Norwegian University of Science and Technology, 2014.

[12] T. Hansen, “Design of an Offshore Vertical Axis Wind Turbine – Progress report 2012,” NORCOWE, 2012.

[13] T. Hansen and Ø. Torvanger, “Design of an Offshore Vertical Axis Wind Turbine Progress report 2011,” NORCOWE, 2012.

[14] Statoil, “Hywind Scotland Pilot Park,” 2014. [Online]. Available: http://www.statoil.com/en/TechnologyInnovation/NewEnergy/RenewablePowerProduction/Offshore/HywindScotland/Pages/default.aspx. [Accessed 08 May 2016].

[15] Gwind, “Flytende vind (Floating wind),” [Online]. Available: http://www.gwind.no/?page_id=369. [Accessed 08 May 2016].

[16] PelaStar, “PelaStar brochure,” 2015. [Online]. Available: http://pelastar.com/wp-content/uploads/2015/02/PelaStar_Brochure_2015.pdf. [Accessed 08 May 2016].

[17] C. Tracy, “Parametric design of floating wind turbines (MSc - MIT),” 2007.

[18] E. Hau, Wind Turbines - Fundamentals, technologies, application, economics, Third ed., Berlin: Springer, 2013.

[19] S. Eriksson, H. Bernhoff and M. Leijon, “Evaluation of different turbine concepts for wind power,” *Renewable & Sustainable Energy Reviews,* vol. 2008, no. 12, p. 1420–1434, 24 May 2006.

[20] Gwind, “About Gwind,” [Online]. Available: http://www.gwind.no/?page_id=14. [Accessed 15 February 2015].

[21] DNV GL AS, “DNV-OS-J103 – Design of offshore floating wind turbine structures,” DNV GL AS, 2013.

[22] J. Journée and W. Massie, Offshore Hydromechanics, First ed., Delft: Delft University of Technology, 2001.

[23] J. W. Jewett and R. A. Serway, Physics for Scientists & Engineers Volume 1, 8. ed., Lachina Publishing Services, 2010.

[24] Ø. Vollen, Mekanikk for ingeniører - Statikk og fasthetslære (Mechanics for engineers – Statics), Second ed., Bekkestua: NKI Forlaget AS, 2010.

[25] DNV GL AS, “DNV-RP-C205 - Environmental Conditions and Environmental Loads,” DNV GL, 2014.

[26] O. M. Faltinsen, Sea loads on ships and offshore structures, Cambridge: Cambridge University Press, 1998.

[27] Orcina Ltd., “Environment: Data for Random Waves (OrcaFlex User Manual),” 2014.

[28] Orcina, “Theory > Vessel Theory > Stiffness, Added Mass and Damping,” 2016. [Online]. Available: http://www.orcina.com/SoftwareProducts/OrcaFlex/Documentation/Help/. [Accessed 14 March 2016].

[29] E. E. Bachynski and T. Moan, “Design considerations for tension leg platform wind turbines,” *Marine Structures,* no. 29, pp. 89-114, 16 September 2012.

[30] DNV GL, Sesam User Manaual – Wadam (Wave analysis by diffraction and morison theory), 8 ed., Høvik: DNV GL, 2010.

[31] J. N. Newman, Marine Hydrodynamics, Cambridge, Massachusetts: The MIT Press, 1980.

[32] M. B. Sumer and J. Fredsøe, Advanced Series on Ocean Engineering : Hydrodynamics Around Cylindrical Structures (Revised Edition) (Revised), WSPC, 2006.

[33] DNV GL, “Sesam User Manual – HydroD,” DNV GL, Høvik, 2013.

[34] Orcina Ltd. , “Dynamic analysis (OrcaFlex User Manual),” 2014.

[35] A. Naess and T. Moan, Stochastic Dynamics of Marine Structures, Cambridge University Press, 2012.

[36] E. E. Bachynski and T. Moan, “Ringing loads on tension leg platform wind turbines,” *Ocean Engineering,* 2014.

[37] A. P. Boresi and R. J. Shcmidt, Advanced Mechanics of Materials, 6. ed., John Wiley & Sons, 2003.

[38] DNV GL, “DNV-RP-F205 Global performance analysis of deepwater floating structures,” DNV GL, 2010.

[39] Kongsberg Maritime AS, “High Precision Acoustic Positioning - HiPAP”.

[40] J. Sverdrup-Thygeson, *Hywind Demo Construction and Installation (Technip),* 2010.

[41] DNV KEMA, “Hywind Assembly Executive Summary (Statoil),” [Online]. Available: http://innovate.statoil.com/challenges/hywind/Documents/HywindAssemblyAndInstallationStudy.pdf. [Accessed 19 April 2016].

[42] DNV GL, “DNV-RP-H103 Modelling and analysis of marine operations,” DNV GL, 2014.

[43] S. T. R. Nilsen, Artist, *3-D model of vertical axis wind turbine.* [Art]. University of Stavanger, 2016.

[44] Wärtsilä, “Glass Reinforced Epoxy Resin Composite (GRE),” [Online]. Available: http://www.shipham-valves.com/en/materials/glass-reinforced-epoxy-resin-composite-gre. [Accessed 22 April 2016].

[45] Cameron, *Collet Connectors,* 2015.

[46] P. K. Larsen, A. H. Clausen and A. Aalberg, Stålkonstruksjoner Profiler og Formler, 3. ed., Trondheim: Tapir Akademisk Forlag, 2003.

[47] NORSOK, “NORSOK N-003 Actions and action effects,” Standard Norge, 2015.

[48] K. J. Eik and E. Nygaard, “Statfjord Late Life Metocean Design Basis (Statoil),” Statoil, 2003.

[49] DNV GL AS, “DNV-OS-J101 Design of Offshore Wind Turbine Structures,” DNV GL, 2013.

[50] DNV GL, “Sesam User Manual – GeniE Volume 1,” Det Norske Veritas Software, Høvik, 2014.

[51] S. R. Singiresu, The Finite Element Method in Engineering, Burlington, MA: Butterworth–Heinemann, 2011.

[52] Orcina Ltd., “Vessel types (OrcaFlex User Manual),” 2014.

[53] Orcina Ltd., “Vessel types: Sea State Disturbance RAOs,” 2014.

[54] Orcina Ltd., “Vessel types: Stiffness, added mass and damping,” 2014.

[55] Orcina Ltd., “Lines (OrcaFlex user manual),” 2014.

[56] Orcina Ltd. , “General Data: Integration & time steps (OrcaFlex User Manual),” 2014.

[57] R. M. C. Ratnayake, “A mathematical framework for parameter designing under the noise: A case strudy from a conventional turning machine,” *IEEE International conference on industrial engineering and engineering management,* 2013.

[58] Orcina Ltd., “Dynamic Analysis: Calculation method (OrcaFlex User Manual),” 2014.

17 List of figures

18 List of tables

19 List of Appendices

Appendix	Description	Format	Pages	Comment
A	Results from spreadsheet analysis	.xlsx	N/A	Stored electronically on disc
B	Physical properties of combined cases	.pdf	7	
C	Numerical error in A1-B1-Ms2	.pdf	3	
D	Wave record of environmental condition 3	.pdf	5	

Appendix B

Physical properties for the combined cases

Properties exported from AutoDesk Inventor models

Number of pages: 7

A1-B1

Dimensions

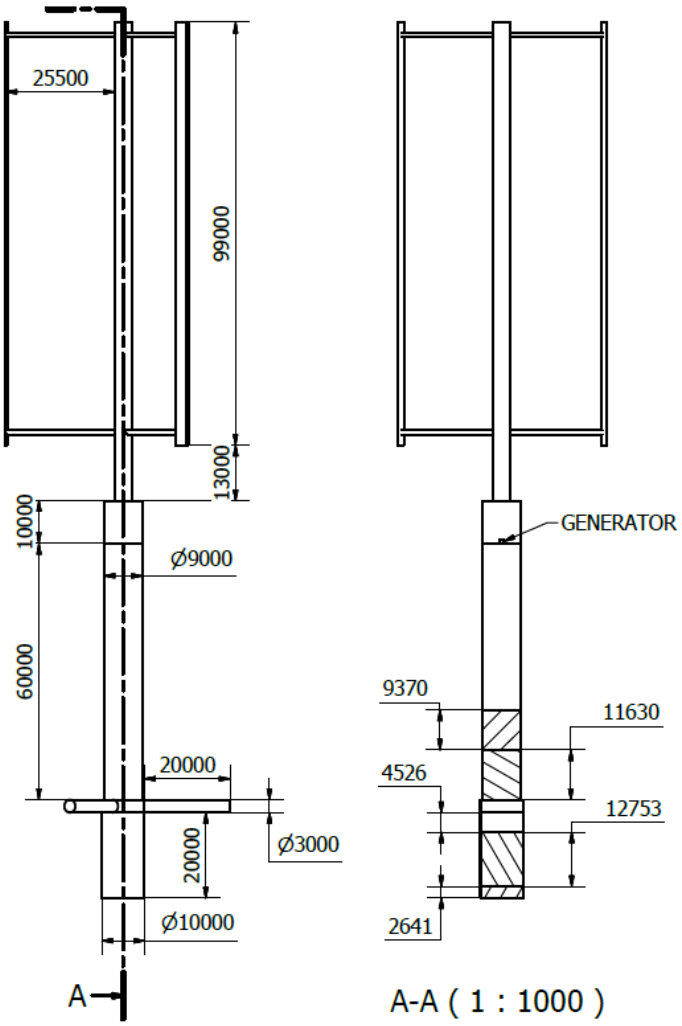

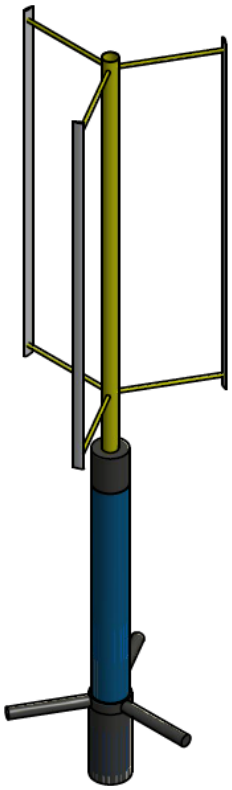

With temporary ballast

General Properties:

Material:	{}	
Density:	2,067 g/cm^3	
Mass:	6195016,067 kg	(Relative Error = 0,002064%)
Area:	1,4535246768347E+010 mm^2	(Relative Error = 0,000365%)
Volume:	2,997775779672126E+012 mm^3	(Relative Error = 0,002064%)

Center of Gravity:

X:	-0,000 mm	(Relative Error = 0,002064%)
Y:	0,000 mm	(Relative Error = 0,002064%)
Z:	33050,864 mm	(Relative Error = 0,002064%)

Principal Moments of Inertia with respect to Center of Gravity

I1:	8,441697930704455000E+015 kg mm^2	(Relative Error = 0,002064%)
I2:	8,441697930704455000E+015 kg mm^2	(Relative Error = 0,002064%)
I3:	2,39695652825926280E+014 kg mm^2	(Relative Error = 0,002064%)

Radius of gyration with respect to Center of Gravity

R1:	36914,2191 mm
R2:	36914,2191 mm
R3:	6220,26461 mm

Without temporary ballast

General Properties:

Material:	{}	
Density:	3,220 g/cm^3	
Mass:	4580501,673 kg	(Relative Error = 0,000917%)
Area:	1,3593948578736E+010 mm^2	(Relative Error = 0,000390%)
Volume:	1,422639786036966E+012 mm^3	(Relative Error = 0,000917%)

Center of Gravity:

X:	-0,000 mm	(Relative Error = 0,000917%)
Y:	0,000 mm	(Relative Error = 0,000917%)
Z:	37513,371 mm	(Relative Error = 0,000917%)

Principal Moments of Inertia with respect to Center of Gravity

I1:	7,717609174289945000E+015 kg mm^2	(Relative Error = 0,000917%)
I2:	7,717609174289952000E+015 kg mm^2	(Relative Error = 0,000917%)
I3:	2,21218295707077840E+014 kg mm^2	(Relative Error = 0,000917%)

Radius of gyration with respect to Center of Gravity

R1:	41047,3257 mm
R2:	41047,3257 mm
R3:	6949,50702 mm

A2-B2

Dimensions

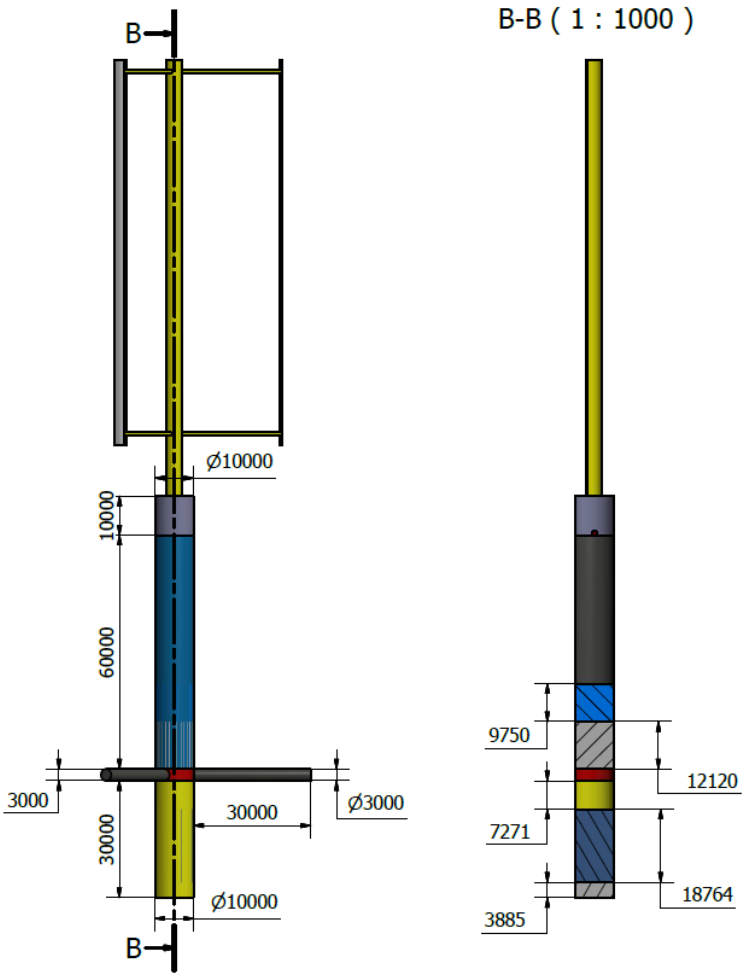

With temporary ballast

General Properties:

Material:	{}	
Density:	2,047 g/cm^3	
Mass:	8134372,529 kg	(Relative Error = 0,002223%)
Area:	1,6593245234124E+010 mm^2	(Relative Error = 0,000320%)
Volume:	3,973295880051755E+012 mm^3	(Relative Error = 0,002223%)

Center of Gravity:

X:	0,000 mm	(Relative Error = 0,002223%)
Y:	-0,000 mm	(Relative Error = 0,002223%)
Z:	37623,127 mm	(Relative Error = 0,002223%)

Principal Moments of Inertia with respect to Center of Gravity

I1:	1,030639720437621200E+016 kg mm^2	(Relative Error = 0,002223%)
I2:	1,030639720437621600E+016 kg mm^2	(Relative Error = 0,002223%)
I3:	3,969953341262100E+014 kg mm^2	(Relative Error = 0,002223%)

Radius of gyration with respect to Center of Gravity

R1:	35595,1977 mm
R2:	35595,1977 mm
R3:	6986,03364 mm

Without temporary ballast

General Properties:

Material:	{}	
Density:	3,326 g/cm^3	
Mass:	5870826,672 kg	(Relative Error = 0,004641%)
Area:	1,5393619116362E+010 mm^2	(Relative Error = 0,000345%)
Volume:	1,764958458813232E+012 mm^3	(Relative Error = 0,004641%)

Center of Gravity:

X:	0,000 mm	(Relative Error = 0,004641%)
Y:	-0,000 mm	(Relative Error = 0,004641%)
Z:	42138,920 mm	(Relative Error = 0,004641%)

Principal Moments of Inertia with respect to Center of Gravity

I1:	9,124642837406528000E+015 kg mm^2	(Relative Error = 0,004641%)
I2:	9,124642837406534000E+015 kg mm^2	(Relative Error = 0,004641%)
I3:	3,690940072387570 60E+014 kg mm^2	(Relative Error = 0,004641%)

Radius of gyration with respect to Center of Gravity

R1:	39423,7841 mm
R2:	39423,7841 mm
R3:	7929,00821 mm

A3-B3

Dimensions

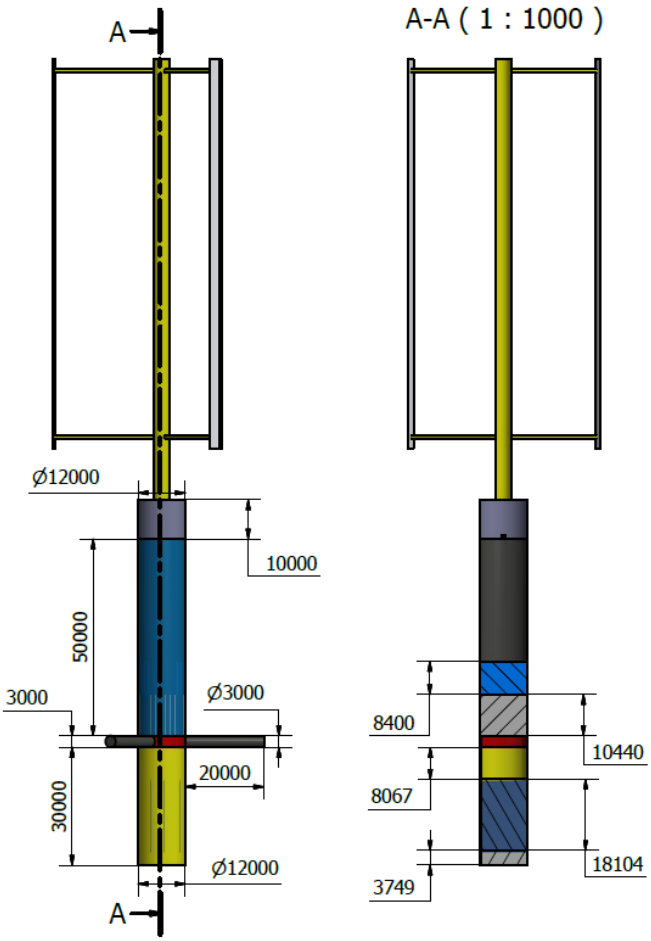

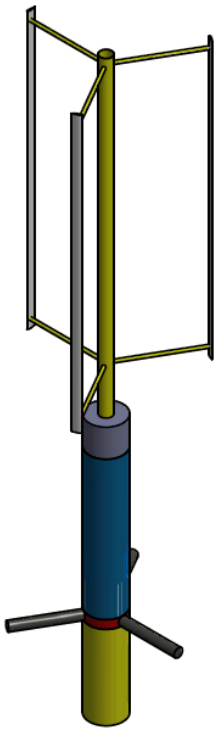

With temporary ballast

General Properties:

Material:	{}	
Density:	1,981 g/cm^3	
Mass:	10054509,962 kg	(Relative Error = 0,002185%)
Area:	1,7404333426424E+010 mm^2	(Relative Error = 0,000305%)
Volume:	5,074404138675259E+012 mm^3	(Relative Error = 0,002185%)

Center of Gravity:

X:	-0,000 mm	(Relative Error = 0,002185%)
Y:	0,000 mm	(Relative Error = 0,002185%)
Z:	33757,102 mm	(Relative Error = 0,002185%)

Principal Moments of Inertia with respect to Center of Gravity

I1:	9,877160808276334000E+015 kg mm^2	(Relative Error = 0,002185%)
I2:	9,877160808276346000E+015 kg mm^2	(Relative Error = 0,002185%)
I3:	3,63109271317423120E+014 kg mm^2	(Relative Error = 0,002185%)

Radius of gyration with respect to Center of Gravity

R1:	31342,6424 mm
R2:	31342,6424 mm
R3:	6009,49827 mm

Without temporary ballast

General Properties:

Material:	{}	
Density:	3,323 g/cm^3	
Mass:	7018053,990 kg	(Relative Error = 0,004777%)
Area:	1,5963532021597E+010 mm^2	(Relative Error = 0,000332%)
Volume:	2,112008068501491E+012 mm^3	(Relative Error = 0,004777%)

Center of Gravity:

X:	-0,000 mm	(Relative Error = 0,004777%)
Y:	0,000 mm	(Relative Error = 0,004777%)
Z:	38015,058 mm	(Relative Error = 0,004777%)

Principal Moments of Inertia with respect to Center of Gravity

I1:	8,567944536838527000E+015 kg mm^2	(Relative Error = 0,004777%)
I2:	8,567944536838542000E+015 kg mm^2	(Relative Error = 0,004777%)
I3:	3,09092944534670560E+014 kg mm^2	(Relative Error = 0,004777%)

Radius of gyration with respect to Center of Gravity

R1:	34940,5688 mm
R2:	34940,5688 mm
R3:	6636,4556 mm

Appendix C

Numerical error potential damping A1-B1-Ms2

Contains plots exported from HydroD regarding potential damping in D66.

Number of pages: 3

The following three figures presents the disappearing numerical error with increased refinement near to the values presented for A1-B1-Ms2.1-3. Notice that the peak between 0 and 1 rad/s is more or less identical across these three cases. The change in the interval 1-5 rad/s gradually worsens for Ms2.2 (compared to Ms2.1), then becomes zero for Ms2.3, which falls in line with A1-B1-Ms1 and A1-B1-Ms3 as previously discussed in the main document. It is thus, based on the underlying evidence provided in this appendix, concluded that the solution is suitably converged for A1-B1-Ms3 justifying its use for development of RAOs and further export to OrcaFlex.

The plots for potential damping D66 are presented in ascending order for cases A1-B1-Ms2.1-3.

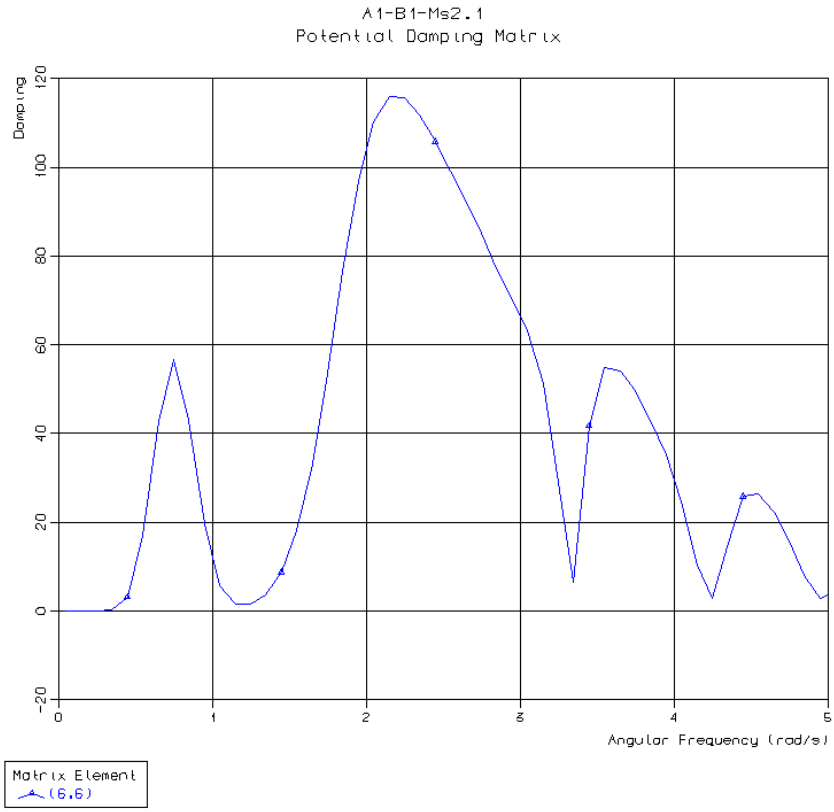

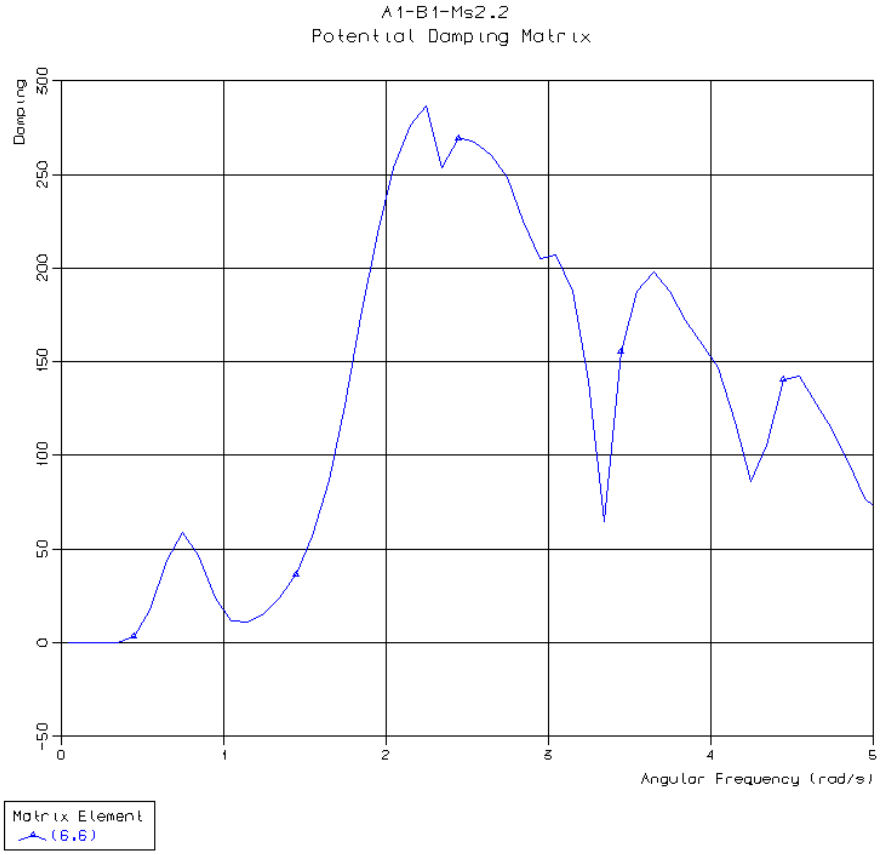
A1-B1-Ms2.2
Potential Damping Matrix
Damping
300
250
200
150
100
50
0
-50
0
1
2
3
4
5
Angular Frequency (rad/s)
Matrix Element
(6,6)

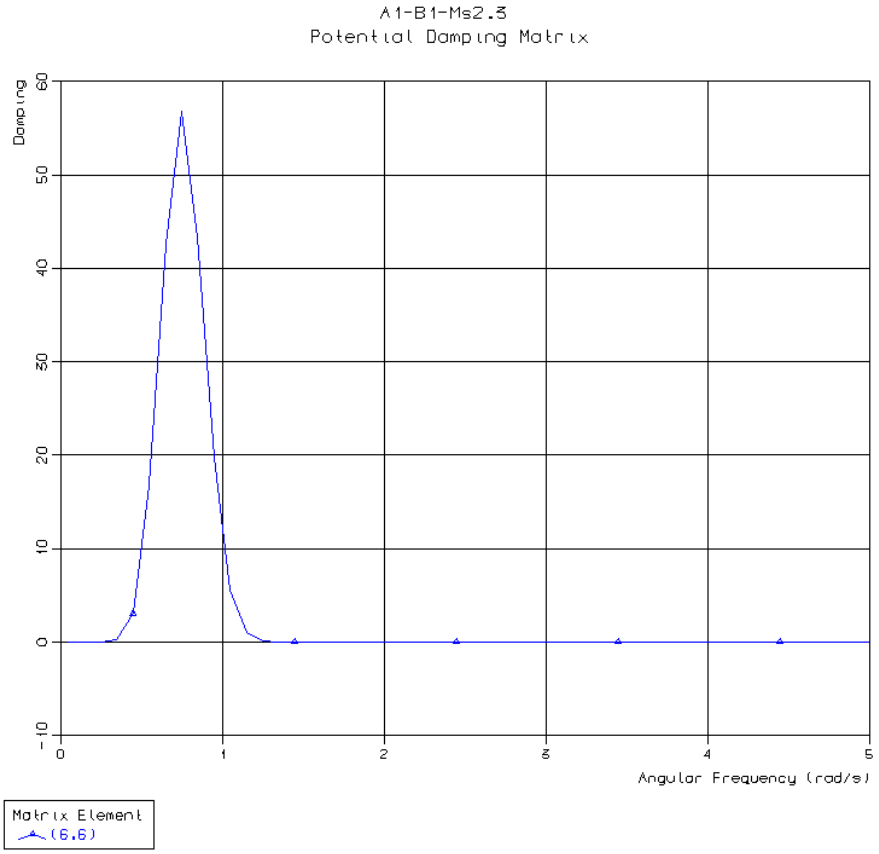
A1-B1-Ms2.3
Potential Damping Matrix
Damping
60
50
40
30
20
10
0
-10
0
1
2
3
4
5
Angular Frequency (rad/s)
Matrix Element
(6,6)

Appendix D

Wave record for EC3

Wave record for environmental condition 3. Generated by JONSWAP spectra with parameters presented in the table below. The wave records are split into intervals of 360 s for the entire simulation duration of 3600 s.

H_S [m]	T_P [s]	T_Z [s]	Spectral peak shape factor
12.7	14.1	10.96	3.3

Number of pages: 5

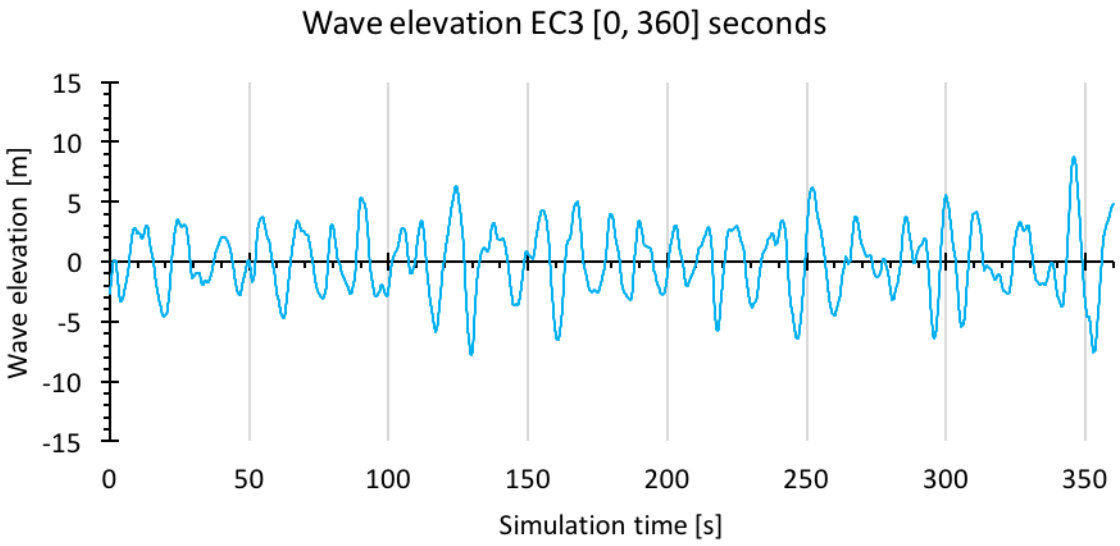
Wave elevation EC3 [0, 360] seconds
Wave elevation [m]
15
10
5
0
-5
-10
-15
0
50
100
150
200
250
300
350
Simulation time [s]

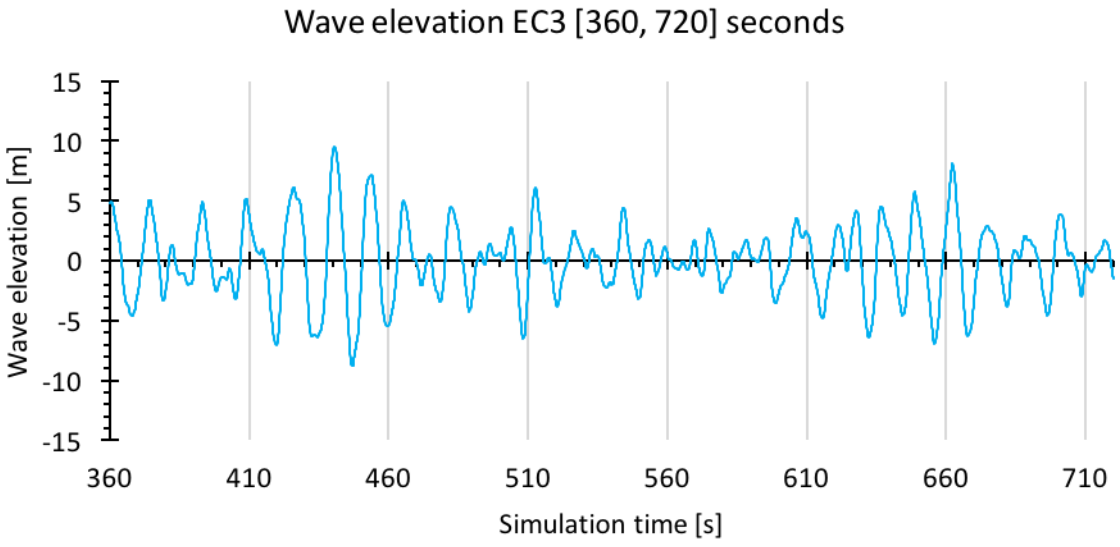
Wave elevation EC3 [360, 720] seconds
Wave elevation [m]
15
10
5
0
-5
-10
-15
360
410
460
510
560
610
660
710
Simulation time [s]

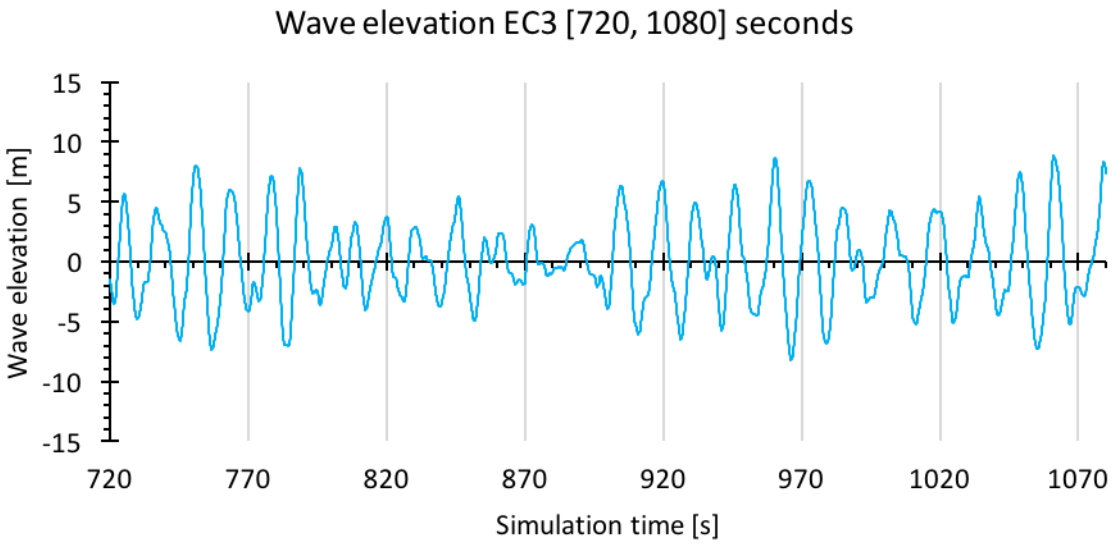
Wave elevation EC3 [720, 1080] seconds
Wave elevation [m]
15
10
5
0
-5
-10
-15
720
770
820
870
920
970
1020
1070
Simulation time [s]

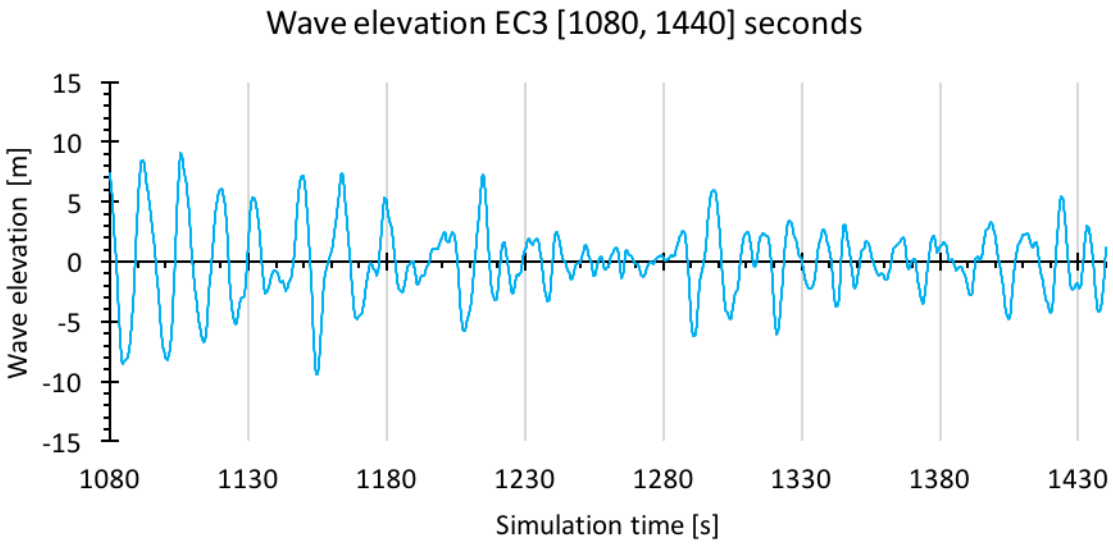
Wave elevation EC3 [1080, 1440] seconds
Wave elevation [m]
15
10
5
0
-5
-10
-15
1080
1130
1180
1230
1280
1330
1380
1430
Simulation time [s]

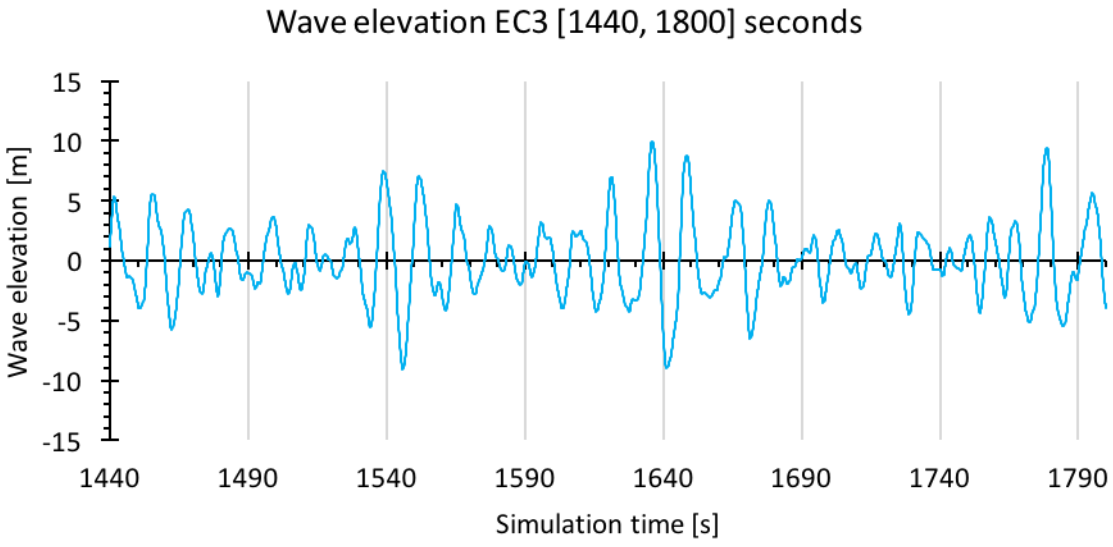
Wave elevation EC3 [1440, 1800] seconds
Wave elevation [m]
15
10
5
0
-5
-10
-15
1440
1490
1540
1590
1640
1690
1740
1790
Simulation time [s]

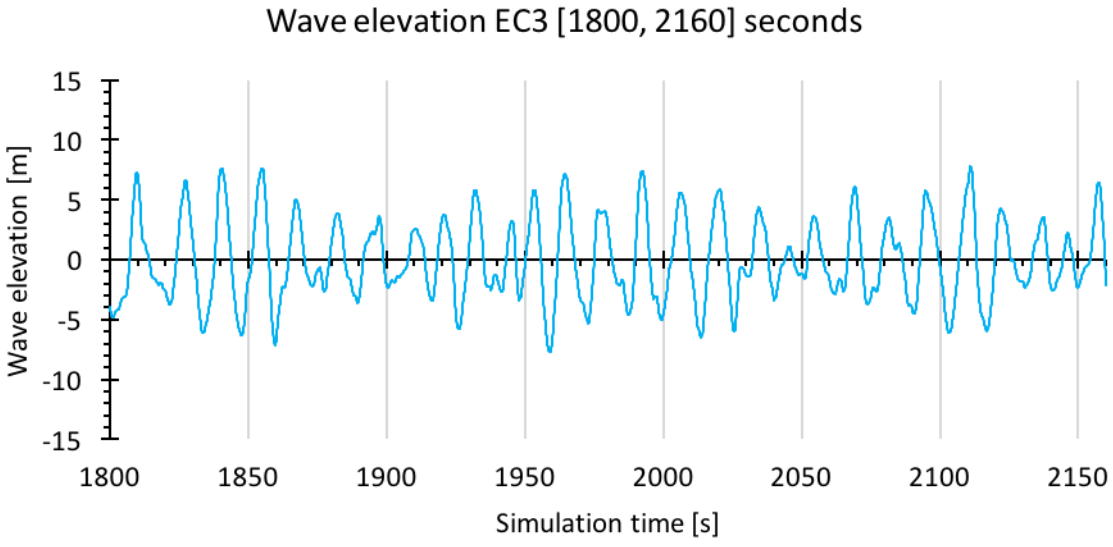
Wave elevation EC3 [1800, 2160] seconds
Wave elevation [m]
15
10
5
0
-5
-10
-15
1800
1850
1900
1950
2000
2050
2100
2150
Simulation time [s]

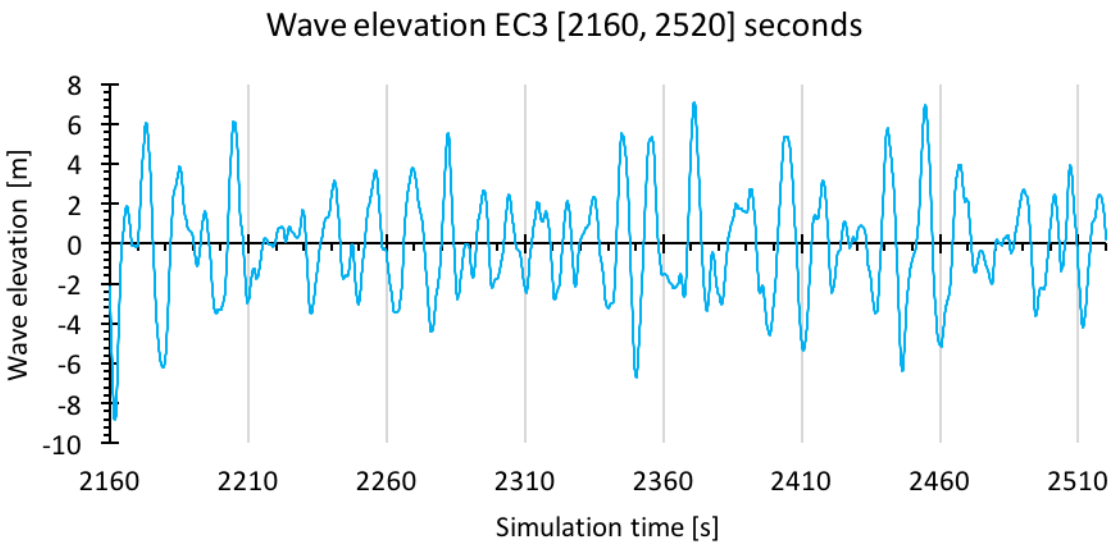
Wave elevation EC3 [2160, 2520] seconds
Wave elevation [m]
8
6
4
2
0
-2
-4
-6
-8
-10
2160
2210
2260
2310
2360
2410
2460
2510
Simulation time [s]

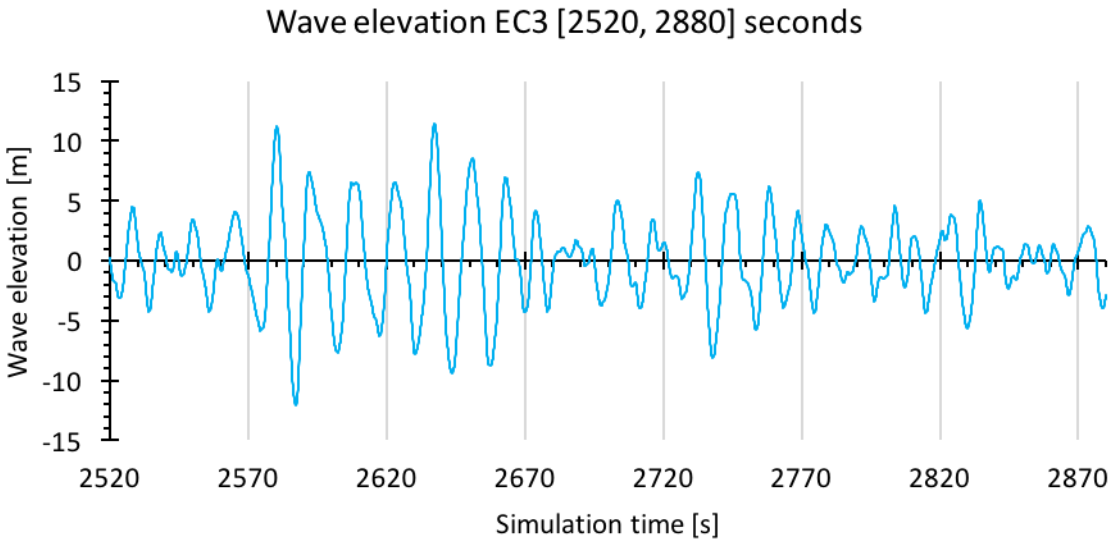
Wave elevation EC3 [2520, 2880] seconds
Wave elevation [m]
15
10
5
0
-5
-10
-15
2520
2570
2620
2670
2720
2770
2820
2870
Simulation time [s]

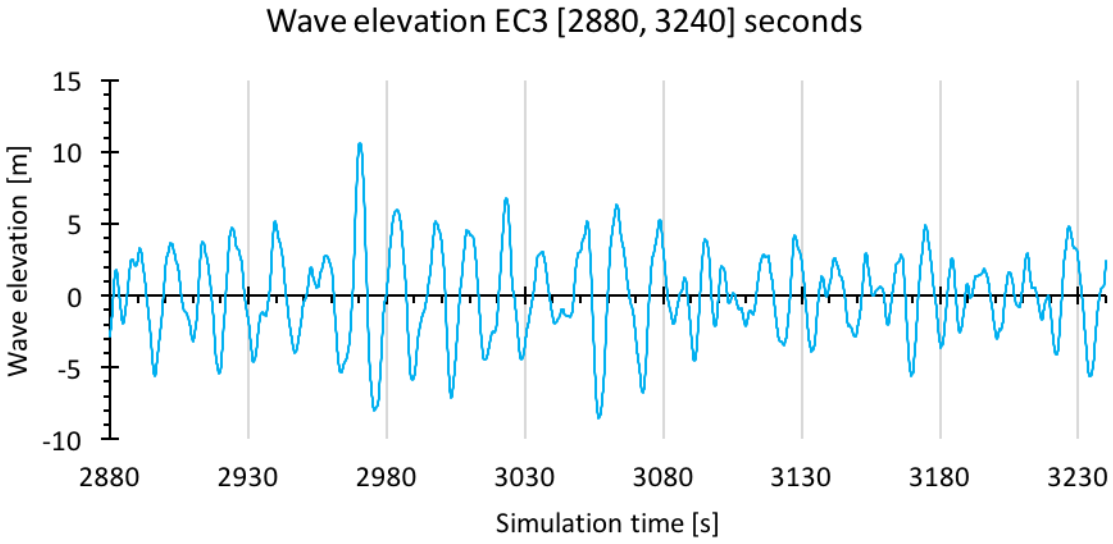
Wave elevation EC3 [2880, 3240] seconds
Wave elevation [m]
15
10
5
0
-5
-10
2880
2930
2980
3030
3080
3130
3180
3230
Simulation time [s]

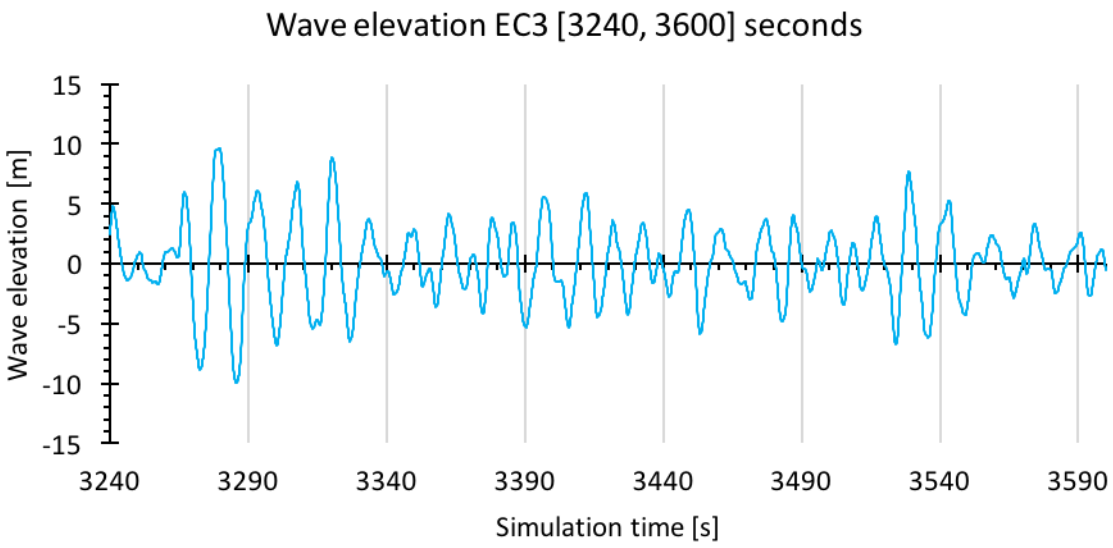
Wave elevation EC3 [3240, 3600] seconds
Wave elevation [m]
15
10
5
0
-5
-10
-15
3240
3290
3340
3390
3440
3490
3540
3590
Simulation time [s]